UNIVERSITY OF STRATHCLYDE

Faculty of Science

COMPACT DIFFUSE CORRELATION SPECTROSCOPY SYSTEMS

By

QUAN WANG

A thesis submitted for the degree of Doctor of Philosophy

May 2024

This thesis is the result of the author's original research. It has been composed by the author and has not been previously submitted for the examination which has led to the award of a degree.

Signed: Quan Wang Date: 15-May-2024

Abstract

Diffuse correlation spectroscopy (DCS) is a powerful tool for investigating microvascular dynamics in deep tissues. It has been used for non-invasive blood flow assessment at the bedside. This study first provides a thorough literature review on system setups (continuous-wave, frequency-domain, and time-domain) and derive corresponding theoretical models. I then present an innovative deep learning algorithm, DCS-NET, which is easy and robust to train, fast, and insensitive to measurement noise for data processing. The absolute blood flow index (BFi) at different depths with/without measurement noise was calculated, followed by a relative blood flow calculation. I then calculated the intrinsic sensitivity, and calculated BFi with varied optical properties and scalp/skull thicknesses finally.

Compared with the semi-infinite, and three-layer fitting methods, I show that the DCS-NET is approximately 17,000 times faster than the traditional three-layer model and 32 times faster than the semi-infinite model, respectively. It provides increased inherent sensitivity to deep tissues compared to fitting methods. DCS-NET demonstrates remarkable noise resilience and is minimally affected by variations in μ_a and μ_s'. Additionally, we have shown that DCS-NET can extract relative blood flow index (rBFi) with a substantially lower error of 8.35%. In comparison, the semi-infinite and three-layer fitting models produce considerable errors in rBFi, amounting to 43.76% and 19.66%, respectively.

Additionally, a DCS prototype is developed by integrating an advanced CMOS single-photon avalanche diode array, which employing a parallel light detection scheme, exhibits exceptional photon-counting throughput. The system tested on a milk phantom, showing SNR gain with the entire sensor is improved nearly 160-fold compared with a single pixel. An *in vivo* blood occlusion test was also performed. In conclusion, our system works well, and this research can offer peers effective guidance to embark on DCS research.

Acknowledgements

The duration dedicated to working on this dissertation has been marked by positive experiences, during which I experienced intellectual and personal growth. I would like to thanks to all those who played a role in the success of my research and the fulfilment of this thesis.

I would like to thank my supervisor Dr David Li for his patience and support in advising me through this research project. David always inspires me to create new ideas, that is the process of viewing a particular problem every imaginable angle, drawing connections to related problems, and then weeding the abundance of ideas down to a few that warrant further pursuit. I hope that I have acquired this ability from David as well as the critical thinking and excitement with which he approaches scientific projects. I also want to thank my second supervisor Dr Yu Chen for her support. I am deeply indebted to David and Yu for their guidance. I hope to utilize the skills and knowledge that they have passed to me and pursue a healthy scientific career.

I am grateful to my colleagues and friend for their direct and indirect support throughout the course of my research. I am happy to have had the opportunity to work through so many challenges with them. I am grateful to have had various interactions with Dr Haochang Chen, who provided me guidance in operating the SPAD systems in both the firmware and software. I am particularly grateful to Dr Dong Xiao, who was generous enough to spend so much time via zoom and share his hard-earned expertise in artificial intelligence (AI) design. I also extend my gratitude to the research group led by Professor Robert K. Henderson at the University of Edinburgh for supporting me with their QuantiCAM SPAD sensor for my PhD and the QuantiC Smart DCS projects. Thank you also to Mingliang Pan for his help with some of the figures that appear in this dissertation. I would also like to thank you the other group members including Dr Wujun Xie, Dr Ziao Jiao, Yuanzhe Zhang, Yu Wang, Zhenya Zang, Xi Chen, and XingDa Li. At the same time, I fondly reminisce about the time I worked with Dr Natakorn Sapermsap on the development of flow cytometry devices.

I extend my heartfelt gratitude to Professor Stefan A. Carp, Massachusette General Hospital, Harvard Medical School, for his invaluable guidance on Monte Carlo simulations using MCX. Additionally, I am deeply appreciative of the insightful discussions with Dr Saeed Samaei and Professor Mamadou Diop from the Department of Medical and Biophysics at the University of Western Ontario, Canada, as well as Professor Johannes D. Johansson from Linköping

University, Linköping, Sweden. Special thanks are also due to Professor Roarke Horstmeyer, Dr Melissa Wu, Dr Lucas Kreiss and Dr Wenhui Liu from the Department of Biomedical Engineering at Durham, North Carolina, United States. Thanks to their patience, as I repeatedly posed questions to them through emails, they tirelessly provided me with answers and guidance.

Last, but not least, a heartfelt thank you to my father, Xuewen Wang and my mother, Zhuhua Fang, for letting me indulge my academic curiosity for far too long. I highly appreciate the encouragements from them during the ups and downs of this Ph.D. journey. Simultaneously, I express gratitude to my sister, Xin Wang for her continual care and support in my life. I dedicate this thesis to all of them, and I am eternally thankful for their love and support!

This work is supported by the EPSRC (EP/T00097X/1): the Quantum Technology Hub in Quantum Imaging (QuantiC), and the University of Strathclyde. I would like to thank EPSRC and the University for providing me with the opportunity to undertake this research project, and without their financial support it would not be possible for me to continue to the research.

Contents

List of Figures

List of Tables

List of Abbreviations

DCS	Diffuse correlation spectroscopy
DCT	Diffuse correlation tomography
SPAD	Single-photon avalanche diode
APD	Avalanche photon diode
PMT	Photomultiplier
SNSPD	Superconducting nanowire single-photon detector
DL	Deep learning
BF	Blood flow
BFi	Blood flow index
CBF	Cerebral blood flow
PET	Positron emission tomograph
SPECT	Single photon emission computed tomograph
XeCT	Xenon-enhanced computed tomography
MRI	Magnetic resonance imaging
DSC-MRI	Dynamic susceptibility contrast magnetic resonance imaging
LDF	Laser Doppler flowmetry
NIR	Near-infrared
NIRS	Near-infrared spectroscopy
DOS	Diffuse optical spectroscopy
CBV	cerebral blood volume
FCS	Fluorescence correlation spectroscopy
DLS	Dynamic light scattering
QELS	Quasi-elastic light
DWS	Diffusing wave spectroscopy
CHS	Coherent hemodynamics spectroscopy
RBC	Red blood cells
AI	Artificial intelligence
CMOS	Complementary metal-oxide-semiconductor
CW	Continuous wave
TD	Time domain
FD	Frequency domain
RTE	Radiative transfer equation
PDE	Photon detection efficiency of detectors
CTE	Correlation transport equation
CDE	Correlation diffusion equation
MRI-ASL	MRI-based arterial spin labelling
RF	Radio-frequency
ANSI	American National Standards Institute
MPE	Maximal permissible exposure
PDE	Photon detection efficiency
LSCA	Laser Speckle Contrast Analysis
LSCI	Laser Speckle Contrast Imaging
DSCA	Diffuse speckle contrast analysis
DWS	Diffusing wave spectroscopy
DUS	Doppler ultrasound
PDT	Photodynamic therapy
TCD	Transcranial Doppler ultrasound
pO_2	Oxygen partial pressure
$CMRO_2$	Cerebral metabolic rate of oxygen
FPGA	Field Programmable Gate Arrays

SNR	Signal to noise ratio
SVR	Support vector regression
EEG	electroencephalogram
ECG	electrocardiogram
2DCNN	2-dimentional convolution neural networks

List of Main Symbols

D	Core diameter of multimode fiber
d	Speckle diameter
SNR	Signal to noise ratio
g	Anisotropy factor
μ_s	Scattering coefficient
μ_s'	Reduced scattering coefficient
$\langle \Delta r^2(\tau) \rangle$	mean square displacement of moving scatterers
D_B	Effective diffusion coefficient for moving particles
V^2	mean square velocity
r_1	Distance between the detector and an approximated positive isotropic imaging source for a semi-infinite geometry
r_2	Distance between the detector and an approximated negative isotropic imaging source for a semi-infinite geometry
$G1/g1$	Unnormalized/normalized electric field autocorrelation function
$G2/g2$	Unnormalized/normalized intensity autocorrelation function
λ	Wavelength
k_0	Wavenumber in the medium
n	Refraction index
α	Fraction of scattering events due to dynamic
β	Coherent factor
τ	Correlation delay time
R_{eff}	Effective reflection coefficient
ρ	Distance between source and detection fibers
J_0	The zeros order Bessel function of the first kind
s_0	Point-like monochromatic light source
l_c	Coherence length
$\Delta\lambda$	The optical bandwidth
w	frequency corresponding to time in Fourier domain
q	The radial spatial frequency
p	Layer number of tissues
ω	The source modulation frequency
T	The correlator bin time interval
T_{int}	Integration time (measurement duration) or the measurement time window
τ_c	Decay constant
$\langle M \rangle$	Average number of photons within bin time T
I	Detected photon count
m	Bin index
s	Photon pathlength
ToF	Time-of-flight
t	Photon time-of-flight
NL	N^{th}-order

List of Publications

Peer-Reviewed Journal Articles

1. **Quan Wang**, Mingliang Pan, Zhenya Zang, and David Day-Uei Li, "Quantification of the blood flow index in Diffuse Correlation Spectroscopy (DCS) using a robust deep learning method", J. Biomed. Opt., 29(1) 2024.
2. **Quan Wang**, Mingliang Pan, Lucas Kreiss, Saeed Samaei, Stefan A. Carp, Johannes D. Johansson, Yuanzhe Zhang, Melissa Wu, Roarke Horstmeyer, Mamadou Diop, and David Day-Uei Li, "A comprehensive overview of diffuse correlation spectroscopy: theoretical framework, recent advances in hardware, analysis, and applications" to appeal in NeuroImage 2024.
3. **Quan Wang**, Mingliang Pan, Haochang Chen, Ziao Jiao, Francescopaolo Mattioli Della Rocca, Robert K. Henderson, and David Day-Uei Li, "High-throughput multispeckle diffuse correlation spectroscopy using a 192 × 128 SPAD camera" to appear in Appl. Phys. Lett. 2024.
4. **Quan Wang**, Yahui Li, Dong Xiao, Zhenya Zang, Yu Chen, and David Day-Uei Li, "Simple and Robust Deep Learning Approach for Fast Fluorescence Lifetime Imaging", Sensors, 22, 7293, 2022.
5. Zhenya Zang, **Quan Wang**, and David Day-Uei Li, “Towards high-performance deep learning architecture and hardware accelerator design for robust analysis in diffuse correlation spectroscopy” to appear in Comput. Meth. Prog. Bio. 2024.
6. Dong Xiao, Zhenya Zang, Natakorn Sapermsap, **Quan Wang**, Wujun Xie, Yu Chen, and David Day-Uei Li, "Dynamic fluorescence lifetime sensing with CMOS single-photon avalanche diode arrays and deep learning processors", Biomed. Opt. Express, 12(6), 3450-3462, 2021.
7. Zhenya Zang, Dong Xiao, **Quan Wang**, Zinuo Li, Wujun Xie, Yu Chen, and David Day-Uei Li, "Fast analysis of time- domain fluorescence lifetime imaging via extreme learning machine", Sensors, 22(10), 3758, 2022.
8. Zhenya Zang, Dong Xiao, **Quan Wang**, Ziao Jiao, Yu Chen, and David Day-Uei Li, "Compact and robust deep learning architecture for fluorescence lifetime imaging and FPGA implementation", Methods Appl. Fluoresc. 11, 025002 2023.

9. Ziao Jiao, Zhenya Zang, **Quan Wang**, Yu Chen, Dong Xiao, and David Day-Uei Li, "PAIM (πM): portable AI-enhanced fluorescence microscope for real-time target detection", Optics and Laser Technology, 163, 109356 2023.

Paper in Preparation

10. Mingliang Pan, **Quan Wang**, and David Day-Uei Li, “Deep learning techniques for diffuse correlation spectroscopy: A Review” manuscript under revisions.
11. Mingliang Pan, **Quan Wang**, and David Day-Uei Li, “Investigation of variables impact on diffuse correlation spectroscopy measurements of cerebral blood flow with continuous-wave analytical models” to be submitted to Biomed. Opt. Express.

Conference Papers

12. Dong Xiao, Zhenya Zang, **Quan Wang**, Ziao Jiao, Francescopaolo Mattioli Della Rocca, Yu Chen, and David Day-Uei Li, "Smart Wide-Field Fluorescence Lifetime Imaging System with CMOS Single-Photon Avalanche Diode Arrays", 44th Annual International Conference of the IEEE Engineering in Medicine & Biology Society (EMBC 2022), Glasgow, UK.
13. Zhenya Zang, Dong Xiao, **Quan Wang**, Ziao Jiao, Zinuo Li, Yu Chen, and David Day-Uei Li, "Hardware Inspired Neural Network for Efficient Time-Resolved Biomedical Imaging", 44th Annual International Conference of the IEEE Engineering in Medicine & Biology Society (EMBC 2022), Glasgow, UK.

Chapter 1 Introduction

1.1 Motivation

Blood flow (BF) in a healthy person ensures stable delivery of oxygen and energy substrates (such as glucose) to and timely removal of metabolic waste products from organs [1]. Specifically, well-regulated cerebral blood flow (CBF) ensures healthy brain functions [2,3], brain metabolism [4,5] and metabolic responses to functional stimuli [6,7]. The average CBF for an adult human is around 50 ml/(100 g min) [8] and around 10-30 ml/(100 g min) for a newborn [9]. Insufficient CBF, even for a brief period, can result in irreversible brain damage, ischemic stroke, and death [10]. On the other hand, excessive CBF has the potential to harm the blood-brain barrier, leading to seizures, headaches, encephalopathy, and stroke [11]. Therefore, monitoring CBF is crucial in unconscious or anesthetized patients. In addition, CBF measurements can also be employed to differentiate between hypoxia and ischaemia, prevent hyperperfusion injury, characterize various hypoxic conditions and neurophysiology, specifically neurovascular coupling, in healthy patients for applications in neuroscience. Ultimately, CBF monitoring also finds applications in noninvasive brain-computer interfaces [12,13].

In fact, the motivation to assess local microvascular blood flow (BF) extends beyond the human brain. Blood flow abnormalities are seen in a wide range of medical conditions affecting various tissues and organs within the human body. Measurements of blood flow have shown to be beneficial from paediatrics to adults in conditions such as cancer and peripheral arterial diseases, as well as in monitoring muscle diseases and understanding normal exercise physiology. Example applications are:

- Perinatal care [14,15]
- Neonate cardio-cerebral vascular diseases [16,17]
- Neonate brain development [18]
- Children brain health evaluation [19]
- Cardio-cerebrovascular diseases [20]
- Skeletal muscle and exercise physiology [21]
- Tumor diagnosis and therapy evaluation (including human breast [22], prostate [23], head, and neck tumor [24])

Among these applications, breast cancer stands as the most commonly diagnosed and the leading cause of cancer-related deaths in women [25]. As a result, even slight enhancements in detecting breast cancer could significantly impact the identification of this disease. Prior research indicates that blood flow in cancerous tissues is higher compared to normal tissues [26,27].

1.2 Project Aims

Usually, pulse oximeters, cerebral tissue oximeters or Doppler-based ultrasound scanners employed in modern medical diagnostics, allowing for the continuous, non-invasive monitoring of patients' vital parameters and helping in the early detection and treatment of potentially life-threatening. But Oximeters are primarily designed to measure oxygen saturation levels in the blood instead of blood flow. Ultrasound Doppler devices require a trained and skilled operator at the bedside and patients need to receive anaesthesia. However, the toxicity of anaesthetic drugs can post threats on immature neural systems. There are others CBF measurement technique, including positron emission tomography (PET) [28] single photon emission computed tomography (SPECT) [29], xenon-enhanced computed tomography (XeCT) [30], dynamic susceptibility contrasts magnetic resonance imaging (DSC-MRI) [31], and arterial spin labeling MRI (ASL-MRI) [32]. However, they only provide 'snapshot' observations and cannot provide continuous monitoring. In practical scenarios, there is only a short gold period within 6-24 hours from the first attack that newborns should receive timely treatment. In addition, these imaging modalities are often limited by practical and technological hurdles. For example, while intended for use throughout a patient's hospitalization, these devices are costly and not portable. Furthermore, MRI, PET, and CT techniques require a supine scan and cannot offer continuous BF measurements for clinically unstable patients. Notably, PET and SPECT entail additional risks of radiation exposure. Laser Doppler flowmetry (LDF) [33] can only observe superficial tissue blood flow, and tissue samples need to be thin to ensure a detectable power level. For a thorough comparison of these modalities, readers are encouraged to refer to the reviews [3,8,34].

Hence, there is a need for an affordable, continuous, noninvasive, portable, bedside, and nonionzing imaging/sensing modality tailored for CBF measurements. In the following

paragraph, I present a detailed description of the necessary specifications for an idealized CBF measurement. Ideally this measurement should have the following characteristics:

- Providing a centimeter penetration to effectively distinguish regional flow variations across the entire brain.
- The measurement would be acquired using a non-ionizing, non-invasive, and portable instrument that complies with all applicable safety standards.
- Resilient to motion artifacts and ambient light, factors that support effective and continuous long-term monitoring in a clinical environment.
- Instrumentation and per-measurement expenses should be low, and the measurement technique should be suitable for patients of all age groups.
- High sensitivity on the smallest physical scale.
- Operating in real-time with a temporal resolution in the millisecond range in vivo sample dynamics measurement.

Diffuse correlation spectroscopy (DCS), also known as diffusing wave spectroscopy (DWS), initially pioneered by Boas *et al.* in the 1990s [35], is a noninvasive technique for real-time CBF measurements [36]. Nevertheless, DCS faces several challenges: 1) there is a trade-off between SNR and the detection depth, as deeper detection requires a greater source-detector separation, reducing SNR and photon detection. It is well known that the detection depth ranges approximately one-third to one-half of the source-detector separation (ρ). 2) a single source-detector pair cannot discriminate photon paths, leading to potential contamination from extracerebral tissues [37]; 3) Traditional fitting methods to extract *BFi* are computationally intensive and less accurate at lower SNR levels [38].

To overcome the above limitations, several techniques have been investigated, including multispeckle detection strategies [12,39,40], time-domain DCS (TD-DCS) [41,42], interferometric approaches [43–45], improved analytical modelling [46,47], and longer wavelength approach [48]. Motivated by these strategies, I summarized a theoretical framework and conducted an extensive literature review. Subsequently, I introduced a deep DL technique for analyzing DCS data and assembled a DCS prototype with a 192 × 128 SPAD sensor.

To investigate the viability and potential benefits of DCS-NET and DCS prototype with 192 × 128 SPAD arrays, the following primary research goals were pursued in this thesis:

1. Develop the DCS-NET model;
2. Derive and validate a continuous-wave three-layer analytical model;
3. Compare the DCS-NET model with semi-infinite and three-layer analytical models in terms of BFi estimation time, relative BFi, errors in BFi estimation induced by optical properties and geometry parameters (e.g., thickness of scalp and skull), and BFi estimation varying source-detection separation;
4. Demonstrate the intrinsic sensitivity and SNR benefits of using SPAD arrays.

1.3 Main Achievements

The thesis yields the following summary of contributions to knowledge:

1. I conducted a thorough literature review to provide peers with valuable guidance for initiating research in DCS. Given that newcomers to the DCS field might feel overwhelmed by its complex theoretical framework and the array of component options and system architectures, this review servers as a comprehensive introduction. The thesis presents an in-depth overview of DCS, covering system setups (continuous-wave, frequency-domain, and time-domain) and deriving corresponding theoretical models. Additionally, considering the widespread use of deep learning (DL) techniques in data analysis, we review both recent advancements and our contributions in applying DL to DCS. The exploration concludes by highlighting potential applications in medical diagnosis.

2. I have adopted a simple DL method to address the challenge of complex DCS data analysis. This algorithm offers unparalleled advantages, encompassing an efficient architecture with reduced parameters, quicker training times, accelerated analysis speeds, and a robust capability to address noisy DCS data. In contrast to traditional fitting approaches, the proposed algorithm improves computational speed by more than 17,000 times and 32 times over three-layer and semi-infinite models, respectively. It also improves the accuracy of rBFi estimation (see Chapter 4).

3. I have developed a prototype DCS with the aim of improving SNR. Our configuration incorporates a parallel light detection strategy using the cutting-edge CMOS 192 × 128 SPAD array. The system was validated on a milk phantom and the results showed that the SNR gain of the entire sensor is improved by nearly 160 times compared to a single pixel (see Chapter 5).

1.4 Thesis Outline

In Chapter 2, I provided the literature review pertinent to cerebral blood flow (CBF) measurements techniques, including non-optical and optical methods, with an emphasis on DCS. DCS is ideal for deep tissue analysis, offering continuous, noninvasive, and real-time CBF measurement, but its depth penetration and spatial resolution are limited by the properties of diffuse optics. I review the various approaches that have been used to overcome these limitations.

In Chapter 3, I presented the theoretical basis of DCS and derived analytical models (semi-infinite, two-, and three-layer models) for CW-DCS, TD-DCS, and FD-DCS (only for semi-infinite model). This chapter also includes analytical simulations based on these derivations and a summary of the noise DCS model with corresponding simulations.

In Chapter 4, I proposed a deep learning model, DCS-NET, for analyzing DCS data, addressing research goals 1–4 in this chapter. The model's performance was validated using simulation $g_2(\tau)$ from Monte Carlo simulations. Traditionally, BFi is derived through nonlinear least-square fitting of the measured intensity autocorrelation function (ACF), which is computationally demanding and sensitive to measurement noise and variations in optical properties (absorption coefficient μ_a and reduced scattering coefficient μ_s') and scalp and skull thicknesses. I assessed the impact of these variables on BFi and β estimations using DCS-NET and traditional fitting methods across various conditions, including different source-detector distances. I also describe potential barriers and limitations of the DL technique.

Chapter 5 focuses on the research goal 5, where I demonstrated the DCS prototype and tested it on a milk phantom. Quantitative analysis showed an approximately 5-fold enhancement in the SNR gain over a previously reported 32 × 32 multispeckle DCS system.

In Chapter 6, I conclude my research by providing a summary of the thesis and outlining the contribution to knowledge it contains. Additionally, I examine the implications of my findings in comparison to similar work by other researchers, discuss the limitations of the research, and suggest future avenues for extending the investigations presented in this thesis.

Chapter 2 Literature Review

2.1 Overview of Blood Flow Measurement Modalities

The ideal blood flow measurement would accurately capture data from both macro- and micro-vasculatures with millisecond temporal resolution. These measurements should be continuous, noninvasive, and safe for subjects, ideally extending into deep tissues. Regrettably, there is currently no existing modality that meets all of these ideal criteria [49]. To date, several imaging techniques are available to assess CBF, each possessing unique strengths and weaknesses. These modalities can be broadly categorized according to the criteria outlined in Table 2.1.

Table 2.1 Main properties of current technique to measure cerebral blood flow based on Ref. [8]

Method	Technique	Invasiveness	Spatial extent	Absolute or relative	Snapshot or continuous
Intravascular measurements	N_2O inhalation	✓	Global	Absolute	Snapshot
	Thermodilution	✓	Global	Absolute	Continuous
Nuclear medicine	^{133}Xe, ^{85}Kr	✓	Regional	Absolute	Snapshot
	SPECT	Minimally invasive	Local	Relative	Snapshot
	PET	Minimally invasive	Local	Absolute	Snapshot
X-ray imaging	Xe-CT	×	Local	Absolute	Snapshot
	Perfusion CT	Minimally invasive	Local	Absolute Or Relative	Snapshot
Magnetic resonance imaging	DSC-MRI	Minimally invasive	Local	Absolute Or Relative	Snapshot
	ASL	×	Local	Absolute	Snapshot (repeatable)
Ultrasound	TCD	×	Regional	Relative	Continuous
	Transit-time ultrasonic flowmetry	✓	Regional	Relative	Continuous
Thermal diffusion	TDF	✓	Regional/local	Absolute	Continuous
Biomedical optics	LDF	✓	Regional/local	Relative	Continuous
	DCS	×	Regional/local	Relative	Continuous
	Qualitative NIRS	×	Regional/local	Relative	Continuous
	Quantitative NIRS	Minimally invasive	Regional/local	Absolute	Snapshot
	CHS	×	Regional/local	Absolute	Continuous

In this chapter, there is a brief overview and evaluative analysis of methods for measuring CBF. The chapter is divided into sections discussing non-optical methods, optical methods, and hybrid approaches. We then focus on DCS, including an overview of instrumentation and applications. Non-optical methods are reviewed at the beginning of the chapter. These methods typically do not excel in providing continuous, noninvasive, and portable monitoring of CBF.

2.2 Non-Optical Methods

Except for transcranial Doppler ultrasound (TCD), all the non-optical methods outlined in this section have certain limitations. These drawbacks include invasive measurement procedures, impracticality for bedside use due to non-portable equipment and the need for patient transportation, single measurements instead of continuous monitoring, and high associated costs involving both the instrument and the time required to perform it.

2.2.1 Thermal Diffusion

Thermal diffusion flowmetry (TDF), also known as the heat or thermal clearance method, quantifies the absolute blood flow in the cerebral cortex or in the white matter [50]. This method has the capability to assess a spherical volume approximately ranging from 20 to 30 mm^3 surrounding the probe. TDF offers continuous bedside monitoring of local CBF with an excellent temporal resolution, but in a notably invasive manner. TDF operates on the principles of thermal transfer facilitated by the conductive characteristics of brain tissues and the convective influences of BF. Temperature measurement is achieved using a thermistor, which detects changes in electrical resistance. The TDF probe comprises two thermistors – a passive one for monitoring brain temperature, kept at a constant temperature (neutral plate), and an active one maintained at a slightly elevated temperature (heated plate). However, to ensure safety, TDF is refrained from use in patients with a high fever to prevent additional heating of the tissue. Additionally, the reliability of the technique may be influenced if the probe is positioned near large vessels [51]. If the probe is incorrectly positioned or undergoes displacement, the validity of the assumption that the heat-conducting properties of tissue remain constant becomes invalid [8].

2.2.2 X-ray Techniques

Xenon computed tomography (Xe-CT) includes obtaining an initial computed tomography (CT) scan of the patient's brain, inhaling a stable mixture of xenon gas, conducting additional CT scans, and subtracting the baseline values from the xenon-enhanced CT images in a sequential manner. This process results in a series of voxelwise tracer accumulation curves, enabling the calculating of cerebral blood flow (CBF) for each voxel. Xe-CT is notably prone to artifacts caused by patient motion. Despite being noninvasive and offering an absolute measurement, the instrument and the necessary gas for this technique are both costly [8]. Additionally, its

capacity to measure CBF is confined to obtaining snapshot results at specific discrete time points [52]. Dynamic perfusion computed tomography (PCT) is a technique akin to Xe-CT. It begins with obtaining a baseline CT scan of the patient's brain without contrast. Following this, an iodine-based contrast agent is administrated intravenously. Subsequently, a series of rapidly acquired CT scans captures time-concentration curves of the contrast agent, allowing for the inference of CBF. Although this method does not achieve real-time acquisition, it completes in a relatively short period of 40 seconds. PCT boasted a spatial resolution of approximately 1.5 mm, making it competitive with magnetic resonance imaging (MRI) in this aspect [3]. Similar to Xe-CT, PCT is susceptible to artifacts due to patient movement and is not suitable for continuous monitoring.

2.2.3 Intravascular Measurements

The Kety-Schmidt arteriovenous difference method [53] emerged as the widely adopted method for measuring global cerebral blood flow after its release in 1945. This procedure includes the patient inhaling nitrous oxide (N_2O) and then utilizing its characteristics as an intravascular tracer that can freely diffuse into the brain. After inhalation, the duration needed to achieve a stable concentration of $N_2O_{arterial} = N_2O_{venous}$, (determined from blood samples taken from the femoral artery and right, respectively) is observed to be inversely correlated with CBF. This yields an immediate quantitative result at the bedside [8]. This procedure is somewhat time-intensive, taking approximately 10 – 15 minutes to reach a stable concentration. Throughout this period, CBF is presumed to remain constant. Moreover, this method is invasive, making it impractical for clinical applications, and it is limited to measuring global CBF. Continuous jugular thermodilution operates similarly to the previously mentioned technique, but it employs a cold miscible tracer as the intravascular marker. This usually involves catheterizing an internal jugular vein to enable the injection of a suitable fluid tracer. The process also includes measuring the temperatures of the blood and its mixture with the tracer. Calculating jugular BF is then achieved by considering factors such as the rate of tracer fluid injection, the densities of blood and the tracer, and their mixture. Assuming equal drainage of the brain by the left and right internal jugular veins and knowing the total brain mass, CBF can be deduced from jugular blood flow. An alternative non-continuous method involving a double-indicator dilution technique has also been suggested, utilizing injections of indocyanine green (ICG) dye and iced water [54].

2.2.4 Nuclear Medicine

The Kety-Schmidt method can be adapted to utilize the radioactive characteristics of ^{133}Xe or ^{85}Kr. These gases can be introduced to a patient through intra-arterial, intravenous, or inhalation routes, and once administered, they become diffusible and inert within the body. In contrast to N_2O, a significant benefit of employing these noble gases is that they do not disrupt brain metabolism. The concentration clearance curve of the isotope can be measured at different regional locations across the brain hemispheres. From this data, CBF can be calculated by modelling the observed clearance curve as an exponentially decaying function. This method has a clear drawback of subjecting the patient to a specific amount of ionizing radiation, and it provides measurements over a duration of minutes utilizing relatively large equipment. This method is also prone to overlooking regions with low CBF because there is a chance that an adequately perfused region might be superimposed on an inadequately perfused region, a phenomenon known as the “look-through” phenomenon.

SPECT and PET are two additional methods that necessitate exposure to ionizing radiation and require arterial blood sampling for quantifying CBF [49]. PET offers additional diagnostic insights, including cerebral blood volume (CBV), and details about both oxygen and glucose metabolism [8]. Both techniques are associated with significant costs, particularly PET, involve the administration of a radioactive nucleotide by the patient (which may limit suitability in certain clinical settings), have limited clinical availability, may cause patient discomfort, and are unsuitable for long-term monitoring [52], especially in populations such as neonates [3]. It's noteworthy that SPECT increases the overall radiation dose due to the utilization of both a radioactive nucleotide and X-rays.

2.2.5 Magnetic Resonance Imaging

MRI measurements of CBF can be conducted through dynamic susceptibility contrast MRI (DSC-MRI), also known as perfusion-weighted imaging or bolus-tracking MRI. This method involves the intravenous injection of a gadolinium-based contrast agent. In contrast to the Kety-Schmidt technique, this contrast agent remains within the vascular space and does not penetrate the blood-brain barrier. The retention of the paramagnetic contrast agent in the vascular space creates a magnetic field gradient between the brain's capillaries and its surrounding tissues, serving as the basis for contrast in DSC-MRI measurements, which is influenced by local CBF.

The use of a bolus injection makes this technique minimally invasive. Additional MRI techniques that are noninvasive, as they depend on endogenous contrast and do not necessitate the use of an external contrast agent, include arterial-spin labelling (ASL-MRI), flow-sensitive alternating inversion recovery (FAIR-MRI), and blood oxygen level-dependent (BOLD-MRI). BOLD-MRI, which exemplifies a functional MRI (fMRI) modality, utilizes the inherent contrast linked to the magnetic characteristics of deoxyhemoglobin [55]. This information can be employed to deduce brain activity based on the principle of neuro-vascular (or activation-flow) coupling [3,56]. ASL-MRI operates on the principle of magnetically labelling water in the arterial inflow of the brain within a labelling plane. Subsequently, it measures local CBF by quantifying the reduction in magnetization in the imaging plane caused by the inflow of arterial blood, which possesses negative magnetization. Similarly, FAIR-MRI functions pulse and another with a non-slice-selective inversion pulse. The signal enhancement between these two images is directly associated with CBF.

These MRI techniques can capture images of the entire head with a spatial resolution as fine as 2 mm [49,52]. However, the utilization of MRI machines necessitates robust magnetic fields, which might limit their application in certain clinical environments and in patients with metallic implants, such as pacemakers. Claustrophobic individuals and neonates may not be well-suited for this imaging modality, and the latter might require sedation or anaesthesia, or need to be asleep to minimize patient movement [57]. Additionally, ASL-MRI may experience noise issues during low perfusion readings, a situation frequently encountered with neonatal patients. Moreover, MRI technology is costly, requires patient transportation, and is associated with a low patient throughput. Many patients typically undergo MRI examinations only once during their hospital stay, and this examination often involves a snapshot measurement of CBF within a canning time that can extend up to one hour [52]. Such measurements are usually performed in conjunction with a specify research protocol [49].

2.2.6 Ultrasound Techniques

Transcranial Doppler (TCD) ultrasound offers noninvasive assessments of blood flow velocity (units: cm/s) in the basal brain arteries, including the middle cerebral arteries (MCA), proximal anterior cerebral arteries, and posterior cerebral arteries. Typically, measurements are taken in either the left or right MCAs [58]. The fundamental concept is that an ultrasound wave with a

frequency f undergoes a Doppler frequency shift (Δf) upon reflection by red blood cells in motion at a velocity v_B. The relationship between v_B and Δf is as follows:

$$v_B = \frac{C_s}{2f\cos(\theta)}\Delta f \quad (2.1)$$

here, Cs represents the speed of ultrasound in tissue, and θ is the angle between the direction of ultrasound propagation and the direction of the blood vessel. The challenge lies in the uncertainty associated with the angle θ, making precise measurements of v_B difficult. Additionally, the variation in blood vessel diameter introduces further uncertainty when translating the blood flow speed (measured in cm/s) into a volumetric blood flow measure (in units of ml/s) within the blood vessel. Obtaining an accurate estimate of volumetric blood flow would also necessitate knowledge of the brain mass perfused by the artery to calculate the absolute CBF. Due to these factors, TCD provides only a relative index of CBF.

2.3 Optical Methods

Light possesses a notable advantage as its photon energies align with the electronic and vibrational energy levels of numerous biological compounds. This alignment proves beneficial for detecting precise molecular-level changes, enabling the calculation of functional alterations in physiological parameters. Hence, light has the capability to selectively focus on and offer intricate details about molecules within biological tissue. In comparison to alternative imaging methods such as MRI or CT, optical imaging allows for the real-time evaluation of patients using relatively portable and cost-effective equipment [59]. Throughout our work, we focus only on optical methods applied to biomedical applications, which is called biomedical optics. Biomedical optics pertains to the interplay between light and biological tissue, exploring how this interaction can be utilized for sensing, imaging, and therapeutic purpose. In this context, "light" encompasses visible wavelengths (380 nm – 750 nm), as well as slightly shorter (ultraviolet) and longer (NIR) wavelengths. The field of diffuse biomedical optics can be generally categorized into incoherent and coherent approaches. The objective of incoherent methods is to measure and characterize the optical properties of tissue, providing information from which oxygen saturation can be deduced. Near-infrared spectroscopy (NIRS) exemplifies an incoherent method; however, we will not delve into its details in this discussion. The objective of coherent methods is to directly assess sample dynamics by analyzing the spatiotemporal fluctuations of scattered coherent light. There are many existing coherent

methods for blood flow measurement, including Laser speckle contrast imaging (LSCI) [60,61], Multiple exposure speckle imaging [62], Laser Doppler flowmetry [4,33], diffuse laser speckle contrast analysis [63], DCS [3]. Figure 2.1 shows the optical-based blood flow monitoring modalities with representative affiliations.

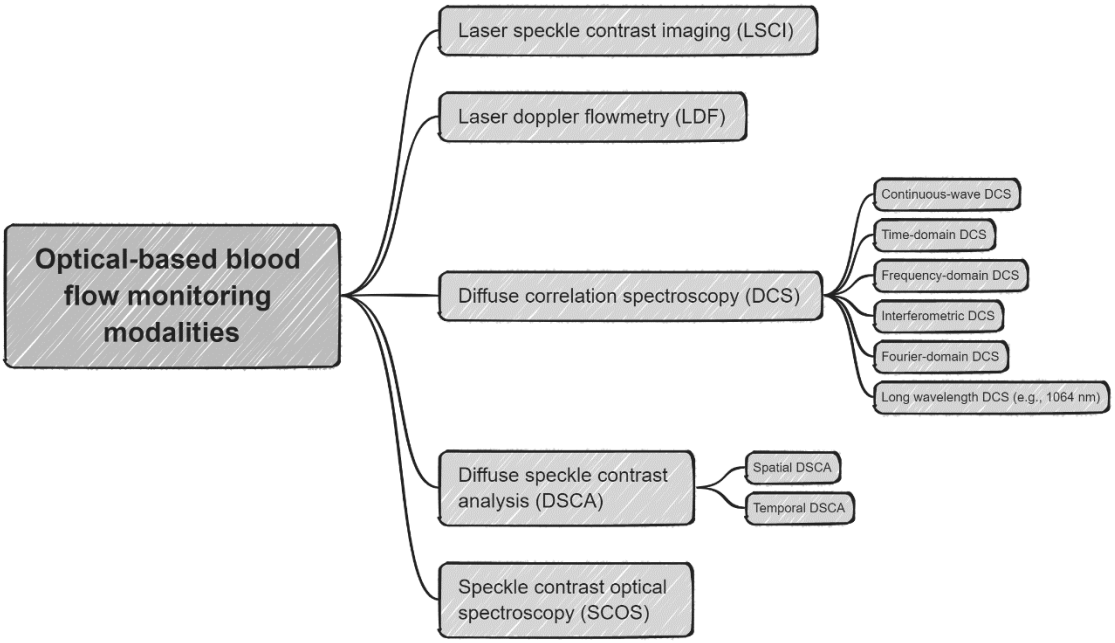

Figure 2.1 Optics-based blood flow monitoring modalities, including laser speckle contrast imaging (LSCI), laser doppler flowmetry (LDF), diffuse correlation spectroscopy (DCS), diffuse speckle contrast analysis (DSCA)/speckle contrast optical spectroscopy (SCOS).

2.4 Diffuse Correlation Spectroscopy

Near-infrared diffuse correlation spectroscopy (DCS), also known as diffusing wave spectroscopy (DWS) [64,65], a complementary optical technique, which relates multi-scattered light's fluctuations to underlying dynamics of scattering media. The term 'DCS', originating from Yodh's lab in 2001 [6], has gained popularity as it precisely describes the underlying signal processing principle (the correlation of diffused photons). A comprehensive diffuse correlation theory of diffuse speckle fields for predicting particle motions in highly scattered media was first introduced by Boas and Yodh in 1995 [66,67]. This theory offers a natural framework for investigation tissue dynamics and tomography [49]. DCS can provide a noninvasive method to estimate deep tissue microvascular BF as a BFi with the unit cm^2/s, proven to be a good surrogate for *in vivo* BF [68]. In the last two decades, DCS technologies have been developed [35,66,67], extensively validated, and vigorously employed to non-

invasive BF measurements in deep tissue vasculatures (up to ~ 1.5 centimeters), such as skin, muscle [32,69–75], breast tumor [26,27,76–80] and the brain [6,81–88]. In 2001, the combination DCS with NIRS/DOS was first introduced for cerebral monitoring in rats [6], and then in adult brains in 2004 [83]. This combination allows measuring BF and oxygenation measurement consumption rate simultaneously.

A diagram of the history of DCS development is shown in Figure 2.2(a). Figure 2.2(b) displays the number of publications in the DCS field over the past 20 years, with more than 400 publications to date (we only counted articles containing “DCS”). Figure 2.2(c) depicts DCS measurements obtained from human brain tissue, organizing current studies based on ρ (x-axis) and the sampling rate of blood flow (y-axis). It shows a trend towards using parallel or multispeckle and interferometric DCS when a higher sampling rate is required at large ρ. Additionally, it marks how deep the measurement must be to penetrate the scalp (see the top of Figure 2.2(c)) and the different regimes of speed to measure 1) more general changes (<1 Hz sampling rate); 2) pulsatile blood flow (1-10 Hz) or even faster, potentially enabling the detection of rapid events (>10 Hz).

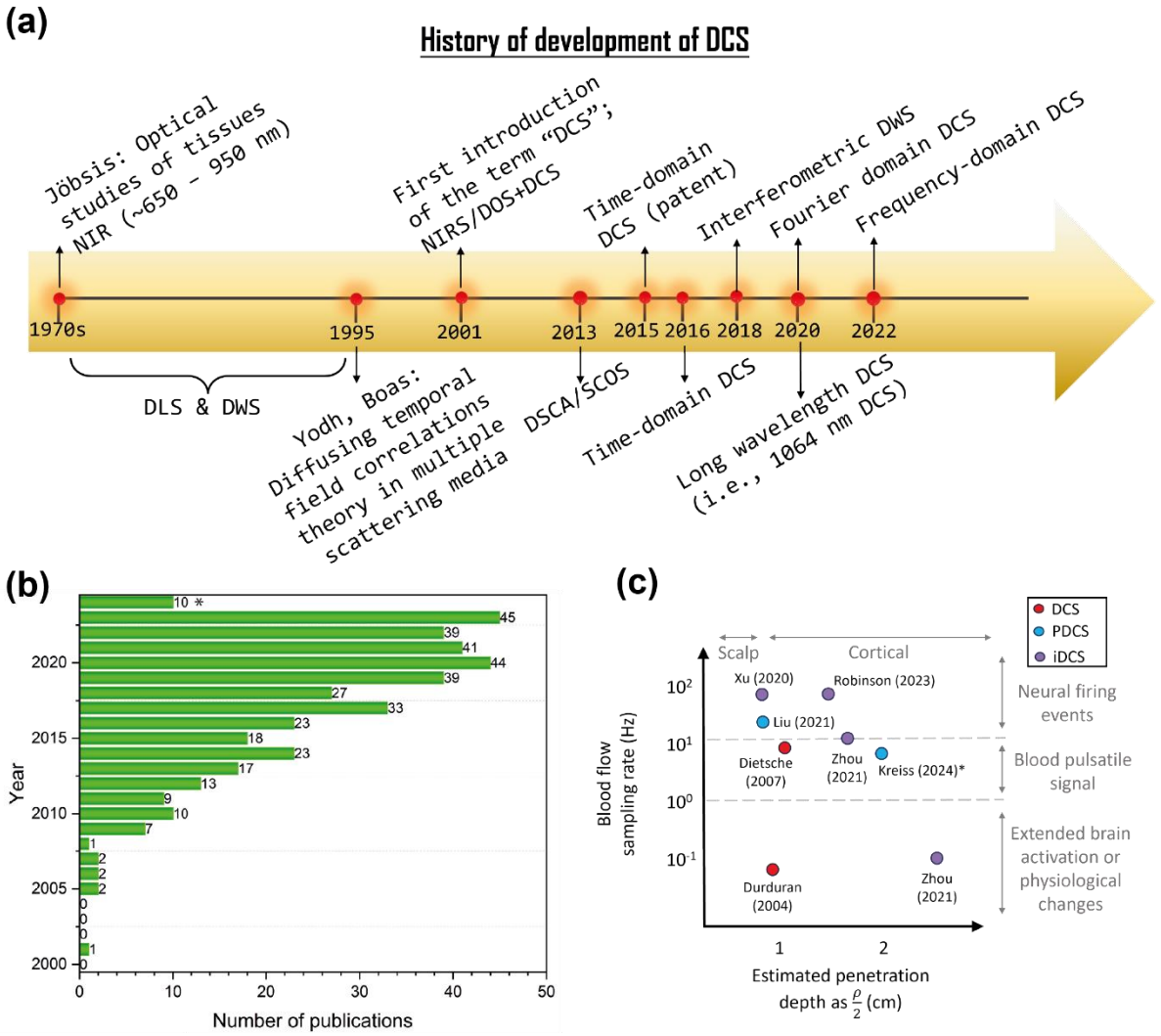

Figure 2.2 (a) The roadmap of DCS historical development; (b) The number of published DCS papers based on PUBMED (*value for 2024 extrapolated as of the date of writing); (c) Blood flow sampling rate vs. measurement depths. PDCS: parallelized DCS, iDCS: interferometric DCS.

Figure 2.3 illustrates the principle of DCS. Briefly, a long-coherence laser emits NIR light through an optical fiber to the tissue, Figure 2.3(a), and the recorded light intensity exhibits temporal fluctuations, Figure 2.3(b). These fluctuations are attributed to the motion of moving scatterers, such as red blood cells (RBC). To quantify the motion of RBC, a hardware or software correlator calculates the normalized intensity autocorrelation, $g_2(\tau)$ as shown in Figure 2.3(c). Typically, DCS systems are implemented in a reflection geometry, where a source and a detector are placed at a finite distance, ρ. Photons travelling from the source to the detector follow a "banana-shaped", stochastic scattering profile, as shown in Figure 2.3(d), where the penetration depth of these DCS instruments is roughly between ρ/3~ρ/2 [57]. Figure 2.3(c) and (e) show that the g_2 (τ) curves decay faster with increased flow or ρ. The slope or the decay

rate provides information about the optical properties and the motion of the scatters. The largest ρ in the current state-of-the-art is 4 cm, corresponding to a depth of about 2 cm [89].

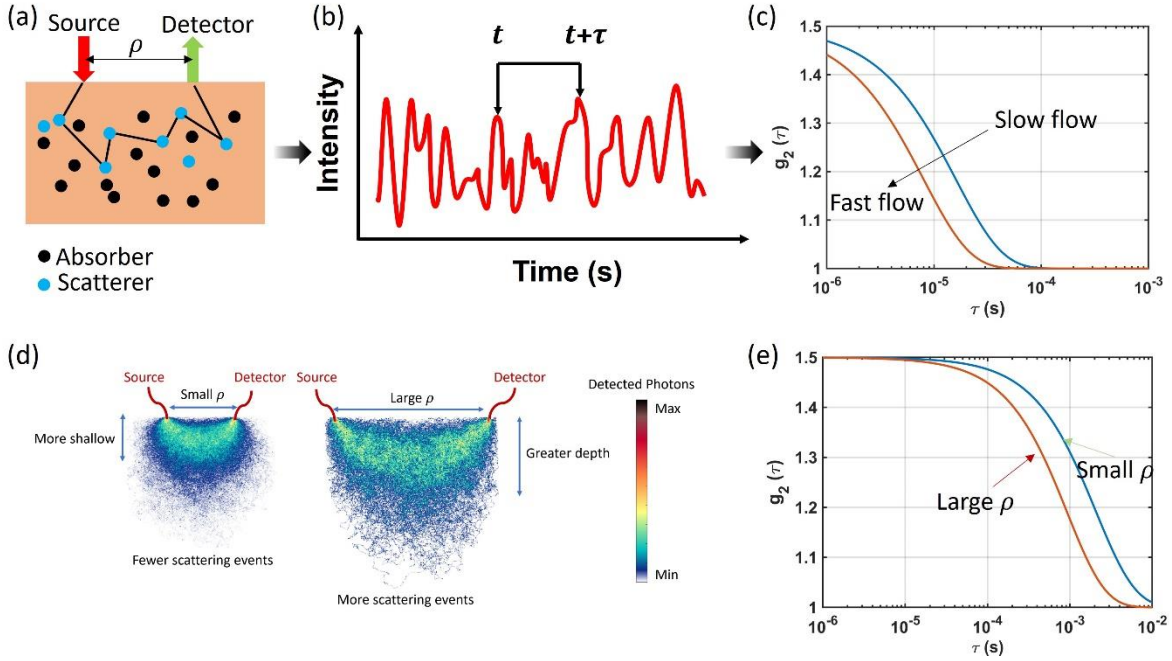

Figure 2.3 The DCS principle for blood flow measurements. (a) The schematic of DCS measurements in the semi-infinite geometry. Highly coherent laser light is used to illuminate the sample via optical fibers. The source and detector fibers are placed on the tissue surface within a distance ρ; (b) the scattered light intensity fluctuates due to moving scatterers (e.g., red blood cells); (c) two intensity autocorrelation curves ($g_2(\tau)$) showing different flow rates. (d) Photons scattered from moving particles travel along "banana-shaped" paths between source and detection fibers; (e) Autocorrelation functions for different ρ.

2.4.1 DCS Instrumentation

Typically, a DCS system consists of a laser source, source/detection fibers, and sensors. Figure 2.4 shows representative systems for CW-, TD-, FD-, and Hybrid DCS. Figure 2.4(a) and (b) depict portable CW- and TD-DCS systems, respectively. The primary difference lies in the use of a pulse laser (VISIR-500) in the TD system. Figure 2.4(c) showcases the FD-DCS system, representing the latest DCS technology in the frequency domain. Lastly, Figure 2.4(d) presents a typical Hybrid DCS system. However, very few companies have initiated commercialization of DCS systems, including Hemophotonics (http://www.hemophotonics.com), and ISS Inc. (https://iss.com/biomedical/metaox).

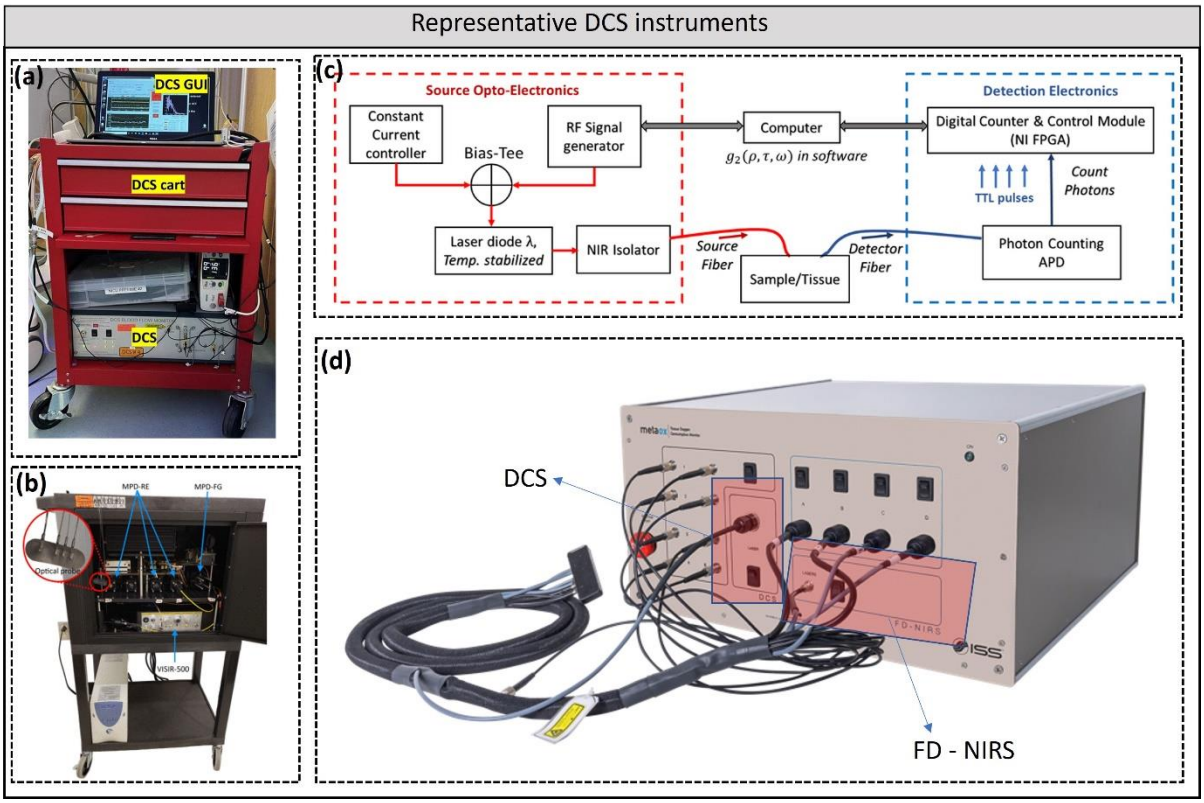

Figure 2.4 (a) Sunwoo *et al.*'s CW-DCS system; the figure adopted from Ref. [90]; (b) Tamborini *et al.*'s TD-DCS system; the figure adopted from Ref. [91]; (c) Block diagram of Sadhu *et al.* FD-DCS system; the figure adopted from Ref. [92]; (d) Zavriyev *et al.*'s [93] Hybrid DCS system; the figure adopted from https://iss.com/biomedical/metaox.

2.4.2 Lasers

There are three laser types commonly used in DCS, depending on the configuration: CW, modulated, and pulsed lasers corresponding to CW-, FD- [92], and TD-DCS systems. As we have mentioned above, the estimated BFi is derived from intensity fluctuations of the speckle pattern of back scattered light from the tissue surface, and the bright and dark patterns arise because photons emerging from the sample have travelled along different paths that interfere constructively and destructively at different detector positions [3,52,65]. Consequently, one of the main challenges is to select a laser with a long coherence length [65], l_c, designed by Eq. (2.2) assuming that the measured power spectral density has a Gaussian profile [94],

$$l_c = \frac{\lambda^2}{\Delta\lambda} \tag{2.2}$$

where λ is the central wavelength and Δλ is the optical bandwidth. The diffusion theory and Monte Carlo simulations of light transport show that the minimum coherence length must be longer than the width of the photon path-length distribution [95], typically around 5ρ~10ρ (e.g.,

100 mm for ρ = 10 mm) [96]. Also, considering the photons traveling through source and detection fibers, usually a laser with l_c>10 m is recommended [3]. Because most practical DCS systems utilize ρ~3 cm [3,48,88], meaning that the minimum coherence length $l_{c,min}$≫10ρ~15ρ namely 35~50 cm accounting for the variations of differential pathlength distances [97].

For clinic applications, the laser power should comply with the American National Standard for Safe Use of Lasers (ANSI) [98] limit for safe skin exposure with an irradiance of less than 200 mW/cm^2 for 400-700 nm and 300 mW/cm^2 for NIR. Spacers or prisms [93,96,99,100] are often between source fibre and sample to illuminate a larger area, which allows a higher laser power (more photons) to maintain the same maximal permissible exposure (MPE) limit for intensity. Typically, lasers with wavelengths of 670 nm [40], 760nm [101], 785 nm [96,102], or 1064 nm [48] are employed. Although NIR wavelengths provide a higher number of photons for the same output power (P = E/t = h c / λ, E is photon energy), a higher MPE (more photons) and a deeper penetration depth, the photon detection efficiency (PDE) of most detectors is typically reduced for longer wavelengths. As a result, 785 nm lasers are the most prevalent choice for most DCS techniques. This trade-off between the laser and the detector PDE is discussed in detail below.

Regarding TD-DCS, we can pinpoint the photons (either through gating or time-correlated single-photon counting [103]) that exhibit a similar path length in the tissue to provide depth-resolved information. This allows relaxing the requirement for a high coherence length compared with the scenario that all the photon paths are considered. Moreover, the maximum coherence length for a pulse laser is limited by the laser pulse width. Usually, a narrow laser pulse is preferable for precise depth-resolved measurements, however, a narrow pulse means a lower l_c, meaning a g_2 curve is closer to the noise floor. Therefore, there is a trade-off between l_c and the pulse width [91]. In fact, g_2's maximum amplitude depends on l_c, with β ranging from 0 for incoherence light to maximum 1 for linearly polarized light (0.5 for unpolarized light) with l_c longer than the longest photon path. Therefore, the main limitation of broad use of TD-DCS is the availability of an ideal pulsed laser considering power settings, pulse width, coherence, stability, and robustness. To obtain a more in-depth investigation, reader can check Refs. [91,101,104]. In Table 2.2 we extended the conclusions made by Samaei *et al.* [101], Ozana, *et al.* [104] and Tamborini *et al.* [91] to show the relevant parameters of pulse lasers.

Table 2.2 Parameters of laser source used in TD-DCS, adopted from Samaei, *et al.* [101], Ozana, *et al.*[104] and Tamborini *et al.*[91].

Laser	Central wavelength (nm)	Temporal Coherenece length (mm)	Spectrum bandwidth [nm]	Pulse width (ps)	Average output power (mw)
VIRIS-500 [91]	767	38	NA	550	50
LDH-P-C-N-760 [101]	760.4	6.1	0.095	106	12
Ti: Sapphire [101]	763.8	6.3	0.093	185	50
VisIR-765-HP "STED" [101]	765.7	1.6	0.359	535	50
PicoQuant GMBH [104]	1064	60	N.A	600	100

2.4.3 Source and Detection Fibres

In DCS experiments, a pair source and detection fibres are strategically placed on the tissue surface, with a separation of ρ (ranging from millimeters to centimeters). The laser emits long-coherence light through the source fibres into tissues, and the scattered light is collected by the detection fibre to a sensor. The diagram in Figure 2.5(a), (b) and (c) illustrate three fibres with distinct modes, namely single-mode, few-mode, and multimode. Most often, a multi-mode fibre (core diameter = 62.5, 200, 400, 600, 1000 μm) [24,104–106] is used for the source side. Here, it should be noted that a larger diameter fibre translates to a larger illumination area allowing a higher laser power (more photons) at the same MPE limit for intensity (see Section 2.4.2). For the detection, previously published DCS systems used single-mode (e.g., 5 μm) [38,107–112], few-mode [84,86], or multi-mode fibres [12,40,113,114]. Single-mode fibres are usually directly coupled to the respective detector. For parallelized DCS with SPAD arrays, multi-mode fibres are used for detection. Using single-mode fibres limits the measured light intensity, because there is only the fundamental mode of light can be transported, limiting ρ's dynamic range. Unlike conventional fibres, few-mode fibres allow not only the fundamental mode but also a select number of higher-order modes of light. Expanding the fibre diameter and numerical aperture (NA) in few-mode fibres to encompass multiple speckles enhances the detected signal intensity, consequently enhancing SNR. However, the multiple speckles detected by the few-mode fibres exhibit uncorrelated behaviour, and the decrease in β effectively counteracts the SNR enhancement. Finally, this flattens the autocorrelation function curve, potentially diminishing the sensitivity of DCS flow measurements [85,115]. To further increase the detected light intensity, multimode fibres with a larger core diameter have been used to accommodate larger sensors (e.g., 5 × 5, 32 × 32, 500 × 500 SPAD arrays). However,

this leads to a greater number of speckles on each detector, causing higher spatial decorrelation and reducing β [12]. He *et al.* [116] compared single-mode, few-mode and multi-mode fibres in detection side of DCS, and conclude that few-mode and multi-mode detection fibres can improve SNR compared with single-mode fibres, but it reduces β.

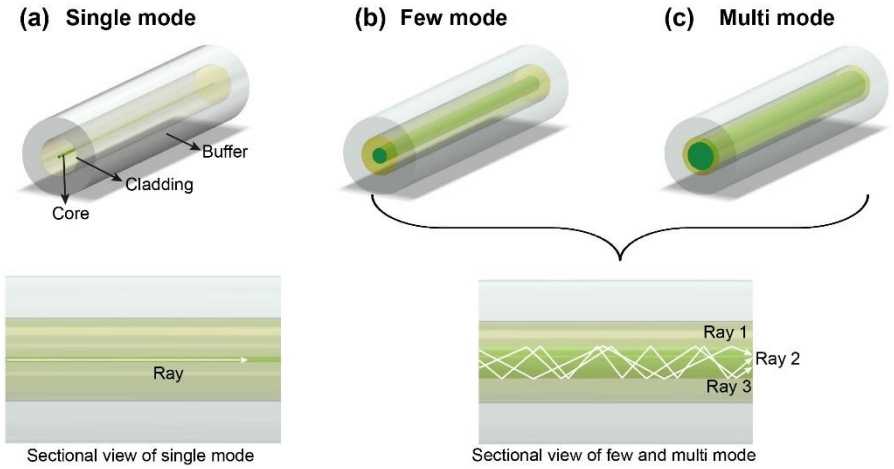

Figure 2.5 different mode optical fiber: (a) single-mode fiber (SMF), (b) few-mode fiber, (3) multi-mode fiber.

2.4.4 Sensors

Selecting an appropriate detector poses another challenge. Detectors are pivotal in DCS systems for accurate BF measurements, with the advances being intricately connected to the adoption of new high-efficiency massively parallel detectors. In early DCS systems, photomultipliers (PMTs) were commonly employed for detecting single photons [35,66]. However, PMTs are bulky, and therefore early systems only contain a few channels. Additionally, driving these PMTs requires a high bias voltage, at least hundreds of volts, to start the electron multiplication process. These requirements pose challenges for developing compact and portable devices. Typically, avalanche photon diodes (e.g., APDs, such as the SPCM series, Excelitas, Canada) [108,116,117] were used nearly exclusively in DCS systems. These detectors offer several benefits compared with PMTs, including lower cost, simpler operations, and a smaller size. While APDs offer high quantum efficiency, they are prone to higher dark current and noise in low-light conditions [118]. Additionally, these detectors are typically single-channel devices. In DCS, each speckle grain carries independent information about the dynamic scattering process. By averaging the autocorrelation signals from multiple speckles, random noise is reduced, improving the SNR. However, advances in CMOS manufacturing technologies have enabled the integration of large SPAD arrays on a single chip, offering highly parallel single-photon detection. The use of SPAD arrays in a multispeckle

approach directly enhances SNR, with the improvement scaling with the square root of the number of independent speckle measurements. Using such new sensors in DCS experiments is straightforward without increasing the setup complexity. Dietsche *et al.* [119] verified this method by grouping 28 individual SPADs, enhancing SNR by $\sqrt{28}$. Johansson *et al.* [120] first developed a 5 × 5 SPAD DCS system to demonstrate an improved SNR on milk phantoms and *in vivo* blood occlusion tests, followed by 32 × 32 [12,40,121,122], 192 × 128 [123], and 500 × 500 [89,113]. These systems significantly improve SNR by a factor of $\sqrt{N}$, where N is the number of individual pixels, as shown in Fig. 2.6. In it, we highlight the evolution of DCS systems with SPAD sensors (from APD to the state-of-the-art large SPAD arrays 500 × 500) with an enhanced SNR gain from 1 to ~500.

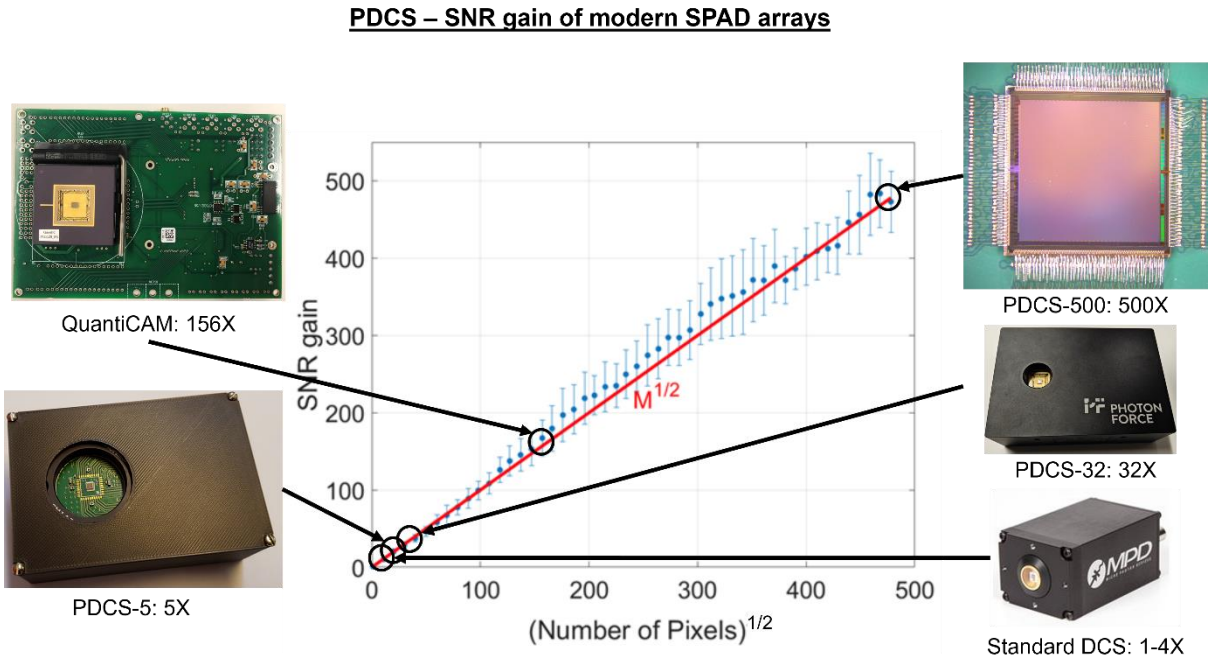

Figure 2.6 SNR-vs-pixels plot adopted from Wayne *et al.* [113], with different SPAD sensors employed in DCS systems.

Besides SNR and PDE, the exposure time of SPAD arrays is another critical consideration, as it defines the distance between two adjacent time lags $\Delta\tau$ of the autocorrelation curves. Especially for fast decay rates (e.g., at large source-detector separations or for high flow rates), the relatively slow frame rate of large SPAD arrays (3 μs for 32 × 32 [12,40,122] or 10 μs for 500 × 500 [113]) can be a limiting factor in real in vivo experiments. Another limitation of the SPAD arrays, though, is the difficulty in light coupling and the thinner active areas – thus an element of the SPAD array has a sensitivity quite a bit lower than a dedicated SPAD. Nevertheless, the large number of elements allows one to exceed the performance of individual SPADs. Figure 2.7 shows the basic processing of the current Parallelized DCS (PDCS).

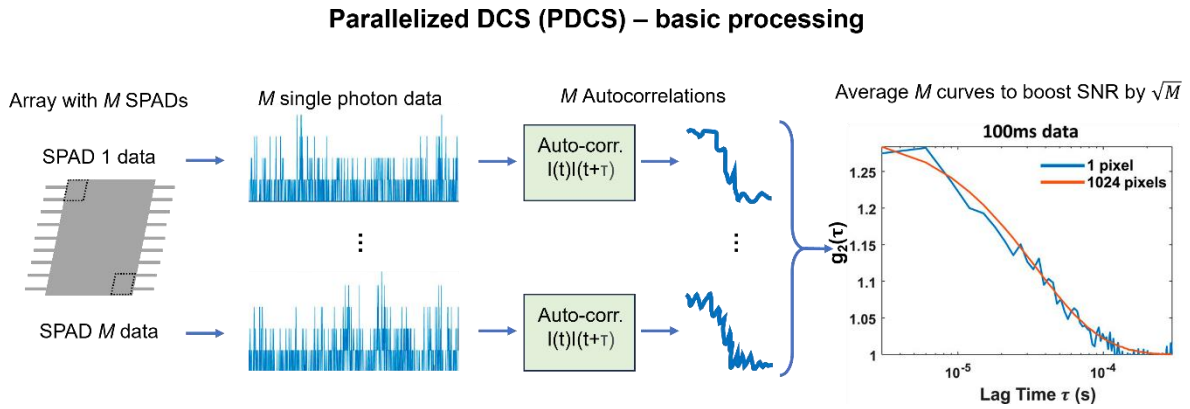

Figure 2.7 A schematic layout of the SPAD array with representative raw data of temporal light intensity fluctuations from single pixels and the corresponding intensity autocorrelation curves. The blue and red lines in the rightmost figure represent the autocorrelation curves of a single pixel and the whole SPAD array (1024 pixels), respectively. Data and plots are adopted from Liu *et. al.* [40].

Commercial CMOS cameras are also used in DCS due to their larger array sizes, higher fill factor, and lower cost. However, they do not have single-photon sensitivity. To address this, Zhou *et al.* [44] employed a heterodyne detection method to enhance the signal, they also used MMFs to capture multiple speckle patterns, thereby increasing the throughput. They successfully conducted pulsatile blood flow measurements. Meanwhile, Liu *et al.* [124] integrated a CMOS detector into a wearable, fiber-free probe, enabling the testing of CBF in neonatal pigs. Of note, the heterodyne detection approach can also be applied in SPAD-based DCS systems where it offers at least a doubling of SNR and together with reduced sensitivity to dark counts and environmental light [45].

Very recently, superconducting nanowire single-photon detectors (SNSPDs), a relatively new class of photodetectors, have been used in TD-DCS systems [125]. SNSPD has many advantages, including a high PDE of >80% at longer wavelengths (e.g., 1064 nm), a shorter dead time (<50 ns), and a better timing resolution (< 20 ps) [126]. Nevertheless, SNSPD detectors come with a high cost, substantial size, and noise, necessitating cryostats to maintain an operational temperature of 2-3.1 K. Moreover, their activation time spans over several hours, presently constraining their practical applicability in clinical settings. Table 2.3 summarizes the existing DCS systems with SPAD sensors and representative non-SPAD sensors. Some SPAD and SPAD arrays are equipped with Time-correlated Single Photon Counting (TCSPC), and TD-DCS systems can timetag detected photons to obtain their ToF. This feature in TD-DCS

allows distinguishing early and late arriving photons from fewer or more scattering events respectively, thereby enabling depth-resolved evaluation of BFi within tissues.

Table 2.3 Existing DCS systems using SPAD arrays and other representative sensors.

Approaches	Detector	wavelength (nm)	N_{pixel}	Applications	PDE	Fill factor	Frame rate (kHz/kfps)	ρ (cm)	year	Ref.
CW	SPAD	785	5 × 5	Phantom, blood perfusion	8%	1.5%	1000	2.5	2019	[120]
CW	SPAD	785	32 × 32	Food, skin	8%	1.5%	333	1.1	2020	[12]
CW	SPAD	670	32 × 32	Phantom, in vivo	16%	1.5%	333	2.1	2021	[40]
CW	SPAD	785	500 × 500	Milk phantom, rotating diffuser	15%	10.6%	92.2	3.3	2023	[113]
CW	SPAD	785	192 × 128	rotating diffuser	8%	13%	26	N.A.	2023	[123]
CW	SPAD	785	500 × 500 128 × 500	Human forearm and brain, in vivo	15%	10.6%	100 for arm, 300 for brain	4	2024	[89]
iDCS	SPAD	785	1 × 1	Intralipid phantom	61%	N.A.	N.A.	3.6	2020	[45]
LW-iDCS	InGaAs Linescan camera	1064	2048 × 1	Human brain, in vivo	N.A.	N.A.	300	3.5	2023	[127]
iDWS	CMOS	852	512 × 2	Human brain, in vivo	N.A.	N.A.	333	2.5	2018	[44]
fiDWS	Line-scan CMOS	852	512 × 2	Human brain, in vivo	>35%	N.A.	333	4	2021	[37]
πNIRS	CMOS	785	1024×1024	Forearm, forehead, human brain	80%	N.A.	16	2.5	2022	[114]
TD	SNSPD	785	N.A.	Phantom, in vivo	99%	N.A.	N. A	1	2023	[125]

Note: iDCS stands for interferometric diffuse correlation spectroscopy; iDWS is interferometric diffusing wave spectroscopy; fiDWS presents functional interferometric diffusing wave spectroscopy; πNIRS is abbreviation of parallel interferometric near-infrared spectroscopy, ρ is source-detection separation; SNSPD stands for superconducting nanowire single-photon detectors; PDE is photon detection efficiency.

2.4.5 Correlators (Incl. on-FPGA Correlators)

To date, most DCS instruments employ commercial hardware correlator [6,73,81,83] to record the arrival of Transistor-Transistor Logic (TTL) digital pulse for every photon generated from a photon counting detector. The correlator uses the distribution of arrival times to quantify the temporal fluctuation of detected intensity. Traditionally, correlators embed a multi-τ processor [128–130] to compute the autocorrelation functions over a massive range of delay times (from ~1 μs up to ~2 μs); this design was derived from early experiments in dynamic light scattering (DLS) [88] and diffusing wave spectroscopy (DSW) [119], primarily conducted on non-biological samples.

There are two kinds of hardware digital correlators, including linear correlators and multi-τ correlator. Usually, the multi-τ framework is based on a semi-logarithmic spacing spanning shows a massive lag-time range with a small number of channels without resulting in substantial sampling errors. Additionally, the multi-τ scheme significantly reduces the computational load compared with linear correlators. Although, hardware correlators can operate at a faster sampling speed, offer real-time computing with a wide lag time dynamic range, they are relatively costly (as shown in Table 2.4) and not flexible since the fixed number of bits per channel results in a fixed lag time scale. Meanwhile, software correlators [131,132] (e.g., Fourier transform software correlators [133]) have also been developed. Software correlators show comparable performances with commercial hardware correlators, and show notable advantages, specifically, in terms of flexibility, cost-effectiveness, and seamless adaptability to evolving PC and data acquisition technologies. For most DCS applications with SPAD array, the autocorrelations are usually post-processed from raw data.

Table 2.4 Existing commercial correlator

Company	Correlator	Ref.
LSI Instruments	LSI Correlator	[134]
Becker & Hickl GmbH	SPC-QC-004	[135]
ALV	ALV-5000/EPP	[136]

2.4.6 Comparison Between CW-, TD- and FD-DCS

Conventionally, enhancing depth sensitivity in CW-DCS measurements involves employing large source-detection separations. This allows for the detection of photons with longer pathlengths within these separations. An inherent drawback of this approach is the reduced detection of photons at large ρ, which negatively impacts the signal-to-noise ratio (SNR) of the measured temporal autocorrelation function. While Yodh *et al.* [137] previously demonstrated the viability of the path-length resolved DCS approach, their method involved nonlinear optical gating and necessitated high laser powers, rendering it unsuitable for *in vivo* applications. Sutin *et al.* [125] first reported a novel approach for time-domain (or pathlength-resolved) DCS on phantoms and in a rat brain, which open the time-domain DCS regime in clinic applications.

Compared with CW-DCS, there are many advantages in TD-DCS:

Firstly, using time-domain measurement, akin to TD- NIRS, enables the measurement of the time point spread function (TPSF) of the tissue. Consequently, we can apply photon diffusion theories developed for TD-NIRS to directly estimate the optical properties of the tissue using the TPSF. Thus, we eliminate a large portion of the error in estimating dynamical properties that is caused by imprecise optical property values [125].

Secondly, the time domain approach added one further variable time which can be exploited to select photon with increasing depth sensitivities [138]. Typically, the photons with a longer pathlength travelled deeper into the medium before reaching the detector while those with a shorter pathlength took a more direct path from source to detector, reaching only superficial tissue layers as shown in Figure 2.8(b). By utilizing time-of-flight (ToF) measurements, we effectively achieve depth resolution, as the ToF is directly proportional to the path length through the medium at the speed of light. Consequently, when computing the autocorrelation solely with photons having a ToF below a specific threshold, we can estimate the dynamic properties of the superficial layers, while longer ToF allow us to assess deeper layers.

Thirdly, the pulsed laser utilized in the TD-DCS system can be integrated into the TD-NIRS setup. This integration enables simultaneous measurements of NIRS and DCS, providing a comprehensive understanding of blood flow and hemodynamics variations. A temporal

resolution of approximately one second and a favourable SNR in dynamic in vivo measurements was validated [139].

However, the primary obstacle preventing the broad adoption of TD-DCS in laboratory and applicable environments, including preclinical and clinical studies, is lack of an optimal pulse laser source processing suitable characteristics such as power, pulse width, coherence, stability, and the cost of pulse laser (around 6 time expensive than CW laser). The effect of each of these factors has been evaluated in different studies, and various data processing strategies have been introduced to overcome the destructive influence of the instrument response function (IRF) [140] and limited coherence length of the emitter. Moreover, Colombo *et al.* [141] demonstrated the contamination of non-moving scatters on the TPSF using a coherent pulsed laser utilized in the TD-DCS technique. Samaei *et al.* [101] have conducted the systematic discussion. Another downside is that the use of narrow time gates to calculate the autocorrelation limits the SNR due to the scarcity of photons within a certain gate; Consequently, it's applicability to *in vivo* experiments on humans' tissue is also restricted [139]. Although Ozana *et al.* [104] have designed a functional TD-DCS system that combines an optimized pulsed laser (a custom 1064 nm pulse-shaped, quasi transform-limited, amplified laser source), it is still costly, primarily due to the SNSPD.

Unlike the CW-DCS technique, both TD- and FD-DCS can retrieve dynamic optical (e.g., BFi) and static optical properties (e.g., μ_a and μ_s'), which are typically assumed in the conventional CW-DCS measurements. FD-DCS eliminates the requirement for collocated sources and phase-sensitive detectors, resulting in a portable and cost-effective system. Through data acquisition at a single ρ, FD-DCS effectively minimizes partial volume effects. This technology eliminates the need for extensive calibration in data analysis by acquiring flow and absorption from intensity-normalized data. FD-DCS enables higher speeds of data acquisition, as flow and oxygenation information are inherently present in the dataset. Moreover, the implementation of FD-DCS is simplified by replacing a traditional DCS system's source with an intensity-modulated coherent laser. The detector mechanism remains unchanged, leading to reduced build time and cost.

Typically, to separate deep from superficial blood flow signals for CW-DCS, adding more detectors at different ρ to obtain multiple-distance measurements is needed, as is shown in Figure 2.8(a), which however increases the cost. In TD-DCS, the time-gating approach we only

need to choose the interested photons by gating or using a TCSPC, as is shown in Figure 2.8(b). Figure 2.8(c) shows that the FD-DCS, which can measure BFi, μ_a and μ_s' simultaneously. Table 2.5 summarizes representative existing TD-DCS systems. General linear models (GLM) have been used for CW-DCS data from multiple source-detector separations (ρ) to regress out the effect of superficial flow. Thereby large- ρ DCS data is expressed as a linear combination of superficial blood flow (measured as small ρ) and the desired deep blood flow [142], a method that was borrowed from fNIRS [143]. In contrast to fNIRS, however, which measures flow volume, DCS direct measures the BFi, which is related to flow speed. Since the flow speed differs significantly over different vessel diameters and different tissue layers, the relation between superficial BFi and deep BFi is not actually linear. Therefore, new analysis tools that integrate additional data on vasculature structure are required to derive more accurate deep flow estimation from such multiple-distance DCS measurements.

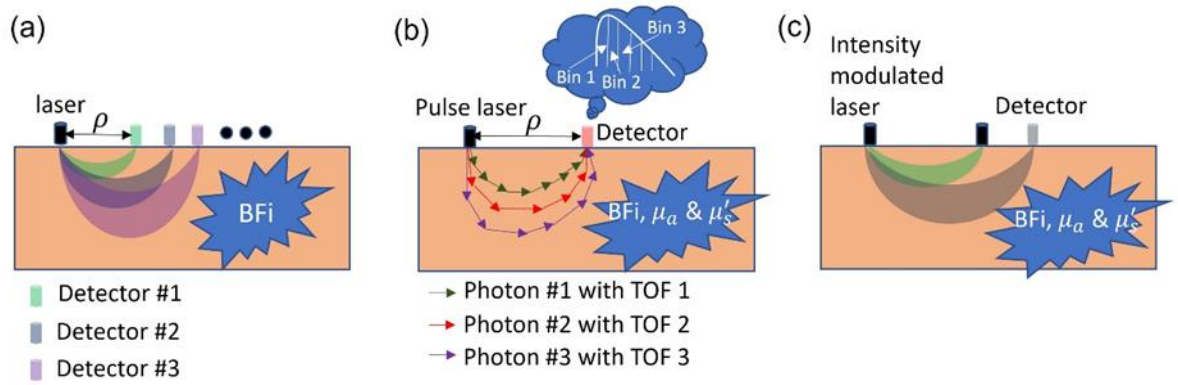

Figure 2.8 (a) DCS data collected at different ρ to improve depth sensitivity, (b) measurement principle for TD-DCS, (c) measurement using FD-DCS.

Table 2.5 Representative existing time-domain DCS systems

Year	Laser	Wavelength (nm)	Average power (mW)	Repetition rate (MHz)	Detection technique	IRF FWHM (ps)	Applications	Ref.
2016	DBR	852	50	150	Red-enhanced SPAD	150	Homogenous liquid phantom and small animal	[41]
2017	Ti: Sapphire	785	NA	100	SPAD	100	Two-layer liquid phantoms, forearm muscle, and adult human forehead	[139]
2018	VisIR STED, PicoQuant	767	50	NA	Red-enhanced SPAD	500	Homogenous liquid phantoms	[144]
2018	Ti:Sapphire	785	NA	100	Gated single-photon avalanche diode	350	Forearm muscle	[145]
2019	VisIR-500	767	≤ 1500	≤ 80	SPAD	550	Homogenous liquid phantoms, forearm muscle, and adult human forehead	[91]
2019	Ti:Sapphire	785	NA	100	SPAD	400	Homogenous liquid phantoms	[140]
2020	Ti:Sapphire	1000	30	100	InGaAs PMT	NA	Homogenous liquid phantoms and forearm muscle	[146]
2021	LDH-P-C-760, Picquant	760	12	80	SPAD	90	Two-layer liquid phantoms, forearm muscle, and adult human forehead	[42]
2022	Custom-made two-stage fiber amplified pulsed laser	1064	100	1-100	SNSPD	150-600	Two-layer liquid phantoms and adult human forehead	[104]
2023	Ti:Sapphire	785	NA	100	SNSPD	100-200	Homogenous liquid phantoms and adult human forehead	[125]

Note: SPAD stands for Single-Photon Avalanche Diode, and SNSPD stands for Superconducting Nanowire Single-Photon Detector.

2.5 Data Processing

The accuracy and performance of multilayered analytical models have been extensively evaluated in prior literatures [42,47,147–149]. In addition to the analytical models described in Chapter 3, other data processing methods have been introduced to distinguish cerebral and extracerebral information. Baker *et al.* [150] introduced a pressure measurement paradigm combined with the modified Beer-Lambert law and multi-distance measurement to reduce the extracerebral contamination from the signal associated with the deep layers. Furthermore, Samaei *et al.* [42] extended the bi-exponential model utilized in interferometric near-infrared spectroscopy (iNIRS) [151] to describe the TD-DCS signals influenced by scatterers moving at different speeds. They also conducted experimental validation using layered phantoms and *in vivo* experiments.

Traditionally, to extract BFi and β, the measured $g_2(\tau)$ fit to the analytical solution of the correlation-diffusion equation by minimizing the cost function $\chi^2 = \sum_i [g_{2,analytical}(\rho, \tau_i) - g_{2,measured}(\rho, \tau_i)]^2$. Nonlinear least square fitting routines, e.g., Levenberg-Marquardt [84,152], fminsearchbnd [148] are usually used to quantify BFi. These approaches, however, are iterative, and sensitive to data noise. To address these constraints, the Nth-order (NL) algorithm [153,154], least-absolute minimization (L1 norm), and support vector regression (SVR) were introduced [155]. Yet, with the NL framework, the extraction of BFi is determined by the chosen linear regression approach. While L1 norm and SVR represent novel methods for processing DCS data, they are sensitive to signal deviations [156]. Moreover, the computation time for BFi is 28.07 and 52.93 seconds [155] (using the Lenovo ThinkCentre M8600t desktop with a 3.4 GHz CPU and 16 GB memory) when employing L1 norm and SVR, respectively, still too slow for real-time applications.

In 1986, Dechter introduced the term “deep learning” (DL) to the machine learning community [157]. Due to the recent surge in big data, deep learning (DL) has effectively various significant areas of scientific research. DL falls under representation subset of artificial intelligence (AI). With rapid advances in computing technologies, DL has become a game-changer in many traditional research fields, including photonics [158], chemistry [159], biology [160] and medical diagnosis (such as EEG and ECG [161,162]), but is not yet broadly used in DCS. Recently, Zhang *et al.* [163] proposed the first recurrent neural network (RNN) regression

model to DCS, followed by 2D convolution neural networks (2DNN) [38], long short-term memory (LSTM) [164] and ConvGRU [165]. LSTM, as a typical RNN structure, has proven stable and robust for quantifying relative blood flow in previous studies in phantom and *in vivo* experiments [164]. 2DCNN, on the other hand, tends to require massive training datasets for complex structures, demanding memory resources. ConvGRU, the newest deep learning method introduced to DCS, has also exhibited excellent performances in BFi extraction. Although the training of DL takes a long time, once it is done, DL is much faster than traditional fitting methods, more promising for real-time analysis and display. Figure 2.9 summarize the current deep learning architecture applied to DCS system. Table 2.6 displays the existing deep learning methods applied to DCS techniques. It shows that DCS-NET's training is much faster than 2D-CNN, approximately 140-fold faster. Although the remaining models, RNN, LSTM and ConvGRU have fewer total layers, they are limited to a specific ρ. Xu *et al.* [122] introduced a different approach of DL and trained a deep neural network on DCS data of temporal speckle fluctuations from 12 fibers at different surface locations to reconstruct videos of flow dynamics 8 mm beneath a decorrelating tissue phantom. The reconstructed images had a millimetre-scale spatial resolution and a temporal resolution of 0.1-0.4 s.

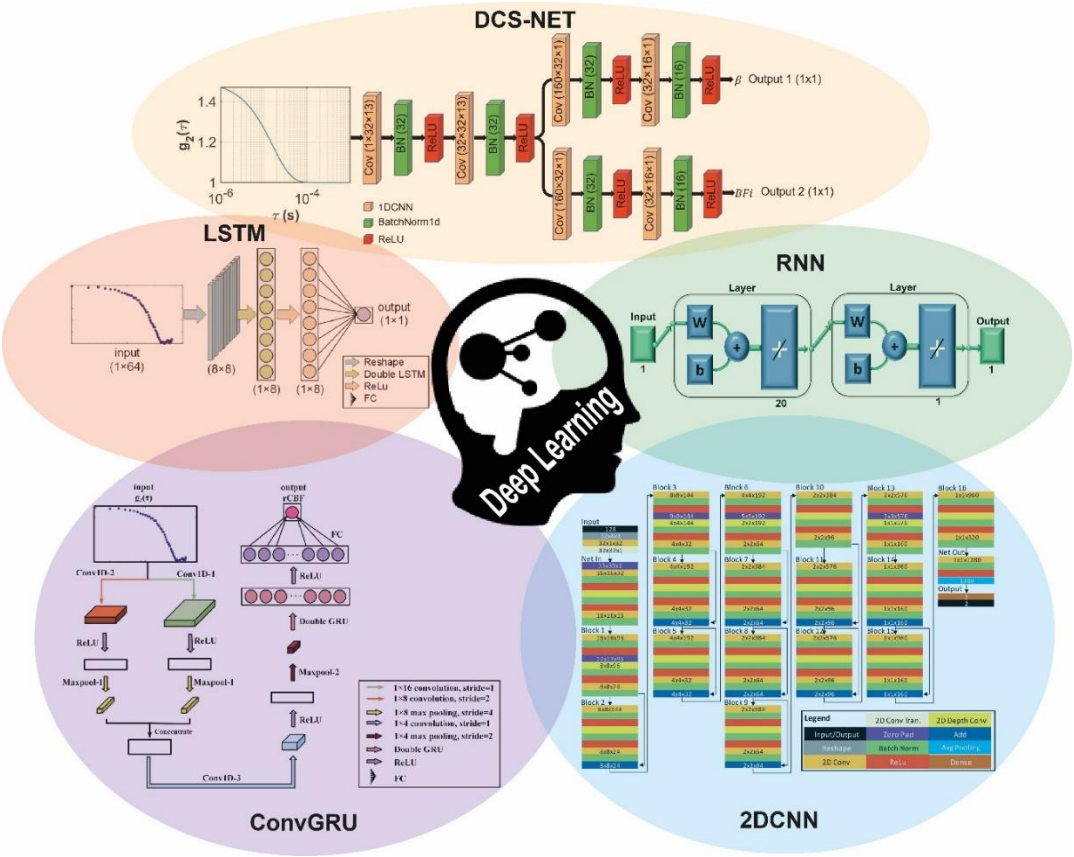

Figure 2.9 The existing deep learning model applied in DCS, including RNN [163], 2DCNN [38], LSTM [164], ConvGRU [165] and DCS-NET. All the graphs are re-printed from the published literatures.

Table 2.6 Comparison of Existing AI methods for BFi estimation

Model	Training Parameters	Training time	Total layer	ρ (mm)	Year
DCS-NET	25506	~ 13 (minute)	18	5 ~ 30	2023
RNN	174080	N/A	20	25	2019
CNN(2D)	75552	~ 30.5 (hour)	161	27.5	2020
LSTM	1161	N/A	2	15	2021
ConvGRU	11557	N/A	10	20	2022
LSTM	N/A	N/A	5	30	2023

Note: the training parameters of RNN and CNN(2D) are not given in the literature; we calculate them according to the structure shown in the literature.

2.6 Other Approaches Used in DCS

2.6.1 Long Wavelength Approaches

Since DCS relies on light scattering, recent findings suggest significant advantages in operating at longer wavelengths, specifically within the water absorption local minimum between 1050

and 1100 nm. Practically at 1064 nm, where a broad range of optoelectronic components, including high-power laser sources initially developed for the telecom industry, is readily available, substantial benefits have been demonstrated [48]. In DCS system, employing a wavelength of 1064 nm provides a SNR advantage compared to the more commonly used wavelength of 785 nm. By evaluating the complete photon budget, Carp *et al.* illustrate that at 1064 nm, the detection of photons would be 10.5 times than at 785 nm [48], which results in an increase in photon availability to increase SNR. The limited of availability of suitable detector technology at 1064 nm hinders the widespread adoption of the longer wavelength in DCS. For example, the commonly used SPAD have a higher photon detection efficiency (PDE) of 50% [166], but which drops to 3% at 1064 nm [48]. One of the solutions for this is using superconducting nanowire single-photon detection (SNSPD), which have a PDE of >80% at 1064 nm. However, SNSPD detectors are costly, larger in size, and emit noise. Achieving an operating temperature of 2 – 3.1K necessitates cryostats, and these detectors have a turn-on time of several hours, currently limiting their clinic application. More details about SNSPD can be seen in Section 2.4.4.

2.6.2 Heterodyne/Interferometric Approaches

Traditionally, the DCS systems are based on homodyne detection (self-interference of scattered light) that related to the motion of the sample. Heterodyne DCS, also known as interferometric DCS, employs a reference arm to effectively enhance the speckle fluctuations caused by the motion of scatterers within the tissue. Constructing an interferometric diffuse correlation spectroscopy (iDCS) system involves modifying a homodyne DCS setup with a pair of fiber couplers to establish a Mach-Zehnder interferometer. And $g_2(\tau)$ can be computed as:

$$g_2(\tau) = 1 + \beta_1 g_1(\tau)^2 + \beta_2 g_1(\tau)$$

$$= 1 + \beta_0 (1 - \frac{I_R}{I_T})^2 g_1(\tau)^2 + 2\beta_0 \frac{I_R}{I_T}(1 - \frac{I_R}{I_T}) g_1(\tau) \quad (2.3)$$

where I_R is the reference intensity, and $\frac{I_R}{I_T}$ is the fractional reference intensity, where $I_T = I_R + I_S$ is the total intensity, and I_S is the sample arm intensity. Interferometric methods offer advantages as they can offset detector imperfections (e.g., afterpulsing, read noise, and dark noise) [45]. They are resilient to environmental noise, including ambient light found in clinical settings. Additionally, they facilitate accurate measurements even in the presence of extremely low signal levels, enabling the assessment of CBF within brief acquisition times under low-

light conditions [167]. This means the important advantage of heterodyne detection is enabling the use of lower cost, noisier devices, and making it possible to use non-photon counting detectors, such as complementary metal-oxide-semiconductor (CMOS) cameras. Samaei *et al.* recently proposed Continuous-wave parallel interferometric near-infrared spectroscopy (CW πNIRS), which makes use of a fast 2D detector array, and which measures brain BFi using a ρ of 30 mm and an integration time of 0.01 s [114].

2.6.3 Improved Analytical Models

Since DCS is a diffuse optical method, it faces limitations due to the absence of inherent depth discrimination within the illuminated area of each source-detector pair. Consequently, the CBF signal is susceptible to contamination by the extracerebral tissues through which the light travels. To minimize these extracerebral tissues, various methods have been suggested, generally categorized into one of two groups: (1) hardware modifications or (2) improved analytical modelling. On the hardware side, it can be achieved through either interferometric approaches, or using laser with longer wavelength such as 1064 nm. Although these methods shown promise and may represent the future of DCS, current constrains related to detector speed, accessibility, and cost hinder their broad implementation. Alternatively, enhanced analytical modelling techniques are accessible, aiming to eliminate the influence of extracerebral hemodynamic. For instance, there are two-layer models comprising an extracerebral layer encompassing the laser, scalp, skull, and cerebrospinal fluid (CSF), in addition to a cerebral layer encompassing gray and white matter. Another example is the three-layer model involving the scalp, skull, and brain. The theory of the multi-layer analytical model will be discussed in Chapter 3.

2.7 Applications

DCS has a broad range of applications. The integrated DCS systems with near-infrared spectroscopy (NIRS) [57], Doppler ultrasound, time-resolved near-infrared technique (TR-NIR) [168,169], frequency domain near-infrared spectroscopy (FD-NIRS) [170] are powerful for collecting abundant information. This integration yields valuable insights in tissue oxygenation, blood oxygen metabolism and hemodynamics. Consequently, DCS has the potential for tissue and skeletal muscle blood flow monitoring, tumor diagnosis and therapy and neonate cardio-cerebrovascular health evaluation.

The hypothesis proposed by Roy and Sherrington suggests that the increase in CBF is attributed to increased neuronal metabolic activity [171]. There exists a strong correlation between changes in CBF and psychological conditions. The tight coupling between neuronal activity and cerebral perfusion has been demonstrated in many articles [172–174]. As a result, studying regional CBF allows for observing local neuronal activities, performing diagnosis, and developing treatment procedures. Many articles have been published for studying CBF based on DCS in the last decade. Interested readers can also refer to these review articles [3,57,175].

In this section, we categorize DCS applications into three main categories: animals, human pediatrics, and human adults. The structure of this section includes: first, we provide a comprehensive overview of DCS applications in animals. We list application scenarios and preclinical trials. Next, we delve into DCS applications in neonates, focusing on perinatal care, cardio-cerebral diseases in neonates, neonatal brain development, and children's brain health. Finally, we explore DCS applications in adults, categorizing them into four sections: neuroscience, cardio-cerebrovascular diseases, skeletal muscle, and exercise physiology, as well as tumor diagnosis and therapies.

2.7.1 Animals

DCS has been applied to animals since the end of the 1990s for estimating the burn depth in pigs [35], as shown in Figure 2.10(b). After that, a hybrid instrument integrating DCS with NIRS was applied to probing rat vascular dynamic by Cheung *et al.* in 2001 [130]. Carp *et al.* used DCS to examine CBF during hypercapnia-induced cerebrovascular perturbation, with MRI-based arterial spin labeling (ASL) serving as the standard measuring reference [176]. Furthermore, the first DCS application in tumor monitoring was conducted by Menon *et al.* [131]. They assessed tumor oxygenation in athymic mice (aged 6-8 weeks) bearing hypervascular human melanoma xenografts, achieved through vascular endothelial growth factor (VEGF) transfection. They combined DCS with Doppler ultrasound (DUS) to investigate microvessel density (MVD), BF, blood volume (BV), blood oxygen saturation, tissue pO_2, and oxygen consumption rates. Moreover, DCS plays a pivotal role in monitoring tumor blood flow changes in animal studies related to photodynamic therapy (PDT). Marrero *et al.* [177], Yu *et al.* [178] and Busch *et al.* [179] have employed DCS to monitor BF in tumors before, during, and after PDT. Additionally, Sunar *et al.* [180] have used DCS to assess anti-vascular and ionizing radiation therapies. These preclinical investigations have paved the way

for human cancer research and clinical applications. Table 2.7 shows the DCS applications in animals.

Ischemia monitoring assesses potential damage to the brain or the secondary brain injury as well as paraparesis. Experiments have been conducted to study the perturbation of hemodynamic and cerebral blood metabolism induced by ischemia brain injury in rats [82], piglets [169] and sheep [169], see Figure 2.10. Notably, Diop *et al.* developed a method integrating TR-NIR and DCS to quantify the absolute cerebral metabolic rate of oxygen ($CMRO_2$).

Table 2.7 Table of classification of DCS application on animals.

Application	Subject	Overview	System	Reference
Hypercapnia	Rodent	rCBF and blood oxygen information	DCS & NIRS	[6]
	Rodent	DCS: rCBF; MRI: validation	DCS & MRI (ASL)	[181]
Tumor diagnosis/therapy	Rodent	Tumor oxygen status monitoring	DCS & DUS	[182]
	Rodent	Tumor blood flow monitoring before, during and after PDT	DCS	[177–179]
	Rodent	Anti-vascular therapy and ionizing radiation of malignant mouse melanoma tumor models	Contrast enhanced DUS & DCS	[180]
Ischemia	Rodent	rCMRO2	DOT & DPDW & DCS	[82]
	Piglet	Absolute CMRO2 and CBF	DCS & TR-NIRS	[169,183]
	Sheep	Spinal cord ischemia	DCS & DOS	[184]
Neurovascular coupling	Rodent	Effects of the secondary and late cortico-cortical transmission in neurovascular coupling	EEG & DOI & DCS	[185]
Head injury	Piglet	Hemodynamic changes monitoring after a head injury	DRS & DCS	[186]
Intracranial pressure	Monkey	Cerebral blood flow monitoring as an indicator of intracranial pressure	DCS	[187]
Diffuse optical correlation tomography	Rodent	Measuring blood flow contrast	DCT	[85,188]

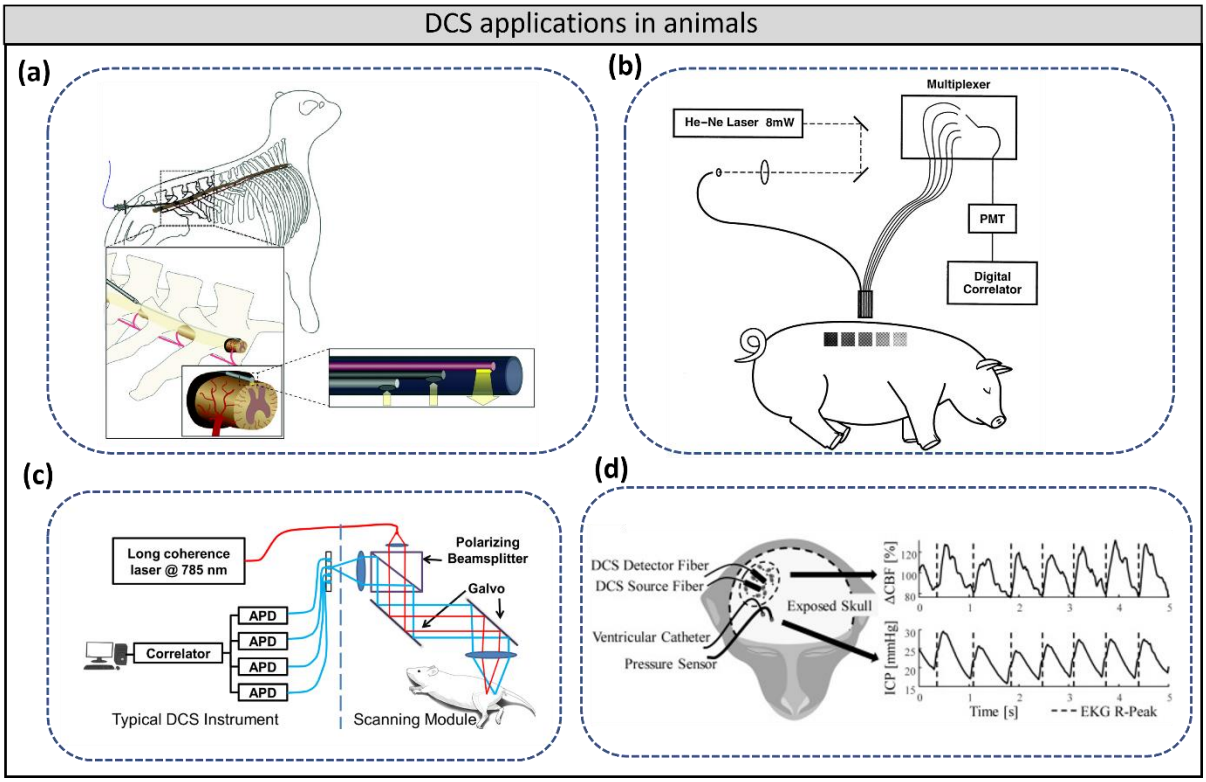

Figure 2.10 (a) Detailed schematics of measurements on sheep, featuring the instrument and its thin fiber optic probe, images adopted from Ref. [184]; (b) The setup for pig experiments. The shaded areas on the pig indicate burns of various depths. Figures were reproduced from Ref. [35]; (c) The non-contact scanning system set-up for mice. (black lines: outline of the bones; red lines: outline of the graft). Figures were reproduced from Ref. [188]; (d) Experiment setup with the placement of optical fibers and pressure sensor as well as the catheter on the exposed skull of monkey. The traces at the right show an example of changes in cerebral blood flow (ΔCBF) and ICP. Figures were reproduced from Ref. [187].

To further investigate vessel hemodynamic, diffuse correlation tomography (DCT) has been developed by measuring blood flow perturbation, contributed by optical heterogeneities, to provide blood flow contrast imaging of the region of interest [85,188]. DCT is a safe and cost-effective imaging technique, providing deep tissue imaging, real-time monitoring, and functional information of hemodynamic. DCT can complement other imaging modalities, such as MRI, CT, or PET scans, by providing additional functional and physiological information. This can enhance the overall understanding of a patient's health condition.

2.7.2 Pediatrics

The cortex of newborns is more easily detectable as the scalp and skull are much thinner in newborns and more light reaches the cerebral tissue as compared to adults. Thus, neonates are an attractive population for bedside DCS measurements, as discussed below. Generally, DCS

is often combined with NIRS, as well as FD-NIRS and transcranial Doppler ultrasound (TCD), offers a synergistic approach to obtaining comprehensive measurements of microvascular blood flow and blood oxygen metabolism in neonatal human subjects [57].

2.7.2.1 Perinatal Care

Premature infants, born before 37 weeks of pregnancy, are increasingly common due to factors such as inadequate prenatal care, maternal health conditions, and infections [14]. Perinatal health refers to health from 22 completed weeks of pregnancy to 7 completed days after birth. However, premature babies are more likely to suffer from brain injuries such as hypoxia-ischemia, stroke, and periventricular leukomalacia, which are associated with neurological deficits [15]. To study brain hemodynamic and blood oxygen metabolism in premature neonates, Roche-Labarbe *et al.* developed a hybrid instrument that combined DCS for measuring CBF with quantitative FD-NIRS measuring cerebral tissue oxygenation (StO_2) and cerebral blood volume (CBV). The results indicate that the CBF-CBV correlation is unstable in premature neonates [189]. In addition, Germinal matrix-intraventricular hemorrhage (GM-IVH) in premature neonates can be monitored by measuring CBF and cerebral oxygen metabolism ($CMRO_2$) to identify the vulnerability of potential brain damage in newborns [190]. Buckley *et al.* used DCS to continuously monitor CBF in the middle cerebral arteries of low birthweight premature infants during a postural manipulation. They discovered a significant correlation between TCD and DCS measurements [87]. CBF monitoring during the first 3 days after birth has been used to assess the risk of brain injury due to CBF instabilities in preterm infants [190]. DCS holds a promising potential for preterm human infants' brain health care.

2.7.2.2 Neonate Cardio-cerebral Diseases

DCS is also a promising tool for the monitoring of congenital heart defects in newborns. Durduran *et al.* used a hybrid NIRS-DCS instrument to study the changes of oxyhemoglobin, deoxyhemoglobin, total hemoglobin concentrations, $CMRO_2$, and CBF during hypercapnia. Measurements validation of CBF and $CMRO_2$ were conducted using MRI-ASL and the results showed a good agreement with DCS measurements ($R=0.7$, $p=0.01$) [191]. Buckley *et al.* [16] and Shaw *et al.* [17] measured changes of cerebral hemodynamics and oxygen metabolism during neonates cardiac surgery using DCS and diffuse optical spectroscopy (DOS) to evaluate the risk of surgery duration and surgical procedures, respectively. In addition, neonatal hypoxic ischemic encephalopathy (HIE) has also been studied using hybrid FD-NIRS and DCS [236].

Researchers revealed the effects presented by therapeutic hypothermia (TH) on cerebral hemodynamics and blood oxygen metabolism by measuring CBF and $CMRO_2$ during and after the TH for neonate HIE. Furthermore, another work studied neurodevelopmental outcomes 18 months after TH of neonate HIE, researchers pointed that $CMRO_2$ is a good indicator of TH evaluation and can be measured repeatedly at point of care [192]. These studies demonstrated the feasibility of using NIR diffuse optical technologies, such as DCS and DOS, to monitor neonate cardio-cerebral diseases and effect therapeutic surgery procedures.

2.7.2.3 Neonates Brain Development

Hemodynamics and cerebral metabolic rate of oxygen are potential indicators of neonates' brain health and development [193–195]. DCS combined with FD-NIRS also has been used to monitor the newborns brain development, which revealed the difference of CBF in cortical regions and $CMRO_2$ in frontal region between male and female babies with the right-left brain functional asymmetry [196]. Besides, activities in somatosensory cortex of premature neonates have also been studied using DCS to evaluate brain neurodevelopment [197].

2.7.2.4 Children Brain Health Evaluation

Busch *et al.*[198] employed DCS to observe CBF fluctuations in children's brains (aged 6-16 years) diagnosed with obstructive sleep apnea syndromes (OSAS) and were prone to experiencing hypercapnia during sleep. Notably, children with OSAS and those exhibiting habitual snoring displayed attenuated CBF responses to hypercapnia in comparison to the healthy control group. These observations provide valuable insights into the neurovascular response mechanisms underpinning the physiopathology of OSAS in the pediatric demographic. Besides, Nourhashemi *et al.*[199] combined electroencephalography (EEG), NIRS, and DCS to simultaneously capture changes in electrical and optical dynamics in children (aged 6-10 years) affected by absence seizures. The outcomes revealed a consistent correlation among EEG, NIRS and DCS, suggesting that DCS holds promise in detecting hemodynamic changes of pediatric brain disorders. Moreover, DCS has been employed for real-time CBF measurements during the chronic transfusion therapy for children with sickle cell diseases [19,99,200]. Figure 2.11 shows representative applications of DCS in neonates.

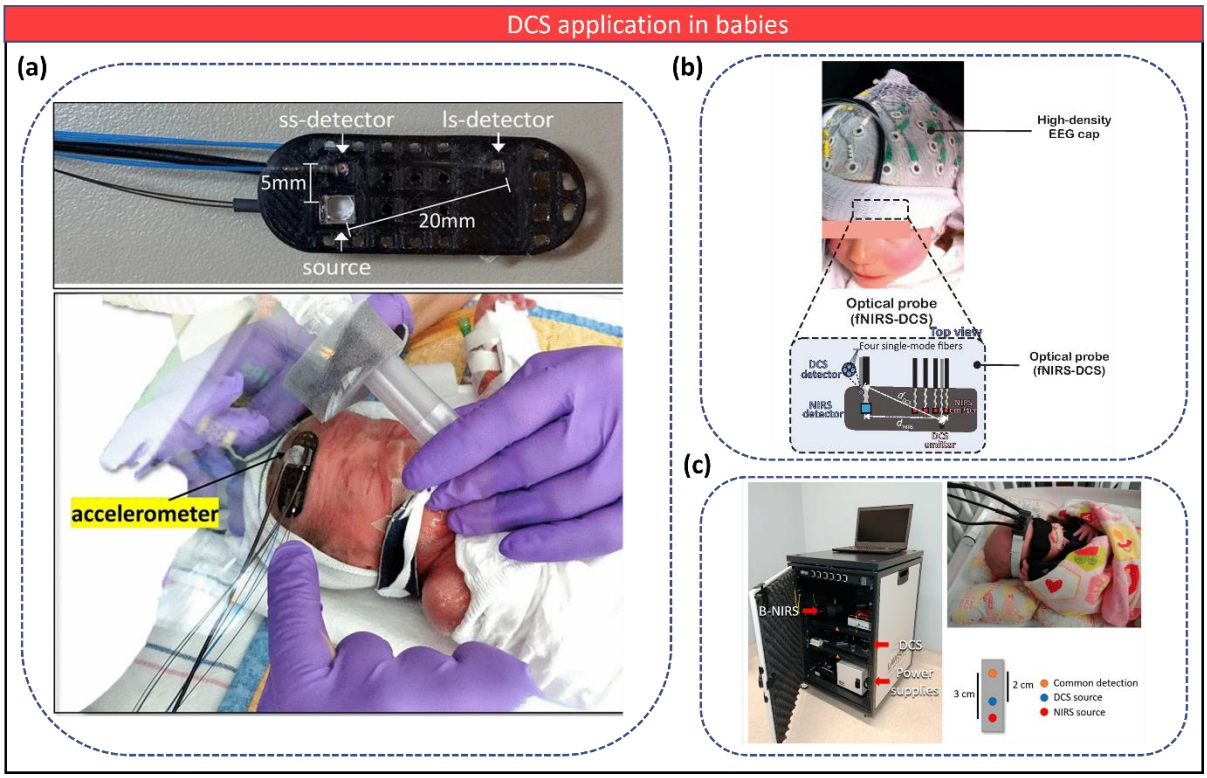

Figure 2.11 (a) DCS sensor was attached to the infant's head for blood flow monitoring, figures adopted from Ref. [90]; (b) The high-density EEG cap and optical probe (NIRS-DCS) and schematic representation of the location of the EEG and optical probes on a child's head. Figure was reproduced from Nourhashemi *et al.* [199]. (c) The hybrid DCS system for neonatal blood flow monitoring, figures reproduced from Ref. [201].

2.7.3 Adults

In this section, we focus on DCS applications on human adults and divide them into four sections: neuroscience study, cardio-cerebrovascular disease study, skeletal muscle and exercise physiology study, and tumor diagnosis and therapy evaluation. Figure 2.12 shows the use of DCS in adults.

2.7.3.1 Neuroscience Study

Measuring CBF facilitates the investigation of neurovascular coupling, brain injuries, stroke, and neurological disorders. Neurovascular coupling denotes the connection between regional neural activity and subsequent alterations in CBF. The extent and spatial positioning of blood flow fluctuations are intricately connected to shifts in neural activity through a sophisticated sequence of coordinated processes involving neurons, glial cells, and vascular elements [202]. DCS can quantify changes in human cerebral blood flow in response to various stimuli, including but not limited to sensorimotor cortex activation [83], visual cortex activation

[86,203], transcranial magnetic stimulation (TMS) [204], and vasoactive stimuli [142]. These studies presented noninvasive and straightforward means of monitoring cognitive neuronal activity in human brains. Older adults with mild cognitive impairment exhibit significantly higher CBF increments during motor and dual-task activities whereas the counterparts displaying normal cognitive functions [205]. Another investigation highlighted the consistency of CBF with the posture changes within a healthy population (aged 20 to 78 years). And the role of DCS during hypothermic circulatory arrests (HCA) therapy has also been studied among older people (mean age 61.8 ± 19.4 years) [93]. These findings hold significant relevance as reference points for future research focused on age-related alterations in CBF [206]. In addition, DCS has been effectively applied for assessing cerebral hemodynamics under hypotension [207], obstructive sleep apnea [198], and adult comatose [208].

2.7.3.2 Cardio-cerebrovascular Disease Study

Several studies have been undertaken to assess human artery diseases and monitor treatment outcomes. Carotid endarterectomy (CEA), for instance, has been associated with hypoperfusion syndrome in the internal carotid artery (ICA), leading to potential cerebral ischemia. Evaluating and monitoring cerebral hemodynamics during and after CEA emerge as critical measures to assess associated risks. Shang *et al.* conducted a comparative analysis between DCS and EEG, revealing that DCS-measured CBF exhibited more prompt responses to ICA clamping than EEG measurements [209]. Furthermore, the integration of DCS with NIRS has demonstrated feasibility in real-time monitoring of cerebral hemodynamics and oxygen metabolism during CEA procedures [210]. And Mesquita *et al.* also established a physiological connection between CBF and oxygenation in patients with peripheral artery diseases [211]. CBF during the cardiac cycle has been acquired using DCS before and during ventricular arrhythmia in adults [20]. DCS has also been used for monitoring CBF [81,212] and critical closing pressure (CrCP) [213] of ischemic stroke patients and the stroke therapy evaluation [262]. Notably, in neurocritical care units, DCS coupled with NIRS serves as a bedside monitoring tool for individualized CBF management and manipulation of head-of-bed treatment for patients with critically brain injuries [88,214].

2.7.3.3 Skeletal Muscle and Exercise Physiology Study

DCS has found applications in the investigation of human skeletal muscle physiology, offering a valuable approach for assessing tissue vascular diseases and enhancing clinicians'

understanding of muscle exercise physiology. For instance, Yu *et al.* compared muscle blood flow and oxygenation between healthy individuals and those with peripheral arterial diseases during cuff occlusion and plantar flexion exercises [69]. Subsequently, they integrated arterial spin-labelled perfusion MRI with DCS to monitor BFi during cuff inflation and deflation [32]. Shang *et al.* characterized muscle blood flow, oxygenation, and metabolism in women with fibromyalgia during leg fatiguing exercise and arm arterial cuff occlusion [215]. Another investigation evaluated local skeletal muscle blood flow during manipulative therapy (MT), suggesting that MT can enhance blood flow with minimal effects on systemic circulatory function [216].

Nevertheless, conventional technologies such as DUS, electromyography (EMG), and MRI encounter challenges when measuring physiological signals due to motion-induced artifacts. These artifacts can lead to inaccurate blood flow measurements. DCS has demonstrated superiority in providing more reliable measurements and greater resistance to experimental variations [217]. However, it is noteworthy that muscle fibre motion artifacts may still result in an overestimation of the change in BFi and researchers have proposed methods to extract accurate blood flow measurements, including the co-registration of dynamometer [71]. Additionally, alternative techniques, such as hardware-integrated gating [218,219] and a random walk correction model with FD-NIRS [75], have been introduced to address fiber motion artifacts in DCS measurements.

2.7.3.4 Tumor Diagnosis and Therapy Evaluation

DCS has been employed in the diagnosis of human breast cancer, prostate tumour, head and neck tumour. Durduran *et al.* conducted an initial comparative analysis of blood flow disparities between tumor and normal tissues in human breast. The investigation revealed a noteworthy increase in blood flow within tumour tissues [26]. This observation paves the way for noninvasive tumour diagnosis. Choe *et al.* used DCS in human breast cancer diagnosis [79]. And the findings align with the results reported by Durduran *et al.*, which underscored the increased blood flow within tumour regions. Besides, noncontact DCT has been adopted for three-dimensional (3-D) visualizing of blood flow distribution in human breast tumors, showing that DCS is a promising technique for localizing human tumours [79].

For tumor therapy evaluation, Yu *et al.* combined DCS with NIRS to measure tumour blood flow and oxygenation of human prostate cancer [23], human head and neck tumour [24]. Also, DCS has been used to evaluate the photosensitizer 2-1[hexyloxyethyl]-2-devinylpyropheophorbide-a (HPPH)- mediated PDT (HPPH-PDT), showed that HPPH-PDT could induce a significant drug photobleaching with a reduction of blood flow and blood oxygenation [220]. In addition, DCS can evaluate chemotherapy [27,80] or radiation therapies [24] in human tumours.

However, there is a limitation in terms of patient statistics when applied DCS in human tumour diagnosis and therapy. Currently, the majority of earlier prediction studies involved a range of 7 to 11 patients [22], segmented into two or three response groups. This is additionally complicated by the varying definitions of responding and non-responding groups utilized by each research team. As a result, longitudinal studies in large patient populations for a longer monitoring period, to provide more precise references for clinic applications are needed. Besides, more precise DCS theoretical models according to application scenarios are also needed [170,221].

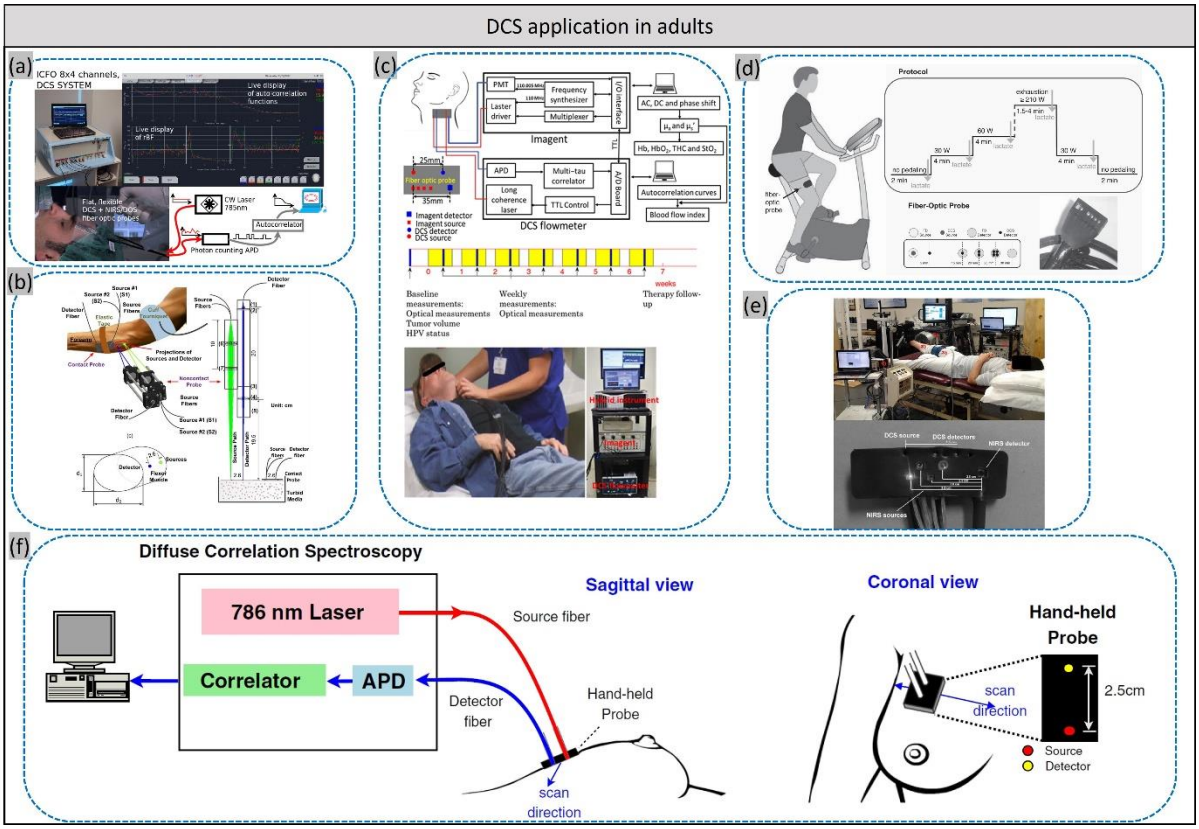

Figure 2.12 (a) Hybrid DCS system applied to human forehead, image taken from Ref. [3]; (b) Experimental configuration with contactless probe, figures adopted from Ref. [222]; (c) Schematic of hybrid instrument, hybrid Imagent/DCS instrument for simultaneous measurement of tumour oxygenation and blood flow during chemoradiation therapy, images adopted from Ref. [223]; (d) Drawing of a subject cycling on a stationary bicycle with a frequency-domain (FD) multi-distance near-infrared spectroscopy (FDNIRS)-diffuse correlation spectroscopy (DCS) probe attached to the right superficial rectus femoris. Figure was adopted from Ref. [93]; (e) Hybrid DCS/NIRS device for muscle measurement. Figures were adopted from Ref. [219]; (f) Diagram of DCS working on a breast, figures adopted from Ref. [79].

In addition to the applications listed above (Figure 2.12), DCS has also been used for critical care [224] and anaesthesiology [225]. DCS is a relatively new and evolving technology, and its applications continue to expand as research advances. The non-invasive and portable nature of DCS makes it particularly attractive for studying dynamic physiological processes *in vivo*. To get more precise measurements, theory models have evolved from semi-infinite to multi-layer model and expanded from CW-DCS to TD- and FD-DCS. Besides, DCT visualized blood flow contrast deep in tissues make it more understandable for blood related diseases diagnosis and therapy. However, restrictions for DCT, such as the limited SNR and high data processing time consumption, hinders its further clinic applications. Therefore, efforts are necessary to further propel the development of DCS, and it can anticipate that DCS will offer increasingly

reliable BFi measurements and will find expanded applications contributing to human health in the future.

2.8 Simulation Tool Related to DCS

To assist researchers in performing and detailing experimental analysis with growing levels of sophistication, several general-purpose analysis platforms and software tools tailored for specific applications have been created. The most used DCS-related tools are summarized in Table 2.8.

Table 2.8 Existing software tools related to DCS.

Name	Language	Website
MCML	Standalone	https://omlc.org/software/mc/
MMC	Standalone/Matlab	http://mcx.space/#mmc
MCX	Standalone/Matlab	http://mcx.space/

2.9 Summary

This chapter aims to outline the existing gap for an affordable, continuous, non-invasive, portable, bedside, and non-ionizing imaging/sensing modality designed to measure CBF. I have summarized all the non-optical methods and discussed their advantages and disadvantages. Having provided a brief introduction to biomedical optics, this chapter also outlines the different incoherent and coherent optical modalities applicable for measuring CBF. Diffuse optical methods are necessary for imaging deeper into the brain; however, the challenge lies in the low SNR linked to the substantial ρ needed for deeper imaging. Among these techniques, DCS stands out as a promising method for BFI. Numerous researchers have endeavoured to enhance the SNR in DCS, employing approaches such as multispeckle analysis, the utilization of lasers with longer wavelengths, interferometric techniques, and advancements in analytical models. In terms of post-data processing, the introduction of AI methods shows significant promise, and there is a great potential for their integration into hardware to enable real-time measurements.

Chapter 3 Theoretical Frameworks

3.1 Introduction

In this chapter, I present fundamental information essential for understanding the critical aspects of photon propagation in tissues. The provided details are kept minimal, aiming to offer only the necessary information required to grasp the limitations and pertinent scales of the physical models employed for the analysis of the data presented in this thesis. Furthermore, I outline the basic theory of dynamic models of photon diffusion, derived analytical models based on existing semi-infinite, two-, and three-layer models and frequency models, and have conducted analytical simulations accordingly. Several new contributions are presented; (1) Systematically derived the analytical models, including a semi-infinite layer, two-layer and three-layer models for diffuse correlation and (2) compared the CW, TD, and FD models.

3.2 Basical Theoretical Background

3.2.1 Scattering and Absorption

The movement of photons within tissue can be effectively represented as a stochastic process. Light exhibits a likelihood of interacting with microscopic centres that encompass a wide size range, ranging from ~Å (e.g., ~ 64Å for hemoglobin) to several micrometers, equivalent to the diameter of large mammalian cells [226]. Photon interaction can lead to the dissipation of energy through absorption or a redirection of its path through scattering [227]. Concentrating on an individual photon trajectory: the likelihood of interaction (either scattering or absorption) is directly related to the reciprocal of the number density of centres (representing the average volume of tissue containing one centre) divided by the total cross-section of both processes. This establishes a characteristic length or mean free path, $\ell_t = 1/\mu_t$. Assume that the interaction occurrences are both independent and distributed in an identical manner.

In the case where scattering and absorption act as separate and unrelated processes, the transport coefficient (μ_t) can be expressed conveniently as the combined sum of absorption (μ_a) and scattering (μ_s) coefficients. An advantageous feature for modelling photon migration is that, typically in tissue, μ_a is significantly lower than μ_s. Frequent elastic scattering within tissue has the consequence of unpredictably altering the direction of light propagation. Photons

rapidly lose details about their original direction, significantly limiting imaging possibilities, such as microscopy, especially in samples with thickness of just a few tens of microns. The specific thickness of tissue required for complete randomization is influenced not only by the scattering coefficient (μ_s) but also by the preferred direction of re-emission of scattered light. These microscopic properties exhibit significant variability among different tissues. A broader mean scattering angle corresponds to a shorter distance that photons need to traverse to exhibits diffusive behavior in a three-dimensional random walk. Another characteristic length, known as the transport mean free path (TMFP), can be introduced, defined as ℓ_{tr}, signifying the average distance a photon must cover to transition into a diffusive state. The corresponding reduced scattering coefficient can be characterized as the reciprocal of the TMFP, l_{tr}, as shown in Eq. (3.1),

$$\mu_s' = \frac{1}{l_{tr}} = (1-g)\mu_s \tag{3.1}$$

where $g \equiv \langle \cos\theta \rangle$ represents the anisotropy factor ranging from -1 to 1 as the average of the cosine of the scattering angle. In tissue, particularly in the near-infrared (NIR) water window, the typical range for g is approximately 0.6 to 0.9. This range indicates a tendency toward predominantly forward-directed scattering [228].

3.2.2 Speckle Fluctuations and Light Scattering Dynamics

3.2.2.1 Interference

It is well-known that a one-dimensional scalar description can aptly characterize light as,

$$E(z,t) = E_0 \cos(kz - \omega t + \emptyset) = Re\{E_0 e^{i(kz-\omega t+\emptyset)}\} = Re\{\tilde{E}(z,t)\}, \tag{3.2}$$

where Euler's formula (Eq. 3.3) has been used, and $\mathrm{Re}\{\cdot\}$ represents the real part.

$$\cos(kz - \omega t + \emptyset) = \frac{e^{i(kz-\omega t+\emptyset)} + e^{-i(kz-\omega t+\emptyset)}}{2}. \tag{3.3}$$

Usually, it is left out from the notation as it is aways assumed to be implicit, and thus, we commonly denote an electromagnetic wave by,

$$\tilde{E}(z,t) = E_0 e^{i(kz-\omega t+\emptyset)}. \tag{3.4}$$

In fact, it is not feasible to directly measure the electromagnetic field. Instead, all optical detectors, including our eyes, can only measure intensity, representing the average energy per unit area per unit time. The intensity is correlated with the electric field through the following relation:

$$I(z) = \frac{\langle \tilde{E}(z,t)\tilde{E}^*(z,t)\rangle}{2\eta} = \frac{E_0^2}{2\eta}, \tag{3.5}$$

where $\eta = \sqrt{\mu/\epsilon}$ is the impedance. E* represents the complex conjugate and $\langle\cdots\rangle$ represents the time average.

Now, let us consider two monochromatic waves, denotes as E_1 and E_2 (as per Eq. 3.4), sharing the same wavelength, propagating along a common axis and reaching a screen positioned at *z*, where their intensity can be observed. According to the principle of superposition, the electric field at any spatial point is merely the summation of individual electric fields. Therefore, at a specific location on the screen, the electric field is expressed as:

$$\tilde{E}_s(z,t) = \tilde{E}_1(z,t) + \tilde{E}_2(z,t) = E_{10}e^{i(kz-\omega t+\phi_1)} + E_{20}e^{i(kz-\omega t+\phi_2)}, \tag{3.6}$$

As we mentioned above, we only detect the intensity rather than the electric field. We substitute Eq. (3.6) into Eq. (3.5),

$$I_s(z) = \frac{\langle \tilde{E}_s(z,t)\tilde{E}_s{}^*(z,t)\rangle}{2\eta} = \frac{\langle \tilde{E}_1(z,t)\tilde{E}_1{}^*(z,t)\rangle + \langle \tilde{E}_2(z,t)\tilde{E}_2{}^*(z,t)\rangle + \langle \tilde{E}_1(z,t)\tilde{E}_2{}^*(z,t)\rangle + \langle \tilde{E}_1{}^*(z,t)\tilde{E}_2(z,t)\rangle}{2\eta}$$

$$= \frac{E_{10}^2 + E_{20}^2 + 2E_{10}E_{20}\cos(\phi_1 - \phi_2)}{2\eta}$$

$$= I_1 + I_2 + I_{21}. \tag{3.7}$$

In Eq. (3.7), I_{21} is referred to as the interference term, and it is evidently contingent on the relative phase of the electric fields. When $\phi_1 - \phi_2 = 2m\pi$ (for any integer m), the intensity exceeds the sum of the two individual intensities. Conversely, when $\phi_1 - \phi_2 = m\pi$ ($m \neq 0$), the intensity is less than the sum of the individual intensities.

3.2.2.2 Speckle

Speckle, also known as speckle pattern or speckle noise, refers to a granular noise texture that diminishes the quality of images due to interference among wavefronts in coherent imaging system. Examples of such systems include radar, synthetic aperture radar (SAR), medical

ultrasound, and optical coherence tomography [229–231]. It is important to note that speckle is not an external source of noise, instead, it arises as an inherent fluctuation in diffuse reflections. This occurs because the scatterers within each cell are not identical, and the coherent illumination wave is highly sensitive to small variations in phase changes [232]. When laser light reflects off a textured surface like paper or a wall, a granular pattern typically appears on the reflecting surface. This "speckle" pattern results from the interference among laser beams with slightly varied light paths. It is often considered an undesirable characteristic of laser light. To mitigate this speckle pattern in images, some individuals opt to use optical diffusers. However, speckles inherently carry a wealth of information about the reflecting surface and/or potential movement of scatterers beneath the surface. Speckles generated by stationary scatterers remain constant, while those produced by moving scatterers exhibit temporal fluctuations. Leverage the dynamic aspect of speckle images allows for the evaluation of the flow characteristics of scatterers.

3.2.2.3 Dynamic Light Scattering (DLS)

Dynamic light scattering (DLS), known alternatively as quasi-elastic light scattering (QELS) or photon correlation spectroscopy (PCS), boasts diverse applications. Extensive theoretical and experimental efforts have been dedicated to this field [233–235]. At the beginning, DLS is employed to assess particle sizes in a solution through the measurement of its diffusivity or diffusion constant, D_B. For instance, utilizing the Stokes-Einstein relationship $D_B = \frac{\kappa_B T}{6\pi\eta R}$ allows the calculation of the particle's radius (R). Depending on the specific measurement setup and application, this principle may go by alternative names such as laser Doppler velocimetry (LDV), electrophoretic light scattering (ELS), Doppler shift spectroscopy (DSS), and various others. This technique might be known as laser speckle contrast imaging (LSCI) and is applicable for estimating blood flow [236]. In this section, we specifically address the essential aspects of the theory and applications of DLS that are crucial for the subsequent discussions on DWS and DCS.

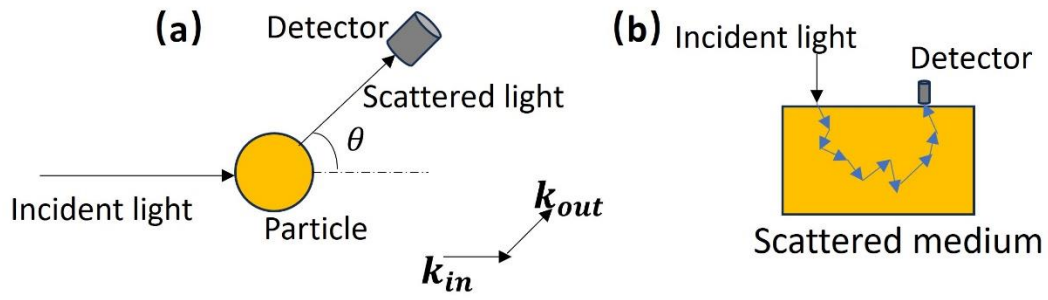

Figure 3.1 (a) Experiment schematic for DLS, with the detector positioned at angle θ. (b) Experiment schematic for DWS, with the detector positioned in reflectance geometry.

The fundamental experimental arrangement for DLS is illustrated in Figure 3.1(a). A coherent light wave strikes a volume, scattering in various directions. A detector is positioned at an angle θ relative to the path of the source light and captures the scattered light. Due to the movement of particles, the scattered light undergoes a Doppler shift to a distinct frequency, contingent on the direction and velocity of the particle's motion. An alternative understanding of this phenomenon arises directly from the intensity autocorrelation function. In the absence of particle motion (in contrast to static light scattering (SLS)), the scattered field from one particle would exhibit a phase creates an interference pattern in the far-field, commonly recognized as a speckle pattern. Suppose that the particles are in motion. As described in section 3.3.1, phase differences cause either destructive or constructive interference. Changes in phase therefore cause variations in the interference pattern. By means of the recording of the intensity changes of the speckle over time, it is possible to determine the correlation between the intensity at time t and the intensity at time $t+\tau$. Using the commonly accepted notation in the field, the unnormalized field autocorrelation function is represented as $G_1(\tau) = \langle E(t)E^*(t+\tau)\rangle$, where E(t) is the complex amplitude. The normalized field autocorrelation function can be calculated as:

$$g_1(\tau) = \frac{G_1(\tau)}{G_1(0)} = \frac{\langle E(t)E^*(t+\tau)\rangle}{\langle E(t)E^*(t)\rangle}. \tag{3.8}$$

Similarly, we calculated the unnormalized intensity autocorrelation function $G_2(\tau) = \langle I(t)I(t+\tau)\rangle$ and the normalized intensity autocorrelation function is given by:

$$g_2(\tau) = \frac{G_2(\tau)}{G_2(0)} = \frac{\langle I(t)I(t+\tau)\rangle}{\langle I(t)\rangle^2}. \tag{3.9}$$

By the Siegert relation, we can obtain:

$$g_2(\tau) = 1 + \beta|g_1(\tau)|^2, \tag{3.10}$$

where β adjusts for the spatial and temporal coherence of the light in the experimental setup and ranges from 0 to 1.

The most straightforward method for gauging intensity autocorrelation involves directly recording the scattered light, with the detector's output current showing a linear proportionality to the incident light's intensity. The graph depicting intensity across time can be employed to compute the intensity autocorrelation using Eq. (3.9). Let us take a simple example, we showcase the autocorrelation of a solution containing non-interacting colloidal monodisperse spherical particles experiencing Brownian diffusion, as derived in Ref. [35]. The scattered fields result from combining the scattered fields produced by each of the N particles that interacted with the light is given by:

$$E(t) = \sum_{j=1}^{N} E_0 e^{i(\omega_0 t - \boldsymbol{q}\cdot\boldsymbol{r}_j(t))}, \tag{3.11}$$

where q = k_{out} - k_{in} denotes as the scattering wavevector and $r_j(t)$ is the time-varying position of the j^{th} particle. Substituting Eq. (3.11) into Eq. (3.8) and assuming a single scattering event, then we obtain,

$$g_1(\tau) = e^{-q^2 D_B \tau} = e^{-(2k_0 sin\frac{\theta}{2})^2 D_B \tau}, \tag{3.12}$$

where |q| = $2k_0$sin(θ/2) is the magnitude of the scattering wavevector, and $k_0 = 2\pi/\lambda$ is the wavenumber of the light in the medium. The case of the multiple scattering events is discussed in section 3.2.3.

3.2.3 Diffuse Wave Spectroscopy (DWS)

Similar to DLS, diffuse wave spectroscopy (DWS) was initially investigated in relation to particle motion and sizing. However, its applications have been expanded to include biomedical contexts [237]. In 1987, Maret and Wolf pioneered an experimental approach to examine the Brownian dynamics of light scatterers within realm of multiple scattering [65], as shown in Figure 3.1(b). Quantitative analysis of the data was conducted using photon diffusion theory, leading to the nomenclature of the technique as diffusing wave spectroscopy (DWS). In DWS, it assumes the strong multiple-scattering limit of light and like NIRS, light propagate in tissue can be modelled as a diffusion process. To begin with, let's presume that we have knowledge of the distance travelled by a photon, denotes as s. The field autocorrelation function can then be calculated to be,

$$g_1(s,\tau) = e^{-2k_0^2 D_B \tau \frac{s}{\ell_{tr}}}. \tag{3.13}$$

In Contrast to Eq. (3.12), it can be noted that the term $q^2 = (2k_0 sin\frac{\theta}{2})^2$ has been substituted with a simpler expression, namely, $2k_0^2$ [238]. Additionally, take note of the extra terms $\frac{s}{\ell_{tr}}$, which represents the count of random walk steps the photon undergoes along its path of length s. This term suggests that, on average, each scattering step leads to a decay of $e^{2k_0^2 D_B \tau}$ in the autocorrelation. Most often, we are unable to directly measure the pathlength covered by a photon. Therefore, we must account for all conceivable pathlengths. The overall autocorrelation function of the total field is thus a weighted mean across all potential pathlengths, can be written as:

$$g_1(\tau) = \int_0^\infty P(s) g_1(s,\tau) ds, \tag{3.14}$$

where $P(s)$ is the probability of detecting a photon with path length s in the sample. A comparable representation can be obtained by replacing the time-of-flight $t = s/v$ in cases where the refractive index n is homogenous. Two notable enhancements of DWS compared to DLS, in addition to operating in the multiple scattering regime, include its sensitivity to the motion of scatterers on length scales significantly smaller than λ and a substantially reduced dependence on the size variation among the light-scattering particles [64]. When contemplating extended paths with a substantial number of scattering events, which implies the involvement of numerous scattering occurrences, each particle only requires a minor displacement for the overall path length to vary by a wavelength. A significant outcome of multiple scattering is that light relinquishes all its polarization characteristics as it undergoes scattering throughout the medium. If we consider the source light to be linearly polarized, the polarization of the detected light will exhibit equal amplitudes in both parallel and perpendicular orientations to the initial polarization direction. As the two polarizations of light are mutually independent, this situation is equivalent to measuring light from two speckles, resulting in the averaging out of their intensity fluctuations. Consequently, when the detected light is unpolarized, the maximum achievable value for β is 0.5. Additionally, owing to multiple scattering, the pathlength traversed by photons within the medium is significantly greater compared to a DLS experiment. Therefore, it becomes imperative that the laser's coherence length exceeds this pathlength. Otherwise, the decrease in the autocorrelation function would stem from a short coherence length rather than the impacts of scattering.

3.3 Diffuse Correlation Spectroscopy

Typically, blood flow measurements obtained through DCS are examined utilizing the correlation diffuse spectroscopy (CDE) [3,66]. The CDE is formulated based on the correlation transfer equation (CTE) assuming that the likelihood of light scattering significantly surpasses the likelihood of light absorption, namely $\mu_s' \gg \mu_a$. The CTE enables the computation of the electric field autocorrelation function ($G_1(\tau)$) under broader conditions of photon migration. It is analogous to the traditional radiative transfer equation (RTE), which describes the movement of light intensity through scattering media. In this section, I will derive DCS analytical models (semi-infinite, two-layer and three-layer) for CW-, TD-, and FD-DCS. Figure 3.2 shows the analytical models I will discuss.

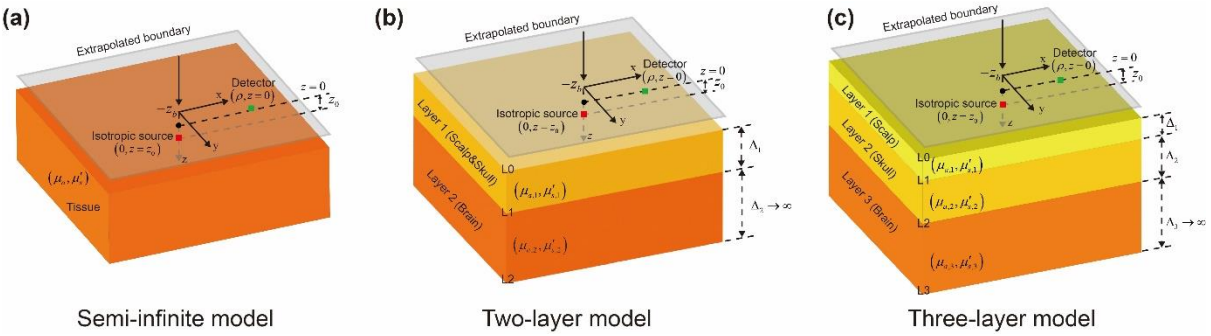

Figure 3.2(a) The homogenous semi-infinite analytical model, (b) Two-layer analytical model, (c) Three-layer analytical model. All of the geometric schemes including the position of the source and detector, each layer has its own thickness $\Delta_{(1,2,3)}$ and characterized by the absorption coefficient $\mu_{a(1,2,3)}$ and reduced scattering coefficient $\mu'_{s(1,2,3)}$.

3.3.1 CW Semi-infinite (One Layer) Model

In traditional DCS systems, it is commonly assumed that the tissue is a homogenous semi-infinite medium, as shown in Figure 3.2(a). Under the standard diffusion approximation, we can obtain CDE as:

$$\left(-\frac{D(\boldsymbol{r})}{v}\nabla^2 + \mu_a + \frac{1}{3}\alpha\mu_s' k_0^2\langle\Delta r^2(\tau)\rangle\right) G_1(\boldsymbol{r},\tau) = S(\boldsymbol{r}), \tag{3.15}$$

where $G_1(r,\tau) \equiv \langle \vec{E}(r,\tau)\cdot\vec{E}^*(r,t+\tau)\rangle$is the electric field autocorrelation function. D(r) = v/(3μ_s') is the photon diffusion coefficient, v is the speed of light in the medium. k_0 is the wavenumber in the medium, α represents the probability that a light scattering event is with a moving scatterer (e.g., a flowing red blood cell), and $\langle\Delta r^2(\tau)\rangle$ represents the mean square

displacement of moving scatterers, and is commonly described using two different models, including the Brownian motion and random ballistic models in biological tissues. For the Brownian motion, $\langle \Delta r^2(\tau) \rangle = 6D_B\tau$ [105], where D_B is an 'effective' diffusion coefficient for moving particles. For random ballistic flow, $\langle \Delta r^2(\tau) \rangle = 6V^2\tau^2$, where V^2 is the mean quare velocity of the scatterer in the vasculature.

Consider a semi-infinite homogenous system with a point source $S(\vec{r}) = S_0\delta(\boldsymbol{r})$, where S_0 represents the amplitude of light source. The solution $G_1(r,\tau)$ to Eq. (3.15) is obtained using an image source approach, flowing Kienle and Patterson [239]:

$$G_1(\vec{r},\tau) = \frac{3\mu_s' S_0}{4\pi}\left[\frac{exp(-Kr_1)}{r_1} - \frac{exp(-Kr_2)}{r_2}\right], \tag{3.16}$$

where $K = \sqrt{3\mu_s'\mu_a + \alpha\mu_s'^2 k_0^2\langle \Delta r^2(\tau) \rangle}$, r_1 and r_2 are the distances between the detector and the source/image source, respectively, as shown in Figure 3.3. $r_1 = \sqrt{\rho^2 + {z_0}^2}$ and $r_2 = \sqrt{\rho^2 + (z_0 + 2z_b)^2}$; $z_0 = 1/\mu_s'$ is the depth at which a collimated source on the tissue surface can be approximate as a point source; $z_b = {2(1+R_{eff})}\big/{3\mu_s'(1-R_{eff})}$ and $R_{eff} = -1.440n^{-2} + 0.71n^{-1} + 0.668 + 0.0636n$ is the effective reflection coefficient, $n = \frac{n_{tissue}}{n_{air}} \approx 1.33$. Typically, αD_B is referred to as the blood flow index (BFi) in biological tissues [240]. In practice, the Brownian model can fit the observed correlation decay curves better over a wide range of tissue types, including rat brain [6,82,85,181], piglet brain [186,241], human brain [86,203,242,243], mouse tumours [178,180], human skeletal muscle [69–71,244], human tumors [23,24,24]. Figure 3.4 shows sets of autocorrelation functions for different ρ, β, and D_B. The curves decay faster with increasing D_B, i.e. increased flow, and increased ρ. The slope and/or the decay rate provides information about the optical properties and the motion of the scatters. Figure 3.4(c) shows that the autocorrelation curve tends to flatten as β increases.

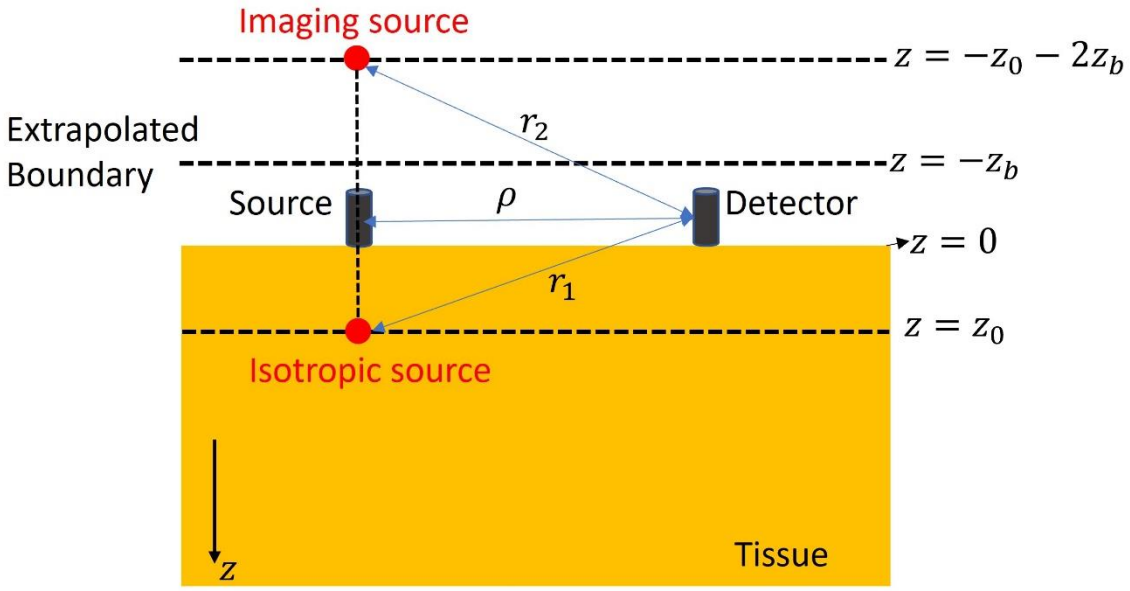

Figure 3.3 Illustration of semi-infinite geometry with boundary condition.

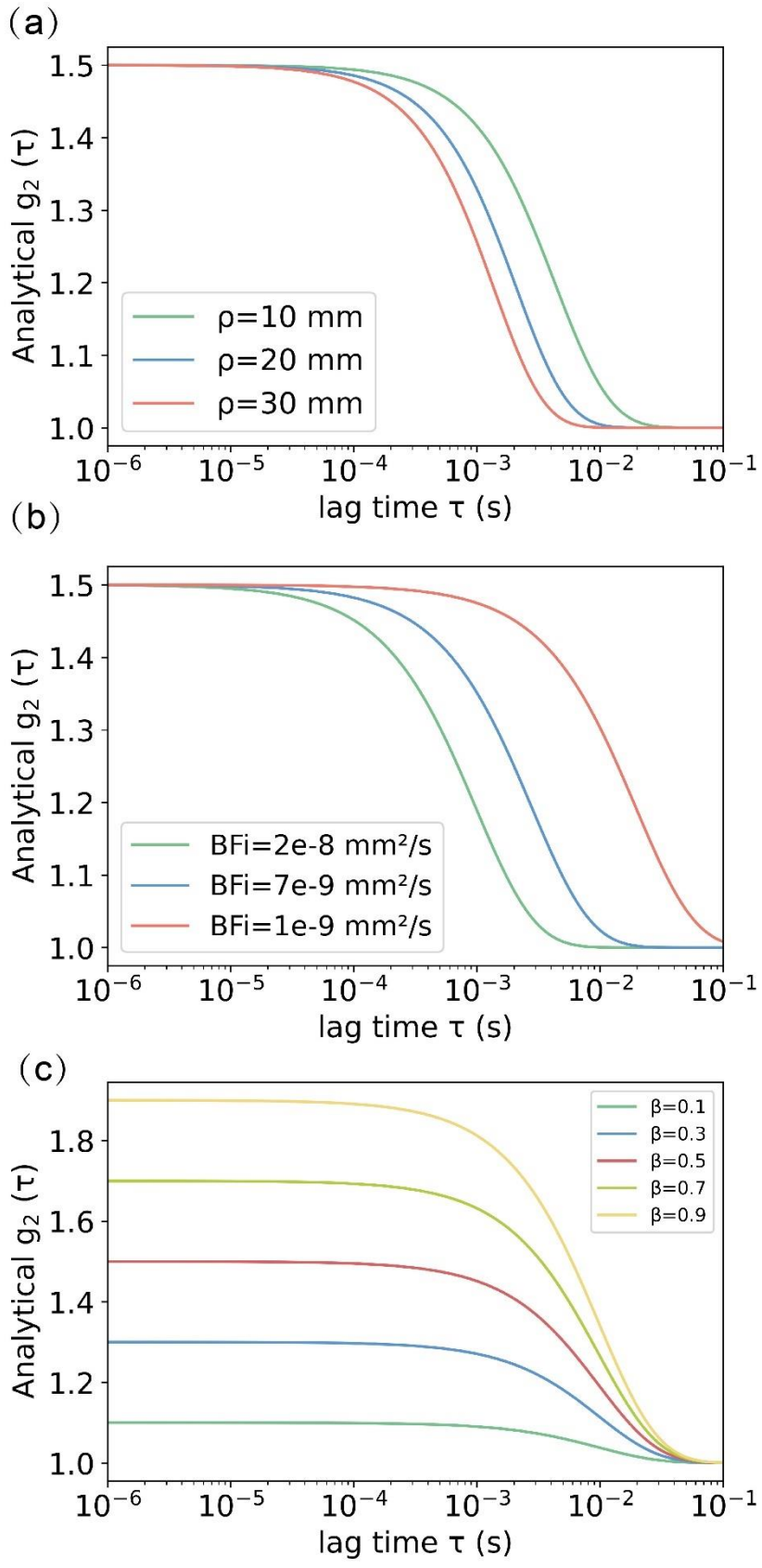

Figure 3.4 Assuming μ_a = 0.013 mm^{-1}, μ_s' = 0.86 mm^{-1}. (a) Autocorrelation functions for $D_B = 1\times10^{-8}$ mm^2/s for different ρ, (b) Autocorrelation functions for ρ = 30 mm for different D_B, (c) Autocorrelation functions for $D_B = 1\times10^{-8}$ mm^2/s, and ρ=30 mm for different β.

3.3.2 CW Two-layer Model

We have stated above that the DCS theory is based on the correlation transport [66,245,246], which can be approximated by CDE [35,238]. By assuming that light propagates in a homogenous medium, the solution of Eq. (3.15) is simple and has been widely used in DCS communities [240]. However, biological tissues (e.g., skin, esophagus, stomach, intestine, bladder, and head [247]) are layered with each layer encompassing unique physiological and optical properties [248,249]. Gagnon [147] *et al.* first proposed a two-layer analytical model, based on Kienle *et al.*'s model for reflectance spectroscopy with the two-layered geometry in Figure 3.2(b).

We assume an infinitely thin beam incident onto a turbid, two-layered medium. The first layer of this two-layer medium has a thickness Δ_1 and the second layer is semi-infinite. Within the first layer, the beam undergoes isotropic scattering at a depth z = z_0, where $z_0 = 1/(\mu_{a1} + \mu'_{s1})$. Here, μ_{a1} and μ'_{s1} represent the absorption and reduced scattering coefficients of Layer 1, respectively. We also assume that the Brownian movement is independent in each layer which means that the particles can not move from one layer to the other in the medium. The incident light is perpendicular to the surface of turbid medium, in which the x-y plane lies on. Then Eq. (3.15) becomes:

$$\left(-D_1\nabla^2 + \mu_{a1} + \frac{1}{3}k_0^2\mu'_{s1}\langle\Delta {r_1}^2(\tau)\rangle\right) G_1^1(x,y,z,\tau) = S(x,y,z-z_0), 0 \le z \le \Delta_1 \quad (3.17)$$

$$\left(-D_2\nabla^2 + \mu_{a2} + \frac{1}{3}k_0^2\mu'_{s2}\langle\Delta {r_2}^2(\tau)\rangle\right) G_1^2(x,y,z,\tau) = 0, \Delta_1 \le z \quad (3.18)$$

where $D_i = 1/3(\mu_{a(i)} + \mu'_{s(i)})$ is the diffusion constant of Layer i. The mean-squared displacement $\langle\Delta {r_i}^2(\tau)\rangle = 6D_{B(i)}\tau$ for Layer i.

Although Kienle *et al.*'s derivations [247,250] are originally for diffuse reflectance spectroscopy (DRS), we re-derive them for DCS following the same procedure and obtain the solution of Eqs. (3.17) and (3.18) at z = 0 (Layer 1) in the Fourier domain by

$$\tilde{G}_1^1(\boldsymbol{q},z,\tau) = \frac{\sinh[\beth_1(z_b+z_0)]}{D_1\beth_1} \times \frac{D_1\beth_1\cosh[\beth_1(\Delta_1-z)]+D_2\beth_2\sinh[\beth_1(\Delta_1-z)]}{D_1\beth_1\cosh[\beth_1(\Delta_1+z_b)]+D_2\beth_2\sinh[\beth_1(\Delta_1+z_b)]} - \frac{\sinh[\beth_1(z_0-z)]}{D_1\beth_1}, \quad (3.19)$$

where $\beth_j^2 = (D_j\boldsymbol{q}^2 + \mu_{aj} + 2c\mu'_{sj}k_0^2D_{Bj})/D_j$, j =1 and 2, **q** is the radial spatial frequency and

$$z_b = \frac{1+R_{eff}}{1-R_{eff}} 2D_1, \tag{3.20}$$

And $G_1^1(\boldsymbol{\rho}, z = 0, \tau)$ at r = {ρ, z = 0} on the surface of the medium is then obtained from the inverse spatial Fourier transform as,

$$G_1^1(\boldsymbol{\rho}, z = 0, \tau) = \frac{1}{2\pi} \int_0^\infty \tilde{G}_1^1(\boldsymbol{q}, z = 0, \tau) \boldsymbol{q} \boldsymbol{J_0}(\boldsymbol{q}\boldsymbol{\rho})\, d\boldsymbol{q}, \tag{3.21}$$

where J_0 stands for the zeroth order Bessel function of the first kind computed by the MATLAB function *besselj*.

3.3.3 CW Three-layer Model

Also, in the three-layer DCS model, $G_1(r, z, \tau)$ can be modelled by CDE. A turbid medium consisting of 3 slabs was considered as shown in Figure 3.2(c). Each slab has thickness $\Delta_n = L_p - L_{p-1}$, p =1, 2, 3. To solve $G_1(r, z, \tau)$, Eq. (3.15) can be revised for the three-layer model as:

$$\left[\nabla^2 - \left(3\mu_a^{(n)}\mu_s'^{(n)} + 6k_0^2\mu_s'^2 D_B^{(n)}\tau\right)\right] G_1(r, \tau) = -s_0\delta(r - r'), \tag{3.22}$$

where s_0 is a point-like monochromatic light source located at $r' = \{\rho' = 0, z'\}$ inside Layer 1; ρ represents for the transverse coordinate. The field autocorrelation at the tissue surface, G_1 (r, τ), can be obtained by solving Eq. (3.21) in the Fourier domain with respect to as:

$$\hat{G}(\boldsymbol{q}, z, \tau) = \int d^2\rho G_1(r, \tau) \exp\,(i\boldsymbol{q} \cdot \rho), \tag{3.23}$$

where q is the radial spatial frequency. Thus, in the Fourier domain Eq. (3.21) can be rewritten:

$$\left[\frac{\partial^2}{\partial z^2} - \kappa^2(\boldsymbol{q}, \tau)\right] \hat{G}(\boldsymbol{q}, z, \tau) = -s_0\delta(z - z'), \tag{3.24}$$

where $\kappa_{(n)}^2(\boldsymbol{q}, \tau) = 3\mu_a^{(n)}\mu_s'^{(n)} + 6k_0^2\mu_s'^2 D_B^{(n)}\tau + \boldsymbol{q}^2$.

We divided the top layer into two sublayers: Sub-layer 0 (0 < z< z') identified by p = 0, and Sub-layer 1 (z' < z< L_1), identified by p in the following. The solution of Eq. (3.24) inside the Layer p (p = 1, 2, 3) can be written as:

$$\hat{G}_p(\boldsymbol{q}, z, \tau) = A_p \exp\left(\kappa_{(p)} z\right) + B_p \exp\left(-\kappa_{(p)} z\right), \tag{3.25}$$

where A_p and B_p are constant factors for Layer p determined by the boundary conditions:

$$\hat{G}_0(q,z,\tau) - z_0 \frac{\partial}{\partial z}\hat{G}_0(q,z,\tau) = 0, z = 0$$

$$\hat{G}_0(q,z,\tau) = \hat{G}_1(q,z,\tau), z = z'$$

$$\frac{\partial}{\partial z}\hat{G}_0(q,z,\tau) = \frac{\partial}{\partial z}\hat{G}_1(q,z,\tau) + 3\mu_s'^1, z = z'$$

$$\hat{G}_p(q,z,\tau) = \hat{G}_{p+1}(q,z,\tau), z = L_p, p = 1,2$$

$$D_p \frac{\partial}{\partial z}\hat{G}_p(q,z,\tau) = D_{p+1}\frac{\partial}{\partial z}\hat{G}_{p+1}(q,z,\tau), z = L_p, p = 1,2$$

$$\hat{G}_3(q,z,\tau) + z_3 \frac{\partial}{\partial z}\hat{G}_3(q,z,\tau) = 0, z = L_3, \tag{3.26}$$

where $z_0 \sim 1/\mu_s'^1$ and $z_3 \sim 1/\mu_s'^3$ are the extrapolation lengths considering internal reflections at the external (z = 0 and z = L_4) boundaries.

Substituting Eq. (3.26) into Eq. (3.25), we can obtain A_p and B_p (p = 1, 2, 3). The Fourier transform G_0 (q, z, τ) measured at z = 0 (the surface of the slab) is then obtained by substituting A_0 and B_0 into Eq. (3.25) under $\Delta_3 \rightarrow \infty$ to obtain:

$$\hat{G}_0(\boldsymbol{q},z,\tau) = \frac{Num}{Denom}, \tag{3.27}$$

where Num and Denom when $p = 3$ and $\Delta_3 \rightarrow \infty$ are:

$$Num = 3\mu_s'^1 z_0(\kappa_1 D_1 cosh\big(\kappa_1(\Delta_1 - z')\big)(\kappa_2 D_2 \cosh(\kappa_2\Delta_2) + \kappa_3 D_3 \sinh(\kappa_2\Delta_2)) + \kappa_2 D_2(\kappa_3 D_3 \cosh(\kappa_2\Delta_2) + \kappa_2 D_2 \sinh(\kappa_2\Delta_2))\sinh(\kappa_1(\Delta_1 - z'))), \tag{3.28}$$

$$Denom = \kappa_2 D_2 \cosh(\kappa_2 D_2)(\kappa_1(D_1 + \kappa_3 D_3 z_0)\cosh(\kappa_1 D_1) + (\kappa_3 D_3 + \kappa_1^2 D_1 z_0)\sinh(\kappa_1 D_1)) + (\kappa_1(\kappa_3 D_1 D_3 + \kappa_2^2 D_2^2 z_0)\cosh(\kappa_1 D_1) + (\kappa_2^2 D_2^2 + \kappa_1^2 \kappa_3 D_1 D_3 z_0)\sinh(\kappa_1 D_1))\sinh(\kappa_2\Delta_2). \tag{3.29}$$

By performing the inverse Fourier transform of Eq. (3.25) with respect to q, G_0 (**q**, z, τ) can be obtained as:

$$G_0(r,\tau) = \frac{1}{(2\pi)^2}\int d^2\,\boldsymbol{q}\hat{G}_0(\boldsymbol{q},z=0,\tau)\exp(-i\boldsymbol{q}\cdot\boldsymbol{\rho})$$

$$= \frac{1}{2\pi}\int d\boldsymbol{q}\,\hat{G}_0(\boldsymbol{q},z=0,\tau)qJ_0(\rho\boldsymbol{q}), \tag{3.30}$$

where J_0 denotes the zero-order Bessel function of the first kind.

This three-layered solution has been tested with Monet Carlo simulations and used to analyze in vivo measurements [47,148].

Figure 3.5 shows numerically simulated g_1 from semi-infinite, two-, and three-layer analytical models. Figure 3.5(a), (b), and (c) show g_1 curves for semi-infinite, two-, and three-layer analytical models, respectively. Typically, in DCS data analysis, the measured intensity autocorrelation functions g_2 was fit to one of the models chose as shown in Figure 3.2, using the Siegert relation $g_2(\tau) = 1 + \beta g_1^2(\tau)$. Commonly, homogenous semi-infinite analytical model was used in data analysis, which assuming free diffusion as mechanism for speckle decorrelation, gave rather poor agreement with the experimental scenarios, this is because homogeneous fitting procedure is more sensitive to the dynamic properties of the superficial layers. Compared with semi-infinite model, two- and three-layered model allows distinction between changes in superficial layers and brain and layered models can mitigate the discrepancies between one-layer model and realistic. Especially, using the three-layer analytical model have been investigated [47,84,251] that it is more accurate. Although, multi-layered models provide a superior fit to measured data and more accurate, they are highly sensitive to measurement noise and much longer *BFi* estimation time is needed.

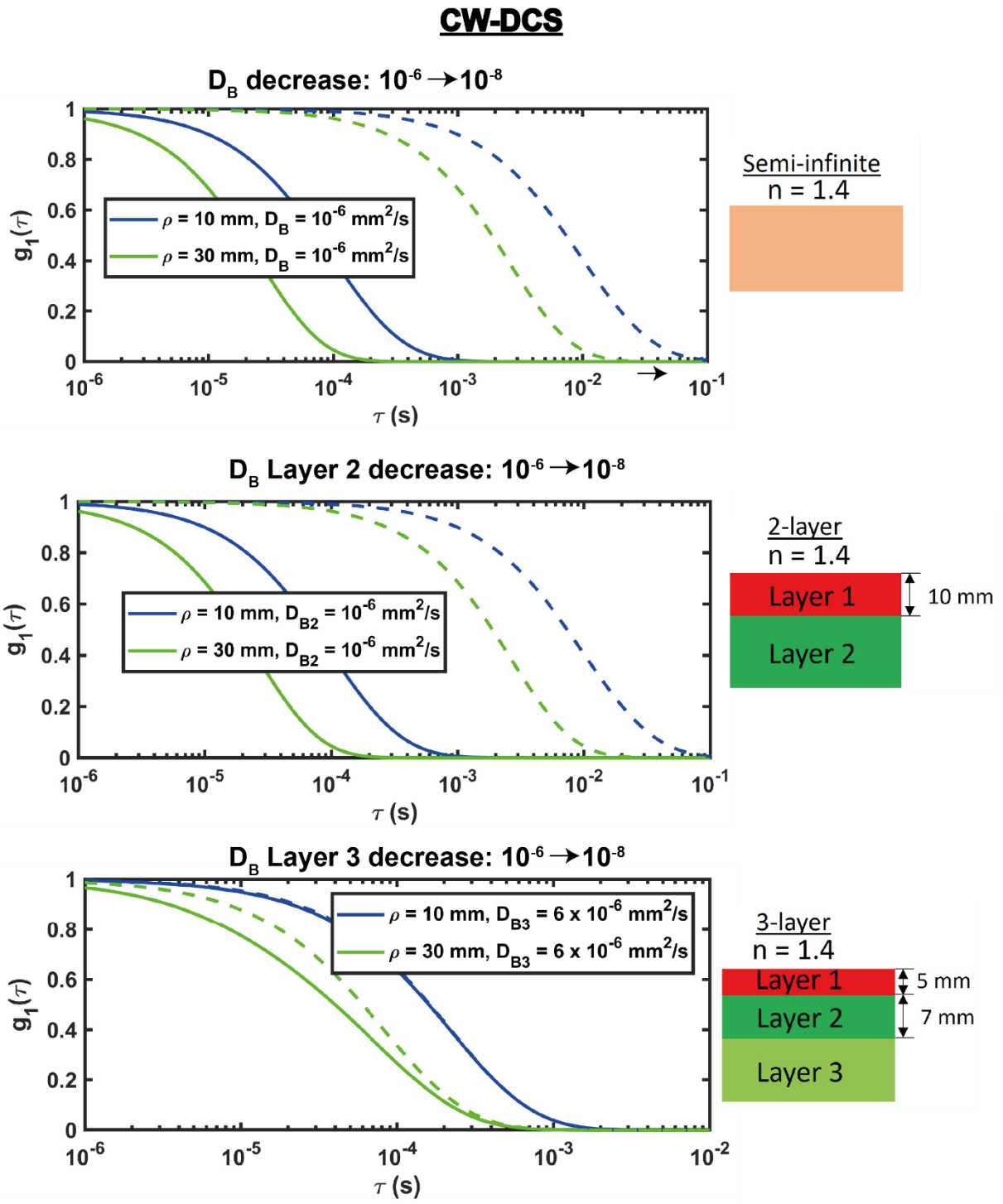

Figure 3.5 (a) Representative $g_1(\tau)$ simulated from a sample with ρ = 10 mm (blue solid line) and ρ = 30 mm (green solid line), varying D_B from 1 × 10^{-6} mm^2/s to 1 × 10^{-8} mm^2/s (blue and green dot lines), μ_a = 0.013 mm^{-1}, μ_s'= 0.86 mm^{-1}, λ = 785 nm. (b) Representative $g_1(\tau)$ simulated from a sample with ρ = 10 mm (blue solid line) and ρ = 30 mm (green solid line), characterized with $\mu_a^{(1)}$ = 0.013 mm^{-1}, $\mu_s'^{(1)}$ = 0.86 mm^{-1}, Δ_1 = 10 mm, $D_B^{(1)}$ = 1 × 10^{-6} mm^2/s, (parameters for the top layer); $\mu_a^{(2)}$ = 0.018 mm^{-1}, $\mu_s'^{(2)}$ = 1.11 mm^{-1}, varying $D_B^{(2)}$ from 1 × 10^{-6} mm^2/s to 1 × 10^{-8} mm^2/s (parameters for the bottom layer; blue and green dot lines); (c) Representative $g_1(\tau)$ data simulated from a sample with ρ = 10 mm (blue solid line) and ρ = 30 mm (green solid line) characterized with $\mu_a^{(1)}$ = 0.013 mm^{-1}, $\mu_s'^{(1)}$ = 0.86 mm^{-1}, Δ_1 = 5 mm, $D_B^{(1)}$ = 1 × 10^{-8} mm^2/s (Parameters for the first layer);

$\mu_a^{(2)}$ = 0.018 mm^{-1}, $\mu_s'^{(2)}$ = 1.11 mm^{-1}, Δ_2 = 7 mm, $D_B^{(2)}$ = 1 × 10^{-6} mm^2/s (Parameters for the second layer); $\mu_a^{(3)}$ = 0.03 mm^{-1}, $\mu_s'^{(3)}$ = 1.19 mm^{-1}, varying $D_B^{(3)}$ from 1 × 10^{-6} mm^2/s to 1 × 10^{-8} mm^2/s (Parameters for the third layer), the spatial frequency q ∈ (0 30) mm^{-1}. All graphs are plotted using homemade software using MATLAB (Mathworks, Inc.).

3.3.4 TD Semi-infinite (One Layer) Model

For TD DCS systems, similarly, $G_1(r, \tau, t)$ obeys the time-dependent correlation equation:

$$\left(-\frac{D(\boldsymbol{r})}{v}\nabla^2 + \mu_a + \frac{1}{3}\alpha\mu_s' k_0^2\langle\Delta r^2(\tau)\rangle + \frac{\mathbf{1}}{\boldsymbol{v}}\frac{\partial}{\partial_t}\right) G_1(\boldsymbol{r}, t, \tau) = S(\boldsymbol{r}, t), \tag{3.31}$$

For a semi-infinite medium, it is straightforward to obtain the analytical solution of Eq. (3.30) under the boundary condition [252]. Thus, thus $G_1(\rho, t, \tau)$ on the tissue surface (z = 0) is [41]:

$$G_1(\rho, t, \tau) = c\left(\frac{3\mu_s'}{4\pi ct}\right)^{\frac{3}{2}} \exp[-(\mu_a + 2\mu_s' D_B k_0^2 \tau)ct] \exp\left(-\frac{3\mu_s'\rho^2}{4ct}\right) \times [\exp\left(-\frac{3\mu_s' z_0^2}{4ct}\right) - \exp\left(-\frac{3\mu_s'(z_0+2z_b)^2}{4ct}\right)]. \tag{3.32}$$

Thus, $g_1(\tau, s)$ for a photon pathlength s can be written as:

$$g_1^{single}(\tau, s) = \frac{G_1(\rho, t, \tau)}{G_1(\rho, t, \tau = 0)}$$

$$= \exp(-2\mu_s' D_B k_0^2 s\tau). \tag{3.33}$$

However, it is not easy to measure the pathlength travelled of a photon in tissues. Therefore, the total scattered electric-field autocorrelation function $g_1(\tau, s)$ is obtained by incoherently summing the contributions over all s taking into consideration [65,137]. Thus $g_1(\tau, s)$ is then a weighted average over all possible pathlengths, expressed as:

$$g_1(\tau) = \int_0^\infty P(s) g_1^{single}(\tau, s) ds$$

$$= \int_0^\infty P(s)\exp(-2\mu_s' D_B k_0^2 s\tau) ds. \tag{3.34}$$

where P(s) represents the probability that an incident photon travels a distance s before emerging from the medium; it can be calculated as [253]:

$$P(s) = \frac{v}{(4\pi Ds/v)^{3/2}} \exp(-\mu_s s) \times [\exp\left(-\frac{r_1^2}{4Ds}\right) - \exp(-\frac{r_2^2}{4Ds})], \tag{3.35}$$

where the variables are the same as in Eq. (3.16) and s = *vt*, *t* is the photon time-of-flight (ToF), *v* is the speed of light in the medium.

According to the model of Bellini *et al.* [95] in 1991, we can calculate $g_2(\tau)$ as:

$$g_2(\tau) = 1 + \iint_0^\infty P(s)P(s')g_1(\tau,s)g_1(\tau,s)e^{-2(\frac{s-s'}{l_c})^2}dsds', \tag{3.36}$$

here, s and s' represent the photon pathlength through the medium and l_c is the coherence length of the light source.

3.3.5 TD Two-layer Model

For the second layer model, the Equation (3.31) can be rewrite:

$$\left[\nabla^2 - \left(3\mu_a^{(p)}\mu_s'^{(p)} + 6k_0^2\mu_s'^2 D_B^{(p)}\tau\right) - \frac{3\mu_s'}{v}\frac{\partial}{\partial t}\right]G(r,\tau,t) = -3\mu_s'\delta(r-r')\delta(t). \tag{3.37}$$

Similarly, we can derive the Fourier transform of G(r, τ) for the real space (ρ, z), as well as time *t*, and then solve Eq. (3.37) in the Fourier space (q, z, w).

$$\hat{G}(q,z,w,\tau) = \int dt exp(iwt)\int d^2\boldsymbol{\rho}\, G(\boldsymbol{\rho},z,t,\tau)\exp(i\boldsymbol{q}\cdot\boldsymbol{\rho}), \tag{3.38}$$

yielding

$$\left[\frac{\partial^2}{\partial z^2} - \left(3\mu_a^{(p)}\mu_s'^{(p)} + 6k_0^2\mu_s'^2 D_B^{(p)}\tau - 3\mu_s'^{(p)}\cdot\frac{iw}{c}\right) - \boldsymbol{q}^2\right]\hat{G}(q,z,w,\tau) = -3\mu_s'\delta(z-z'). \tag{3.39}$$

The solution of Eq. (3.39) can be written as:

$$\hat{G}(q,z,w,\tau) = \gamma_p \exp(\Psi_p z) + \varphi_p \exp(-\Psi_p z), \tag{3.40}$$

where $\Psi_p = \sqrt{\left(3\mu_a^{(p)}\mu_s'^{(p)} + 6k_0^2\mu_s'^2 D_B^{(p)}\tau - 3\mu_s'^{(p)}\cdot\frac{iw}{c}\right) + \boldsymbol{q}^2}$, γ_p and φ_p are constant for Layer *p* (*p* = 1, 2), which can be determined by the boundary conditions:

$$\hat{G}_0(q,z,w,\tau) - z_0\frac{\partial}{\partial z}\hat{G}_0(q,z,w,\tau) = 0, \mathrm{z} = 0$$

$$\hat{G}_0(q,z,w,\tau) = \hat{G}_1(q,z,w,\tau), \mathrm{z} = z'$$

$$\frac{\partial}{\partial z}\hat{G}_0(q,z,w,\tau) = \frac{\partial}{\partial z}\hat{G}_1(q,z,w,\tau) + 3\mu_s'^1, \mathrm{z} = z'$$

$$\hat{G}_p(q,z,w,\tau) = \hat{G}_{p+1}(q,z,w,\tau), z = L_p, p = 1,2$$

$$D_p\frac{\partial}{\partial z}\hat{G}_p(q,z,w,\tau) = D_{p+1}\frac{\partial}{\partial z}\hat{G}_{p+1}(q,z,w,\tau), z = L_p, p = 1,2$$

$$\hat{G}_3(q,z,w,\tau) + z_3 \frac{\partial}{\partial z}\hat{G}_3(q,z,w,\tau) = 0, z = L_3 \quad (3.41)$$

Thus, we obtained the solution of Eq. (3.38),

$$\hat{G}_0(q,z=0,w,\tau) = \frac{3\mu_s' z_0[\Psi_1 D_1 \cosh(\Psi_1(\Delta_1 - z_0)) + \Psi_2 D_2 \sin(\Psi_1(\Delta_1 - z_0))]}{\Psi_1(D_1 + \Psi_2 D_2 z_0)\cosh(\Psi_1\Delta_1) + (\Psi_2 D_2 + \Psi_1{}^2 D_1 z_0)\sinh(\Psi_1\Delta_1)}, \quad (3.42)$$

Then the inverse Fourier transform for G(ρ, z, t, τ) at z = 0 is:

$$G_0(\rho,z=0,t,\tau) = \frac{1}{2\pi}\int dw \exp(-iwt)\frac{1}{(2\pi)^2}\int d^2q\, \hat{G}_0(q,z=0,w,\tau)\exp(-iq\cdot\rho) =$$

$$\frac{1}{(2\pi)^2}\int dw \int dq \hat{G}_0(q,z=0,w,\tau) q J_0(\rho q)\exp(-iwt). \quad (3.43)$$

3.3.6 TD Three-layer Model

We start from Eq. (3.37), but derive similarly with Section 3.3.3 and $\Delta_3 \to \infty$, to obtain derive G(ρ, z, t, τ) for the three-layer model as the same with Eq. 3.43, where $\hat{G}_0(q,z=0,w,\tau) = \frac{Num}{Demo}$, where Num and Demo are shown below respectively,

$$Num = 3\mu_s' z_0[\Psi_1 D_1 \cosh(\Psi_1(\Delta_1 - z'))(\Psi_2 D_2 \cosh(\Psi_2 D_2) + \Psi_3 D_3 \sinh(\Psi_2 D_2)) +$$
$$\Psi_2 D_2(\Psi_3 D_3 \cosh(\Psi_2 D_2) + \Psi_2 D_2 \sinh(\Psi_2 D_2))\sinh(\Psi_1(\Delta_1 - z'))], \quad (3.44)$$

$$Demo = \Psi_2 D_2 \cosh(\Psi_2\Delta_2)\left[\Psi_1(D_1 + \Psi_3 D_3 z_0)\cosh(\Psi_1\Delta_1) + (\Psi_3 D_3 + \right.$$
$$\left.\Psi_1{}^2 D_1 z_0)\sinh(\Psi_1\Delta_1)\right] + [\Psi_1(\Psi_3 D_1 D_3 + \Psi_2{}^2 D_2{}^2 z_0)\cosh(\Psi_1\Delta_1) + (\Psi_2{}^2 D_2{}^2 +$$
$$\Psi_1{}^2\Psi_3 D_1 D_3 z_0)\sinh(\Psi_1\Delta_1)]\sinh(\Psi_2\Delta_2). \quad (3.45)$$

Then $G_0(q, z = 0, t, \tau)$ measured on the top of surface (z = 0) of the slab is the inverse Fourier transform of $G_0(q, z = 0, w, \tau)$,

$$G_0(\rho,z=0,t,\tau) = \frac{1}{(2\pi)^2}\int dw \int dq \hat{G}_0(q,z=0,w,\tau) q J_0(\rho q)\exp(-iwt). \quad (3.46)$$

Figure 3.6 displays the numerical simulation g_1 for time-domain DCS from the semi-infinite, two-, and three-layer analytical models. Figure 3.6(a) is $g_1(\tau)$ for the early gate and late gate; Figure 3.6(b) is corresponding $g_2(\tau)$ for the early gate and late gate and Figure 3.6(c) is the $g_2(\tau)$ at different gate and lag time. Figure 3.6(d) is performed for $\rho = 10$ mm, two pathlengths are selected, t = 4.67×10^{-10} s and t = 9.34×10^{-10} s. Similarly, figure 3.6(e) is performed for $\rho = 10$ mm, two pathlengths are selected, t = 4.67×10^{-10} s and t = 1.40×10^{-9} s.

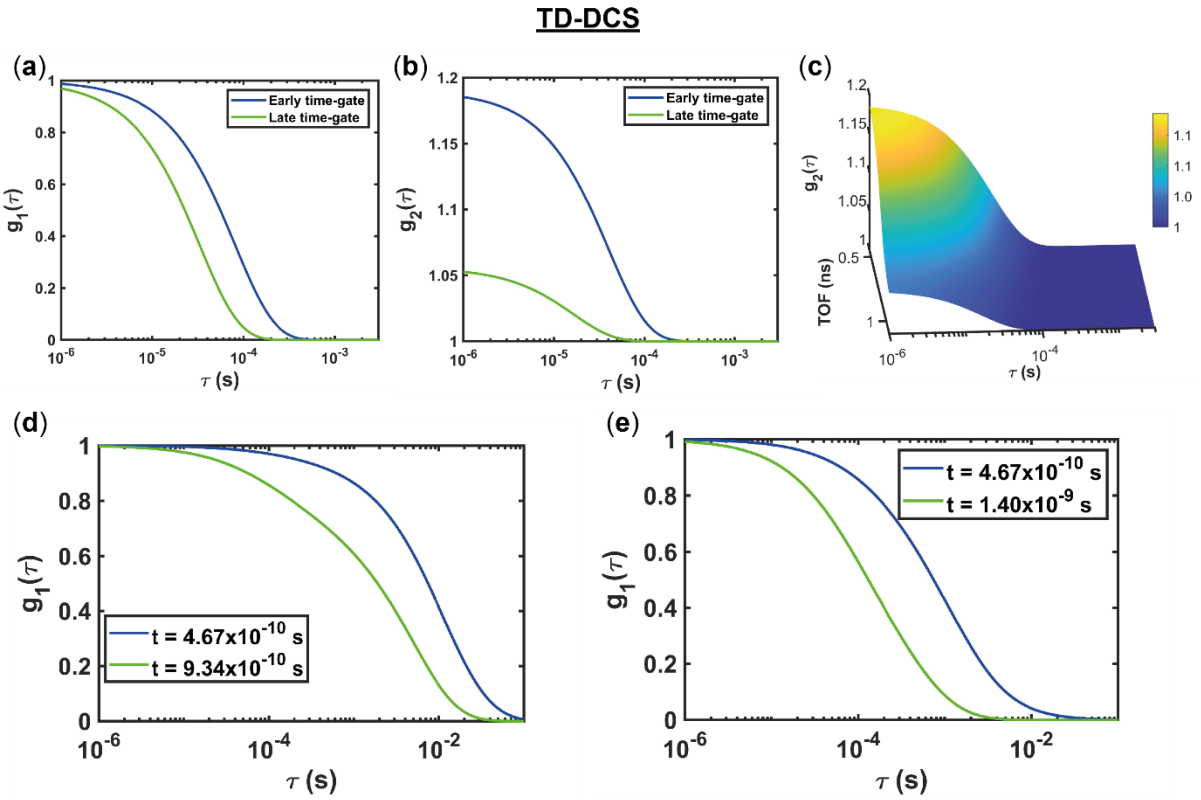

Figure 3.6 Simulated $g_1(\tau)$ with Eq. (3.34) and $g_2(\tau)$ with (3.36), with ρ = 10 mm, $D_B = 1.09 \times 10^{-8}$ mm^2/s, μ_a = 0.013 mm^{-1}, μ_s'= 0.86 mm^{-1}, λ = 785 nm, s =135 mm (ToF = 450 ps, data provided by Samaei); (b) Simulated $g_1(\tau)$ from Eqs. (3.42) and (3.43) with $\mu_a^{(1)}$ = 0.013 mm^{-1}, $\mu_s'^{(1)}$ = 0.86 mm^{-1}, Δ_1 = 10 mm, $D_B^{(1)} = 1 \times 10^{-6}$ mm^2/s; $\mu_a^{(2)}$ = 0.018 mm^{-1}, $\mu_s'^{(2)}$ = 1.11 mm^{-1}, $D_B^{(2)} = 1 \times 10^{-6}$ mm^2/s, q $\in$ (0 30), w $\in$ (0 20] Hz and $t = 4.67 \times 10^{-10}$ s and $t = 9.34 \times 10^{-10}$ s. We adopted these parameters from Ref. [254]. (c) Simulated $g_1(\tau)$ with $\mu_a^{(1)}$ = 0.013 mm^{-1}, $\mu_s'^{(1)}$ = 0.86 mm^{-1}, $D_B^{(1)} = 1 \times 10^{-6}$ mm^2/s, Δ_1 = 2 mm; $\mu_a^{(2)}$ = 0.018 mm^{-1}, $\mu_s'^{(2)}$ = 1.11 mm^{-1}, $D_B^{(2)} = 1 \times 10^{-7}$ mm^2/s, Δ_2 = 5 mm^{-1}; $\mu_a^{(3)}$ = 0.03 mm^{-1}, $\mu_s'^{(3)}$ = 1.19 mm^{-1}, $D_B^{(3)} = 1 \times 10^{-6}$ mm^2/s, q $\in$ (0 30) mm^{-1}, w $\in$ (0 20) Hz, and $t = 4.67 \times 10^{-10}$ s and $t = 1.40 \times 10^{-9}$ s. The settings are the same with Ref. [254].

3.3.7 Frequency Domain Semi-infinite Model

We also obtain $G_1(\rho, \omega, \tau)$ when modulated illumination is used, $G_1(\rho, \omega, \tau)$ follows a slightly different CDE as:

$$\left[\nabla^2 - 3\mu_s'\left(\mu_a + 2\mu_s' k_0^2 D_B \tau - \frac{i\omega}{v}\right)\right] G_1(\rho, \omega, \tau) = -3\mu_s' s_0 e^{-i\omega t}, \tag{3.47}$$

where ω is the source modulation frequency and $s_0 e^{-i\omega t}$ is the modulated source term. For a semi-infinite homogeneous tissue, the solution of Eq. (3.47) is given by:

$$G_1(\rho, \omega, \tau) = \frac{3\mu_s'}{4\pi}\left[\frac{\exp(-K_D(\omega,\tau) r_1)}{r_1} - \frac{\exp(-K_D(\omega,\tau) r_2)}{r_2}\right], \tag{3.48}$$

where $K_D(\omega,\tau) = \sqrt{3\mu_s'(\mu_a + 2\mu_s' k_0^2 D_B \tau - i\omega/v)}$ is the frequency dependent wave vector. The remaining parameters remain unchanged from the previous set. Figure 3.7 shows $g_1(\tau)$ for the FD semi-infinite model. By fitting the measurement data from TD-DCS systems to Figure 3.7, we can retrieve optical properties (μ_a and μ_s') and blood flow simultaneously. In contrast, the traditional DCS system only for blood flow measurements. Another merit is that the laser source for FD-DCS is much cheaper than CW-DCS and TD-DCS.

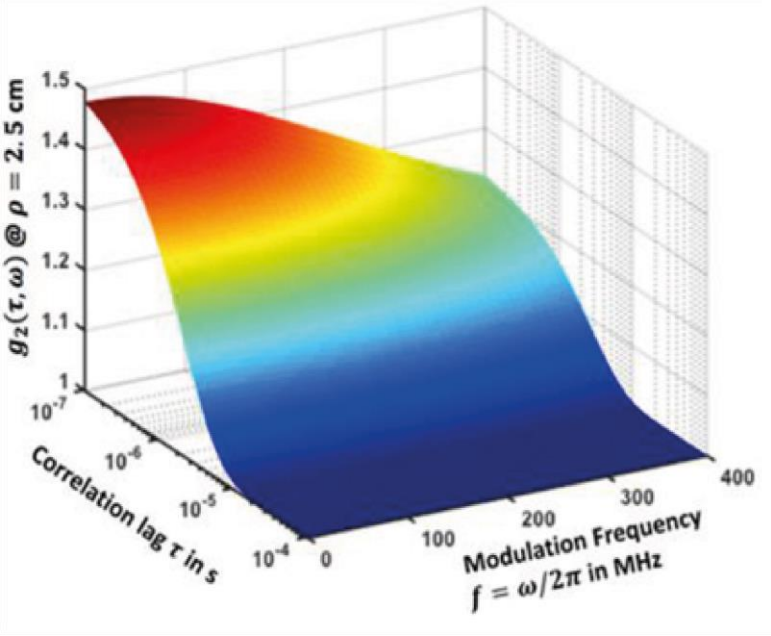

Figure 3.7 Numerical simulated FD $g_1(\rho, \omega, \tau)$ at ρ = 25 mm with various modulation frequency. Image adopted from Ref. [6].

3.3.8 Noise Model

In practical applications, we must include a proper noise model. A noise model suitable for photon correlation measurements was previously developed for a single scattering limit [255,256]. Later, the noise model developed by Koppel [256] for fluorescence correlation spectroscopy (FCS) in the single scattering limit was introduced into DCS in multiple scattering limit in 2006 [85]. In DCS, the noise comes from photon counting statistics [255], and it has been derived [85]. The standard deviation of $(g_2(\tau) - 1), \sigma(\tau)$ is estimated as:

$$\sigma(\tau) = \sqrt{\frac{T}{T_{int}}}\left[\beta^2 \frac{\left(1+e^{-T/\tau_c}\right)\left(1+e^{-\tau/\tau_c}\right)+2m(1-e^{-T/\tau_c})e^{-\tau/\tau_c}}{1-e^{-T/\tau_c}} + \langle n\rangle^{-2}\left(1+\beta e^{-\tau/2\tau_c}\right) + 2\langle n\rangle^{-1}\beta(1+e^{-\tau/\tau_c})\right]^{1/2}, \quad (3.49)$$

where T is the frame exposure time (which is equal to the correlator bin time interval). T_{int} is the integration time (measurement duration) or the measurement time window. τ_c is the speckle correlation time. ⟨n⟩ (⟨n⟩ = IT, where I is the detected photon count rate) is the average number of photons within bin time T, m is the bin index. To obtain τ_c, $g_2(\tau)$ usually approximated with a single exponential function as $g_2(\tau) \approx 1 + \beta \exp\left(-\tau/\tau_c\right)$ under the Brownian motion model [85]. Once get τ_c, we can obtain $\sigma(\tau)$. This noise model then was adopted by [12,13,155,257].

Figure 3.8 shows noise (orange line) and noiseless (blue line) $g_2(\tau)$. The noise model predicted standard deviations for $g_2(\tau)$ at each τ were applied by randomly sampling a normal distribution, where the T_{int} = 1s and the delay time $1 \times 10^{-6}\ s \leq \tau \leq 1 \times 10^{-1} s$ (128 data points) was used. Considering realistic photon budgets, the photon count rate at 785 nm was assumed to be 8.05 kcps [48]. In Fig 3.8 we can see that the DCS measurement noise decreases as τ increases.

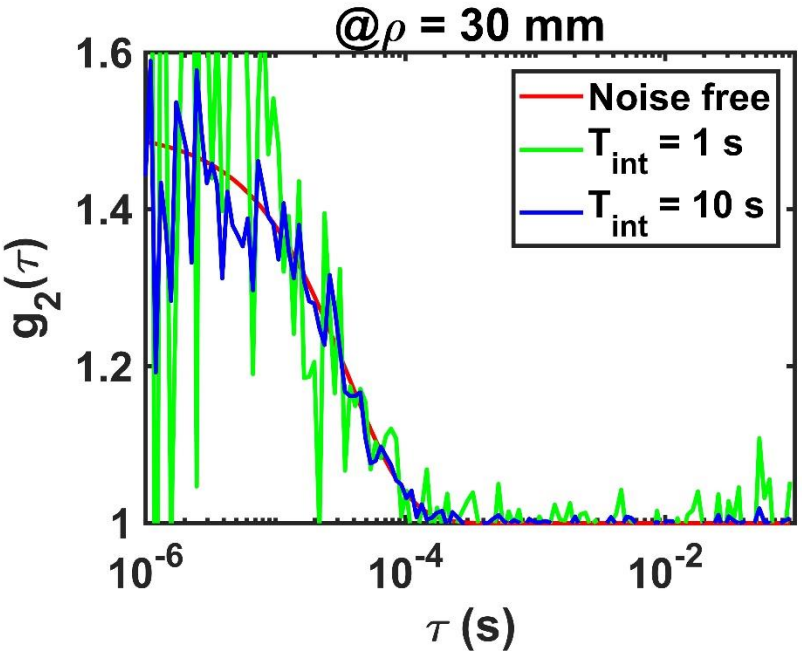

Figure 3.8 Simulated $g_2(\tau)$ curves with ρ = 30 mm on a homogeneous sample with μ_a = 0.01 mm^{-1}, μ_s' = 1.2 mm^{-1}, λ = 785 nm, β = 0.5, and T_{int} = 1 s (green line) and T_{int} = 10 s (blue line), and $D_B = 2 \times 10^{-9}$ mm^2/s, noise free (red solid line) and with Eq. (3.49) considered added assuming a 8.05 kcps at 785 nm.

3.4 Summary

In this chapter I have described the basic background of DCS, which lays foundation for the development of the proposed DCS system. I also re-derived and summarized existing analytical DCS models, including semi-infinite, two-, and three-layer models for CW, TD, and FD domains. This is an essential step to allow fast catching up and surpassing the most advanced DCS method. Meanwhile, I have performed analytical simulations based on these models, see Figs. 3.5, 3.6, 3.7. In the next chapter, I will design a deep learning architecture to estimate BFi, contrasting it with conventional fitting methods based on the analytical model.

Chapter 4 Deep Learning (DL) in DCS

4.1 Introduction

In the previous **three chapters** I discussed the history of DCS development, and the theoretical background for DCS and relevant knowledge of DCS instrumentation. As we all known, non-linear least-square fitting method is a well-established approach to extract blood flow index in DCS data analysis. And the fitting procedural commonly based on Levenberg-Marquardt optimization or trust-region-reflective methods [84,117,258]. In this chapter I have shown that a deep learning approach can also be used to extract the relevant parameters we are interested in. This technique is called "feature extraction" method, which involves reducing the dimensionality of data, transforming it from a high-dimensional to a low-dimensional representation. Afterward, the reduced-dimensional data, often referred to as "features," can be employed in the development of learning algorithms. This procedure is shared by most of the machine learning algorithms, wherein feature extraction precedes the prediction of outcomes or probabilities [259]. Typically, classification and regression models are used where features from images (e.g., shape, texture, color features), features of spectra (e.g., intensity values at specific wavenumbers in Raman spectroscopy), or features of time sequences data (e.g., FLIM, DCS data) are extracted to construct a predictive model.

The introduction of deep learning into DCS field was first proposed can dates back to 2019, Zhang *et al.* [163] proposed the first recurrent neural network (RNN) regression model to DCS, followed by 2D convolution neural networks (2DNN) [38], long short-term memory (LSTM) [164] and ConvGRU [165]. These methods are proved stable and robust for quantification blood flow or relative blood flow in phantom and in vivo experiments.

In section 4.2 I give an overview of deep learning techniques for time sequence data in the biomedical field. The advantage of the deep learning methods over traditional fitting methods is the ease with which predictions can be more accurate under noise consideration and faster in inference process. In the final section of this chapter, I present Monte Carl results which demonstrate the accuracy and fast of BFi extraction. The primary objective of this chapter is to present an AI framework for evaluating AI model's performance we proposed for DCS. Figure 4.1 summarizes the main concept of our work in this chapter.

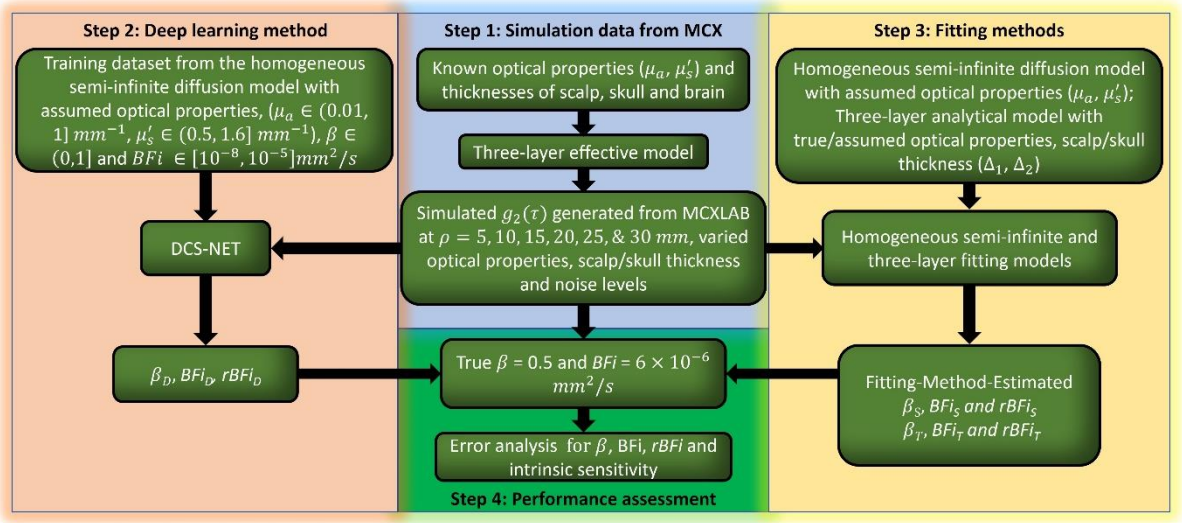

Figure 4.1 Flow chart of the proposed analysis. Step 1 generates the autocorrelation function $g_2(\tau)$ from MCX at different source-detection distances (5mm, 10mm, 15mm, 20mm, 25mm and 30mm), optical properties ($\mu_{a1,2,3}$, $\mu'_{s1,2,3}$), scalp/skull thicknesses (Δ_1, Δ_2), and different noise levels using the three-layer brain effective model. Step 2 obtains training datasets containing noise. The datasets are generated using a semi-infinite diffusion model with $\mu_a \in (0.01, 1)\ mm^{-1}$, $\mu_s' \in (0.5, 1.6)\ mm^{-1}$, $\beta \in (0, 1]$, and $BFi \in [10^{-8}, 10^{-5}]\ mm^2/s$. Then, the simulated data from Step 1 is analyzed by the pre-trained model to predict β and BFi. Step 3 fits the simulated data from Step 1 with semi-infinite and three-layer models with known/assumed optical properties/thicknesses to extract β and BFi. Step 4 assesses BFi and β estimations and concludes the intrinsic sensitivity and errors in terms of the variations in μ_a, μ_s', Δ_1, and Δ_2.

4.2 Deep Learning Overview

4.2.1 What is Deep Learning

Deep learning (DL) can be considered a subset of machine learning (ML), with which is the study of algorithms and statistical models that computer systems use to progressively improve their performance on a specified task [260]. The term "deep learning" was first introduced into the machine learning community by Rina Dechter in 1986 [157]. Due to the surge in big data, it has effectively permeated almost every significant domain of scientific research and it falls within the representation learning category of artificial intelligence (AI). DL leverages deep neural networks, which are composed of multiple layers of interconnected nodes or artificial neurons. These networks can automatically learn to represent data through the hierarchical abstraction of features. Typically, a DL algorithm relies on four primary components: an optimization algorithm, a cost function, a dataset, and a deep learning model. In brief, an optimization algorithm is an iterative approach used to evaluate different solutions to a problem

until an optimal solution is achieved. A cost function is a mathematical expression employed to assess the performance of a deep learning model. A dataset is a crucial element for training deep learning models and can be divided into three segments: training, validation, and testing datasets. The training dataset is employed to train the deep learning model, the validation datasets is utilized to fine-tune the hyperparameters of the deep learning model, and the independent test dataset or holdout set is utilized to assess the model's performance in an unbiased manner [259,261]. The final essential element is a deep learning model composed of layers and hyperparameters, which vary depending on different architectures. DL applies an "end-to-end" data driven optimization (or "learning") of both feature representations and model predictions, as shown in Figure 4.2. This is accomplished by training a versatile and general computational model known as a deep neural network (DNN).

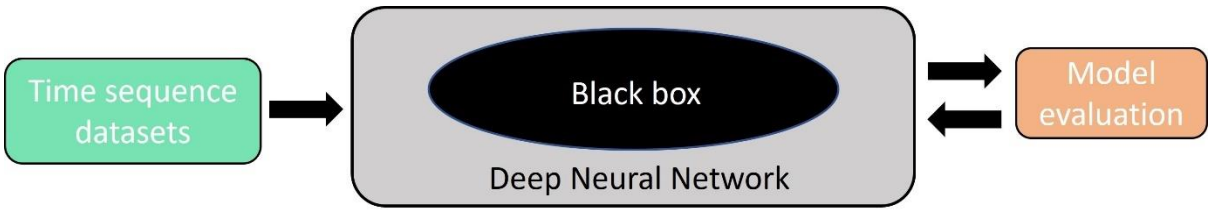

Figure 4.2 Deep learning uses learned features and predictors in an "end-to-end" deep neural network.

4.2.2 How is DL Implemented?

DNNs consist of multiple layers interconnected through computational operations, involving linear weights and nonlinear activation functions. Each layer encapsulates a distinctive feature representation of the input data. The incorporation of multiple layers enables the models to capture both low-level and high-level representations. Let me take an example, for images, low-level representations might include textures and object edges, while higher-level representations would consist of object-like compositions formed from those features. The simultaneous optimization of feature representations at various levels of abstraction and the parameters of the predictive model is what imparts significant power to DNNs.

There are three strategies for deep learning, including unsupervised [262], self-supervised [263], and semi-supervised [264]. Most currently available deep learning models in biomedical optics are developed using the supervised learning approach. In a standard end-to-end deep learning model, the model architecture established the hypothesis class and dictates how hierarchical information is transmitted between each layer of the DNN. Choosing a DNN

architecture is task-dependent and is typically determined empirically by comparing various state-of-the-art architectures.

With recent achievements of deep learning, numerous software frameworks have emerged to facilitate the simplified creation and optimization of DNNs. Many prominent technology companies have actively contributed to this field. Notably, TensorFlow and PyTorch stand out as leaning open-source frameworks, maintained by Google and Facebook, respectively [265,266]. Both frameworks facilitate the straightforward development of customized DNN models, with efficient parallelization of DNN optimization across high-performance graphics computing units (GPUs). These tools have empowered individuals without extensive expertise to train and deploy DNNs, significantly contributing to the expansion of deep learning research into diverse applications, including the domain of biomedical optics.

4.3 Existing DL Methods Used in DCS

4.3.1 Recurrent Neural Network (RNN) and LSTM

In 1997, Hochreiter and Schmidhuber invented the long short-term memory (LSTM) network, a variant of a recurrent neural network (RNN) [267]. LSTM networks incorporate feedback connections, allowing handling complete sequence of data and overcome the vanishing gradient problem. RNNs can accumulate memory in the network over time, contributing to their widespread success in tasks like time-series processing, such as recognizing speech signals. More specifically, in accordance with Pradhan *et al.*, RNN architectures can be categorized into three types: many-to-one architecture, one-to-many architecture, and many-to-many architecture [268]. RNNs have the potential to construct intelligent systems, and future exploration may include their applications in spectrum preprocessing, wavenumber calibration, intensity calibration, spectrum classification, decoding biomolecular markers from bio-spectroscopic data, learning spatial-spectral-temporal features for spectral data, and phase retrieval of nonlinear optical spectroscopic data. However, traditional RNNs exhibits certain limitations. Firstly, they demand increased computational resources and larger training datasets compared to typical convolutional neural network (CNN). A standard RNN computes an output at each time step, relying solely on the past and present elements of the input vector. In the case of spectroscopic data, the past, present, and future states (or wavenumbers) of the spectra influence the output at a given time step, prompting exploration into bidirectional RNNs.

Bidirectional RNNs utilize hidden states from opposite directions to update the output sequence at a specific time step. Another drawback of RNNs is the issue of vanishing gradients, a consequence of the deep structure of RNNs. To address this challenge, alternative RNN variations such as long short-term memory (LSTM) and gated recurrent unit (GRU) networks are employed, demonstrating improved performances [269]. Figure 4.3(a) shows the architecture of RNN used in DCS, in which the data points on autocorrelation curves without noise as labels and use the Tensorflow framework of deep learning to train the RNN model. Figure 4.3(b) shows the LSTM architecture from Li *et al.*, in which the measured $g_2(\tau)$ data with the size of 1 × 64 as the input. The model output is the predicted blood flow index (BFi) of the size is 1 × 1. More parameters for the architecture can be seen in Ref. [164].

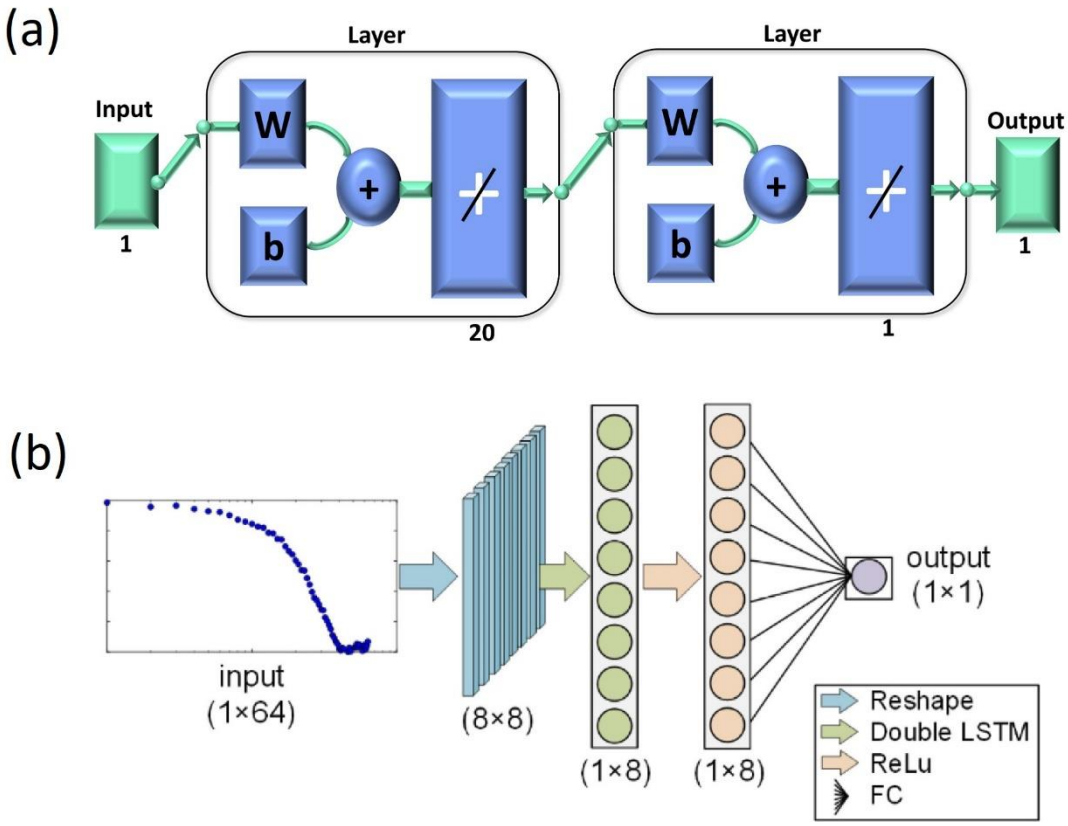

Figure 4.3 (a) RNN training regression model [163]. The network model is a linear model with input dimension of 1, output dimension of 1, minimum mean square error of 1.0×10^{-8} and minimum gradient of 1.0×10^{-20}, and the training epochs are 5000. (b) The structure of proposed LSTM architecture by Li *et al.* [164] The images of models are reused permission are taken from the authors [163,164].

4.3.2 Convolutional Neural Network (CNN)

A convolutional neural network (CNN) [270] is a modified form of a multilayer perceptron (MLP) designed to process grid data, such as spectra or images. It was first introduced by

LeCun *et al.* in 1989 for handwritten zip code recognition. The core component of a CNN is its convolutional layer, complemented by batch normalization layers, pooling layers, and fully connected layers. The input undergoes convolution with the kernels of the convolutional layer, generating input for the subsequent layer. While updating weights, the convolutional kernels in each layer are learned, leading to the updating of the feature maps generated by these kernels. Moreover, pooling layers are employed to decrease data dimensions and computational complexity through subsampling. The two most prevalent types of pooling methods are max pooling and average pooling. Typically, a fully connected layer is positioned at the conclusion of a CNN, linking each neuron from its preceding layer to the output. It is important to highlight that CNNs incorporate two distinctive concepts: parameter sharing and local connectivity. These principles decrease the parameter count and enhance computational efficiency. Commonly, the activation function, including rectified linear unit (ReLU) [271], tanh [272] and sigmoid functions [160] are used to introduce nonlinearity to the model. In contrast to MLPs, CNNs directly incorporate the spatial information of an image or the temporal/spectral information of a signal. Figure 4.4 displays the 2D CNN applied to DCS.

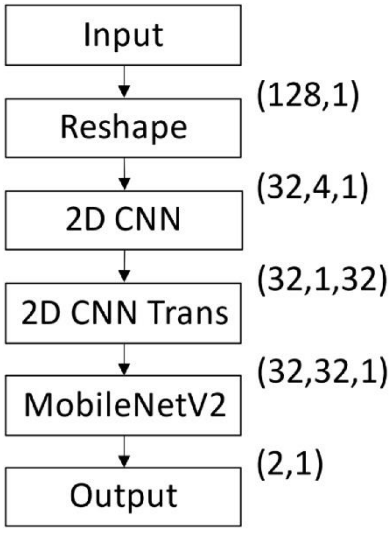

Figure 4.4 The structure of the deep learning 2D convolution neural network (2D CNN). The measured $g_2(\tau)$ data with the size of 1 × 128 as the input, then reshape into a 32 × 4 matrix. Convolutional Neural network (CNN) is used to map the matrix into a 32 × 32 image before passed into MobileNetV2. The output is β and BFi with size of 2 × 1 as output. The structure of the model reprinted from Ref. [38].

4.3.3 Gated Recurrent Unit ConvGRU

One-dimensional convolutional Neural networks (1D-CNN) are highly suitable for time series analysis [273,274], proving to be particularly effective in capturing meaningful features within a fixed-length dataset. In one-dimensional convolution, the kernel window slides along the

sequence length, facilitating convolution operations. In the realm of recurrent neural networks (RNN), the gated recurrent unit (RGU) stands out as a stable and potent structure for modelling time series, as demonstrated in numerous prior studies. The ConvRGU model proposed by Feng *et al.* [165] for DCS as shown in Figure 4.5, in which CNN and RNN were combined. The combination of CNN and RNN can better extract sequence features. Similarly, in this model, the measured $g_2(\tau)$ with the size of 1 × 64 is the input and output are relative cerebral blood flow (rCBF) with size of 1 × 1.

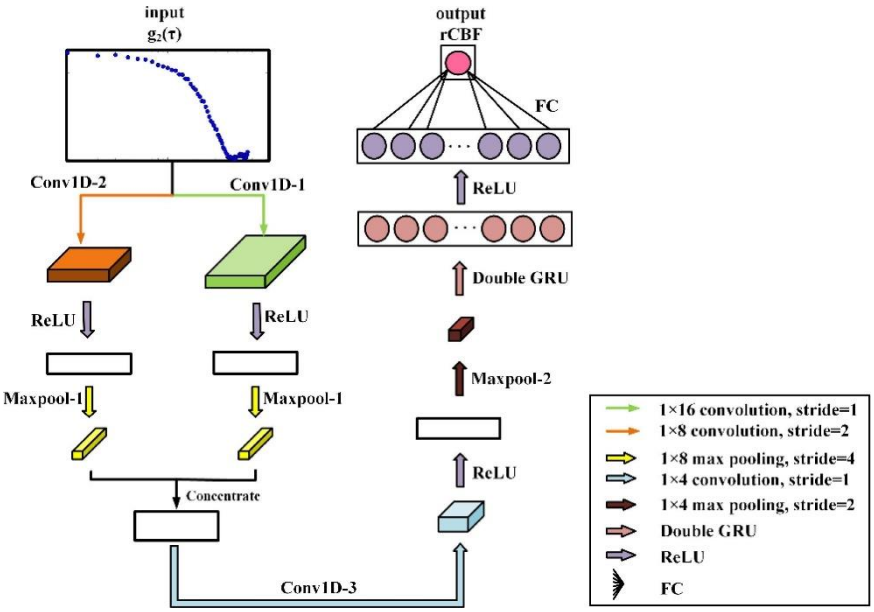

Figure 4.5 The structure of the ConvGRU model. Reprinted from Ref. *[165]*.

4.4 1DCNN Design

Inspired by a recently published one-dimensional convolutional neural network (1D CNN) for fluorescence lifetime imaging (FLIM), we proposed the DCS neural network (DCS-NET) based on 1D CNN for quantifying the coherent fact β and BFi. The structure of DCS-NET is shown in Figure 4.6. DCS-NET takes $g_2(\tau)$ to estimate β and BFi independently. DCS-NET consists of 1) a shared branch for temporal feature extraction and 2) two subsequent independent branches for estimating β and BFi, with a similar structure to the shared branch. The two CNN layers in the shared branch have a wider sliding window with a larger kernel size of 13 and a giant stride of 5. They are expected to capture more general features of the auto-correlation decay curves. The batch normalization (BN) layer [275] is employed after each convolutional layer. It reduces the shift of internal covariance and accelerates network training when processing normalized data. To implement feature pooling and effectively reconstruct β and BFi, we use a pointwise convolution layer with a kernel size of 1 after the convolutional

neural network, followed by the activation function, the Sigmoid function. The model input is the measured (here, we used data from MCX) $g_2(\tau)$, of which the size is 1×127. Both the estimated β and BFi have a size of 1×1.

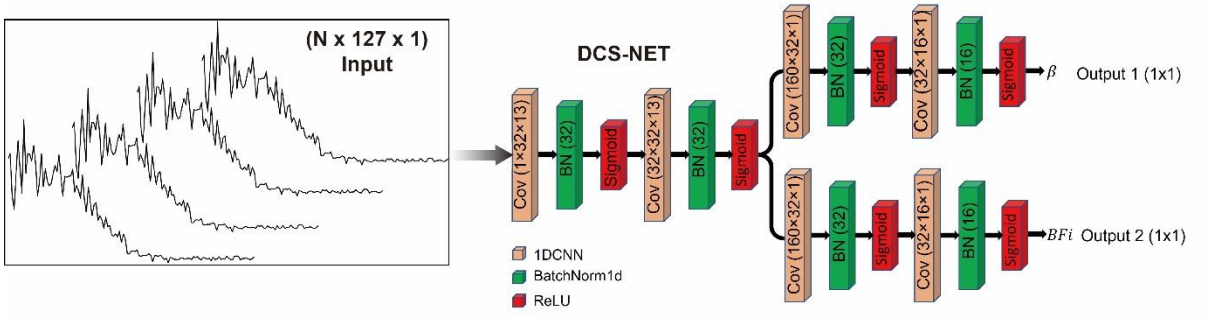

Figure 4.6 The proposed DCS-NET includes a convolution neural network (CNN), batch normalization and sigmoid activation layers. The convolution layer parameters are the filter number × the kernel size × the stride.

4.5 Training Dataset Preparation

The training datasets can be easily obtained using synthetic data based on the homogenous semi-infinite analytical model, as shown in Fig. 3.2(a). Thus, according to Eq. 3.16, 200,000 training datasets (200,000 × 127) were generated and split into the training (80%) and the validation (20%) groups. The training batch size is 128, with 800 training epochs. We used an early stopping callback with 20 patient epochs to prevent overfitting. To match the realistic experiments, in the dataset, we set $\mu_a \in (0.01, 1]\ mm^{-1}$, $\mu_s' \in (0.5, 1.6]\ mm^{-1}$, $\beta \in U(0,1]$, BFi $\in U[10^{-8},10^{-5}]$ mm^2/s and $\rho \in U[5,30]$ mm, where U stands for a uniform distribution. $g_2(\tau)$ training datasets contain noisy and noiseless (the noise model has been described in Ref. 55) autocorrelation functions, as shown in Fig. 4.7(b). The green, yellow, and red lines represent noisy $g_2(\tau)$, and the blue line represents noiseless $g_2(\tau)$. We used the optimizer Adam [348] for the training process, with the learning rate fixed at 1×10^{-5} in the standard back-propagation. We used the mean square error (MSE) loss function for updating the network by controlling the following problem:

$$\mathcal{L}(\wp) = \frac{1}{M}\sum_i^M \left\| \mathcal{F}(X^i, \wp) - Y^i \right\|_2^2, \tag{4.1}$$

where X is the network output (estimated BFi or β), and Y is the corresponding label (true BFi or β) in the i-th training pairs. F is the mapping function, and M is the number of training pairs. Fig. 4.7(a) shows that the training and validation losses decrease rapidly and reach the plateau after 85 epochs. The training process's best score reaches a small value of 0.000725, indicating

that the network is well trained as the estimated β and BFi are close to the ground truth. The model was conducted in Python using Pytorch with Intel (R) Core (TM) i9-10900KF CPU @3.70GHz.

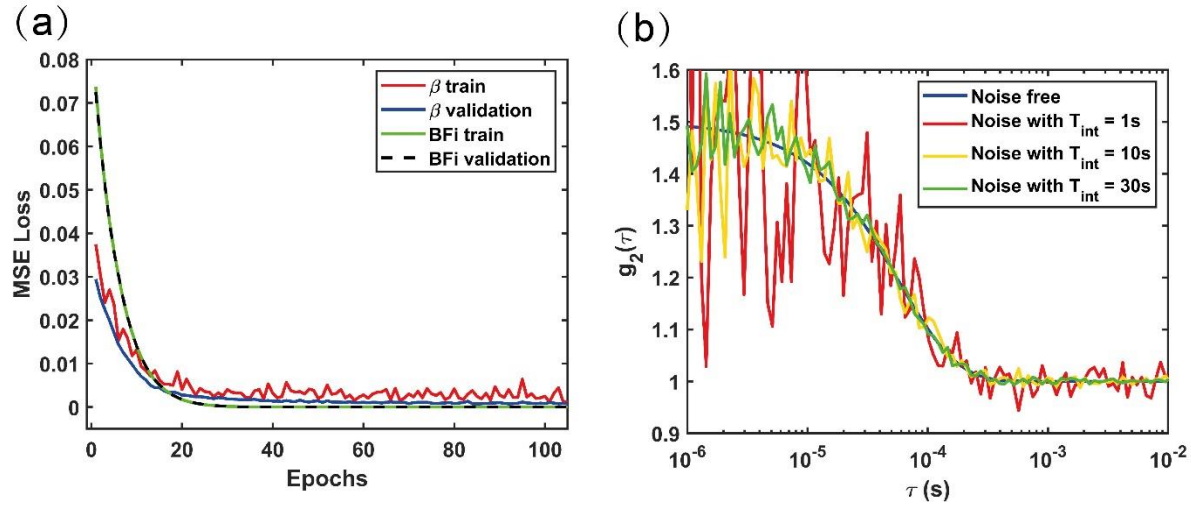

Figure 4.7 Evaluation of the convolution neural network. (a) Training and validation losses of DCS-NET. (b) g_2 (τ) with noise-free (blue), and with realistic noise added, assuming an 8.05 kcps at 785 nm at different noise levels with T_{int} = 1, 10, and 30 s.

4.6 Monte Carlo Simulations

We utilized a simplified model comprising three layers to emulate the scalp (5 mm), skull (7 mm), and brain (50 mm, large enough so that we can treat the medium as semi-infinite), respectively [276]. All layers were assumed homogeneous, as demonstrated in Fig. 4.8, and their corresponding optical properties are summarized in Table 4.1.

Table 4.1 Physiological and optical parameters [277] at 785 nm in the human head model

Layer	Thickness (mm)	μ_a (mm^{-1})	μ_s' (mm^{-1})	Blood flow index (mm^2/s)
Scalp (Δ_1)	5	0.019	0.660	1×10^{-6}
Skull (Δ_2)	7	0.014	0.860	0
Brain	50	0.019	1.110	6×10^{-6}

MCX utilized an anisotropic factor (g) of 0.89 and a refractive index (n) of 1.37 [278] for all layers. We launched 2×10^9 photons from a source with a diameter of 1 mm and set the detector radii to 0.13, 0.28, 0.45, 0.7, 1, and 1.5 mm for ρ = 5, 10, 15, 20, 25, and 30 mm, respectively, recording data from multiple distances simultaneously. An example of the source and the detector was arranged as shown in Fig. 4.8. MCX records the path lengths and momentum

transfer from the detected photons for obtaining the electric field autocorrelation function $G_1(\tau)$ [68]:

$$G_1(\tau) = \frac{1}{N_p}\sum_{s=1}^{N_p} \exp\left(-\frac{1}{3}k_0^2 \sum_{i=1}^{N_t} Y_{s,i}\langle \Delta r^2(\tau)\rangle_i\right) \exp\left(-\sum_{i=1}^{N_t} \mu_{a,i} L_{s,i}\right), \quad (4.2)$$

where N_p is the number of detected photons, N_t is the number of tissue types (3 for our simulations), and $Y_{s,i}$ and $L_{s,i}$ stand for the total momentum transfer and the total path length of Photon s in Layer i, respectively. $\mu_{a,i}$ is the absorption coefficient, and $\langle \Delta r^2(\tau)\rangle_i$ is the mean square displacement of the scattered particles in Layer i. Here, $\langle \Delta r^2(\tau)\rangle_i = 6D_i\tau$, where D_i is the effective diffusion coefficient of Layer i. The simulated $G_1(\tau)$ is normalized to $G_1(0)$, and then we can obtain $g_2(\tau)$ using the Siegert relationship with $\beta = 0.5$. In this simulation, the delay time 1 μs ⩽ τ < 10,000 μs (127 data points) was used for $g_2(\tau)$.

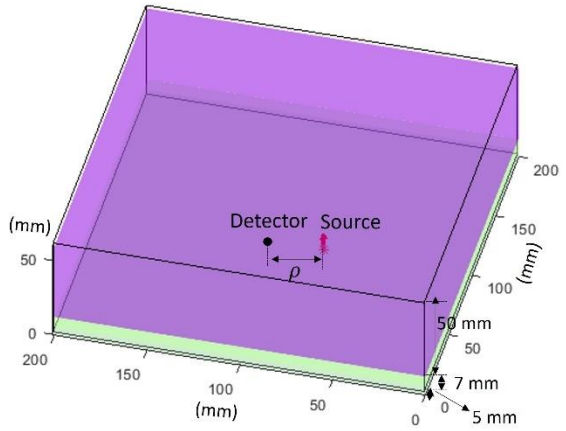

Figure 4.8 A large slab from MCX representing a human brain consisting of three layers of the scalp (5 mm), skull (7 mm), and brain (50 mm).

4.7 Intrinsic Sensitivity Estimation

To evaluate the sensitivity to changes in blood flow in the deeper layer, we fixed the effective diffusion coefficient $D_b = 1 \times 10^{-6}\ mm^2/s$ in Layer 1 and increased D_b in Layer 3 as αDb = [1 + 0.1 × (*w*-1)] × 6 × 10^{-6} mm^2/s, *w* is an integer and *w* = 1, 2…11. The physiological and optical parameters listed in Table 1 are taken as baseline conditions. Similar to Ref. [152], the intrinsic sensitivity (η_H) is defined as:

$$\eta_H = \frac{(BFi_H - BFi_0)/BFi_0}{(CBF_p - CBF_0)/CBF_0} \times 100\%, \quad (4.3)$$

where BFi_H and BFi_0 represent the estimated BFi (H = D, S, or T, meaning DCS-NET, the semi-infinite, and three-layer fitting methods) for the perturbed and baseline conditions, respectively, and CBF_p and CBF_0 are D_b in Layer 3 for the perturbed and baseline conditions, respectively.

4.8 Results

4.8.1 Absolute BFi Recovery vs. Detection Depths

To investigate how the absolute BFi and β behave in terms of ρ among DCS-NET, semi-infinite, and three-layer fitting approaches, we generated $g_2(\tau)$ via MCX Monte Carlo simulations for ρ = 5, 10, 15, 20, 25, and 30 mm, as described in Section 4.6. Table 4.1 shows all the relevant parameters used in MCX simulations. The absolute BFi in this study corresponds to the Brownian diffusion coefficient D_b (assumed α = 1). When using DCS-NET, $g_2(\tau)$ was fed into the pre-trained model. For the semi-infinite fitting procedure, $g_2(\tau)$ was fitted to Eq. 3.16, and we assumed $\mu_a = 0.019\ mm^{-1}$, $\mu_s' = 1.099\ mm^{-1}$, for the brain layer (Layer 3), as provided in Table 4.1.

We also fitted the simulated $g_2(\tau)$ with the three-layer model, Eq. 3.30, and $D_{b1} = 1 \times 10^{-6}\ mm^2/s$, $D_{b2} = 0\ mm^2/s$, $D_{b3} = 6 \times 10^{-6}\ mm^2/s$, $\mu_{a1} = 0.019\ mm^{-1}$, $\mu_{s1}' = 0.635\ mm^{-1}$, $\mu_{a2} = 0.014\ mm^{-1}$, $\mu_{s2}' = 0.851\ mm/s$, $\mu_{a3} = 0.019\ mm^{-1}$, $\mu_{s3}' = 1.099\ mm^{-1}$, Δ_1 = 5mm, and Δ_2 = 7 mm. Meanwhile, we set β = 0.3 and $D_{b3} = 2 \times 10^{-7}\ mm^2/s$ as the initial guesses. For the fitting, we used nonlinear least-square method (NLSM, lsqcurvefit (·) in MATLAB with the Levenberg-Marquardt optimization) to minimize the unweighted least squares objective function,

$$\arg\min \sum_{j=1}^{j=N_\tau} [g_2(\tau)_{MCX} - g_2(\tau)_H]^2,\ \ H = (S,\ T), \tag{4.4}$$

where N_τ is the number of sampled $g_2(\tau)$, and $g_2(\tau)_H$ is from Eq. (3.16) or Eq. (3.30).

Table 4.2 presents the true β and BFi and estimated β and BFi using DCS-NET, semi-infinite, and three-layer fitting methods. All input parameters for fitting are assumed as described above, and $\beta_{GT} = 0.5$. We define BFi_D, BFi_S and BFi_T (also β_D, β_S and β_T) for DCS-NET, the semi-infinite and three-layer fitting methods, respectively. We define $\varepsilon_{BFi,D}$ (%) = |BFiD -

$BFi_{GT}|/BFi_{GT} \times 100\%$, where $\varepsilon_{BFi,D}$ is the BFi error with DCS-NET. Similarly, $\varepsilon_{BFi,S}$ and $\varepsilon_{BFi,S}$ are the BFi estimated errors with the semi-infinite and three-layer fitting methods.

Table 4.2 BFi in the brain estimated using DCS-NET, homogeneous semi-infinite and three-layer fitting models.

$\boldsymbol{\rho}$ (mm)	Layer	$\boldsymbol{BFi_{GT}}$ (mm²/s)	$\boldsymbol{BFi_D}$ (mm²/s)	BFi estimated by fitting methods (mm²/s)	
				$\boldsymbol{BFi_S}$	$\boldsymbol{BFi_T}$
5	1	1×10^{-6}	$\beta_D = 0.521$	$\beta_S = 0.501$	$\beta_T = 0.493$
	2	0	$BFi_D = 8.45 \times 10^{-7}$	$BFi_S = 7.15 \times 10^{-7}$	$BFi_T = 7.15 \times 10^{-7}$
	3	$\mathbf{6 \times 10^{-6}}$			
10	1	1×10^{-6}	$\beta_D = 0.509$	$\beta_S = 0.499$	$\beta_T = 0.493$
	2	0	$BFi_D = 7.36 \times 10^{-7}$	$BFi_S = 5.47 \times 10^{-7}$	$BFi_T = 2.17 \times 10^{-5}$
	3	$\mathbf{6 \times 10^{-6}}$			
15	1	1×10^{-6}	$\beta_D = 0.501$	$\beta_S = 0.498$	$\beta_T = 0.504$
	2	0	$BFi_D = 1.03 \times 10^{-6}$	$BFi_S = 4.79 \times 10^{-7}$	$BFi_T = 1.43 \times 10^{-5}$
	3	$\mathbf{6 \times 10^{-6}}$			
20	1	1×10^{-6}	$\beta_D = 0.499$	$\beta_S = 0.495$	$\beta_T = 0.506$
	2	0	$BFi_D = 2.07 \times 10^{-6}$	$BFi_S = 4.57 \times 10^{-7}$	$BFi_T = 8.17 \times 10^{-6}$
	3	$\mathbf{6 \times 10^{-6}}$			
25	1	1×10^{-6}	$\beta_D = 0.499$	$\beta_S = 0.493$	$\beta_T = 0.505$
	2	0	$BFi_D = 4.82 \times 10^{-6}$	$BFi_S = 4.63 \times 10^{-7}$	$BFi_T = 5.63 \times 10^{-6}$
	3	$\mathbf{6 \times 10^{-6}}$			
30	1	1×10^{-6}	$\beta_D = 0.499$	$\beta_S = 0.491$	$\beta_T = 0.505$
	2	0	$BFi_D = 5.71 \times 10^{-6}$	$BFi_S = 4.88 \times 10^{-7}$	$BFi_T = 4.97 \times 10^{-6}$
	3	$\mathbf{6 \times 10^{-6}}$			

Table 4.2 shows when the semi-infinite model is used, the estimated BFi is closer to Layer 1 ($\alpha D_b = 1 \times 10^{-6}$ mm²/s), even for $\rho = 30$ mm, suggesting that a homogenous fitting procedure is more sensitive to the superficial layers' dynamic properties. This finding is consistent with the results reported by Gagnon *et al.* [147]. Using the three-layer fitting model, we obtained $BFi_T = 7.15 \times 10^{-7}$ mm²/s, close to 1×10^{-6} mm²/s when $\rho = 5$ mm. This is because the mean light penetration depth is approximately $\rho/3 \sim \rho/2$ [57]. When ρ is small, most detected photons predominantly travel through Layer 1. As ρ increases ($\rho \geqslant 10$ mm), the estimated BFi decreases, reaching 5.63×10^{-6} mm²/s at $\rho = 25$ mm, with $\varepsilon_{BFi,T}$ of 6.17%. This is because as ρ increases, the detected photons penetrate inside the skull layer ($\alpha Db = 0$ mm²/s), resulting in an increased contribution of Layer 2. This phenomenon is expected, because the three-layer modelling can

remove the contribution from superficial layers [46] to obtain accurate BFi. Interestingly, when using DCS-NET, the estimated BFi increases as ρ increases, reaching 5.71 $\times 10^{-6}$ mm^2/s with $\varepsilon_{BFi,D}$ of 4.83% at ρ = 30 mm. These results suggest that the AI model can recognize the depth. Regarding β estimation, there is no significant difference among the three methods.

4.8.2 Absolute BFi Recovery with Noise

Figure 4.7(b) displays the semi-infinite analytical example $g_2(\tau)$ curves with noise using the model proposed by Zhou *et al.* [85]. The curves were obtained with ρ = 30 mm at different noise levels (T_{int} = 1, 10, 30 s), $\mu_a = 0.019$ mm^{-1}, and μ_s' = 1.099 mm^{-1} with an assumed BFi = 2 × 10^{-7} mm^2/s. To assess DCS-NET's performance in practical scenarios, we modified the Monte Carlo code to generate g_2 curves including noise according to Zhou *et al.*'s noise model [85]. We generated 100 g_2 sets for each noise level (including noiseless). Still, we minimized Eq. (4.4) using the Levenberg-Marquardt optimization routine. We performed the residual analysis to assess the efficiency of the semi-infinite and three-layer models. We define the residual δ and Resnorm (the squared 2-norm of the residual) ϵ as:

$$\delta = f(\beta, BFi, \tau_q) - g_2(\tau_q),$$

$$\epsilon = \sum_{q=1}^{q=Q} \delta^2, \tag{4.5}$$

where q is the lag time index, and Q is the length of the time trace. $f(\beta, BFi, \tau_q)$ is the fitted value at the lag time τ_q, and the corresponding true value is $g_2(\tau_q)$ from MCX. The fitting results using the semi-infinite and three-layer analytical models are presented in Figure 4.9, in which noisy $g_2(\tau)$ curves from MCX (blue star-shaped) and fitted $g_2(\tau)$ curves (red lines) at different noise levels are shown. Figure 4.9(a-i) – (a-iv) show the MCX-generated and fitted g_2 using the semi-infinite model, and they exhibit an increasing trend in δ, ranging from (-0.0025, 0.0025) to (-0.5, 0.5), indicating that the semi-infinite method becomes inaccurate when the noise level increases. Additionally, ϵ reaches 3.02 when T_{int} = 1 s. Similar behaviors are observed in the three-layer fitting, as shown in Figure 4.9 (b-i) - (b-iv).

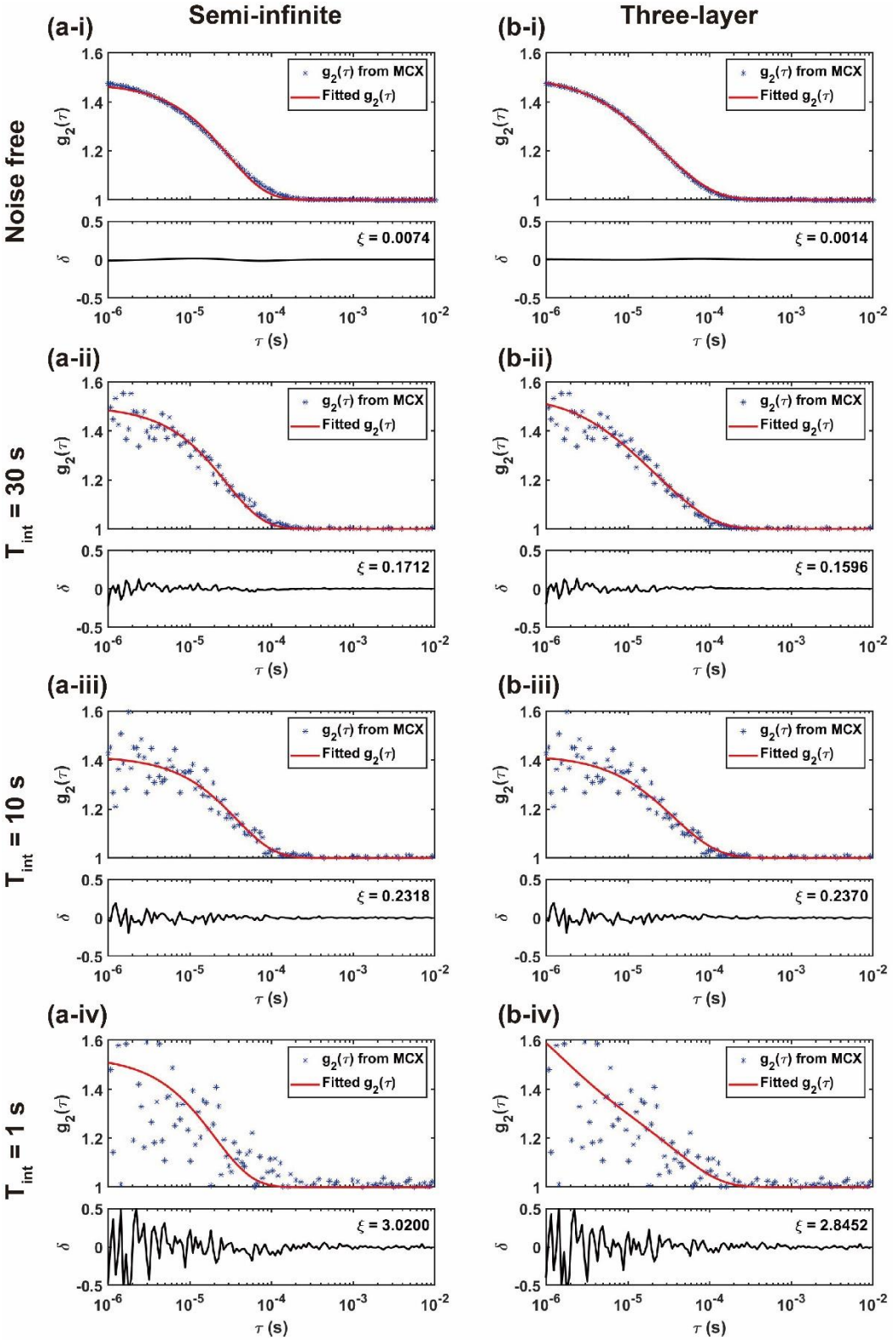

Figure 4.9 MCX-generated (scattered stars) and fitted (red solid lines) g_2 curves using semi-infinite and three-layer fitting methods. (a-i - a-iv, respectively) noisy MCX simulated data (scattered star-shaped) at different noise levels fitted with the semi-infinite homogeneous model; (b-i - b-iv) noisy MCX-generated data fitted with the for the three-layer fitting procedure. The corresponding Residual δ and Resnorm ϵ curves are also included.

We also calculated the mean BFi and β over 100 trials. As for β, we arrive at the same conclusion as Section 4.8.1 that all three methods exhibit similar behaviors at the same noise level. A high noise level (T_{int} = 1 s) leads to a significant standard deviation, as shown in Figure 4.10(a). Figure 4.10(b) shows the estimated BFi. The estimated BFi for the semi-infinite model deviates significantly from the ground truth. When using the three-layer fitting method, $\varepsilon_{BFi,T}$ is 82.30% at the lower noise level (T_{int} = 30 s). As the noise level increases, $\varepsilon_{BFi,T}$ also increases, with $\varepsilon_{BFi,T}$ reaching 390.10% at the high noise level (T_{int} = 1 s). Furthermore, a high noise level leads to a more significant standard deviation, indicating that BFi estimation is highly sensitive to noise when the three-layer fitting method is applied, in accordance with previous findings [46]. In contrast, $\varepsilon_{BFi,D}$ (using DCS-NET) at a high noise level (T_{int} = 1 s) is 12.87%, whereas at a low noise level (T_{int} = 30 s), it is only 1.93%, indicating that DCS-NET is not susceptible to noise. Figure 4.10(b) also shows that when the three-layer fitting method is used, the BFi precision can be enhanced through increasing T_{int}.

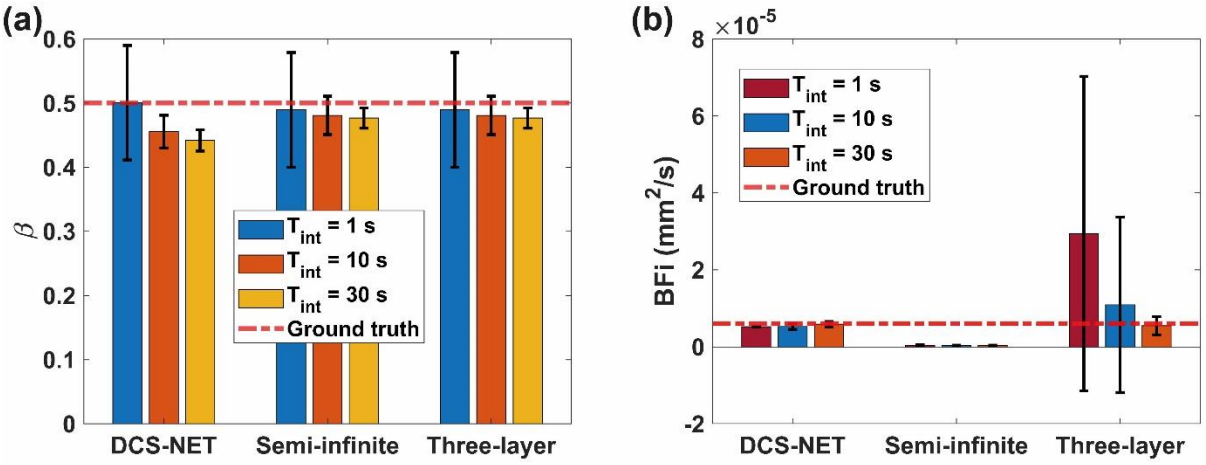

Figure 4.10 (a) The estimated β by DCS-NET, semi-infinite, and three-layer fitting methods at different noise levels (T_{int}=1, 10, 30 s). The bar height means the average value for estimated BFi or β, the error bar means the standard deviations σ; (b) The estimated BFi by the three methods at different noise levels. The red dot line stands for the ground truth. (All the average values were obtained over 100 trials).

We also conducted one-way ANOVA analysis (IBM, SPSS) for β and BFi. For β, the F-value were 22.906 (DCS-NET), 1.394 (semi-infinite), 15.580 (three-layer), with corresponding p-values of <0.001, 0.250, and <0.001, respectively (significance level set as 0.05). This suggests that the DCS-NET and three-layer fitting models are relatively more influenced by noise levels compared to the semi-infinite fitting model. Regarding BFi, the F-values were 14.584 (DCS-NET), 3.473 (semi-infinite), and 21.407 (three-layer), with corresponding p-values of <0.001, 0.032, and <0.001, respectively (significance level set as 0.05). This indicates that the three-layer fitting model is significantly influenced by noise levels.

4.8.3 Relative Blood Flow

In practice, we do not aim to obtain absolute BFi measurements. Instead, the relative variation in blood flow (e.g., $rBFi = BFi/BFi_0$) is oftener used. To evaluate DCS-NET for extracting $rBFi$ in the brain, we assigned $\alpha D_b(w) = [1 + 0.05 \times (w - 1)] \times 6 \times 10^{-6}$ mm^2/s, w is an integer, w = 1, 2…21 in Layer 3 (brain) and fixed αD_b in other layers. Figure 4.11 presents $rBFi$ calculated on noiseless data at $\rho = 30\ mm$.

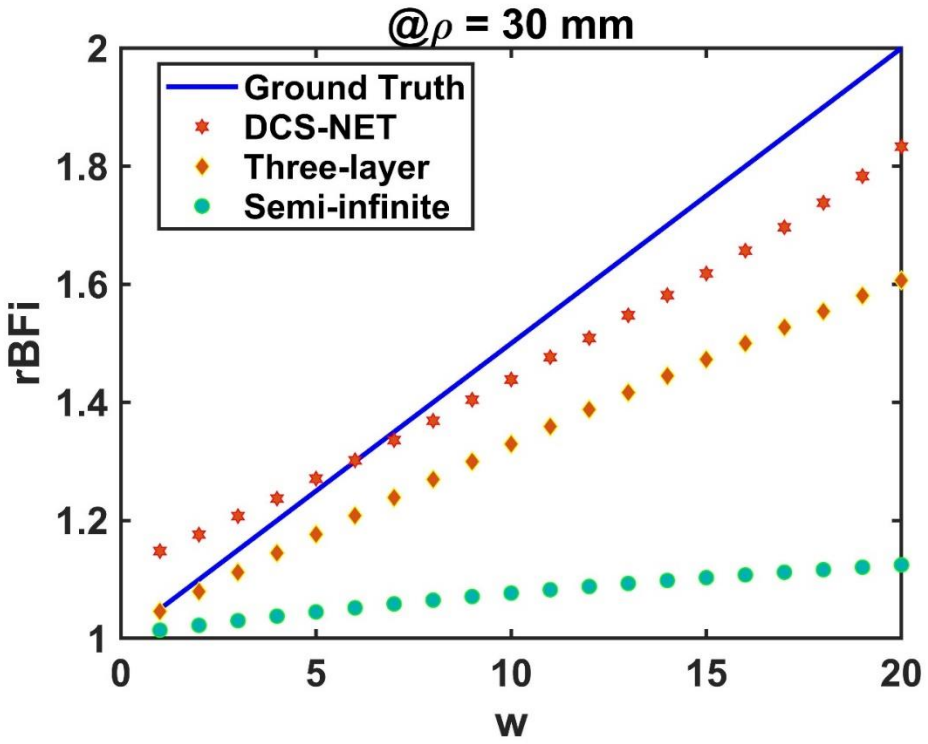

Figure 4.11 rBFi calculated by DCS-NET, the semi-infinite, and three-layer fitting methods on noiseless data for ρ = 30 mm for $\alpha D_b(w) = [1 + 0.05 \times (w-1)] \times 10^{-6}$ mm^2/s, w = 1, 2…21. rBFi = BFi/BFi$_0$, we define the estimated BFi as BFi$_0$ when w = 1.

To compare the accuracy of the three different methods in quantifying $rBFi$, we defined the error in $rBFi$ as $\varepsilon_{rBFi,H} = |rBFi_H - rBFi_{GT}| / rBFi_{GT} \times 100\%$ (H = *D, S, or T*), meaning the rBFi estimation error using DCS-NET, the semi-infinite and three-layer fitting methods, respectively. We can observe that $rBFi_D$ (red star) is close to the true $rBFi$ (blue solid line) with $\varepsilon_{rBFi,D}$ of less than 8.35%. By contrast, the semi-infinite and three-layer methods result in more significant errors of $\varepsilon_{rBFi,S}$ = 43.76% and $\varepsilon_{rBFi,T}$ = 19.66%, respectively. As expected, the semi-infinite homogenous solution resulted in significant errors in $rBFi$, in agreement with Ref. [154].

4.8.4 Intrinsic Sensitivity

As described in Section 4.7, the input D_b in Layer 3, denoted as $CBF_0 = 6 \times 10^{-6}$ mm^2/s, serves as the base point, and its corresponding recovered BFi is denoted as BFi_0. Similarly, we assigned $\alpha D_b = [1 + 0.1 \times (w - 1)] \times 6 \times 10^{-6}$ mm^2/s (w is an integer; w = 1, …, 11), and it is referred as the perturbed blood flow CBF_p. We also define a perturbation level $\zeta = (CBF_p - CBF_0)/CBF_0 \times 100\%$. We calculated the corresponding BFi for αD_b, and then used Eq. (4.3) to obtain η_D, η_S and η_T. We considered physiological noise by utilizing the noise model described in Section 3.3.8. Figure 4.12(a) shows the noiseless intrinsic sensitivity, demonstrating that DCS-NET exhibits $\eta_D > 71.34\%$. In comparison, the three-layer fitting method achieved $\eta_T = 61.96\%$, whereas the semi-infinite fitting method yielded η_S of only 14.12% on noiseless data. Figure 4.12(b-d) illustrate sensitivity curves at various noise levels. Especially noteworthy are the instances where $\eta_D > 0$ at $T_{int} = 10\ s$ and $T_{int} = 30\ s$. Conversely, with the semi-infinite and three-layer fitting models, η predominantly assumes negative values, underscoring the considerable impact of measurement noise on sensitivity. Furthermore, the impact of measurement noise on the sensitivity overgrows, particularly for the three-layer fitting method, as apparent in Figure 4.12(d).

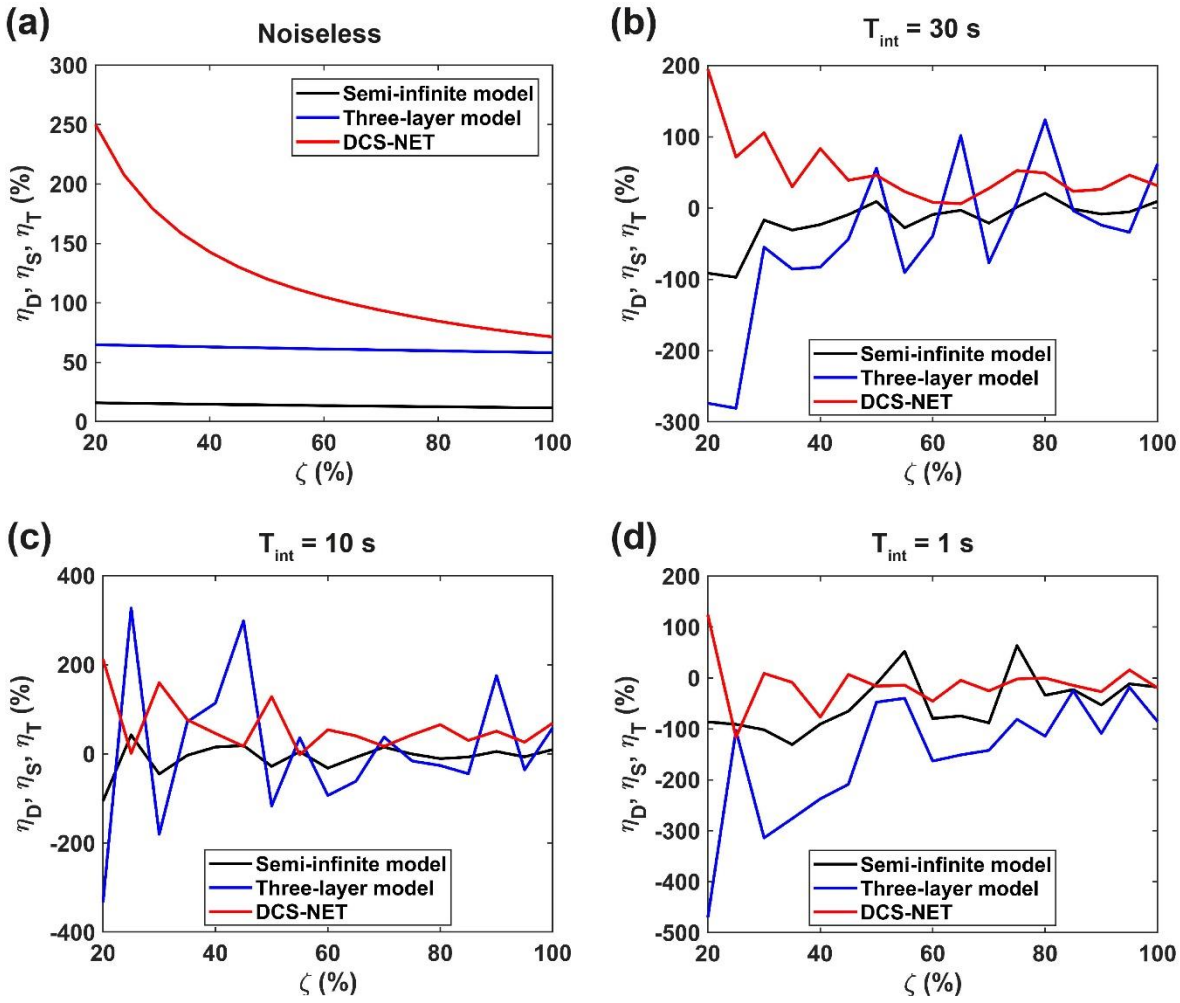

Figure 4.12 (a) Intrinsic sensitivity on noiseless data. (b-d) are the sensitivities for noise with T_{int} = 30 s, T_{int} = 10 s, T_{int} = 1s, respectively. η is the intrinsic sensitivity that defined in Eq. (4.3), and ζ is the perturbation level in Layer 3 (brain). Red, blue, and dark lines present η_D, η_T and η_S, respectively.

4.8.5 BFi Extraction with Varied Optical Properties and Scalp/Skull Thicknesses

In practical applications, a patient's head parameters can vary significantly, and the ideal scenario is to measure them before conducting DCS measurements. However, it is not always straightforward, and we usually assume average values. However, we must evaluate the impact of assumed errors on BFi estimation. Since μ_a and μ_s' are typically unknown and must be measured separately or taken from literature. We examined how μ_a and μ_s' of Layer 3 (brain) impact BFi extraction. Changing the scalp/skull thickness also varies BFi, which can be observed using the multi-layered model fitting method. Here, we use the three-layer fitting method, and *all BFi* were obtained at $\rho = 30$ mm. Additional details are presented in Table 4.3.

Table 4.3 Varying optical properties and scalp (Δ_1) and skull (Δ_2) thicknesses

	-40%	-20%	0%	+20%	+40%
μ_a (mm^{-1})	0.011	0.015	0.019	0.023	0.027
μ_s' (mm^{-1})	0.659	0.879	1.099	1.319	1.539
Δ_1 (mm)	3.000	4.000	5.000	6.000	7.000
Δ_2 (mm)	4.200	5.600	7.000	8.400	9.800

μ_a variation: To study how μ_a impacts *BFi*, we set μ_a = 0.011, 0.015, 0.019, 0.023, 0.027 and $\mu_s' = 1.099\ mm^{-1}$ in MCX. The baseline is at μ_a = 0.019 mm^{-1}, with $\pm 20\%$ and $\pm 40\%$ variation. In this case, two *BFi* groups were calculated. The first group was calculated assuming a constant $\mu_a = 0.019\ mm^{-1}$ (0%), defined as $\mu_{a,m}$, and the calculated *BFi* is defined as BFi_m. The second group was calculated using the known μ_a set in MCX, which we considered as true μ_a, and the corresponding calculated BFi is considered as BFi_{GT}.

μ_s' variation: Similarly, we conducted simulations with μ_s' = 0.666, 0.888, 1.110, 1.332, and 1.554 mm^{-1} and a fixed $\mu_a = 0.019\ mm^{-1}$ to investigate how μ_s' impacts BFi estimation. We define the estimated BFi as BFi_m when $\mu_s' = 1.099\ mm^{-1}$ (at 0%, defined as $\mu_{s,m}'$). Additionally, BFi_{GT} was calculated using the known μ_s' set in MCX, considered as true μ_s'.

The mean and standard deviation of the estimated BFi (vs μ_a) over 100 trials are shown in Figure 4.13(a). We also compare BFi_m and BFi_{GT}. The blue (BFi_{GT}) and green (BFi_m) dashed lines are for the semi-infinite model, whereas the red (BFi_{GT}) and purple (BFi_m) dashed line are for the three-layer model. The red solid (BFi_{GT}) and black dashed lines are for DCS-NET. Similarly, The *BFi*'s mean and standard deviation (vs μ_s') over 100 trials are shown in Figure 4.13(b).

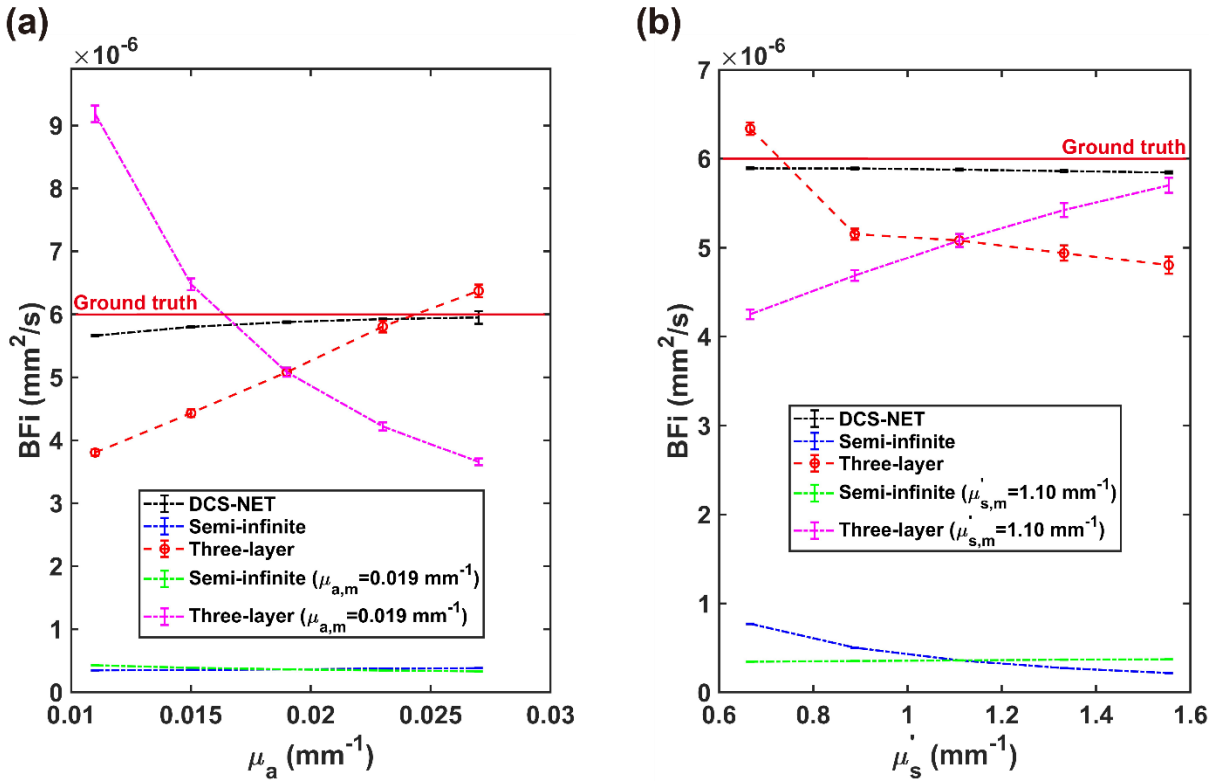

Figure 4.13 (a) Estimated BFi vs. μ_a, the green and purple dashed line are for BFi_m at μ_a = 0.019 mm^{-1} in Layer 3 (brain), the red solid line and the black dashed line are the BFi_{GT} and BFi_D, respectively, and the red and blue dashed lines are for BFi_{GT} using the three-layer and semi-infinite fitting methods. (b) Estimated BFi vs. μ_s', the green and purple dashed line are for the BFi_m at μ_s' = 1.10 mm^{-1} in Layer 3 (brain), the red solid line and the black dashed line are the BFi_{GT} and BFi_D, respectively, and the red and blue dashed lines are for BFi_{GT} using the three-layer and semi-infinite fitting methods.

Figure 4.14 shows the *BFi* variation (in %) vs. the μ_a and μ_s' variations (in %). The percentage error for μ_a is defined as $E_{\mu_a} = \left[\frac{\mu_{a,m}-\mu_a}{\mu_a}\right] \times 100\%$. Similarly, we define the percentage error for μ_s' as $E_{\mu_s'} = \left[\frac{\mu_{s,m}'-\mu_s'}{\mu_s'}\right] \times 100\%$. The *BFi* error (in %) caused by assumed error in E_{μ_a} or $E_{\mu_s'}$ is defined as $E_{BFi} = \left[\frac{BFi_m - BFi_{GT}}{BFi_{GT}}\right] \times 100\%$.

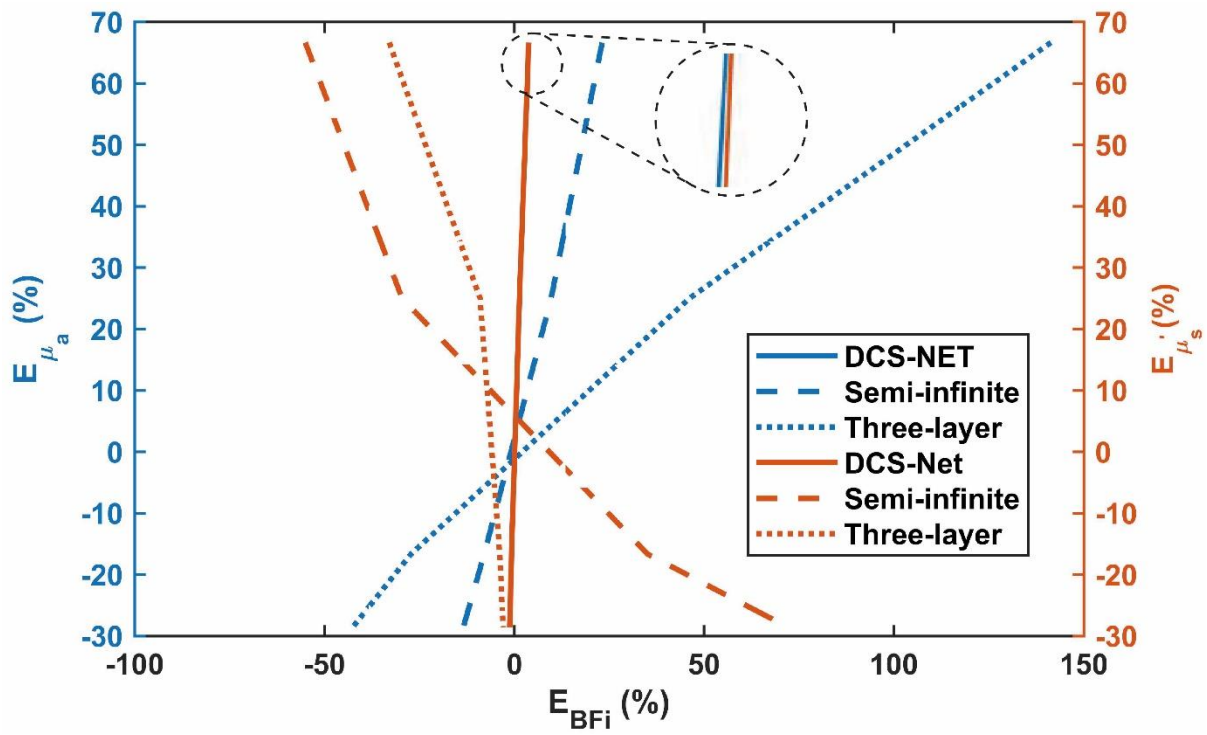

Figure 4.14 BFi error (in %) vs. errors in the μ_a and μ_s' variation (in %) among DCS-NET, semi-infinite, and three-layer fitting methods.

Figure 4.13 and Figure 4.14 show that E_{BFi} is positively related to E_{μ_a} and negatively related to $E_{\mu_s'}$ for semi-infinite and three-layer fitting models, in good agreement with previous findings [47,117]. On the other hand, E_{BFi} curves obtained from DCS-NET are close and are not sensitive to E_{μ_a} and $E_{\mu_s'}$. This result is expected, as from Eq. (3.16), μ_s' should yield a more pronounced impact compared to μ_a, primarily due to the second-order contribution from μ_s' and $\mu_s' \gg \mu_a$ observed in biological tissues. Extreme E_{BFi} examples are shown in Figure 4.14, namely, a more extensive $E_{\mu_a} \sim$ +62% results in $E_{BFi} \sim$ +25% and $E_{\mu_a} \sim$ -30% results in $E_{BFi} \sim$ -10%. When $E_{\mu_s'}$ reaches +62%, E_{BFi} reaches ~ -50% and $E_{\mu_s'} \sim$ -30% gives $E_{BFi} \sim$ +70%.

The results from the three-layer fitting model show similar behaviors. Namely, E_{BFi} is positively related to E_{μ_a} and negatively related to $E_{\mu_s'}$ in Layer 3, this result aligns well with the conclusions from Zhao *et al.'* conclusion [47]. In contrast, DCS-NET only shows -1% ~ +5% in E_{BFi} caused by E_{μ_a} and $E_{\mu_s'}$ (blue solid and brown solid lines for μ_a and μ_s', respectively in Figure 4.14), indicating that the variations in μ_a and μ_s' have negligible impact on BFi estimation.

Scalp thickness variation: To investigate Δ_1's impact on *BFi*, we varied Δ_1 (= 3, 4, 5, 6, and 7 mm) and fixed $\Delta_2 = 7\ mm$ in MCX. We define the estimated BFi as BFi_m when Δ_1 = 5 mm (0%, defined as $\Delta_{1,m}$). Additionally, BFi_{GT} was calculated using the known Δ_1 set in MCX, considered as true Δ_1.

Skull thickness variation: Similarly, to investigate Δ_2's impact on *BFi*, we varied Δ_2 (= 4.2, 5.6, 7.0, 8.4, and 9.8 mm) and fixed $\Delta_1 = 5\ mm$ in MCX. We define the estimated BFi as BFi_m calculated when Δ_2 = 7.0 mm (0%, defined as $\Delta_{2,m}$). Additionally, BFi_{GT} was calculated using the known Δ_2 set in MCX, considered as true Δ_2.

Figure 5.15(a) presents *BFi*'s mean value (represented by bar plots) and standard deviation (depicted by error bars) over 100 trials vs. Δ_1. The rightmost bar group represents the results obtained with Δ_1 = 5 mm. Figure 4.15(b) shows *BFi*'s mean value and standard deviation vs. Δ_2, the rightmost bar group represents the results obtained with $\Delta_2 = 7\ mm$. Still, we can see that the semi-infinite model cannot provide accurate *BFi* at a deeper layer. When Δ_1 changed, $\varepsilon_{BFi,D}$ falls into 1.17% ~ 8.33% (the bar group 1 in Figure 4.15(a)) when using DCS-NET, whereas $\varepsilon_{BFi,T}$ falls into 4.30% ~ 14.66% (the bar group 3 in Figure 4.15(a)) using the three-layer fitting model, slightly larger than that using DCS-NET. However, $\varepsilon_{BFi,T}$ increases to 11.67% ~ 16.05% when Δ_1 estimation error occurs using the three-layer fitting method (shown in the rightmost bar group in Figure 4.15(a)). Whereas for the variation in Δ_2, $\varepsilon_{BFi,D}$ falls into 0.33% ~ 10.33% when DCS-NET is used (the bar group 1 in Figure 4.15(b)), whereas $\varepsilon_{BFi,T}$ falls into 1.50% ~ 13.33% when the three-layer fitting method is used (the bar group 3 in Figure 4.15(b)). Both present similar accuracies. However, when Δ_2 is not accurate, $\varepsilon_{BFi,T}$ becomes more pronounced and reaches 41.09% ~ 193.40% (the rightmost bar group in Figure 4.15(b)).

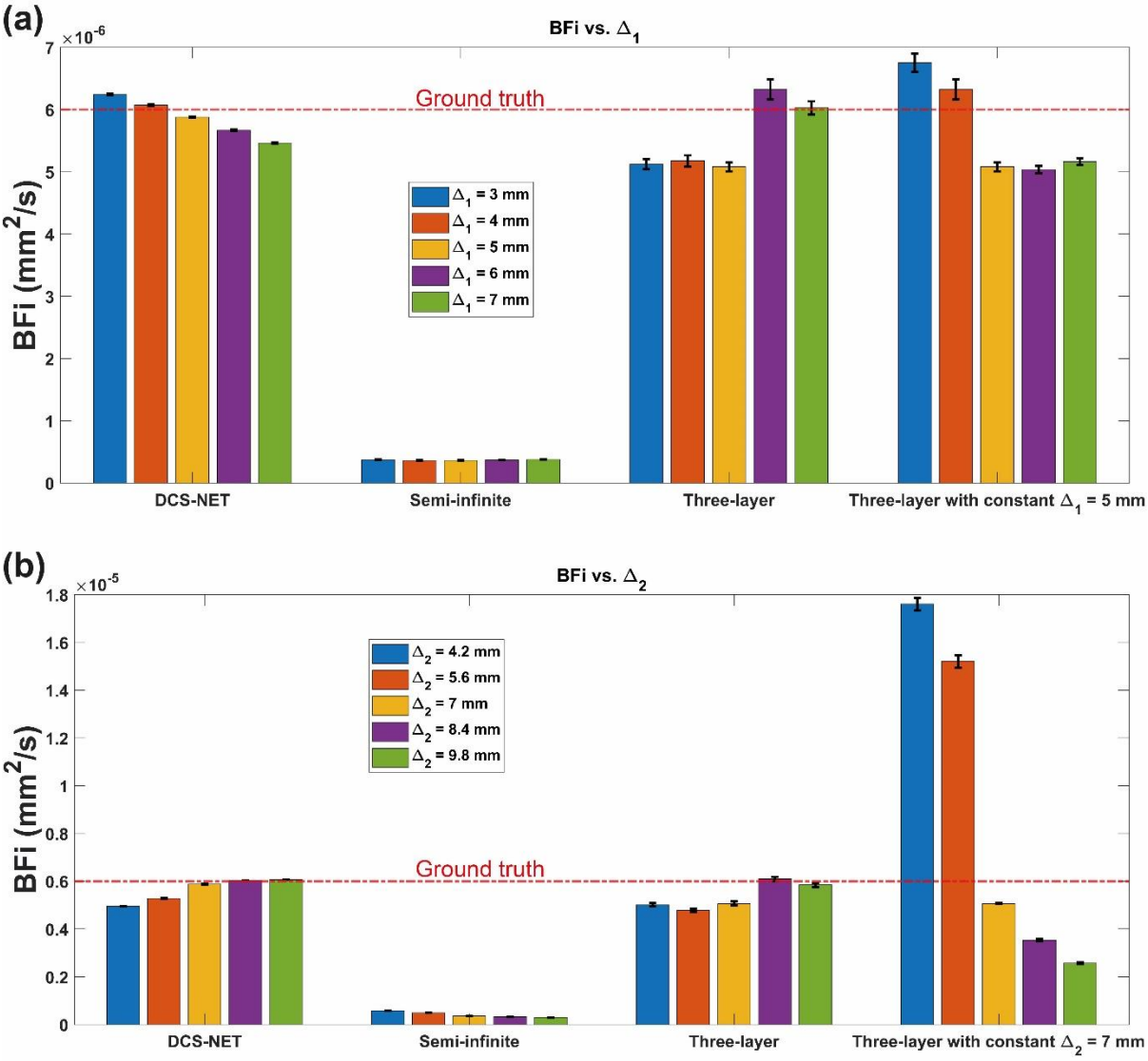

Figure 4.15 (a) BFi's mean value and standard deviation vs. Δ_1, and the rightmost bar group represents the results obtained with Δ_1 = 5 mm. (b) BFi's mean value and standard deviation vs. Δ_2, and the rightmost bar group represents the results obtained with Δ_2 = 7 mm. Each bar in the plot represents the average BFi over 100 trials calculated using three different methods, whereas the error bar stands for the standard deviation of BFi over 100 trials.

Figure 4.16 shows the *BFi* variation (in %) vs. the Δ_1 and Δ_2 variations (in %). The percentage error for Δ_1 is defined as $E_{\Delta_1} = \left[\frac{\Delta_{1,m}-\Delta_1}{\Delta_1}\right] \times 100\%$. Similarly, we define the percentage error for Δ_2 as $E_{\Delta_2} = \left[\frac{\Delta_{2,m}-\Delta_2}{\Delta_2}\right] \times 100\%$. The *BFi* error (in %) caused by assumed error in E_{Δ_1} and E_{Δ_2} is defined as $E_{BFi} = \left[\frac{BFi_m - BFi_{GT}}{BFi_{GT}}\right] \times 100\%$.

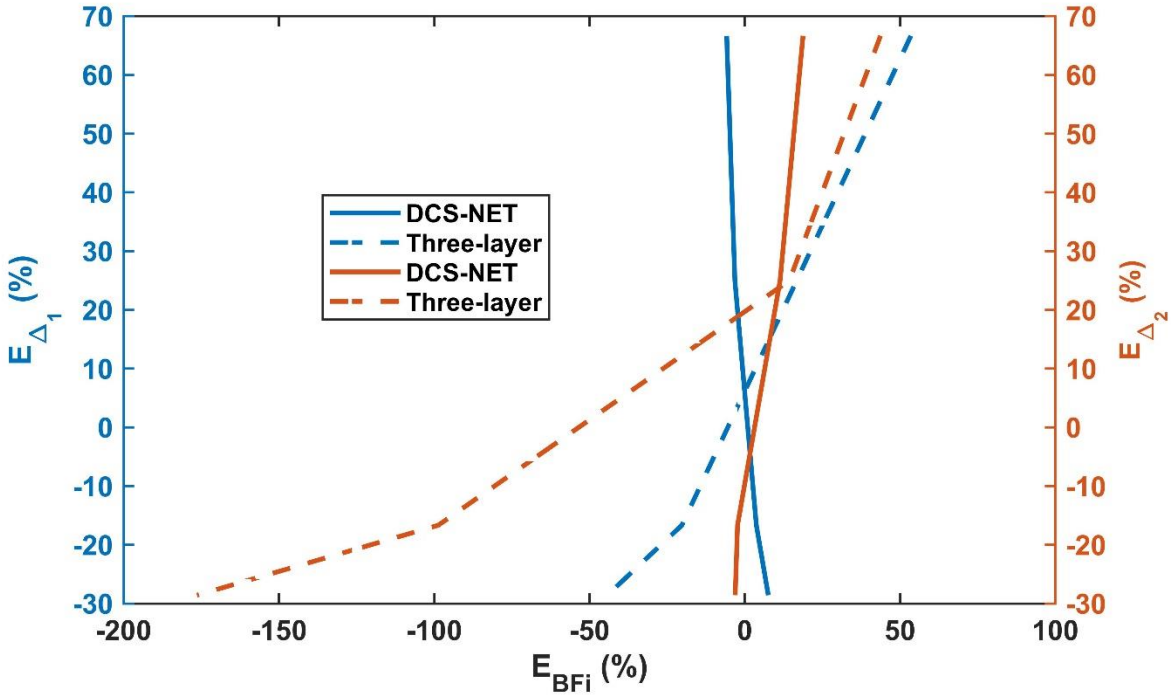

Figure 4.16 BFi error (in %) vs. errors in Δ_1 and Δ_2 (in %) between DCS-NET and three-layer fitting methods.

As it is commonly known, E_{Δ_1} and E_{Δ_2} cause a significant E_{BFi}. Figure 4.15(a) and (b) demonstrate a positive correlation between E_{BFi} and E_{Δ_1} (and E_{Δ_2}). Furthermore, as observed in Figure 4.16, E_{BFi} resulting from E_{Δ_2} ranges from -176.41% to +43.68%. In contrast, E_{BFi} caused by E_{Δ_1} ranges from -44.29% to +53.47%. This error range is significantly narrower than that caused by the skull thickness, agreeing with the findings in Ref. [47]. For DCS-NET, E_{BFi} caused by both Δ_1 and Δ_2 falls within the limited range of -6% to +8%.

4.8.6 BFi Inference Time

The inference time is also an important parameter, especially in real-time measurements, and Table 4.4 compares the three extraction methods. We record the inference time for single decays and batch decays (e.g., 100 trials) at different noise levels. It is clear that DCS-NET is promising for real-time applications.

Table 4.4 The inference time for BFi extraction (with Matlab parfor for semi-infinite and three-layer fitting models)

	1 trial			100 trials		
Noise level	DCS-NET (s)	Semi-infinite (s)	Three-layer (s)	DCS-NET (s)	Semi-infinite (s)	Three-layer (s)
Tint = 30 s	0.001	0.026	15.177	0.002	0.137	184.441
Tint = 10 s	0.001	0.029	17.021	0.004	0.161	199.758
Tint = 1 s	0.004	0.065	50.397	0.005	0.133	292.910
Noiseless data	0.001	0.048	15.391	0.004	0.121	169.679

4.9 Summary

In this chapter, we show that DCS-NET can robustly quantify DCS-based blood flow measurements. We used DCS-NET to analyze the autocorrelation functions generated from MCX. The proposed network is based on 1D CNN [274], which is straightforward, quicker to train, and faster than high-dimension CNNs for time sequence analysis, such as FLIM data [274,279]. To evaluate DCS-NET, we compared it with the semi-infinite, three-layer fitting methods by changing tissue optical properties (μ_a and μ_s'), depths (related to ρ), and scalp/skull thicknesses (Δ_1 and Δ_2). *BFi* estimated by DCS-NET shows a small error range -1% ~ +5% induced by μ_a and μ_s' (see Figure 4.14) and a slightly wider error range -6% ~ +8% induced by Δ_1 and Δ_2 (see Figure 4.16). For *rBFi*, the error from DCS-NET (8.35%) is much less than that of the semi-infinite and three-layer fitting methods (43.76% and 19.66%, respectively). Moreover, DCS-NET yields more than 71.34% sensitivity to brain blood flow, whereas the semi-infinite and three-layer fitting methods yield 14.12% and 61.96%, respectively (Figure 4.12(a)). We considered measurement noise using a stochastic noise model to reflect experimental realities. With DCS-NET, $\varepsilon_{BFi,D}$ is 12.87% at a high noise level ($T_{int} = 1\ s$), whereas it increases to 390.10% when using the three-layer fitting method. At a low noise level ($T_{int} = 30\ s$), the three-layer fitting model yields $\varepsilon_{BFi,T}$ of 82.30%, much worse than 1.93% obtained by DCS-NET, suggesting that DCS-NET is less sensitive to noise (see Figure 4.12 (b)). Figure 4.15(a) and (b) show that the three-layer analytical method (modelling the head, i.e., scalp, skull, brain) can minimize the influence of extracerebral layers on measured DCS signals. However, this model requires a priori knowledge of layer optical properties and thicknesses. Therefore, accurately estimating scalp and skull thicknesses is required for reliable *CBF* estimation when using a three-layer analytical model.

Besides accuracy and robustness, the computational cost is a critical factor that impacts practical applications, especially for real-time monitoring. Table 4.4 reveals that it took 0.004 seconds for DCS-NET to quantify 100 g_2 curves with 127 data points. In contrast, it took 0.110 seconds and 211.697 seconds, respectively, for the semi-infinite fitting and three-layer fitting procedures. For quantifying a single autocorrelation decay curve, it only took 0.002 seconds for DCS-NET. In contrast, it took 0.042 seconds and 24.496 seconds, respectively, for the semi-infinite fitting and three-layer fitting procedures. DCS-NET is the fastest among the three, around 12,000-fold faster than the three-layer model and 21-fold faster than the semi-infinite model.

Although DCS-NET is more robust than the semi-infinite and three-layer fitting methods, our study has several limitations. **Firstly**, DCS-NET's training datasets were generated using the semi-infinite diffusion model as advised in Ref. [38]. Nevertheless, this model does not consider scalp and skull thicknesses, which could potentially explain why the error range (-6% $\sim$ +8%) caused by Δ_1 and Δ_2 is much broader than that (-1% $\sim$ +5%) caused by μ_a and μ_s' (Figure 4.14 and Figure 4.16). The complexity of including training datasets generated from a layered model is beyond the scope of this study, given this report's already long length. In future, we will train new networks using datasets generated from a layered model, and alternatively, obtaining training datasets from *in vivo* measurements, as demonstrated in Refs [164] and [165]. will also be considered. **Secondly**, current *rBFi* calculations do not consider variations in optical properties between the baseline and activation states. Indeed, μ_a and μ_s' in the brain can vary according to interventions (e.g., functional activation), which are recognized to impact perfusion. Failing to account for these changes could introduce additional uncertainties in *rBFi* measurements. **Thirdly**, we did not include a comparison with the two-layered analytical model in this report; it may be worth further investigation. **Last but not least**, our study was solely conducted using simulation data. In future, we will perform phantom and *in vivo* experiments to validate our findings.

Chapter 5 DCS Prototype

5.1 Introduction

In this chapter, I introduce the 192 × 128 SPADs array. I then present a DCS system equipped with a large 192 × 128 SPADs array, along with the data collection software and offline data analysis tools. We tested the system on a milk phantom and the results confirm that our multispeckle approach is effective. The signal-to-noise ratio (SNR) gain across the entire sensor improved by approximately 160-fold compared to a single pixel. Additionally, the system demonstrates a roughly 5-fold enhancement in the SNR gain over a previously reported 32 × 32 multispeckle DCS system.

5.2 SPAD Sensor

5.2.1 192 × 128 SPAD Array

In my investigation, we employed a time-correlated single-photon counting (TCSPC) imager based on SPAD technology, implemented in 40-nm CMOS technology, featuring the most compact time-to-digital converter (TDC) reported to date (9.2 μm × 9.2 μm) [280]. The 12-bit TDC achieves the most precise timing resolution, ranging from 33 to 120 ps, among all reported TCSPC pixels. This comes with an energy efficiency figure of merit (FoM) of fJ/conv, exhibiting less than 1 least significant bit (LSB) differential nonlinearity (DNL) and less than 6 LSB integral nonlinearity (INL). Enhancements to the photon detection efficiency (PDE) of the array involve cylindrical microlenses, providing a mean concentration factor of 3.25% and an effective fill factor of 42%. The sensor exhibits an exceptionally low median dark count rate (DCR) of 25 Hz under conditions of 1.5-V excess bias and room temperature. Additionally, SPADs in the array achieve a peak photon detection probability (PDP) of 34% at 560 nm for 1-V excess bias at room temperature and a quench time of 5 ns [281]. The SPAD array was packaged into a camera module, referred to as QuantICAM [280], as shown in Figure 5.1. The sensor chip comprises addressing circuitry, 64 parallel-to-serial converters, and a pixel array measuring 192 × 128, with individual pixels sizes at 18.4 μm × 9.2 μm. Each pixel comprises a TDC coupled to a SPAD.

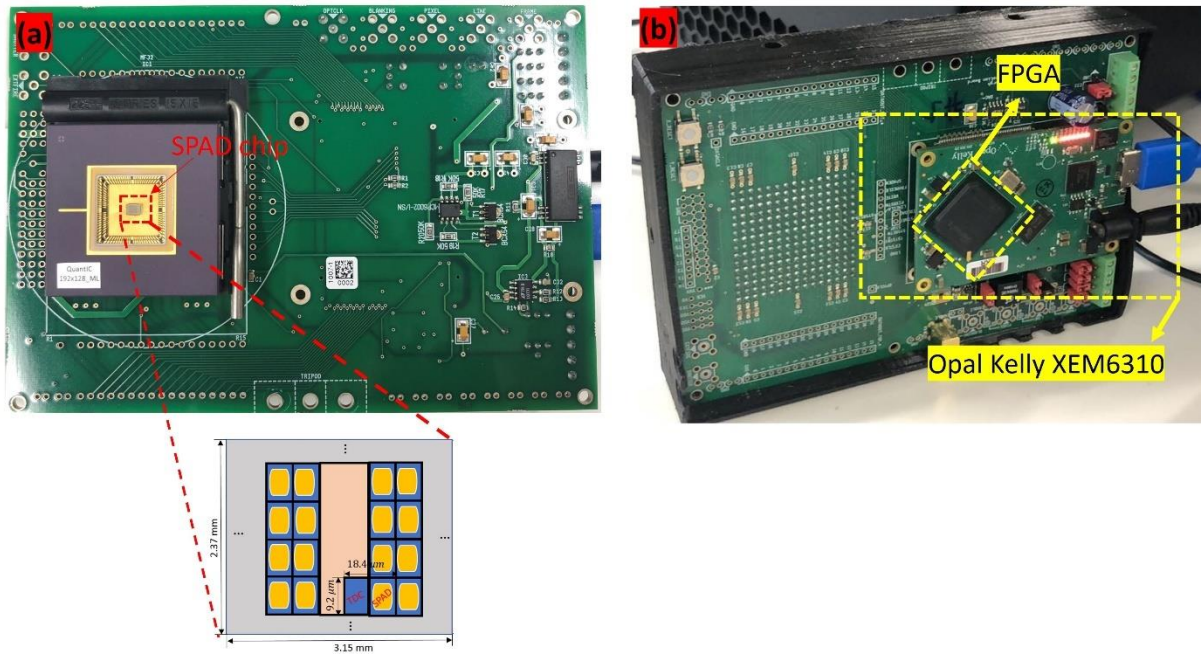

Figure 5.1 (a) SPAD sensor module, front view of QuantICAM with the SPAD chip integrated. (b) Data processing module, back view of QuantICAM, including the Opal Kelly XEM6310 FPGA board.

Table 5.1 Comparison between PF32 and SPAD 192 × 128

	PF32 × 32	SPAD 192 × 128
Pixel pitch (um)	50 um	18.4 × 9.2
SPAD dia. (um)	NA	5.4
Active area	6.95 um Ø	NA
Fill factor	1.5% (optical fill factor)	13%
Photodetection efficiency	Peak 28% @ 500 nm	Peak 34% @ 560 nm
SPAD shape	NA	Square, rounded corners
Sensor wavelength range	NA	400 to 900 nm

5.3 TCSPC and Photon Counting Mode

There are two modes of the QuantICAM, TCSPC mode and photon counting mode.

5.3.1 TCSPC Model

Frequency, TCSPC can be likened to a fast stopwatch, where the start corresponds to the emission of pulsed light and the termination aligned with the detection of a singular photon. Nevertheless, similar to numerous TCSPC setups, the QuantICAM executes measurements in

reverse start-stop fashion: the start of the TDC is triggered by the detection of a single photon, and the subsequent synchronization pulse stops this process. This is explained in Figure 5.2.

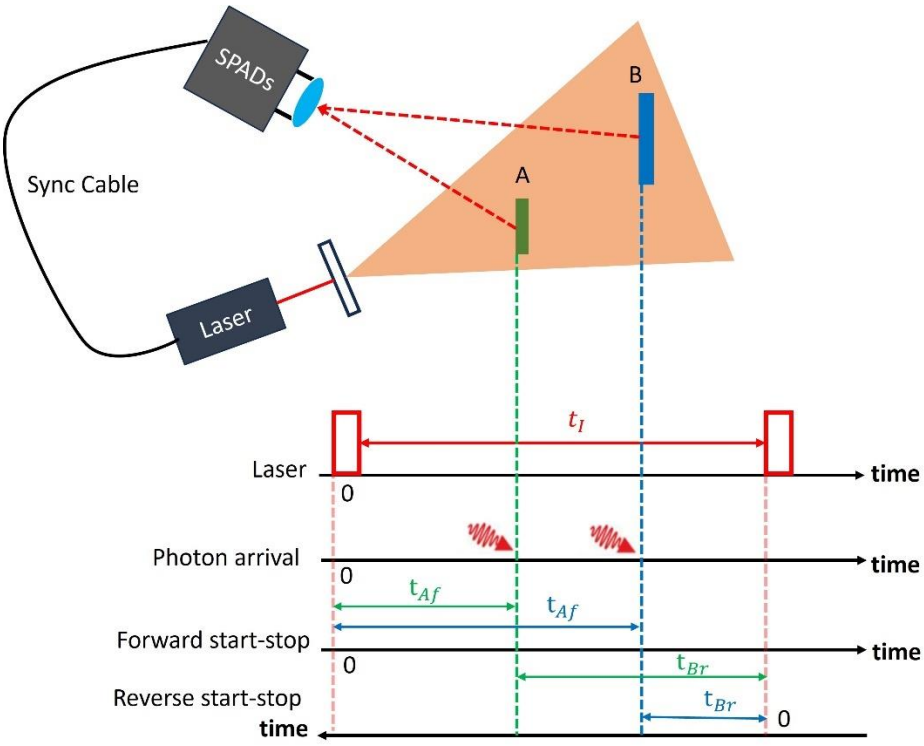

Figure 5.2 illustrates the reverse start-stop principle using a basic laser-ranging setup. A pulsed laser beam, passing through a diffuser, illuminates surfaces A and B. The scattered photons are collected by the QuantICAM. We also depict the process timing: the laser period is t_I, and photons are detected later. In forward start-stop, photon timestamps from surface A (t_{Af}) are lower than those from B(t_{Bf}). Conversely, in reverse start-stop, photon detection initiates timing, with timestamps for surface A(t_{Ar}) higher than those for B(t_{Br}). This method ensures counting electronics are active only upon photon detection, reducing electronics usage compared to forward start-stop where timing starts with the synchronization signal and ends with photon detection. This minimizes readout dead time, lowers power consumption, and reduces heat dissipation.

The QuantICAM can receive a synchronization signal through the Sync connector, or alternatively, use the FPGA within the camera to supply the synchronization signal to the TDC and output it to the light source via the trigger connector.

5.3.2 Photon Counting Mode

When operating in photon counting mode, the TDC is set up to effectively tally the quantity of photons received within each frame duration. This measurement process does not necessitate synchronization, rendering photon counting mode valuable for the preliminary setup and alignment of the system before conducting TCSPC data collection. In our study we only use

photon counting mode. In this mode, individual pixels have the capacity to register multiple photons per frame, as illustrate in Figure 5.3.

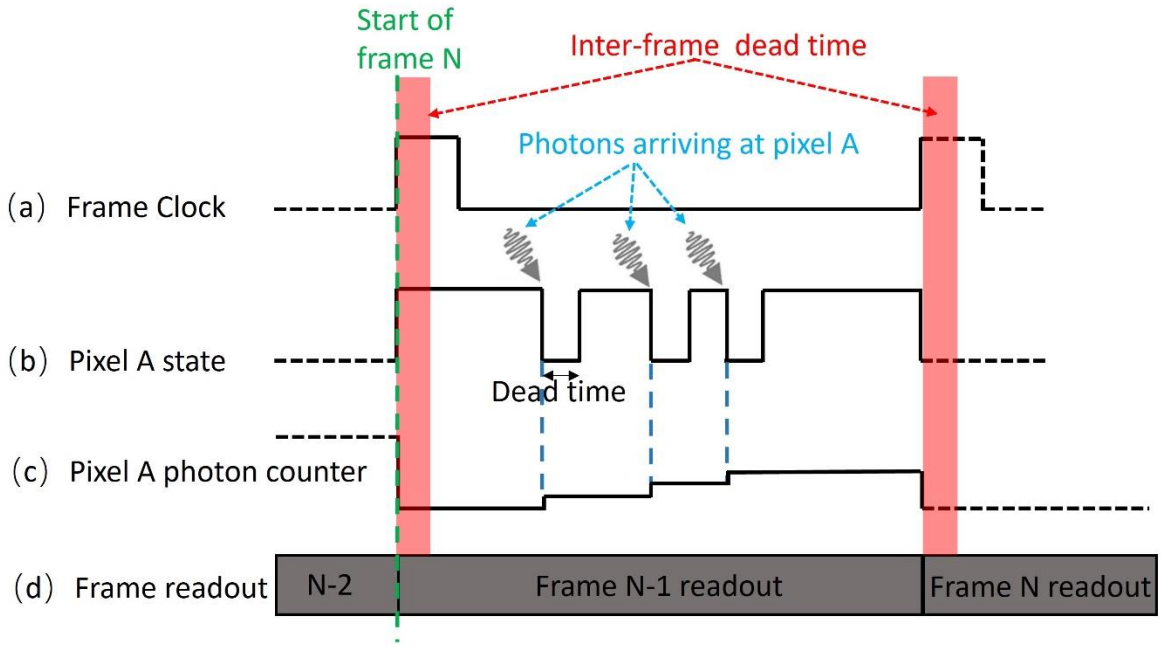

Figure 5.3 illustrates photon counting mode, where the frame clock (a) sets the maximum frame rate, showing a single pixel for simplicity. Each frame begins with a brief deadtime (shown in red), during which incoming photons are not counted. After this deadtime, each pixel can count multiple photons. The sequence of detecting a photon (b), incrementing the counter (c), and resetting the SPAD repeats until the frame ends and the next frame clock pulse transfers data to the readout stage (d). To prevent data wrap-around, a sufficiently short frame time is necessary. The camera's "frame to add" setting allows for digital summation of multiple frames to increase the maximum count value as needed.

5.4 DCS System Using a 192 × 128 SPAD

5.4.1 Laser Coupling

In our setup, the simulation of fiber coupling is performed first, where the free space laser output is coupled to a multimode fiber with a 100 μm core radius and NA of 0.39. We disregard Fresnel (reflection) losses from air-glass interfaces, including the fiber. The fiber core is modeled as a 100 μm radius circular aperture on the Image surface, set as a 'Floating' aperture type controlled by the Image surface's Semi-Diameter. Figure 5.4(a) displays this simulation using Opticalstdudio. Figure 5.4(b) and (c) show the resulting donut-shaped and near-Gaussian output beam profiles, respectively. These figures illustrate that the beam entry angle significantly influences the output beam profile, with normal incidence producing a near-Gaussian shape (Figure 5.4(b) and (e)), and increased angles fielding a donut shape (Figure

5.4(c) and (f)). It is clear to know that the output beam profile can be hugely affected by the beam entry angle. Although in some applications, an alternative beam distribution such as a top hat or donut is desired instead of the inherent Gaussian distribution provided by typical optics. In our study, we only need to have the Gaussian distribution one. Here, I investigated the effect of changing the input angle of a focused laser beam into a multimode fiber. I found that focusing the light perpendicular to the fiber surface resulted in a near-Gaussian output beam profile (Figure 5.4(b) and (e)) and increasing the angle resulted in a donut-shaped beam profile (Figure 5.4(c) and (f)). These results demonstrate how multimode fibers can be used to change the shape of a beam profile. Figures 5.4(b) and (e) depict meridional and skew ray propagation through multimode fiber, respectively, and the associated theoretical beam distribution at the fiber output. As shown in Figure 5.4(e), skew rays propagate in a helical path along the fiber which is tangent to the inner caustic of the path with radius r.

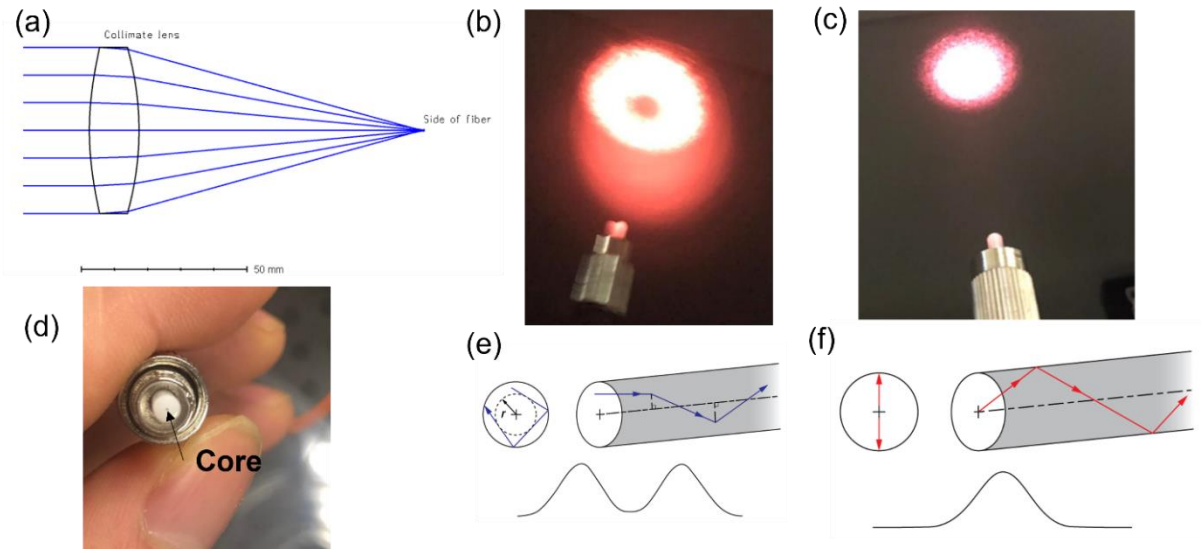

Figure 5.4 (a) Simulation of fiber coupling using Opticalstudio. (b) Donut beam profile obtained at a certain input angle. (c) Near-Gaussian beam profile obtained at 0° input angle (normal to the fiber face). (d) The fiber used in our setup. (e) Skew ray propagation corresponding to donut profile. (f) Meridional ray propagation corresponding to the near-gaussian output profile.

5.4.2 DCS Data Collection Software

For DCS data collection, we designed a software tool, which was implemented by a MATLAB Graphical User Interface (GUI). This software supports several key functions:

1) **Firmware Management**: Downloads and updates firmware directly through the GUI.
2) **Sensor Array Configuration and Control**: Adjust and monitors the sensor array settings.

3) **Data Acquisition and Processing**: Receives pixel data from the sensor array and processes it for imaging purposes.

The software integrates Dynamic Link Library (DLL) files and Application Programmer's Interfaces (APIs) provided by Opal Kelly, compatible across various platforms and programming languages. By incorporating these DLLs and APIs, the software can configure and interact with the hardware over a USB connection using the MATLAB GUI. The main GUI is shown in Figure 5.5, includes a 'Saving intensity' button that captures and stores multiple frames (192 × 128) received from the firmware via the 'OKBTPipeOut' endpoint. Additionally, an 'imaging' button triggers decoding and imaging functions, processing the data captured in photon counting (PC) mode to generate 'Hot' images, also shown in Figure 5.5

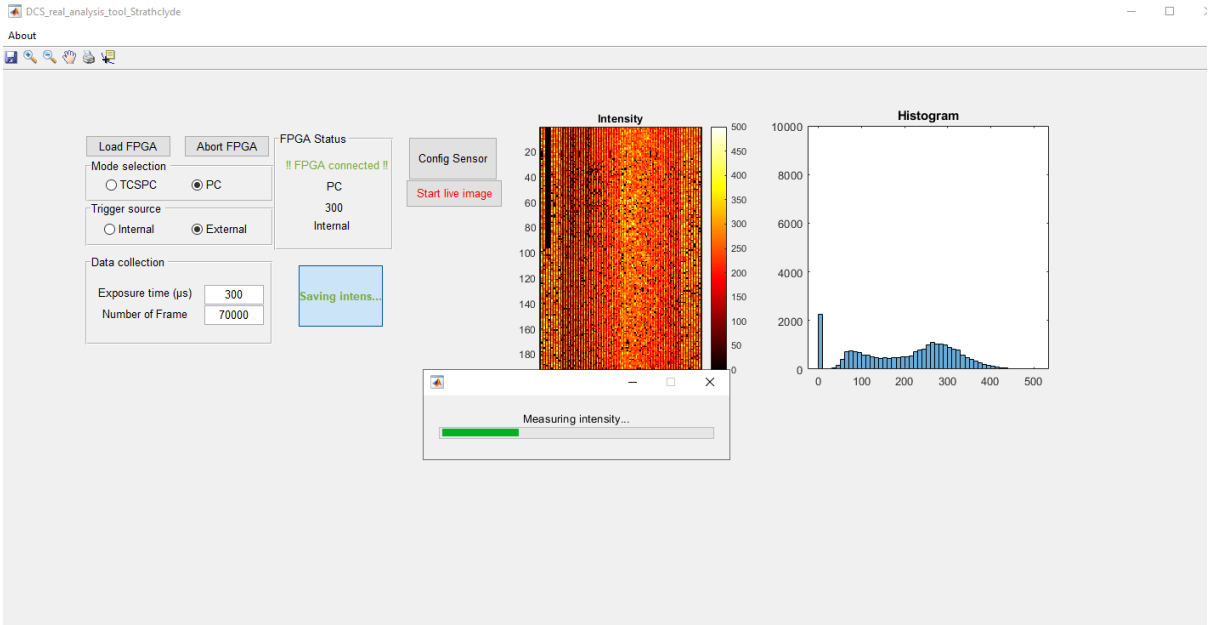

Figure 5.5 Main UI for DCS data collection.

5.4.3 Off-line Analysis Tool (Software) Design

The offline DCS data analysis software is implemented by a MATLAB Graphical User Interface (GUI) to conduct the following tasks: conduct the fitting method and Deep learning method for blood flow index extraction. In this design, the pre-trained AI model based on Pytorch/Tensorflow/ONNX would be called in Matlab, the flow chart as shown in Figure 5.6. As can be seen in Figure 5.7, the main UI of the software, in which the measured data g2 and the delay time tau were loaded via Browser 1 and 2, respectively. By pressing the "Fitting"

button we can obtain beta β and the blood flow index. We can also switch to the AI method, which can also help to obtain β and blood flow index.

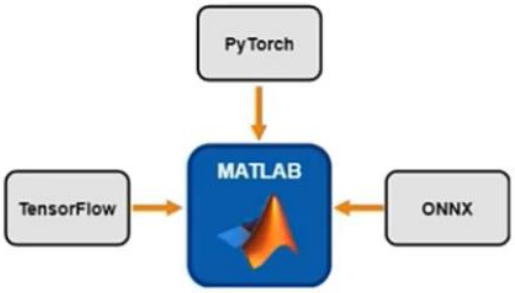

Figure 5.6 The flow chart about calling AI model in MATLAB.

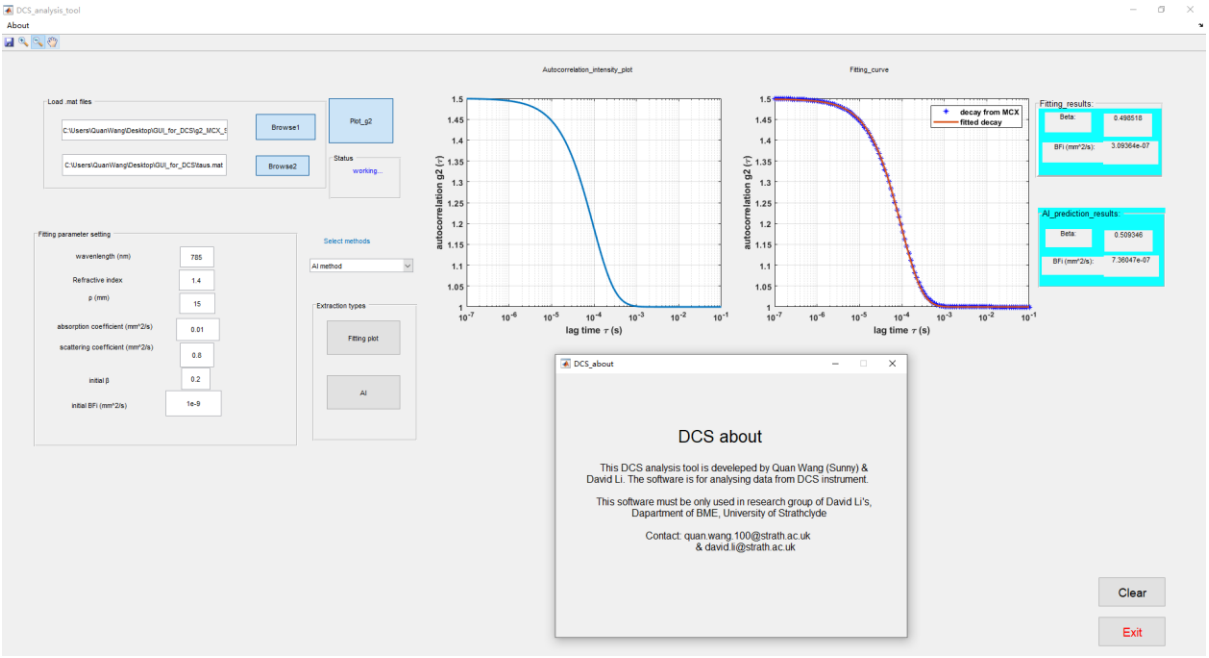

Figure 5.7 Main UI of the DCS offline analysis software.

5.4.4 DCS System Description

The experimental setup for the multispeckle DCS blood flow measurement system is depicted in Figure 5.8. A continuous-wave (CW) laser operating at a wavelength of λ = 785 nm (CrystaLaser, USA) was coupled (coupling efficiency: 88.9%) into a multimode optical fiber (MMF; core diameter = Ø200 μm; NA = 0.39, Thorlabs) through a collimator (*f* = 6.24 mm, NA = 0.37, Thorlabs) serving as an illumination source. The multiple scattered light was collected by a multimode fiber (MMF; core diameter = Ø200 μm; NA = 0.39, Thorlabs) placed at a separation distance ρ away from the source and then coupled to the QuantiCAM camera [280].

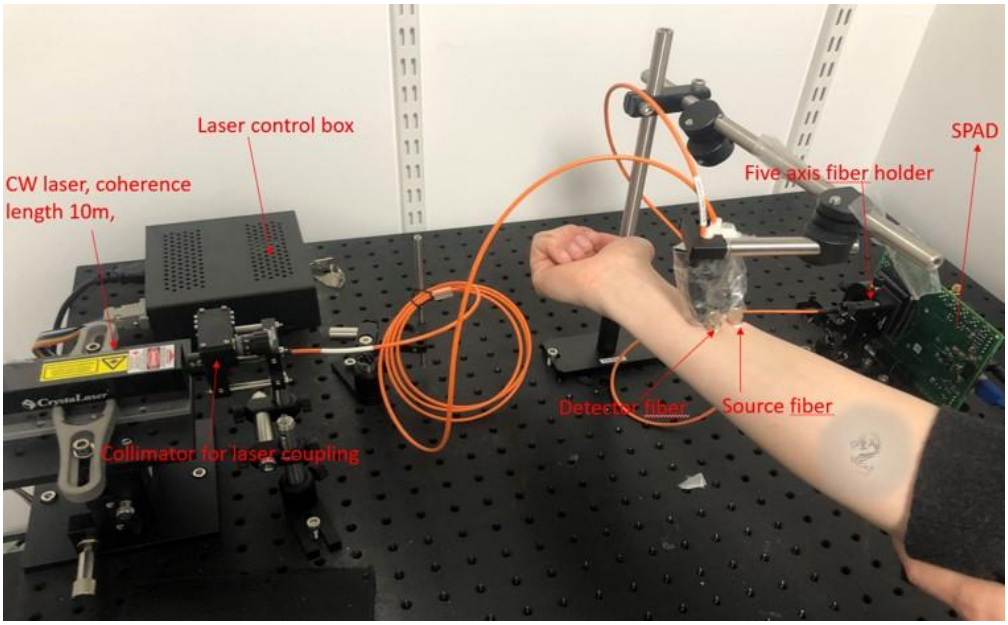

Figure 5.8 Schematic of our DCS system using SPAD camera QuantiCAM. MMF = multimode fiber.

The configuration of the sensor is shown in Figure 5.9. The 3.15 mm × 2.37 mm (an area of 7.4 mm^2) chip was manufactured in STMicroelectronics 40-nm CMOS process [280]. The sensor consists of an addressing circuitry, 64 parallel-to-serial converters, and a 192 × 128, 18.4 μm × 9.2 μm pixel array. Each SPAD pixel consists of a TDC. The photon detection efficiency (PDE) is 43% at the peak of 560 nm and 8% at 785 nm (the wavelength we used in the experiment) at an excess bias of 1V at room temperature. The fiber tips at the output of the detection path were placed on a fiber adapter (SM05SMA, Thorlabs) and mounted on a 5-axis optic mount (K5X1, Thorlabs) to control the distance between the tip and the camera sensor. The sensor was fixed over the optical table. The intensity of the illuminating light was adjusted to 98 mW, which was detected by a power meter (LASERPOINT, Italy). The average diameter of a speckle can be obtained using the following equation [282]:

$$d_s = \frac{\lambda y}{D}, \tag{5.1}$$

where λ is the wavelength of the illumination light source (785 nm), y is the distance between the detection fiber end and the SPAD camera, and D is the core diameter of the detection fiber (200 μm). We calibrated our system by measuring d_s by varying y with the setup shown in Figure 5.9 to ensure d_s matched the size of the pixel active area of 9 μm. We obtained the optimized fiber-SPAD distance y ≈ 2.3 mm. The maximum frame rate set via the clock rate in the firmware is approximately 9.11 kfps. The data collected at the frame exposure time T_{exp}

= 1 μs. The QuantiCAM camera operated in the photon counting mode, capturing the scattered intensity at ρ = 10 mm away from the source.

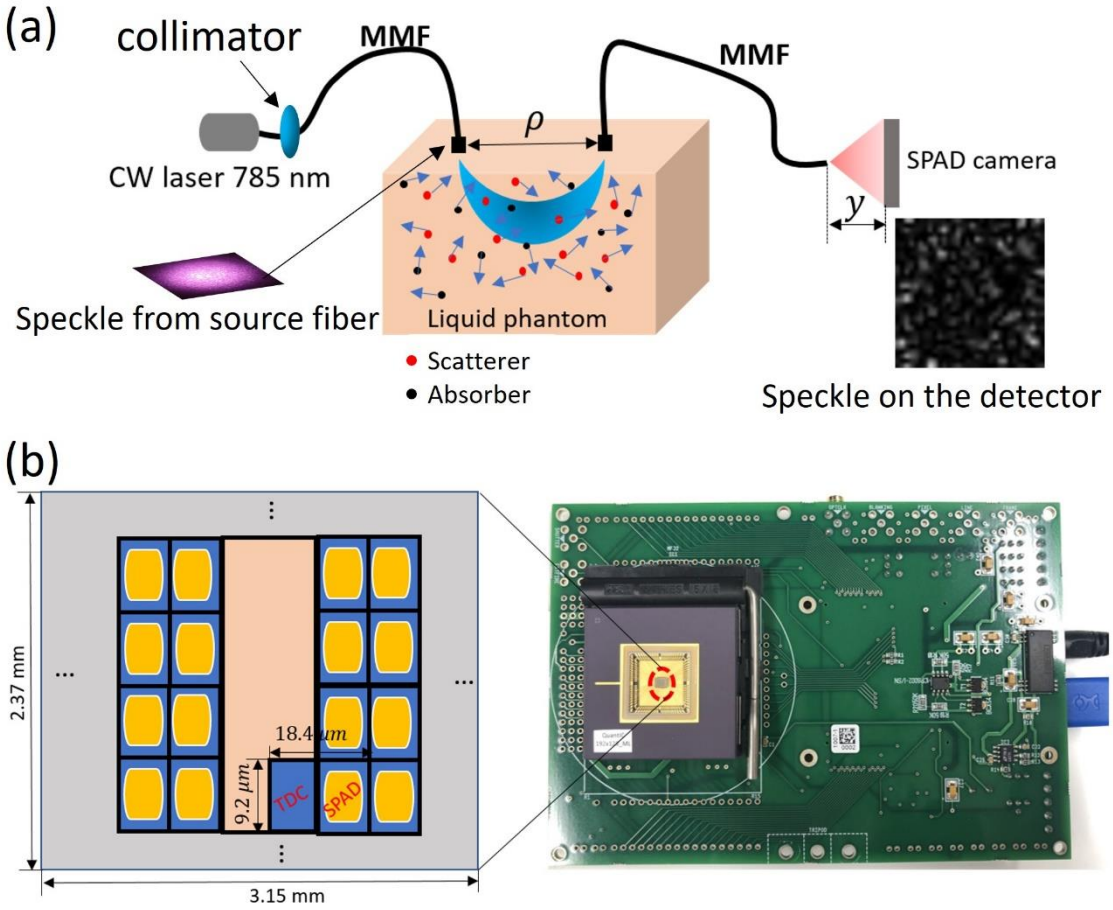

Figure 5.9 (a) Schematic of our DCS system using the SPAD camera; (b) Overview of the QuantiCAM camera. A printed circuit daughter board integrates the SPAD chip and the Opal Kelly XEM6310 FPGA board.

5.5 Data Analysis

5.5.1 DCS Simulation (Monte Carlo Simulations)

In this section, Monte Carlo simulations have been conducted, it is considered the "gold standard" for modelling as its validation for arbitrary three-dimensional configurations of tissue properties and source-detector positioning. In the simulation, a three-dimensional model of the medium with known optical properties was given. Here, we simulate the propagation of individual photons through the medium. The scattering and absorption properties were used to probabilistically generate the photons' trajectories and those that reach the detector were recorded. We define the fiber angulation θ_f as the angulation of the emitting fiber away from the detection fiber, in the plane of the two fibers. The simulations were carried out in MCmatlab

[283]. Figure 5.10 shows the detected light's most likely path of the detected light through the scattering tissue and is assumed to be "banana-shaped".

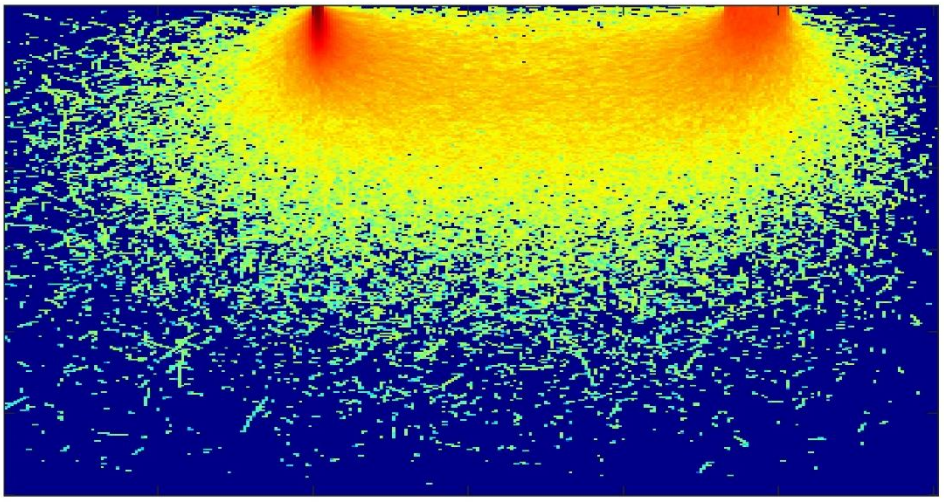

Figure 5.10 Simulation results of the scattered light traveling through a "banana shape" in tissues. The simulation carried out in Matlab based on mcxyz model developed by Jacques and Li [284].

5.5.2 Defect and Hot Pixel Removal

Physical defects in SPAD can make the pixel keep working when the camera exposure dark room and keep dark when the camera exposure on room light. We refer to pixels that have high photon counts (at certain range) (> 320 p.c. and < 40 p.c.) when exposure time equal to 200 µs as bad pixels and those with low photon counts (<10 p.c.) as hot pixels. We identified hot and bad pixels in the whole SPAD camera.

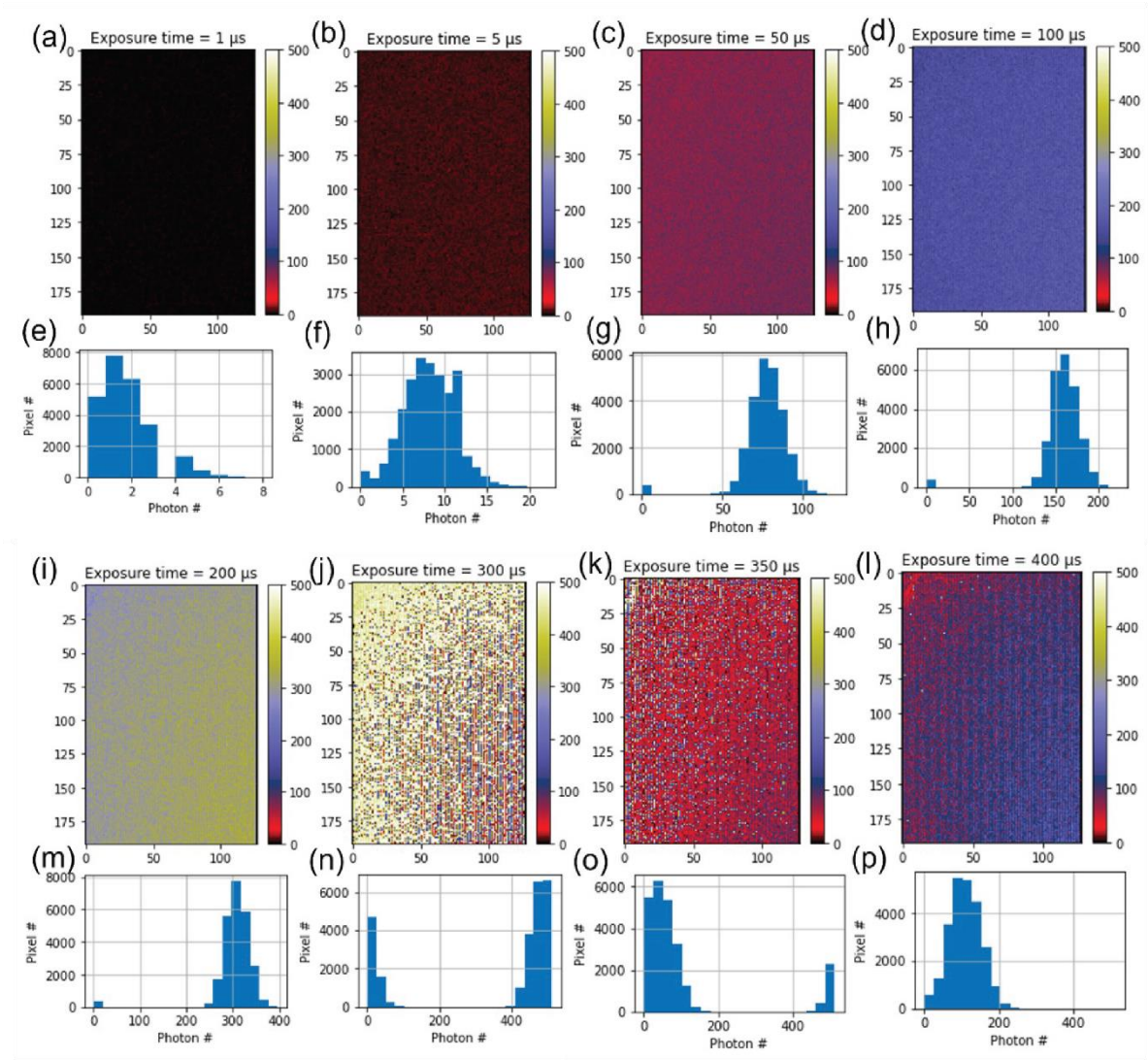

Figure 5.11 Characterizing bad pixels in SPAD camera. (a)-(e) and (i)-(l) intensity image under different exposure time of SPAD camera in room light on, and (e)-(h) and (f)-(k) corresponds to distribution of the photon counts across all pixels.

As we can see from the Figure 5.11, if the photon count is more than 512, the pixel count would overflow, so the exposure time should be set to a proper value to avoid the overflow when collecting DCS data.

5.5.3 g_2 (τ) Calculation

To perform a DCS measurement, we computed the intensity autocorrelation function $g_2(\tau)$ as a function of the time lag τ at each SPAD pixel:

$$g_2^i(\tau) = \frac{\langle n_i(t) \cdot n_i(t+\tau) \rangle}{\langle n_i(t) \rangle^2}, \tag{5.2}$$

where $n_i(t)$ is the number of detected photons of the i-th SPAD pixel at a given time t. We then calculate the final system autocorrelation function across $i = 1$ to N; N is the number of SPAD pixels used for the measurements,

$$\bar{g}_2(\tau)|_N = \frac{1}{N}\sum_{i=1}^{N} g_2^i(\tau). \tag{5.3}$$

The normalized intensity ACF, $g_2(\tau)$ can be linked to the normalized electric field ACF, $g_1(\tau)$ through the Siegert relation [285]:

$$g_2(\tau) = 1 + \beta|g_1(\tau)|^2, \tag{5.4}$$

where β is the coherence parameter.

In DCS experiments, the dynamic scattering media frequently utilized consist of scatterers exhibiting either random flow (ballistic) or Brownian (diffusive) motion. To obtain the decorrelation lifetime [286], τ_c, a simpler functional expression is preferred for fitting $g_2(\tau)$. For example, in the case of ballistic motion [12], the functional form can be simplified to:

$$g_2(\tau) \approx 1 + \beta\exp\left(-{\tau^2}/{\tau^2{}_c}\right), \tag{5.5}$$

Similarly, in the case of diffusive motion [12], it can be simplified to:

$$g_2(\tau) \approx 1 + \beta\exp\left(-{\tau}/{\tau_c}\right). \tag{5.6}$$

In our work, we use diffusive motions, and this simplified single-exponential function [12,68,85] has been validated in liquid phantoms with Brownian motion scattering. We derived the SNR of our DCS system as:

$$SNR(\tau) = \langle\bar{g}_2(\tau) - 1\rangle_K / std(\bar{g}_2(\tau))_K, \tag{5.7}$$

where $g_2(\tau)$ is the spatial average for increasing N = 1, 25, 100, 225, 625, 1024, 10000, and 22500 (by removing defect or hot pixels), K denotes the number of repeated measurements, $\langle\overline{g_2}(\tau)\text{-}1\rangle_K$ is the mean value, $\text{std}(g_2(\tau))_K$ is the corresponding standard deviation. And we define the SNR gain as:

$$SNR_{gain(\tau)} = SNR[\bar{g}_2(\tau)]/SNR[g_2^i(\tau)], \tag{5.8}$$

here we use τ = 1 μs.

The system was initially evaluated in a beaker with 1.7% fat milk (Tesco, Glasgow, Scotland) that mimics the properties of biological tissues. The tests were performed at room temperature

(25 ℃), and the room light was turned off during measurements. The optical fibers were immersed in milk, as shown in Figure 5.13(c). The milk was assumed to have $\alpha = 1$, $n = 1.33$, $\mu_a = 0.027$ cm^{-1}, and $\mu_s' = 16$ cm^{-1} [120]. Milk was used for this study because it exhibits scattering properties to living tissues, and its g_2 shape resembles blood flow. Although milk does not demonstrate true Brownian motions, the motions of scattering lipids and proteins in milk can be considered Brownian [120].

Figure 5.12(a-d) presents the processing pipeline for calculating $g_2(\tau)$ and αDb. Raw data were collected from a milk phantom at $\rho = 10$ mm using a homemade GUI in Matlab (MathWorks, Inc.). In Figure 5.12(a), representative frame data captured by the camera is shown, displaying successive frames along the time axis. We use the camera frame rate ($\eta = 9.11$ kfps) to define the measurement window with an integration period, $T_{int} = M/\eta$, where M is the number of camera frames used for calculating $g_2(\tau)$. Considering the size of the PC memory, in our experiments, we recorded data up to 100000 frames, taking 10.98 seconds. Figure 5.12(b) shows a representative photon stream of raw data from a single SPAD over 7.68 seconds. To estimate $g_2(\tau)$, we started from an integration time of 2.2 seconds and increased it to 7.68 seconds until $g_2(\tau)$ converged. Therefore, an integration time of 7.68 seconds (70000 frames) was applied. Hot SPAD pixels (with much higher dark count rates [280]) were excluded from the analysis. We adopted an uneven step length for τ to put higher weights on short delay times, as described in Ref. [120]. With uneven step lengths (e.g., [1, 2, 3, …, 10, 20, 30, …, 100, 200, …, 1000 μs]), calculating $g_2(\tau)$ took a shorter time. In Figure 5.12(c), representative $g_2(\tau)$ curves measured from the milk phantom are displayed for a single pixel and spatially averaged ensemble pixels acquired with $T_{int} = 7.68$ seconds. The results show that $g_2(\tau)$ fluctuates too much with a small N along τ, especially for a single pixel ($N = 1$), but it becomes smooth with $N = 24576$. Figure 5.12(d) shows an error bar plot of milk's flow index (αDb) obtained through the fitting according to Eqs. (3.16) and (5.6). The blue bar represents the mean αDb over 10 measurements, and the error bar represents the corresponding standard deviation of αDb, which is defined as $\sigma(\alpha D_b)$. Increasing the number of pixels reduces the $\sigma(\alpha D_b)$, indicating more reliable fitting results when $N = 22500$. Another interesting effect is that when $N = 1$, the estimated αDb is larger compared to cases where $N > 1$, as shown in Figure 5.12(d), because the noisier signal may be misinterpreted as contributing to the Brownian motion. This phenomenon can be found in Ref. [120]. Also, the estimated αDb is 1.19×10^{-9} cm^2/s, in agreement with the findings in Ref. [120].

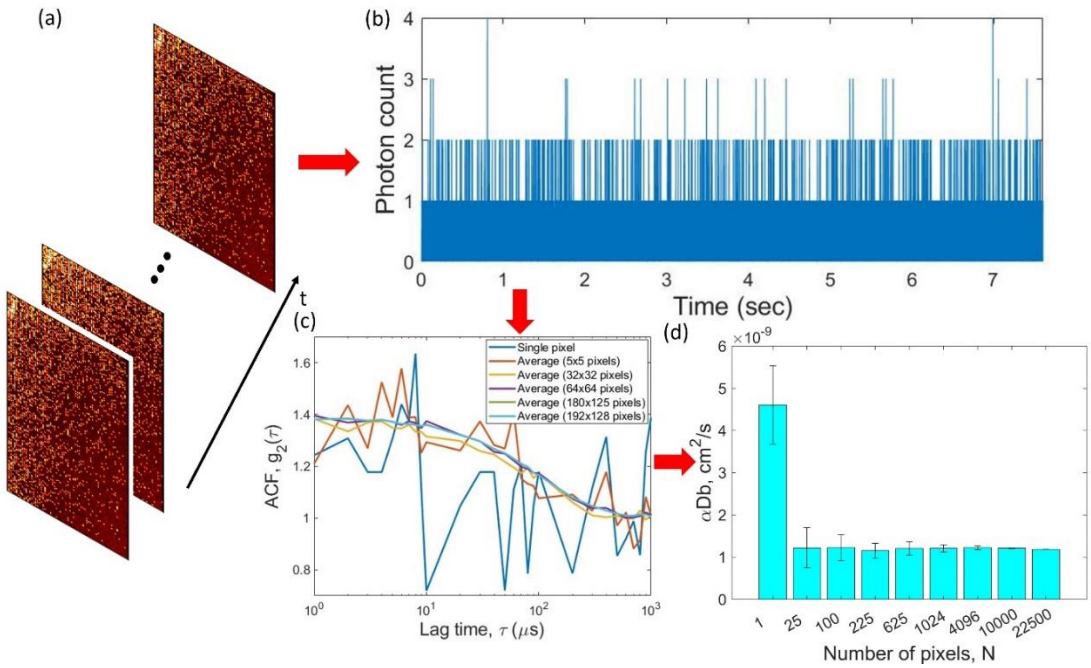

Figure 5.12 The processing pipeline of our system shows a significant SNR improvement by increasing N. (a) Raw data from our SPAD sensor along the time axis. (b) The temporal light intensity fluctuation from one SPAD pixel. (c) Auto-correlation curves for N = 1 (blue), 25, 1024, 4096, 22500, and 24576 pixels. (d) The milk flow index (αDb) obtained by fitting methods as a function of N.

Figure 5.13(c) shows the ensemble-averaged $\bar{g}_2(\tau)$ (N = 24576) (blue line) for the entire sensor, excluding hot and bad pixels. The measured data (blue dots) was calculated by Eqs. (5.2) and (5.3) as shown in Figure 5.13(c), where the "Fitted ACF (solid orange line)" is from the measured data that fits with Eq. (5.2). τ_c = 110.55 μs and β = 0.39 by fitting the measured data to Eq. (5.6), which is a good match with $\beta = g_2(\tau \approx 0) - 1 = 0.39$. When N = 1, the measured SNR of g_2^i for the first correlation bin, SNR($g_2^i(\tau = 1\ \mu s)$) = 1.018. Figure 5.13(a) shows the measured SNR($\bar{g}_2(\tau)$) according to Eq. (5.8) for increasing N up to 22500. Figure 5.13(b) shows the measured SNR gain (red dots) as a function of $\sqrt{N}$, and they agree with the theoretical blue curve. And the SNR gain is enhanced 157-fold from that of a single-pixel DCS system and around 5-fold from that of the previous multispeckle DCS system. A large N gives a higher SNR, which agrees with the expected conclusion that the SNR is proportional to $N_{ph} \times \sqrt{T_{int}} \times \sqrt{N}$, where N_{ph} is the detected photon count rate. Figure 5.13(d) depicts the mean and standard deviation of β in terms of N. Similarly, a converged β is obtained with higher precision when N increases.

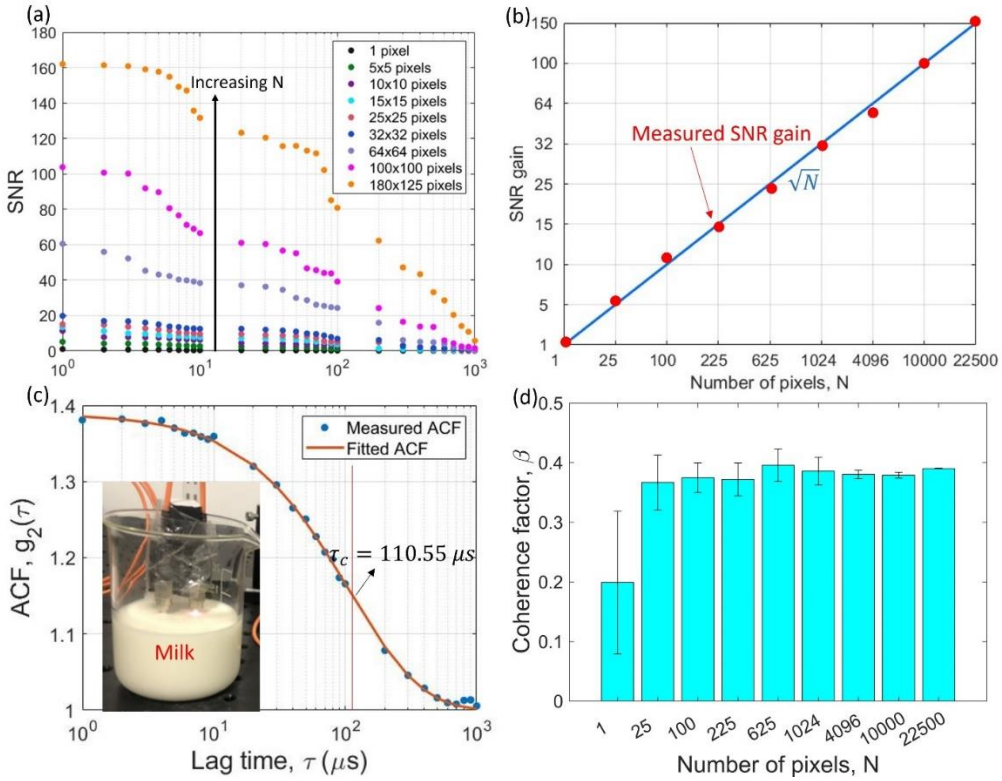

Figure 5.13 (a) SNR of $\bar{g}_2(\tau)$ for N = 1, 25, 100, 225, 625, 1024, 4096, 10000, and 22500. (b) SNR gain of $\bar{g}_2(\tau)$ (τ=1 μs) as a function of N from 1 to 22500. The SNR gain measured over the integration period (red dots) increases as $\sqrt{N}$ (blue line). (c) The measured (blue dot) and fitted ACF (orange line) on the milk phantom. (d) The estimated β.

5.5.4 Milk Phantom Tests

To further validate the system, we adjusted ρ in the milk phantom and documented the results in Figure 5.14. As anticipated, a larger ρ increases the noise in the correlation function. Notably, at ρ = 10 mm, the g_2 curve demonstrates a slower decay, indicating reduced scattering and absorption and primarily superficial sampling of the phantom. Conversely, at ρ = 25 mm, the curve decays more rapidly, reflecting heightened scattering and absorption as light traverses a longer path through the medium.

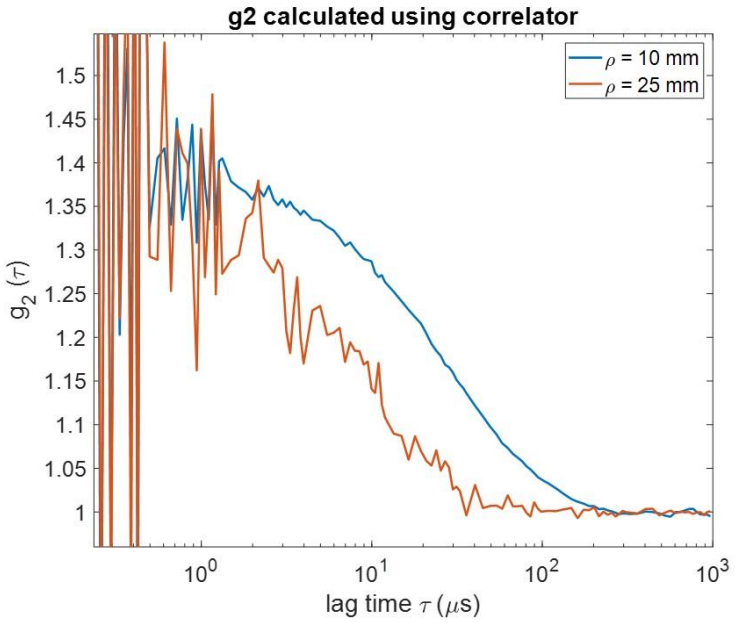

Figure 5.14 Intensity autocorrelation function ($g_2(\tau)$) measurements at ρ = 10 mm (blue line) and ρ = 25 mm (red line) on milk phantom.

For further testing, we used a liquid phantom consisting of a 1:4 volume ratio mixture of milk (3.7% fat) and water, contained in a beaker at room temperature (25 °C). As observed in Figure 5.15, increasing ρ amplifies the noise in the correlation function, aligning with findings from Figure 5.14. In Figure 5.15(a) and (b), it is evident that higher milk concentrations (blue line), which increase the number of scatterers (milk particles), lead to more pronounced scattering and a faster decay of the autocorrelation function. Additionally, greater turbidity from higher concentrations reduces the light's penetration depth, altering the path length distributions of detected photons. In contrast, a lower milk concentration (1:4 ratio) results in reduced light scattering and a slower decay of the autocorrelation function.

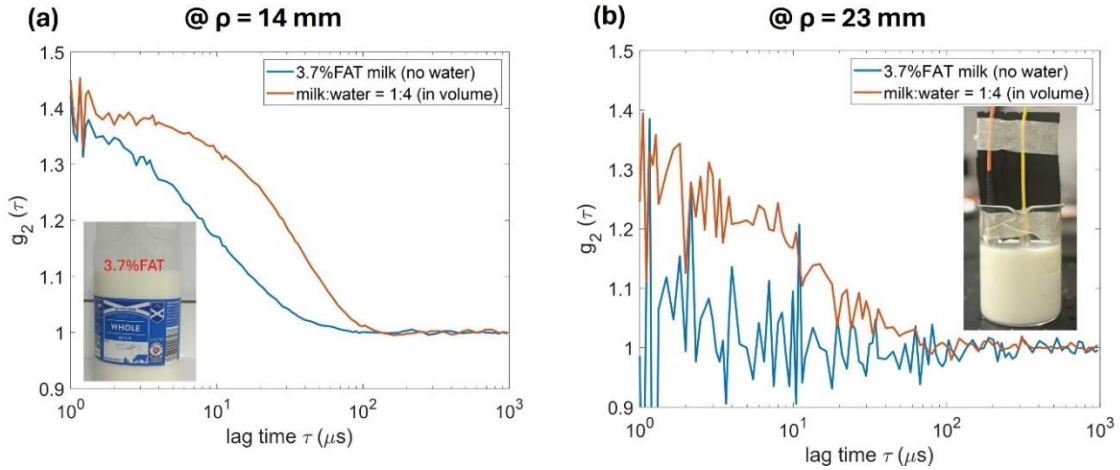

Figure 5.15 Intensity autocorrelation function ($g_2(\tau)$) measurements at ρ = 10 mm (blue line) and ρ = 25 mm (red line) on milk phantom.

5.5.5 *In Vivo* Experiments

Figure 5.16 presents the results from in vivo cuff-occlusion experiments on the upper left arm of a healthy 33-year-old male volunteer. The experiment involved attaching a blood pressure cuff to occlude blood flow to the hand, with DCS measurements taken at three stages: baseline (before cuff application), during occlusion, and immediately post-occlusion. When the pressure cuff is inflated, it restricts blood flow in the arm, and upon deflation, normal blood flow should resume. Like the pump experiments, the DCS probe was positioned on the volunteer's arm as depicted in Figure 5.16(a). For each phase—baseline, occlusion, and post-occlusion—three consecutive DCS measurements were taken, following the protocol used in the pump-flow experiments. The cuff was inflated to 200 mmHg for 1 second to occlude blood flow. The pressure was then released, and DCS measurements were immediately taken post-occlusion. It is anticipated that the blood flow during occlusion will be lower than the baseline measurements, and that post-occlusion flow will exceed the baseline levels, as noted in previous reports [133]. Figure 5.16(b) illustrates that the autocorrelation trace decays more slowly during occlusion (red line) compared to baseline (blue line), while the traces recorded immediately after cuff release (yellow line) decay faster than those at baseline.

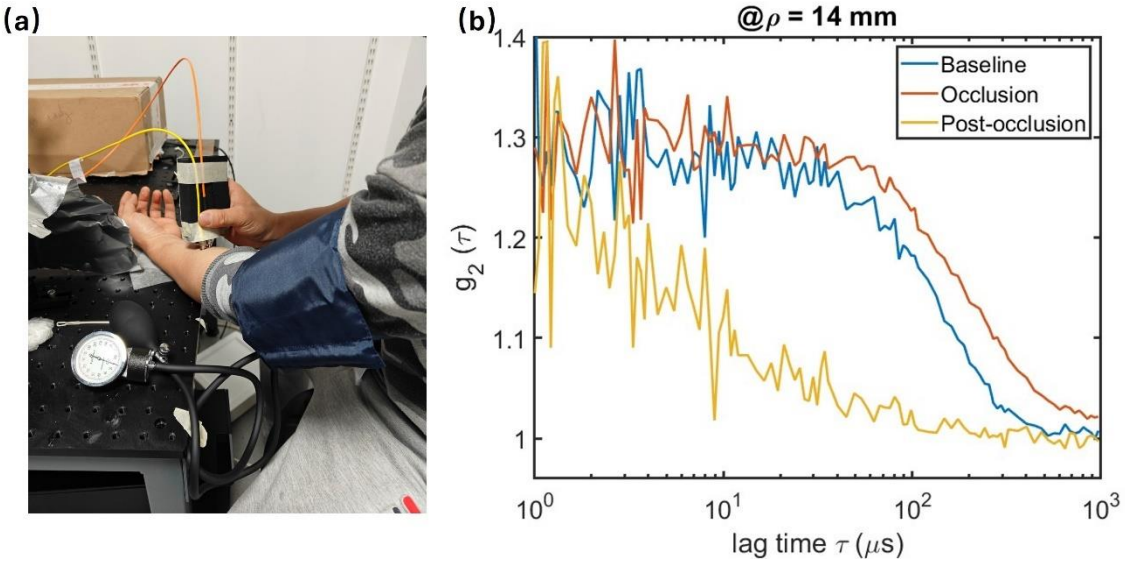

Figure 5.16 Autocorrelation traces in the cuff occlusion experiments (blue line – at baseline; red line – during cuff occlusion; yellow line – immediately post-occlusion) acquired using hardware correlator.

The system was tested *in vivo* on the volar forearm of a volunteer using a blood flow occlusion method with a pressure cuff. Measurements were conducted at approximately 180-second intervals across three phases: 60 seconds of baseline, 60 seconds of occlusion, and 60 seconds

of reperfusion. The optical properties of the forearm were assumed to be μ_a = 0.05 mm^{-1} and μ_s' = 1.8 mm^{-1} for the fittings. The occlusion and reperfusion processes were performed rapidly to prevent the blood volume changes that can occur with prolonged vein occlusion before artery occlusion. As shown in Figure 5.17, there is a significant reduction in Blood rBFi during occlusion, followed by a typical increase during reperfusion.

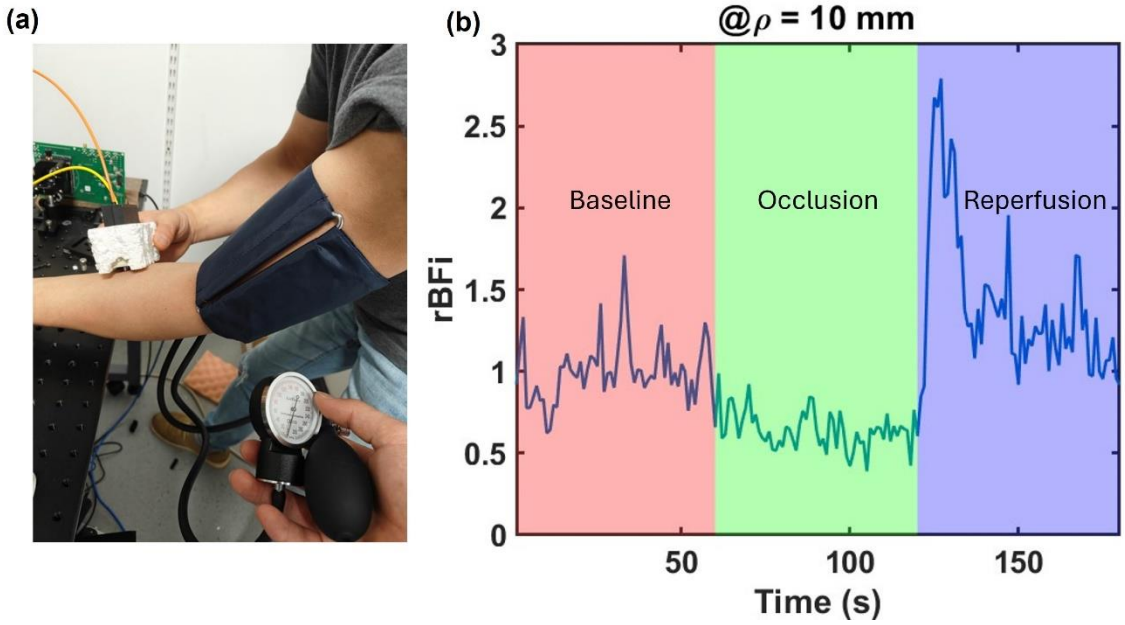

Figure 5.17 BFi measured on the volar forearm during the blood occlusion testing at ρ = 10 mm. After 60 s baseline measurement, the blood flow is occluded with a pressure cuff, and the cuff releases after 60 s and 60 s reperfusion. (a) An example of DCS probe placement on the forearm. (b) rBFi vs time.

In the *in vivo* forehead blood flow measurements, the probe was secured to the forehead as depicted in Figure 5.18(a). Continuous DCS data was recorded for approximately 3 minutes, with each g_2 calculated every second. Figure 5.18(b) shows the representative g_2 (blue line) alongside the fitted g_2 (red line). For these measurements, assumed tissue optical absorption and reduced scattering coefficients were 0.05 and 1.8 mm^{-1}, respectively, used to derive the BFi. Figure 5.18(c) displays the temporal BFi traces over time.

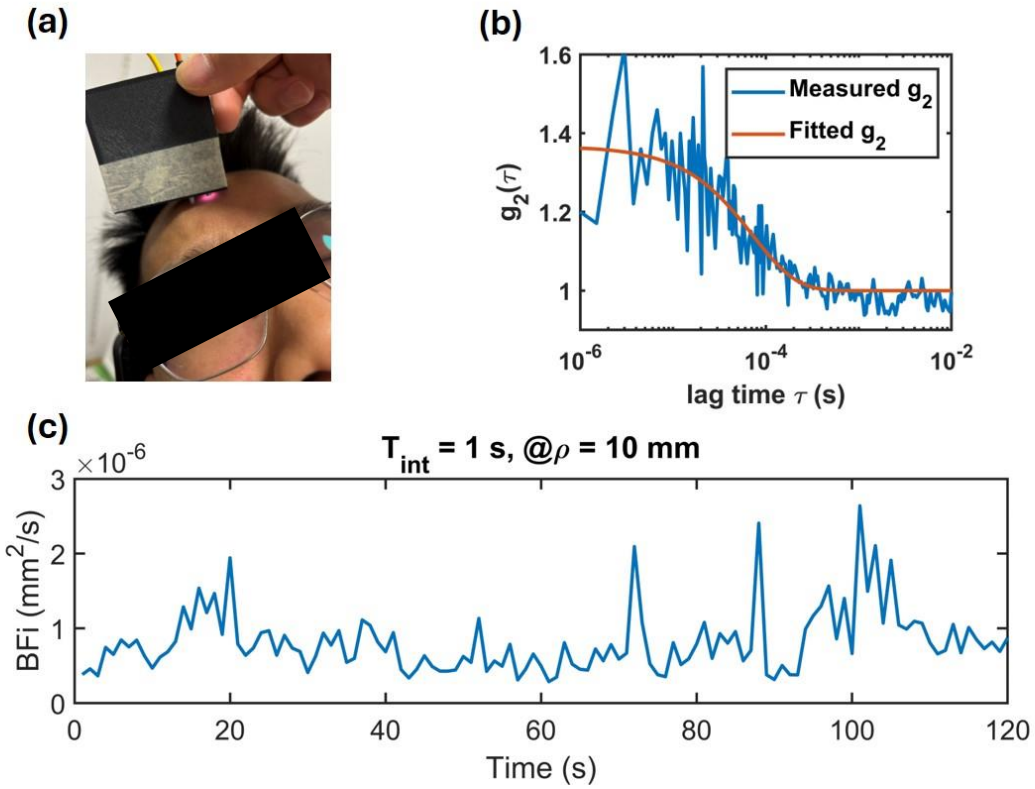

Figure 5.18 (a) An example of DCS probe placement on the forehead. (b) Representative autocorrelation curve (blue) and its best exponential function fit (red). (c) BFi along time axis.

5.6 Summary

This work demonstrated a massively parallel multipixel DCS implementation with a 192×128 SPAD array, a photon-counting camera. When calculating g_2, we adopted the multitau (an uneven step scheme for τ) scheme advised in Ref. [120], significantly reducing the computational load compared with the even delay scheme. Alternatively, we can also adopt the multitau scheme advised in Ref. [133]. The SNR analysis results on the milk phantom show that our system can make rapid and accurate BFi measurements in photon-starved deep tissue scenarios. Figure 5.12(c), (d), and Figure 5.13(a) shows the impact on SNR in g_2 and BFi estimation in terms of the number of pixels. Including more pixels would result in a higher SNR, which is also beneficial for the BFi estimation.

Additionally, our sensor demonstrates a 157-fold improvement in the SNR gain over a single-pixel system and an around 5-fold increase in SNR compared to the previously reported 32 × 32 multipixel DCS system. Moreover, the sensor shows a significant advantage with over 24-fold more pixels than the 32 × 32 SPAD array. This paper's main aim is to demonstrate the high parallelism that a 2D SPAD array can bring to DCS applications. Although there are systems using a few sensor channels showing higher photon detection efficiency (>50%) [166], they are limited to low throughput because of the use of a single channel. Compared with Mattioli della Rocca *et al.*'s earlier results, where only 12288 pixels were used [123], we use nearly the whole imager (except defect pixels) for DCS measurements.

The homemade hardware and firmware were designed to make the camera entirely reconfigurable; we can trade the readout speed for a higher spatial resolution. Transferring correlation data to BFi directly in the FPGA and generating multiple DCS curves simultaneously is also possible. Our sensor also has great potential for time-domain DCS measurements with embedded time-to-digital converters, capable of probing deeper tissues.

In summary, this work primarily demonstrates the application of the QuantiCAM sensor in DCS experiments based on the reflection geometry model. Furthermore, we showed that when the SNR is low, αD_b becomes more significant. Although the measurements here were only performed on the milk phantom, it performed well in SNR. These initial findings will pave the way for deep-tissue blood flow monitors. Although Tint is currently limited to 7.68 seconds,

there is substantial potential for achieving sub-second (ms) performance by optimizing firmware and software soon.

Chapter 6 Conclusions and Future Work

6.1 Thesis Summary

In Chapter 1, I elaborated on the motivation behind measuring CBF and highlight the existing gap in the ability to measure CBF using a continuous, noninvasive, and portable bedside device. Driven by this challenge, I outline the project aims of this thesis and enumerate the research goals intended for investigation.

DCS stands out as the classic optical imaging technique for deep blood flow measurements; however, the SNR performance of conventional DCS is fundamentally constrained due to the utilization of single speckle detection. Considering the capability of DCS for achieving real-time, deep, and spatially localized CBF monitoring, various methods have been explored to enhance the sensitivity of DCS to CBF. These approaches are introduced **in Chapter 2**, and can be categorized into multispeckle detection, interferometric detection, long-wavelength approaches, depth discrimination methods (multi-layered fitting methods), time-of-flight (TOF) resolved detection.

In Chapter 3, I derived theoretical models for semi-infinite, two-, and three-layer geometry for continuous-wave, time-domain, and frequency domain, and we did analytical simulation based on the derivations. Commonly, homogenous semi-infinite analytical model was used in data analysis, which assuming free diffusion as mechanism for speckle decorrelation, gave rather poor agreement with the experimental scenarios, this is because homogeneous fitting procedure is more sensitive to the dynamic properties of the superficial layers. Compared with semi-infinite model, two- and three-layered model allows distinction between changes in superficial layers and brain and layered models can mitigate the discrepancies between one-layer model and realistic. Especially, using the three-layer analytical model has been investigated that it is more accurate. Although, multi-layered models provide a superior fit to measured data and more accurate, they are highly sensitive to measurement noise and much longer BFi estimation time is needed. We summarized the noise model and did simulation consider the realistic scenario.

Chapter 4 presents a deep learning algorithm called DCS-NET that uses a high-efficient 1D CNN architecture for fast DCS analysis. This algorithm achieves state-of-the-art performances,

including high accuracy, a fast BFi estimation speed, and a powerful ability to resolve deeper BFi. This DL algorithm possesses a unique attribute that is conducive to hardware efficiency, making it suitable for edge computing in embedded system. This characteristic pave the way for the creation of portable, cost-effective, and real-time DCS devices. A great challenge for developing more advanced DCS analysis algorithm is the scarcity of extensive, high-quality DCS training datasets. Acquiring such datasets is frequently laborious and challenging. The BFi dynamic range, range of optical properties, and SNR are restricted due to the limited experimental conditions. While DL techniques have exhibits formidable capabilities and experienced rapid development in recent years, their application in DCS is comparatively limited. **Chapter 4** presents a pragmatic solution to tackle this issue by creating a computational framework for generating extensive synthetic DCS training datasets based on semi-infinite analytical model. The key idea is to set a dynamic range for tissue optical properties, source-detection separations to cover a wide range of commonly used parameters about tissues. Also, a wide noise levels are included to cover the realistic scenario. Chapter 4 then demonstrated DCS-NET is around 17,000-fold and 32-fold faster than the traditional three-layer and semi-infinite models in terms of BFi estimation, respectively. Additionally, I demonstrated that relative BFi (rBFi) can be extracted by DCS-NET with a much lower error of 8.35%. By contrast, the semi-infinite and three-layer fitting models result in significant errors in rBFi of 43.67% and 19.66%, respectively.

Chapter 5 presents a prototype of DCS system. In this system, I employed a 192 × 128-pixel array CMOS SPAD sensor (QuantiCAM), as a detector for simultaneous photon detection. This approach achieves an exceptionally high photon counting throughput without encountering a pile-up effect. Additionally, I tested the system on a milk phantom and did quantitative analysis for SNR. This SNR gain with the entire sensor is improved nearly 60-fold compared with a single pixel.

6.2 Future Work

Although the DL algorithm in this thesis have achieved excellent performance and encouraging results, there are still some limitations. Regarding the DCS prototype, there are also have some limitations. This section I will discuss the possible research directions for further improving my study.

- **Training datasets**

In Chapter 4, I show that DCS-NET have unique advantages for DCS analysis. However, in Figure 4.16, we can see the error range (-6% ~ +8%) caused by Δ_1 and Δ_2 is much broader than that (-1% ~ +5%) caused by μ_a and μ_s'. This may because of our training datasets were generated using the semi-infinite diffusion model without considering scalp and skull thicknesses. In the future, I can obtain the training datasets from multi-layered model.

- **Generalization of the model**

As we all know, analytical fitting models suffer from partial volume effects and recover only a fraction of the actual change; hence, they exhibit a more linear relationship with the actual change. However, from Figure 4.11, we observed that the BFi values obtained from DCS-NET reflect different degrees of relative ground truth change based on the corresponding relative change. Therefore, they exhibit a nonlinear correlation with the actual blood flow in the brain. This implies that processing data with our DCS-NET could lead to non-physiological distortions. One possible method to improve the generalization of the model is systematically search for the best hyperparamters, such as learning rate, batch size, or model architecture, to optimize model performance on unsee data.

- **Relative BFi (rBFi) calculations**

In practice applications, our goal is not to acquire absolute measurements of blood flow (BFi). Instead, we frequently focus on the relative variation in blood flow, denoted as rBFi (e.g., rBFi = BFi/BFi_0). The existing rBFi calculations do not account for changes in optical properties between the baseline and activation states. Notably, μ_a and μ_s' in the brain can exhibit variations due to interventions such as functional activation, known to influence perfusion. Neglecting these changes may introduce additional uncertainties in rBFi measurements.

- ***In vivo* experiments using DCS system**

The results shown in Chapter 4 exclusively utilized simulated data. Performance in phantom and in vivo experiments needed to validate the findings. Although the DCS prototype tested in a milk phantom, in vivo experiment is also needed.

Overall, our work has the potential to serve as a valuable resource for both established researchers and newcomers to the field, helping them navigate the evolving landscape of Diffuse Correlation Spectroscopy (DCS). The results from our in vivo experiments have shown that our prototype performs effectively, suggesting that clinical application for measuring hemodynamic processes in the human body could soon be achievable.

Bibliography

1. Zauner, A.; Daugherty, W.P.; Bullock, M.R.; Warner, D.S. Brain Oxygenation and Energy Metabolism: Part I—Biological Function and Pathophysiology. *Neurosurgery* **2002**, *51*, 289.

2. Uludağ, K.; Dubowitz, D.J.; Yoder, E.J.; Restom, K.; Liu, T.T.; Buxton, R.B. Coupling of Cerebral Blood Flow and Oxygen Consumption during Physiological Activation and Deactivation Measured with fMRI. *NeuroImage* **2004**, *23*, 148–155, doi:10.1016/j.neuroimage.2004.05.013.

3. Durduran, T.; Yodh, A.G. Diffuse Correlation Spectroscopy for Non-Invasive, Micro-Vascular Cerebral Blood Flow Measurement. *NeuroImage* **2014**, *85*, 51–63, doi:10.1016/j.neuroimage.2013.06.017.

4. Kaiser, M.G.; During, M.J. Combining Laser Doppler Flowmetry with Microdialysis: A Novel Approach to Investigate the Coupling of Regional Cerebral Blood Flow to Neuronal Activity. *Journal of Neuroscience Methods* **1995**, *60*, 165–173, doi:10.1016/0165-0270(95)00008-I.

5. Devor, A.; Sakadžić, S.; Srinivasan, V.J.; Yaseen, M.A.; Nizar, K.; Saisan, P.A.; Tian, P.; Dale, A.M.; Vinogradov, S.A.; Franceschini, M.A.; et al. Frontiers in Optical Imaging of Cerebral Blood Flow and Metabolism. *J Cereb Blood Flow Metab* **2012**, *32*, 1259–1276, doi:10.1038/jcbfm.2011.195.

6. Cheung, C.; Culver, J.P.; Takahashi, K.; Greenberg, J.H.; Yodh, A.G. *In Vivo* Cerebrovascular Measurement Combining Diffuse near-Infrared Absorption and Correlation Spectroscopies. *Phys. Med. Biol.* **2001**, *46*, 2053–2065, doi:10.1088/0031-9155/46/8/302.

7. Quaresima, V.; Bisconti, S.; Ferrari, M. A Brief Review on the Use of Functional Near-Infrared Spectroscopy (fNIRS) for Language Imaging Studies in Human Newborns and Adults. *Brain and Language* **2012**, *121*, 79–89, doi:10.1016/j.bandl.2011.03.009.

8. Fantini, S.; Sassaroli, A.; Tgavalekos, K.T.; Kornbluth, J. Cerebral Blood Flow and Autoregulation: Current Measurement Techniques and Prospects for Noninvasive Optical Methods. *Neurophotonics* **2016**, *3*, 031411, doi:10.1117/1.NPh.3.3.031411.

9. Rhee, C.J.; Da Costa, C.S.; Austin, T.; Brady, K.M.; Czosnyka, M.; Lee, J.K. Neonatal Cerebrovascular Autoregulation. *Pediatr Res* **2018**, *84*, 602–610, doi:10.1038/s41390-018-0141-6.

10. Tsalach, A.; Schiffer, Z.; Ratner, E.; Breskin, I.; Zeitak, R.; Shechter, R.; Balberg, M. Depth Selective Acousto-Optic Flow Measurement. *Biomed. Opt. Express* **2015**, *6*, 4871, doi:10.1364/BOE.6.004871.

11. Campbell, B.C.; Christensen, S.; Tress, B.M.; Churilov, L.; Desmond, P.M.; Parsons, M.W.; Barber, P.A.; Levi, C.R.; Bladin, C.; Donnan, G.A.; et al. Failure of Collateral Blood Flow Is Associated with Infarct Growth in Ischemic Stroke. *J Cereb Blood Flow Metab* **2013**, *33*, 1168–1172, doi:10.1038/jcbfm.2013.77.

12. Sie, E.J.; Chen, H.; Saung, E.-F.; Catoen, R.; Tiecke, T.; Chevillet, M.A.; Marsili, F. High-Sensitivity Multispeckle Diffuse Correlation Spectroscopy. *Neurophoton.* **2020**, *7*, doi:10.1117/1.NPh.7.3.035010.

13. Cheng, X.; Sie, E.J.; Naufel, S.; Boas, D.A.; Marsili, F. Measuring Neuronal Activity with Diffuse Correlation Spectroscopy: A Theoretical Investigation. *Neurophoton.* **2021**, *8*, doi:10.1117/1.NPh.8.3.035004.

14. Ohuma, E.O.; Moller, A.-B.; Bradley, E.; Chakwera, S.; Hussain-Alkhateeb, L.; Lewin, A.; Okwaraji, Y.B.; Mahanani, W.R.; Johansson, E.W.; Lavin, T.; et al. National, Regional, and Global Estimates of Preterm Birth in 2020, with Trends from 2010: A Systematic Analysis. *The Lancet* **2023**, *402*, 1261–1271, doi:10.1016/S0140-6736(23)00878-4.

15. Kiechl-Kohlendorfer, U.; Ralser, E.; Peglow, U.P.; Reiter, G.; Trawöger, R. Adverse Neurodevelopmental Outcome in Preterm Infants: Risk Factor Profiles for Different Gestational Ages. *Acta Paediatrica* **2009**, *98*, 792–796, doi:10.1111/j.1651-2227.2009.01219.x.

16. Buckley, E.M.; Lynch, J.M.; Goff, D.A.; Schwab, P.J.; Baker, W.B.; Durduran, T.; Busch, D.R.; Nicolson, S.C.; Montenegro, L.M.; Naim, M.Y.; et al. Early Postoperative Changes in Cerebral Oxygen Metabolism Following Neonatal Cardiac Surgery: Effects of Surgical Duration. *J Thorac Cardiovasc Surg* **2013**, *145*, 196–203, 205.e1; discussion 203-205, doi:10.1016/j.jtcvs.2012.09.057.

17. Shaw, K.; Mavroudis, C.D.; Ko, T.S.; Jahnavi, J.; Jacobwitz, M.; Ranieri, N.; Forti, R.M.; Melchior, R.W.; Baker, W.B.; Yodh, A.G.; et al. The Use of Novel Diffuse Optical Spectroscopies for Improved Neuromonitoring during Neonatal Cardiac Surgery Requiring Antegrade Cerebral Perfusion. *Front Pediatr* **2023**, *11*, 1125985, doi:10.3389/fped.2023.1125985.

18. Gressens, P.; Rogido, M.; Paindaveine, B.; Sola, A. The Impact of Neonatal Intensive Care Practices on the Developing Brain. *The Journal of Pediatrics* **2002**, *140*, 646–653, doi:10.1067/mpd.2002.123214.

19. Lee, S.Y.; Brothers, R.O.; Turrentine, K.B.; Quadri, A.; Sathialingam, E.; Cowdrick, K.R.; Gillespie, S.; Bai, S.; Goldman-Yassen, A.E.; Joiner, C.H.; et al. Quantifying the Cerebral Hemometabolic Response to Blood Transfusion in Pediatric Sickle Cell Disease With Diffuse Optical Spectroscopies. *Front. Neurol.* **2022**, *13*, 869117, doi:10.3389/fneur.2022.869117.

20. Lafontant, A.; Mahanna Gabrielli, E.; Bergonzi, K.; Forti, R.M.; Ko, T.S.; Shah, R.M.; Arkles, J.S.; Licht, D.J.; Yodh, A.G.; Kofke, W.A.; et al. Comparison of Optical Measurements of Critical Closing Pressure Acquired before and during Induced Ventricular Arrhythmia in Adults. *Neurophoton.* **2022**, *9*, doi:10.1117/1.NPh.9.3.035004.

21. Hargreaves, M.; Spriet, L.L. Skeletal Muscle Energy Metabolism during Exercise. *Nat Metab* **2020**, *2*, 817–828, doi:10.1038/s42255-020-0251-4.

22. Choe, R.; Durduran, T. Diffuse Optical Monitoring of the Neoadjuvant Breast Cancer Therapy. *IEEE J. Select. Topics Quantum Electron.* **2012**, *18*, 1367–1386, doi:10.1109/JSTQE.2011.2177963.

23. Yu, G.; Durduran, T.; Zhou, C.; Zhu, T.C.; Finlay, J.C.; Busch, T.M.; Malkowicz, S.B.; Hahn, S.M.; Yodh, A.G. Real-Time in Situ Monitoring of Human Prostate Photodynamic Therapy with Diffuse Light. *Photochem Photobiol* **2006**, *82*, 1279–1284, doi:10.1562/2005-10-19-RA-721.

24. Sunar, U.; Quon, H.; Durduran, T.; Zhang, J.; Du, J.; Zhou, C.; Yu, G.; Choe, R.; Kilger, A.; Lustig, R.; et al. Noninvasive Diffuse Optical Measurement of Blood Flow and Blood Oxygenation for Monitoring Radiation Therapy in Patients with Head and Neck Tumors: A Pilot Study. *J. Biomed. Opt.* **2006**, *11*, 064021, doi:10.1117/1.2397548.

25. DeSantis, C.E.; Bray, F.; Ferlay, J.; Lortet-Tieulent, J.; Anderson, B.O.; Jemal, A. International Variation in Female Breast Cancer Incidence and Mortality Rates. *Cancer Epidemiology, Biomarkers & Prevention* **2015**, *24*, 1495–1506, doi:10.1158/1055-9965.EPI-15-0535.

26. Durduran, T.; Choe, R.; Yu, G.; Zhou, C.; Tchou, J.C.; Czerniecki, B.J.; Yodh, A.G. Diffuse Optical Measurement of Blood Flow in Breast Tumors. *Opt. Lett.* **2005**, *30*, 2915, doi:10.1364/OL.30.002915.

27. Zhou, C.; Choe, R.; Shah, N.; Durduran, T.; Yu, G.; Durkin, A.; Hsiang, D.; Mehta, R.; Butler, J.; Cerussi, A.; et al. Diffuse Optical Monitoring of Blood Flow and Oxygenation in Human Breast Cancer during Early Stages of Neoadjuvant Chemotherapy. *J. Biomed. Opt.* **2007**, *12*, 051903, doi:10.1117/1.2798595.

28. Vaquero, J.J.; Kinahan, P. Positron Emission Tomography: Current Challenges and Opportunities for Technological Advances in Clinical and Preclinical Imaging Systems. *Annu. Rev. Biomed. Eng.* **2015**, *17*, 385–414, doi:10.1146/annurev-bioeng-071114-040723.

29. Ljungberg, M.; Pretorius, P.H. SPECT/CT: An Update on Technological Developments and Clinical Applications. *BJR* **2018**, *91*, 20160402, doi:10.1259/bjr.20160402.

30. Yonas, H.; Pindzola, R.R.; Johnson, D.W. Xenon/Computed Tomography Cerebral Blood Flow and Its Use in Clinical Management. *Neurosurgery Clinics of North America* **1996**, *7*, 605–616, doi:10.1016/S1042-3680(18)30349-8.

31. Kwong, K.K.; Belliveau, J.W.; Chesler, D.A.; Goldberg, I.E.; Weisskoff, R.M.; Poncelet, B.P.; Kennedy, D.N.; Hoppel, B.E.; Cohen, M.S.; Turner, R. Dynamic Magnetic Resonance Imaging of Human Brain Activity during Primary Sensory Stimulation. *Proc. Natl. Acad. Sci. U.S.A.* **1992**, *89*, 5675–5679, doi:10.1073/pnas.89.12.5675.

32. Yu, G.; Floyd, T.F.; Durduran, T.; Zhou, C.; Wang, J.; Detre, J.A.; Yodh, A.G. Validation of Diffuse Correlation Spectroscopy for Muscle Blood Flow with Concurrent Arterial Spin Labeled Perfusion MRI. **2007**, 12.

33. Shepherd, A.P.; Öberg, P.Å. *Laser-Doppler Blood Flowmetry*; Springer Science & Business Media, 2013; ISBN 978-1-4757-2083-9.

34. Wintermark, M.; Sesay, M.; Barbier, E.; Borbély, K.; Dillon, W.P.; Eastwood, J.D.; Glenn, T.C.; Grandin, C.B.; Pedraza, S.; Soustiel, J.-F.; et al. Comparative Overview of Brain Perfusion Imaging Techniques. *Stroke* **2005**, *36*, doi:10.1161/01.STR.0000177884.72657.8b.

35. Boas, D.A.; Yodh, A.G. Spatially Varying Dynamical Properties of Turbid Media Probed with Diffusing Temporal Light Correlation. *J. Opt. Soc. Am. A* **1997**, *14*, 192, doi:10.1364/JOSAA.14.000192.

36. Wang, D.; Parthasarathy, A.B.; Baker, W.B.; Gannon, K.; Kavuri, V.; Ko, T.; Schenkel, S.; Li, Z.; Li, Z.; Mullen, M.T.; et al. Fast Blood Flow Monitoring in Deep Tissues with Real-Time Software Correlators. *Biomed. Opt. Express* **2016**, *7*, 776, doi:10.1364/BOE.7.000776.

37. Zhou, W.; Kholiqov, O.; Zhu, J.; Zhao, M.; Zimmermann, L.L.; Martin, R.M.; Lyeth, B.G.; Srinivasan, V.J. Functional Interferometric Diffusing Wave Spectroscopy of the Human Brain. *Sci. Adv.* **2021**, *7*, eabe0150, doi:10.1126/sciadv.abe0150.

38. Poon, C.-S.; Long, F.; Sunar, U. Deep Learning Model for Ultrafast Quantification of Blood Flow in Diffuse Correlation Spectroscopy. *Biomed. Opt. Express* **2020**, *11*, 5557, doi:10.1364/BOE.402508.

39. Murali, K.; Varma, H.M. Multi-Speckle Diffuse Correlation Spectroscopy to Measure Cerebral Blood Flow. *Biomed. Opt. Express* **2020**, *11*, 6699, doi:10.1364/BOE.401702.

40. Liu, W.; Qian, R.; Xu, S.; Chandra Konda, P.; Jönsson, J.; Harfouche, M.; Borycki, D.; Cooke, C.; Berrocal, E.; Dai, Q.; et al. Fast and Sensitive Diffuse Correlation Spectroscopy with Highly Parallelized Single Photon Detection. *APL Photonics* **2021**, *6*, 026106, doi:10.1063/5.0031225.

41. Sutin, J.; Zimmerman, B.; Tyulmankov, D.; Tamborini, D.; Wu, K.C.; Selb, J.; Gulinatti, A.; Rech, I.; Tosi, A.; Boas, D.A.; et al. Time-Domain Diffuse Correlation Spectroscopy. *Optica* **2016**, *3*, 1006, doi:10.1364/OPTICA.3.001006.

42. Samaei, S.; Sawosz, P.; Kacprzak, M.; Pastuszak, Ż.; Borycki, D.; Liebert, A. Time-Domain Diffuse Correlation Spectroscopy (TD-DCS) for Noninvasive, Depth-Dependent Blood Flow Quantification in Human Tissue in Vivo. *Sci Rep* **2021**, *11*, 1817, doi:10.1038/s41598-021-81448-5.

43. Zhou, W.; Zhao, M.; Kholiqov, O.; Srinivasan, V.J. Multi-Exposure Interferometric Diffusing Wave Spectroscopy. *Opt. Lett.* **2021**, *46*, 4498, doi:10.1364/OL.427746.

44. Zhou, W.; Kholiqov, O.; Chong, S.P.; Srinivasan, V.J. Highly Parallel, Interferometric Diffusing Wave Spectroscopy for Monitoring Cerebral Blood Flow Dynamics. *Optica* **2018**, *5*, 518, doi:10.1364/OPTICA.5.000518.

45. Robinson, M.B.; Boas, D.A.; Sakadzic, S.; Franceschini, M.A.; Carp, S.A. Interferometric Diffuse Correlation Spectroscopy Improves Measurements at Long Source–Detector Separation and Low Photon Count Rate. *J. Biomed. Opt.* **2020**, *25*, doi:10.1117/1.JBO.25.9.097004.

46. Zhao, H.; Buckley, E.M. Influence of Source–Detector Separation on Diffuse Correlation Spectroscopy Measurements of Cerebral Blood Flow with a Multilayered Analytical Model. *Neurophoton.* **2022**, *9*, doi:10.1117/1.NPh.9.3.035002.

47. Zhao, H.; Sathialingam, E.; Buckley, E.M. Accuracy of Diffuse Correlation Spectroscopy Measurements of Cerebral Blood Flow When Using a Three-Layer Analytical Model. *Biomed. Opt. Express* **2021**, *12*, 7149, doi:10.1364/BOE.438303.

48. Carp, S.A.; Tamborini, D.; Mazumder, D.; Wu, K.-C. (Tony); Robinson, M.R.; Stephens, K.A.; Shatrovoy, O.; Lue, N.; Ozana, N.; Blackwell, M.H.; et al. Diffuse Correlation Spectroscopy Measurements of Blood Flow Using 1064 Nm Light. *J. Biomed. Opt.* **2020**, *25*, doi:10.1117/1.JBO.25.9.097003.

49. *D. A. Boas, C. Pitris, and N. Ramanujam, Eds., Handbook of Biomedical Optics. Boca Raton, FL : CRC Press, C2011., 2011, Isbn: 1420090372*;

50. Martin, G.T.; Bowman, H.F. Validation of Real-Time Continuous Perfusion Measurement. *Med. Biol. Eng. Comput.* **2000**, *38*, 319–325, doi:10.1007/BF02347053.

51. *Textbook of Neurointensive Care*; Layon, A.J., Gabrielli, A., Friedman, W.A., Eds.; Springer London: London, 2013; ISBN 978-1-4471-5225-5.

52. Durduran, T.; Choe, R.; Baker, W.B.; Yodh, A.G. Diffuse Optics for Tissue Monitoring and Tomography. *Rep. Prog. Phys.* **2010**, *73*, 076701, doi:10.1088/0034-4885/73/7/076701.

53. Kety, S.S.; Schmidt, C.F. THE DETERMINATION OF CEREBRAL BLOOD FLOW IN MAN BY THE USE OF NITROUS OXIDE IN LOW CONCENTRATIONS. *American Journal of Physiology-Legacy Content* **1945**, *143*, 53–66, doi:10.1152/ajplegacy.1945.143.1.53.

54. Wietasch, G.J.K.; Mielck, F.; Scholz, M.; Von Spiegel, T.; Stephan, H.; Hoeft, A. Bedside Assessment of Cerebral Blood Flow by Double-Indicator Dilution Technique. *Anesthesiology* **2000**, *92*, 367–367, doi:10.1097/00000542-200002000-00017.

55. Buxton, R.B. The Physics of Functional Magnetic Resonance Imaging (fMRI). *Rep. Prog. Phys.* **2013**, *76*, 096601, doi:10.1088/0034-4885/76/9/096601.

56. Schmid, W.; Fan, Y.; Chi, T.; Golanov, E.; Regnier-Golanov, A.S.; Austerman, R.J.; Podell, K.; Cherukuri, P.; Bentley, T.; Steele, C.T.; et al. Review of Wearable Technologies and Machine Learning Methodologies for Systematic Detection of Mild Traumatic Brain Injuries. *J. Neural Eng.* **2021**, *18*, 041006, doi:10.1088/1741-2552/ac1982.

57. Buckley, E.M.; Parthasarathy, A.B.; Grant, P.E.; Yodh, A.G.; Franceschini, M.A. Diffuse Correlation Spectroscopy for Measurement of Cerebral Blood Flow: Future Prospects. *Neurophoton* **2014**, *1*, 011009, doi:10.1117/1.NPh.1.1.011009.

58. Aaslid, R.; Markwalder, T.-M.; Nornes, H. Noninvasive Transcranial Doppler Ultrasound Recording of Flow Velocity in Basal Cerebral Arteries. *Journal of Neurosurgery* **1982**, *57*, 769–774, doi:10.3171/jns.1982.57.6.0769.

59. Yun, S.H.; Kwok, S.J.J. Light in Diagnosis, Therapy and Surgery. *Nat Biomed Eng* **2017**, *1*, 0008, doi:10.1038/s41551-016-0008.

60. Postnov, D.D.; Tuchin, V.V.; Sosnovtseva, O. Estimation of Vessel Diameter and Blood Flow Dynamics from Laser Speckle Images. *Biomed. Opt. Express* **2016**, *7*, 2759, doi:10.1364/BOE.7.002759.

61. Boas, D.A.; Dunn, A.K. Laser Speckle Contrast Imaging in Biomedical Optics. *J. Biomed. Opt.* **2010**, *15*, 011109, doi:10.1117/1.3285504.

62. Parthasarathy, A.B.; Tom, W.J.; Gopal, A.; Zhang, X.; Dunn, A.K. Robust Flow Measurement with Multi-Exposure Speckle Imaging. *Opt. Express* **2008**, *16*, 1975, doi:10.1364/OE.16.001975.

63. Lee, K. Diffuse Speckle Contrast Analysis (DSCA) for Deep Tissue Blood Flow Monitoring. *ABE* **2020**, *9*, 21–30, doi:10.14326/abe.9.21.

64. Pine, D.J.; Weitz, D.A.; Zhu, J.X.; Herbolzheimer, E. Diffusing-Wave Spectroscopy: Dynamic Light Scattering in the Multiple Scattering Limit. *J. Phys. France* **1990**, *51*, 2101–2127, doi:10.1051/jphys:0199000510180210100.

65. Maret, G.; Wolf, P.E. Multiple Light Scattering from Disordered Media. The Effect of Brownian Motion of Scatterers. *Z. Physik B - Condensed Matter* **1987**, *65*, 409–413, doi:10.1007/BF01303762.

66. Boas, D.A.; Campbell, L.E.; Yodh, A.G. Scattering and Imaging with Diffusing Temporal Field Correlations. *Phys. Rev. Lett.* **1995**, *75*, 1855–1858, doi:10.1103/PhysRevLett.75.1855.

67. Boas, D.A.; Meglinski, I.V.; Zemany, L.; Campbell, L.E.; Chance, B.; Yodh, A.G. Diffusion of Temporal Field Correlation with Selected Applications.; Tuchin, V.V., Ed.; Saratov, Russia, February 9 1996; pp. 34–46.

68. Boas, D.A.; Sakadžic, S.; Selb, J.; Farzam, P.; Franceschini, M.A.; Carp, S.A. Establishing the Diffuse Correlation Spectroscopy Signal Relationship with Blood Flow. *Neurophoton* **2016**, *3*, 031412, doi:10.1117/1.NPh.3.3.031412.

69. Yu, G.; Durduran, T.; Lech, G.; Zhou, C.; Chance, B.; Mohler, E.R.; Yodh, A.G. Time-Dependent Blood Flow and Oxygenation in Human Skeletal Muscles Measured with Noninvasive near-Infrared Diffuse Optical Spectroscopies. *J. Biomed. Opt.* **2005**, *10*, 024027, doi:10.1117/1.1884603.

70. Belau, M.; Ninck, M.; Hering, G.; Spinelli, L.; Contini, D.; Torricelli, A.; Gisler, T. Noninvasive Observation of Skeletal Muscle Contraction Using Near-Infrared Time-Resolved Reflectance and Diffusing-Wave Spectroscopy. *J. Biomed. Opt.* **2010**, *15*, 057007, doi:10.1117/1.3503398.

71. Shang, Y.; Symons, T.B.; Durduran, T.; Yodh, A.G.; Yu, G. Effects of Muscle Fiber Motion on Diffuse Correlation Spectroscopy Blood Flow Measurements during Exercise. *Biomed. Opt. Express* **2010**, *1*, 500, doi:10.1364/BOE.1.000500.

72. Yu, G.; Shang, Y.; Zhao, Y.; Cheng, R.; Dong, L.; Saha, S.P. Intraoperative Evaluation of Revascularization Effect on Ischemic Muscle Hemodynamics Using Near-Infrared Diffuse Optical Spectroscopies. *J. Biomed. Opt.* **2011**, *16*, 027004, doi:10.1117/1.3533320.

73. Munk, N.; Symons, B.; Shang, Y.; Cheng, R.; Yu, G. Noninvasively Measuring the Hemodynamic Effects of Massage on Skeletal Muscle: A Novel Hybrid near-Infrared Diffuse Optical Instrument. *Journal of Bodywork and Movement Therapies* **2012**, *16*, 22–28, doi:10.1016/j.jbmt.2011.01.018.

74. Guoqiang Yu, K.G. Diffuse Correlation Spectroscopy (DCS) for Assessment of Tissue Blood Flow in Skeletal Muscle: Recent Progress. *Anat Physiol* **2013**, *03*, doi:10.4172/2161-0940.1000128.

75. Quaresima, V.; Farzam, P.; Anderson, P.; Farzam, P.Y.; Wiese, D.; Carp, S.A.; Ferrari, M.; Franceschini, M.A. Diffuse Correlation Spectroscopy and Frequency-Domain near-Infrared Spectroscopy for Measuring Microvascular Blood Flow in Dynamically Exercising Human Muscles. *Journal of Applied Physiology* **2019**, *127*, 1328–1337, doi:10.1152/japplphysiol.00324.2019.

76. Yazdi, H.S.; O'Sullivan, T.D.; Leproux, A.; Hill, B.; Durkin, A.; Telep, S.; Lam, J.; Yazdi, S.S.; Police, A.M.; Carroll, R.M.; et al. Mapping Breast Cancer Blood Flow Index, Composition, and Metabolism in a Human Subject Using Combined Diffuse Optical Spectroscopic Imaging and Diffuse Correlation Spectroscopy. *J. Biomed. Opt* **2017**, *22*, 045003, doi:10.1117/1.JBO.22.4.045003.

77. Grosenick, D.; Rinneberg, H.; Cubeddu, R.; Taroni, P. Review of Optical Breast Imaging and Spectroscopy. *J. Biomed. Opt* **2016**, *21*, 091311, doi:10.1117/1.JBO.21.9.091311.

78. He, L.; Lin, Y.; Huang, C.; Irwin, D.; Szabunio, M.M.; Yu, G. Noncontact Diffuse Correlation Tomography of Human Breast Tumor. *J. Biomed. Opt* **2015**, *20*, 086003, doi:10.1117/1.JBO.20.8.086003.

79. Choe, R.; Putt, M.E.; Carlile, P.M.; Durduran, T.; Giammarco, J.M.; Busch, D.R.; Jung, K.W.; Czerniecki, B.J.; Tchou, J.; Feldman, M.D.; et al. Optically Measured Microvascular Blood Flow Contrast of Malignant Breast Tumors. *PLoS ONE* **2014**, *9*, e99683, doi:10.1371/journal.pone.0099683.

80. Chung, S.H.; Feldman, M.D.; Martinez, D.; Kim, H.; Putt, M.E.; Busch, D.R.; Tchou, J.; Czerniecki, B.J.; Schnall, M.D.; Rosen, M.A.; et al. Macroscopic Optical Physiological Parameters Correlate with Microscopic Proliferation and Vessel Area Breast Cancer Signatures. *Breast Cancer Res* **2015**, *17*, 72, doi:10.1186/s13058-015-0578-z.

81. Durduran, T.; Zhou, C.; Edlow, B.L.; Yu, G.; Choe, R.; Kim, M.N.; Cucchiara, B.L.; Putt, M.E.; Shah, Q.; Kasner, S.E.; et al. Transcranial Optical Monitoring of Cerebrovascular Hemodynamics in Acute Stroke Patients. *Opt. Express* **2009**, *17*, 3884, doi:10.1364/OE.17.003884.

82. Culver, J.P.; Durduran, T.; Furuya, D.; Cheung, C.; Greenberg, J.H.; Yodh, A.G. Diffuse Optical Tomography of Cerebral Blood Flow, Oxygenation, and Metabolism in Rat during Focal Ischemia. *J Cereb Blood Flow Metab* **2003**, *23*, 911–924, doi:10.1097/01.WCB.0000076703.71231.BB.

83. Durduran, T.; Yu, G.; Burnett, M.G.; Detre, J.A.; Greenberg, J.H.; Wang, J.; Zhou, C.; Yodh, A.G. Diffuse Optical Measurement of Blood Flow, Blood Oxygenation, and Metabolism in a Human Brain during Sensorimotor Cortex Activation. *Opt. Lett.* **2004**, *29*, 1766, doi:10.1364/OL.29.001766.

84. Li, J.; Dietsche, G.; Iftime, D.; Skipetrov, S.E.; Maret, G.; Elbert, T.; Rockstroh, B.; Gisler, T. Noninvasive Detection of Functional Brain Activity with Near-Infrared Diffusing-Wave Spectroscopy. *J. Biomed. Opt.* **2005**, *10*, 044002, doi:10.1117/1.2007987.

85. Zhou, C.; Yu, G.; Furuya, D.; Greenberg, J.H.; Yodh, A.G.; Durduran, T. Diffuse Optical Correlation Tomography of Cerebral Blood Flow during Cortical Spreading Depression in Rat Brain. *Opt. Express* **2006**, *14*, 1125, doi:10.1364/OE.14.001125.

86. Li, J.; Ninck, M.; Koban, L.; Elbert, T.; Kissler, J.; Gisler, T. Transient Functional Blood Flow Change in the Human Brain Measured Noninvasively by Diffusing-Wave Spectroscopy. *Opt. Lett.* **2008**, *33*, 2233, doi:10.1364/OL.33.002233.

87. Buckley, E.M.; Cook, N.M.; Durduran, T.; Kim, M.N.; Zhou, C.; Choe, R.; Yu, G.; Schultz, S.; Sehgal, C.M.; Licht, D.J.; et al. Cerebral Hemodynamics in Preterm Infants during Positional Intervention Measured with Diffuse Correlation Spectroscopy and Transcranial Doppler Ultrasound. *Opt. Express* **2009**, *17*, 12571, doi:10.1364/OE.17.012571.

88. Kim, M.N.; Durduran, T.; Frangos, S.; Edlow, B.L.; Buckley, E.M.; Moss, H.E.; Zhou, C.; Yu, G.; Choe, R.; Maloney-Wilensky, E.; et al. Noninvasive Measurement of Cerebral Blood Flow and Blood Oxygenation Using Near-Infrared and Diffuse Correlation Spectroscopies in Critically Brain-Injured Adults. *Neurocrit Care* **2010**, *12*, 173–180, doi:10.1007/s12028-009-9305-x.

89. Kreiss, L.; Wu, M.; Wayne, M.; Xu, S.; McKee, P.; Dwamena, D.; Kim, K.; Lee, K.C.; Liu, W.; Ulku, A.; et al. Beneath the Surface: Revealing Deep-Tissue Blood Flow in Human Subjects with Massively Parallelized Diffuse Correlation Spectroscopy 2024.

90. Sunwoo, J.; Zavriyev, A.I.; Kaya, K.; Martin, A.; Munster, C.; Steele, T.; Cuddyer, D.; Sheldon, Y.; Orihuela-Espina, F.; Herzberg, E.M.; et al. Diffuse Correlation Spectroscopy Blood Flow Monitoring for Intraventricular Hemorrhage Vulnerability in Extremely Low Gestational Age Newborns. *Sci Rep* **2022**, *12*, 12798, doi:10.1038/s41598-022-16499-3.

91. Tamborini, D.; Stephens, K.A.; Wu, M.M.; Farzam, P.; Siegel, A.M.; Shatrovoy, O.; Blackwell, M.; Boas, D.A.; Carp, S.A.; Franceschini, M.A. Portable System for Time-Domain Diffuse Correlation Spectroscopy. *IEEE Trans. Biomed. Eng.* **2019**, *66*, 3014–3025, doi:10.1109/TBME.2019.2899762.

92. Moka, S.; Safi, A.M.; Mohammad, P.P.S.; Eddins, A.; Parthasarathy, A.B. Frequency Domain Diffuse Correlation Spectroscopy: A New Method for Simultaneous Estimation of Static and Dynamic Tissue Optical Properties. In Proceedings of the Multiscale Imaging and Spectroscopy III; Maitland, K.C., Roblyer, D.M., Campagnola, P.J., Eds.; SPIE: San Francisco, United States, March 4 2022; p. 20.

93. Zavriyev, A.I.; Kaya, K.; Farzam, P.; Farzam, P.Y.; Sunwoo, J.; Jassar, A.S.; Sundt, T.M.; Carp, S.A.; Franceschini, M.A.; Qu, J.Z. The Role of Diffuse Correlation Spectroscopy and Frequency-Domain near-Infrared Spectroscopy in Monitoring Cerebral Hemodynamics during Hypothermic Circulatory Arrests. *JTCVS Techniques* **2021**, *7*, 161–177, doi:10.1016/j.xjtc.2021.01.023.

94. Bigio, I.J.; Fantini, S. *Quantitative Biomedical Optics: Theory, Methods, and Applications*; Cambridge University Press, 2016; ISBN 978-1-316-46238-6.

95. Bellini, T.; Glaser, M.A.; Clark, N.A.; Degiorgio, V. Effects of Finite Laser Coherence in Quasielastic Multiple Scattering. *Phys. Rev. A* **1991**, *44*, 5215–5223, doi:10.1103/PhysRevA.44.5215.

96. Biswas, A.; Moka, S.; Muller, A.; Parthasarathy, A.B. Fast Diffuse Correlation Spectroscopy with a Low-Cost, Fiber-Less Embedded Diode Laser. *Biomed. Opt. Express* **2021**, *12*, 6686, doi:10.1364/BOE.435136.

97. Delpy, D.T.; Cope, M.; Zee, P.V.D.; Arridge, S.; Wray, S.; Wyatt, J. Estimation of Optical Pathlength through Tissue from Direct Time of Flight Measurement. *Phys. Med. Biol.* **1988**, *33*, 1433–1442, doi:10.1088/0031-9155/33/12/008.

98. A. N. S Institute, American National Standard for Safe Use of Lasers (Laser Institute of America, 2007).

99. Lee, S.Y.; Cowdrick, K.R.; Sanders, B.; Sathialingam, E.; McCracken, C.E.; Lam, W.A.; Joiner, C.H.; Buckley, E.M. Noninvasive Optical Assessment of Resting-State Cerebral Blood Flow in Children with Sickle Cell Disease. **2019**, *6*.

100. Wu, K.C.; Martin, A.; Renna, M.; Robinson, M.; Ozana, N.; Carp, S.A.; Franceschini, M.A. Enhancing Diffuse Correlation Spectroscopy Pulsatile Cerebral Blood Flow Signal with Near-Infrared Spectroscopy Photoplethysmography. *Neurophoton.* **2023**, *10*, doi:10.1117/1.NPh.10.3.035008.

101. Samaei, S.; Colombo, L.; Borycki, D.; Pagliazzi, M.; Durduran, T.; Sawosz, P.; Wojtkiewicz, S.; Contini, D.; Torricelli, A.; Pifferi, A.; et al. Performance Assessment of Laser Sources for Time-Domain Diffuse Correlation Spectroscopy. *Biomed. Opt. Express* **2021**, *12*, 5351, doi:10.1364/BOE.432363.

102. Huang, C.; Seong, M.; Morgan, J.P.; Mazdeyasna, S.; Kim, J.G.; Hastings, J.T.; Yu, G. Low-Cost Compact Diffuse Speckle Contrast Flowmeter Using Small Laser Diode and Bare Charge-Coupled-Device. *J. Biomed. Opt* **2016**, *21*, 080501, doi:10.1117/1.JBO.21.8.080501.

103. O'Connor, D. *Time-Correlated Single Photon Counting*; Academic Press, 2012; ISBN 978-0-323-14144-4.

104. Ozana, N.; Lue, N.; Renna, M.; Robinson, M.B.; Martin, A.; Zavriyev, A.I.; Carr, B.; Mazumder, D.; Blackwell, M.H.; Franceschini, M.A.; et al. Functional Time Domain Diffuse Correlation Spectroscopy. *Front. Neurosci.* **2022**, *16*, 932119, doi:10.3389/fnins.2022.932119.

105. Shang, Y.; Chen, L.; Toborek, M.; Yu, G. Diffuse Optical Monitoring of Repeated Cerebral Ischemia in Mice. *Opt. Express* **2011**, *19*, 20301, doi:10.1364/OE.19.020301.

106. Lin, Y.; He, L.; Shang, Y.; Yu, G. Noncontact Diffuse Correlation Spectroscopy for Noninvasive Deep Tissue Blood Flow Measurement. *J. Biomed. Opt.* **2012**, *17*, 010502, doi:10.1117/1.JBO.17.1.010502.

107. Cheng, R.; Shang, Y.; Hayes, D.; Saha, S.P.; Yu, G. Noninvasive Optical Evaluation of Spontaneous Low Frequency Oscillations in Cerebral Hemodynamics. *NeuroImage* **2012**, *62*, 1445–1454, doi:10.1016/j.neuroimage.2012.05.069.

108. Han, S.; Hoffman, M.D.; Proctor, A.R.; Vella, J.B.; Mannoh, E.A.; Barber, N.E.; Kim, H.J.; Jung, K.W.; Benoit, D.S.W.; Choe, R. Non-Invasive Monitoring of Temporal and Spatial Blood Flow during Bone Graft Healing Using Diffuse Correlation Spectroscopy. *PLoS ONE* **2015**, *10*, e0143891, doi:10.1371/journal.pone.0143891.

109. Stapels, C.J.; Kolodziejski, N.J.; McAdams, D.; Podolsky, M.J.; Fernandez, D.E.; Farkas, D.; Christian, J.F. A Scalable Correlator for Multichannel Diffuse Correlation Spectroscopy.; Vo-Dinh, T., Mahadevan-Jansen, A., Grundfest, W.S., Eds.; San Francisco, California, United States, March 7 2016; p. 969816.

110. Farzam, P.; Johansson, J.; Mireles, M.; Jiménez-Valerio, G.; Martínez-Lozano, M.; Choe, R.; Casanovas, O.; Durduran, T. Pre-Clinical Longitudinal Monitoring of Hemodynamic Response to Anti-Vascular Chemotherapy by Hybrid Diffuse Optics. *Biomed. Opt. Express* **2017**, *8*, 2563, doi:10.1364/BOE.8.002563.

111. Sathialingam, E.; Lee, S.Y.; Sanders, B.; Park, J.; McCracken, C.E.; Bryan, L.; Buckley, E.M. Small Separation Diffuse Correlation Spectroscopy for Measurement of Cerebral Blood Flow in Rodents. *Biomed. Opt. Express* **2018**, *9*, 5719, doi:10.1364/BOE.9.005719.

112. Cortese, L.; Lo Presti, G.; Pagliazzi, M.; Contini, D.; Dalla Mora, A.; Dehghani, H.; Ferri, F.; Fischer, J.B.; Giovannella, M.; Martelli, F.; et al. Recipes for Diffuse Correlation Spectroscopy Instrument Design Using Commonly Utilized Hardware Based on Targets for

Signal-to-Noise Ratio and Precision. *Biomed. Opt. Express* **2021**, *12*, 3265, doi:10.1364/BOE.423071.

113. Wayne, M.A.; Sie, E.J.; Ulku, A.C.; Mos, P.; Ardelean, A.; Marsili, F.; Bruschini, C.; Charbon, E. Massively Parallel, Real-Time Multispeckle Diffuse Correlation Spectroscopy Using a 500 × 500 SPAD Camera. *Biomed. Opt. Express* **2023**, *14*, 703, doi:10.1364/BOE.473992.

114. Samaei, S.; Nowacka, K.; Gerega, A.; Pastuszak, Ż.; Borycki, D. Continuous-Wave Parallel Interferometric near-Infrared Spectroscopy (CW πNIRS) with a Fast Two-Dimensional Camera. *Biomed. Opt. Express* **2022**, *13*, 5753, doi:10.1364/BOE.472643.

115. Zhou, C. IN-VIVO OPTICAL IMAGING AND SPECTROSCOPY OF CEREBRAL HEMODYNAMICS.

116. He, L.; Lin, Y.; Shang, Y.; Shelton, B.J.; Yu, G. Using Optical Fibers with Different Modes to Improve the Signal-to-Noise Ratio of Diffuse Correlation Spectroscopy Flow-Oximeter Measurements. *J. Biomed. Opt* **2013**, *18*, 037001, doi:10.1117/1.JBO.18.3.037001.

117. Irwin, D.; Dong, L.; Shang, Y.; Cheng, R.; Kudrimoti, M.; Stevens, S.D.; Yu, G. Influences of Tissue Absorption and Scattering on Diffuse Correlation Spectroscopy Blood Flow Measurements. *Biomed. Opt. Express* **2011**, *2*, 1969, doi:10.1364/BOE.2.001969.

118. Lawrence, W.G.; Varadi, G.; Entine, G.; Podniesinski, E.; Wallace, P.K. A Comparison of Avalanche Photodiode and Photomultiplier Tube Detectors for Flow Cytometry.; Farkas, D.L., Nicolau, D.V., Leif, R.C., Eds.; San Jose, CA, February 7 2008; p. 68590M.

119. Dietsche, G.; Ninck, M.; Ortolf, C.; Li, J.; Jaillon, F.; Gisler, T. Fiber-Based Multispeckle Detection for Time-Resolved Diffusing-Wave Spectroscopy: Characterization and Application to Blood Flow Detection in Deep Tissue. *Appl. Opt.* **2007**, *46*, 8506, doi:10.1364/AO.46.008506.

120. Johansson, J.D.; Portaluppi, D.; Mauro Buttafava; Federica Villa A Multipixel Diffuse Correlation Spectroscopy System Based on a Single Photon Avalanche Diode Array. *J. Biophotonics* **2019**, *12*, doi:10.1002/jbio.201900091.

121. Xu, S.; Liu, W.; Yang, X.; Jönsson, J.; Qian, R.; McKee, P.; Kim, K.; Konda, P.C.; Zhou, K.C.; Kreiß, L.; et al. Transient Motion Classification Through Turbid Volumes via Parallelized Single-Photon Detection and Deep Contrastive Embedding. *Front. Neurosci.* **2022**, *16*, 908770, doi:10.3389/fnins.2022.908770.

122. Xu, S.; Yang, X.; Liu, W.; Jönsson, J.; Qian, R.; Konda, P.C.; Zhou, K.C.; Kreiß, L.; Wang, H.; Dai, Q.; et al. Imaging Dynamics Beneath Turbid Media via Parallelized Single-Photon Detection. *Advanced Science* **2022**, *9*, 2201885, doi:10.1002/advs.202201885.

123. Della Rocca, F.M.; Sie, E.J.; Catoen, R.; Marsili, F.; Henderson, R.K. Field Programmable Gate Array Compression for Large Array Multispeckle Diffuse Correlation Spectroscopy. *J. Biomed. Opt.* **2023**, *28*, doi:10.1117/1.JBO.28.5.057001.

124. Liu, X.; Mohtasebi, M.; Safavi, P.; Fathi, F.; Rabienia, S.; Chen, L.; Chen, J.; Bada, H.S.; Chen, L.; Jawdeh, G.A.; et al. A Wearable Fiber-Free Optical Sensor for Continuous Monitoring of Neonatal Cerebral Blood Flow and Oxygenation.

125. Parfentyeva, V.; Colombo, L.; Lanka, P.; Pagliazzi, M.; Brodu, A.; Noordzij, N.; Kolarczik, M.; Dalla Mora, A.; Re, R.; Contini, D.; et al. Fast Time-Domain Diffuse Correlation Spectroscopy with Superconducting Nanowire Single-Photon Detector: System Validation and in Vivo Results. *Sci Rep* **2023**, *13*, 11982, doi:10.1038/s41598-023-39281-5.

126. Schuck, C.; Pernice, W.H.P.; Minaeva, O.; Mo Li; Gol'tsman, G.; Sergienko, A.V.; Tang, H.X. Matrix of Integrated Superconducting Single-Photon Detectors With High Timing Resolution. *IEEE Trans. Appl. Supercond.* **2013**, *23*, 2201007–2201007, doi:10.1109/TASC.2013.2239346.

127. Robinson, M.B.; Renna, M.; Ozana, N.; Martin, A.N.; Otic, N.; Carp, S.A.; Franceschini, M.A. Portable, High Speed Blood Flow Measurements Enabled by Long Wavelength, Interferometric Diffuse Correlation Spectroscopy (LW-iDCS). *Sci Rep* **2023**, *13*, 8803, doi:10.1038/s41598-023-36074-8.

128. Schätzel, K.; Drewel, M.; Stimac, S. Photon Correlation Measurements at Large Lag Times: Improving Statistical Accuracy. *Journal of Modern Optics* **1988**, *35*, 711–718, doi:10.1080/09500348814550731.

129. Schatzel, K. Noise on Photon Correlation Data. I. Autocorrelation Functions. *Quantum Opt.* **1990**, *2*, 287–305, doi:10.1088/0954-8998/2/4/002.

130. Schätzel, K. Correlation Techniques in Dynamic Light Scattering. *Appl. Phys. B* **1987**, *42*, 193–213, doi:10.1007/BF00693937.

131. Magatti, D.; Ferri, F. Fast Multi-Tau Real-Time Software Correlator for Dynamic Light Scattering. *Appl. Opt.* **2001**, *40*, 4011, doi:10.1364/AO.40.004011.

132. Magatti, D.; Ferri, F. 25 Ns Software Correlator for Photon and Fluorescence Correlation Spectroscopy. *Review of Scientific Instruments* **2003**, *74*, 1135–1144, doi:10.1063/1.1525876.

133. Dong, J.; Bi, R.; Ho, J.H.; Thong, P.S.P.; Soo, K.-C.; Lee, K. Diffuse Correlation Spectroscopy with a Fast Fourier Transform-Based Software Autocorrelator. *J. Biomed. Opt* **2012**, *17*, 0970041, doi:10.1117/1.JBO.17.9.097004.

134. Https://Lsinstruments.Ch/En/Products/Lsi-Correlator.

135. Https://Www.Becker-Hickl.Com/Applications/Dcs-Diffuse-Correlation/.

136. Https://Www.Alvgmbh.de/Products/Correlators/Discontinued_Models_/ALV-5000_EPP/Alv-5000_epp.Html.

137. Yodh, A.G.; Kaplan, P.D.; Pine, D.J. Pulsed Diffusing-Wave Spectroscopy: High Resolution through Nonlinear Optical Gating. *Phys. Rev. B* **1990**, *42*, 4744–4747, doi:10.1103/PhysRevB.42.4744.

138. Martelli, F.; Binzoni, T.; Pifferi, A.; Spinelli, L.; Farina, A.; Torricelli, A. There's Plenty of Light at the Bottom: Statistics of Photon Penetration Depth in Random Media. *Sci Rep* **2016**, *6*, 27057, doi:10.1038/srep27057.

139. Pagliazzi, M.; Sekar, S.K.V.; Colombo, L.; Martinenghi, E.; Minnema, J.; Erdmann, R.; Contini, D.; Mora, A.D.; Torricelli, A.; Pifferi, A.; et al. Time Domain Diffuse Correlation Spectroscopy with a High Coherence Pulsed Source: In Vivo and Phantom Results. *Biomed. Opt. Express* **2017**, *8*, 5311, doi:10.1364/BOE.8.005311.

140. Colombo, L.; Pagliazzi, M.; Sekar, S.K.V.; Contini, D.; Mora, A.D.; Spinelli, L.; Torricelli, A.; Durduran, T.; Pifferi, A. Effects of the Instrument Response Function and the Gate Width in Time-Domain Diffuse Correlation Spectroscopy: Model and Validations. *Neurophoton.* **2019**, *6*, 1, doi:10.1117/1.NPh.6.3.035001.

141. Colombo, L.; Samaei, S.; Lanka, P.; Ancora, D.; Pagliazzi, M.; Durduran, T.; Sawosz, P.; Liebert, A.; Pifferi, A. Coherent Fluctuations in Time-Domain Diffuse Optics. *APL Photonics* **2020**, *5*, 071301, doi:10.1063/5.0011838.

142. Cowdrick, K.R.; Urner, T.; Sathialingam, E.; Fang, Z.; Quadri, A.; Turrentine, K.; Lee, S.Y.; Buckley, E.M. Agreement in Cerebrovascular Reactivity Assessed with Diffuse Correlation Spectroscopy across Experimental Paradigms Improves with Short Separation Regression. *NPh* **2023**, *10*, 025002, doi:10.1117/1.NPh.10.2.025002.

143. Von Lühmann, A.; Ortega-Martinez, A.; Boas, D.A.; Yücel, M.A. Using the General Linear Model to Improve Performance in fNIRS Single Trial Analysis and Classification: A Perspective. *Front. Hum. Neurosci.* **2020**, *14*, 30, doi:10.3389/fnhum.2020.00030.

144. Cheng, X.; Tamborini, D.; Carp, S.A.; Shatrovoy, O.; Zimmerman, B.; Tyulmankov, D.; Siegel, A.; Blackwell, M.; Franceschini, M.A.; Boas, D.A. Time Domain Diffuse Correlation Spectroscopy: Modeling the Effects of Laser Coherence Length and Instrument Response Function. *Opt. Lett.* **2018**, *43*, 2756, doi:10.1364/OL.43.002756.

145. Pagliazzi, M.; Sekar, S.K.V.; Di Sieno, L.; Colombo, L.; Durduran, T.; Contini, D.; Torricelli, A.; Pifferi, A.; Mora, A.D. In Vivo Time-Gated Diffuse Correlation Spectroscopy at Quasi-Null Source-Detector Separation. *Opt. Lett.* **2018**, *43*, 2450, doi:10.1364/OL.43.002450.

146. Colombo, L.; Pagliazzi, M.; Konugolu Venkata Sekar, S.; Contini, D.; Durduran, T.; Pifferi, A. In Vivo Time-Domain Diffuse Correlation Spectroscopy above the Water Absorption Peak. *Opt. Lett.* **2020**, *45*, 3377, doi:10.1364/OL.392355.

147. Gagnon, L.; Desjardins, M.; Jehanne-Lacasse, J.; Bherer, L.; Lesage, F. Investigation of Diffuse Correlation Spectroscopy in Multi-Layered Media Including the Human Head. *Opt. Express* **2008**, *16*, 15514, doi:10.1364/OE.16.015514.

148. Verdecchia, K.; Diop, M.; Lee, A.; Morrison, L.B.; Lee, T.-Y.; St. Lawrence, K. Assessment of a Multi-Layered Diffuse Correlation Spectroscopy Method for Monitoring Cerebral Blood Flow in Adults. *Biomed. Opt. Express* **2016**, *7*, 3659, doi:10.1364/BOE.7.003659.

149. Zhao, H.; Sathialingam, E.; Cowdrick, K.R.; Urner, T.; Lee, S.Y.; Bai, S.; Akbik, F.; Samuels, O.B.; Kandiah, P.; Sadan, O.; et al. Comparison of Diffuse Correlation Spectroscopy Analytical Models for Measuring Cerebral Blood Flow in Adults. *J. Biomed. Opt.* **2023**, *28*, doi:10.1117/1.JBO.28.12.126005.

150. Baker, W.B.; Parthasarathy, A.B.; Busch, D.R.; Mesquita, R.C.; Greenberg, J.H.; Yodh, A.G. Modified Beer-Lambert Law for Blood Flow. *Biomed. Opt. Express* **2014**, *5*, 4053, doi:10.1364/BOE.5.004053.

151. Kholiqov, O.; Zhou, W.; Zhang, T.; Du Le, V.N.; Srinivasan, V.J. Time-of-Flight Resolved Light Field Fluctuations Reveal Deep Human Tissue Physiology. *Nat Commun* **2020**, *11*, 391, doi:10.1038/s41467-019-14228-5.

152. Mazumder, D.; Wu, M.M.; Ozana, N.; Tamborini, D.; Franceschini, M.A.; Carp, S.A. Optimization of Time Domain Diffuse Correlation Spectroscopy Parameters for Measuring Brain Blood Flow. *Neurophoton.* **2021**, *8*, doi:10.1117/1.NPh.8.3.035005.

153. Shang, Y.; Yu, G. A *N* Th-Order Linear Algorithm for Extracting Diffuse Correlation Spectroscopy Blood Flow Indices in Heterogeneous Tissues. *Appl. Phys. Lett.* **2014**, *105*, 133702, doi:10.1063/1.4896992.

154. Shang, Y.; Li, T.; Chen, L.; Lin, Y.; Toborek, M.; Yu, G. Extraction of Diffuse Correlation Spectroscopy Flow Index by Integration of *N* Th-Order Linear Model with Monte Carlo Simulation. *Appl. Phys. Lett.* **2014**, *104*, 193703, doi:10.1063/1.4876216.

155. Zhang, P.; Gui, Z.; Guo, G.; Shang, Y. Approaches to Denoise the Diffuse Optical Signals for Tissue Blood Flow Measurement. *Biomed. Opt. Express* **2018**, *9*, 6170, doi:10.1364/BOE.9.006170.

156. Vapnik, V.N. An Overview of Statistical Learning Theory. *IEEE Trans. Neural Netw.* **1999**, *10*, 988–999, doi:10.1109/72.788640.

157. Dechter, R. Learning While Searching in Constraint-Satisfaction-Problems. In Proceedings of the Proceedings of the Fifth AAAI National Conference on Artificial Intelligence; AAAI Press: Philadelphia, Pennsylvania, August 11 1986; pp. 178–183.

158. Ma, W.; Liu, Z.; Kudyshev, Z.A.; Boltasseva, A.; Cai, W.; Liu, Y. Deep Learning for the Design of Photonic Structures. *Nat. Photonics* **2021**, *15*, 77–90, doi:10.1038/s41566-020-0685-y.

159. Mater, A.C.; Coote, M.L. Deep Learning in Chemistry. *J. Chem. Inf. Model.* **2019**, *59*, 2545–2559, doi:10.1021/acs.jcim.9b00266.

160. Ching, T.; Himmelstein, D.S.; Beaulieu-Jones, B.K.; Kalinin, A.A.; Do, B.T.; Way, G.P.; Ferrero, E.; Agapow, P.-M.; Zietz, M.; Hoffman, M.M.; et al. Opportunities and Obstacles for Deep Learning in Biology and Medicine. *J. R. Soc. Interface.* **2018**, *15*, 20170387, doi:10.1098/rsif.2017.0387.

161. Zhang, Y.; Chen, J.; Tan, J.H.; Chen, Y.; Chen, Y.; Li, D.; Yang, L.; Su, J.; Huang, X.; Che, W. An Investigation of Deep Learning Models for EEG-Based Emotion Recognition. *Front. Neurosci.* **2020**, *14*, 622759, doi:10.3389/fnins.2020.622759.

162. Liu, X.; Wang, H.; Li, Z.; Qin, L. Deep Learning in ECG Diagnosis: A Review. *Knowledge-Based Systems* **2021**, *227*, 107187, doi:10.1016/j.knosys.2021.107187.

163. Zhang, P.; Gui, Z.; Hao, L.; Zhang, X.; Liu, C.; Shang, Y. Signal Processing for Diffuse Correlation Spectroscopy with Recurrent Neural Network of Deep Learning. In Proceedings of the 2019 IEEE Fifth International Conference on Big Data Computing Service and Applications (BigDataService); IEEE: Newark, CA, USA, April 2019; pp. 328–332.

164. Li, Z.; Ge, Q.; Feng, J.; Jia, K.; Zhao, J. Quantification of Blood Flow Index in Diffuse Correlation Spectroscopy Using Long Short-Term Memory Architecture. *Biomed. Opt. Express* **2021**, *12*, 4131, doi:10.1364/BOE.423777.

165. Feng, J.; Jiang, M.; Bai, J.; Jia, K.; Li, Z. Cerebral Blood Flow Monitoring Using a ConvGRU Model Based on Diffuse Correlation Spectroscopy. *Infrared Physics & Technology* **2023**, *129*, 104541, doi:10.1016/j.infrared.2022.104541.

166. Tamborini, D.; Farzam, P.; Zimmermann, B.; Wu, K.-C.; Boas, D.A.; Franceschini, M.A. Development and Characterization of a Multidistance and Multiwavelength Diffuse Correlation Spectroscopy System. *Neurophoton* **2017**, *5*, 1, doi:10.1117/1.NPh.5.1.011015.

167. Xu, J.; Jahromi, A.K.; Brake, J.; Robinson, J.E.; Yang, C. Interferometric Speckle Visibility Spectroscopy (ISVS) for Human Cerebral Blood Flow Monitoring. *APL Photonics* **2020**, *5*, 126102, doi:10.1063/5.0021988.

168. Diop, M.; Tichauer, K.M.; Elliott, J.T.; Migueis, M.; Lee, T.-Y.; Lawrence, K.S. Comparison of Time-Resolved and Continuous-Wave near-Infrared Techniques for Measuring Cerebral Blood Flow in Piglets. *JBO* **2010**, *15*, 057004, doi:10.1117/1.3488626.

169. Diop, M.; Verdecchia, K.; Lee, T.-Y.; St Lawrence, K. Calibration of Diffuse Correlation Spectroscopy with a Time-Resolved near-Infrared Technique to Yield Absolute Cerebral Blood Flow Measurements. *Biomed. Opt. Express* **2011**, *2*, 2068, doi:10.1364/BOE.2.002068.

170. Shang, Y.; Li, T.; Yu, G. Clinical Applications of Near-Infrared Diffuse Correlation Spectroscopy and Tomography for Tissue Blood Flow Monitoring and Imaging. *Physiol. Meas.* **2017**, *38*, R1–R26, doi:10.1088/1361-6579/aa60b7.

171. Roy, C.S.; Sherrington, C.S. On the Regulation of the Blood-Supply of the Brain. *J Physiol* **1890**, *11*, 85-158.17.

172. Lou, H.C.; Edvinsson, L.; MacKenzie, E.T. The Concept of Coupling Blood Flow to Brain Function: Revision Required? *Annals of Neurology* **1987**, *22*, 289–297, doi:10.1002/ana.410220302.

173. Dirnagl, U.; Niwa, K.; Lindauer, U.; Villringer, A. Coupling of Cerebral Blood Flow to Neuronal Activation: Role of Adenosine and Nitric Oxide. *American Journal of Physiology-Heart and Circulatory Physiology* **1994**, *267*, H296–H301, doi:10.1152/ajpheart.1994.267.1.H296.

174. Malonek, D.; Grinvald, A. Interactions Between Electrical Activity and Cortical Microcirculation Revealed by Imaging Spectroscopy: Implications for Functional Brain Mapping. *Science* **1996**, *272*, 551–554, doi:10.1126/science.272.5261.551.

175. Carp, S.A.; Robinson, M.B.; Franceschini, M.A. Diffuse Correlation Spectroscopy: Current Status and Future Outlook. *Neurophoton.* **2023**, *10*, doi:10.1117/1.NPh.10.1.013509.

176. Cipelletti, L.; Weitz, D.A. Ultralow-Angle Dynamic Light Scattering with a Charge Coupled Device Camera Based Multispeckle, Multitau Correlator. *Review of Scientific Instruments* **1999**, *70*, 3214–3221, doi:10.1063/1.1149894.

177. Marrero, A.; Becker, T.; Sunar, U.; Morgan, J.; Bellnier, D. Aminolevulinic Acid-Photodynamic Therapy Combined with Topically Applied Vascular Disrupting Agent Vadimezan Led to Enhanced Antitumor Responses. *Photochem Photobiol* **2011**, *87*, 910–919, doi:10.1111/j.1751-1097.2011.00943.x.

178. Yu, G.; Durduran, T.; Zhou, C.; Wang, H.-W.; Putt, M.E.; Saunders, H.M.; Sehgal, C.M.; Glatstein, E.; Yodh, A.G.; Busch, T.M. Noninvasive Monitoring of Murine Tumor Blood Flow

During and After Photodynamic Therapy Provides Early Assessment of Therapeutic Efficacy. *Clinical Cancer Research* **2005**, *11*, 3543–3552, doi:10.1158/1078-0432.CCR-04-2582.

179. Busch, T.M.; Xing, X.; Yu, G.; Yodh, A.; Wileyto, E.P.; Wang, H.-W.; Durduran, T.; Zhu, T.C.; Wang, K.K.-H. Fluence Rate-Dependent Intratumor Heterogeneity in Physiologic and Cytotoxic Responses to Photofrin Photodynamic Therapy. *Photochem Photobiol Sci* **2009**, *8*, 1683–1693, doi:10.1039/b9pp00004f.

180. Sunar, U.; Makonnen, S.; Zhou, C.; Durduran, T.; Yu, G.; Wang, H.-W.; Lee, W.M.F.; Yodh, A.G. Hemodynamic Responses to Antivascular Therapy and Ionizing Radiation Assessed by Diffuse Optical Spectroscopies. *Opt. Express, OE* **2007**, *15*, 15507–15516, doi:10.1364/OE.15.015507.

181. Carp, S.A.; Dai, G.P.; Boas, D.A.; Franceschini, M.A.; Kim, Y.R. Validation of Diffuse Correlation Spectroscopy Measurements of Rodent Cerebral Blood Flow with Simultaneous Arterial Spin Labeling MRI; towards MRI-Optical Continuous Cerebral Metabolic Monitoring. *Biomed. Opt. Express, BOE* **2010**, *1*, 553–565, doi:10.1364/BOE.1.000553.

182. Menon, C.; Polin, G.M.; Prabakaran, I.; Hsi, A.; Cheung, C.; Culver, J.P.; Pingpank, J.F.; Sehgal, C.S.; Yodh, A.G.; Buerk, D.G.; et al. An Integrated Approach to Measuring Tumor Oxygen Status Using Human Melanoma Xenografts as a Model. *Cancer Res* **2003**, *63*, 7232–7240.

183. Quantifying the Cerebral Metabolic Rate of Oxygen by Combining Diffuse Correlation Spectroscopy and Time-Resolved near-Infrared Spectroscopy Available online: https://www.spiedigitallibrary.org/journals/journal-of-biomedical-optics/volume-18/issue-02/027007/Quantifying-the-cerebral-metabolic-rate-of-oxygen-by-combining-diffuse/10.1117/1.JBO.18.2.027007.full#_=_ (accessed on 14 May 2024).

184. Mesquita, R.C.; D'Souza, A.; Bilfinger, T.V.; Galler, R.M.; Emanuel, A.; Schenkel, S.S.; Yodh, A.G.; Floyd, T.F. Optical Monitoring and Detection of Spinal Cord Ischemia. *PLoS One* **2013**, *8*, e83370, doi:10.1371/journal.pone.0083370.

185. Franceschini, M.A.; Radhakrishnan, H.; Thakur, K.; Wu, W.; Ruvinskaya, S.; Carp, S.; Boas, D.A. The Effect of Different Anesthetics on Neurovascular Coupling. *NeuroImage* **2010**, *51*, 1367–1377, doi:10.1016/j.neuroimage.2010.03.060.

186. Zhou, C.; Eucker, S.A.; Durduran, T.; Yu, G.; Ralston, J.; Friess, S.H.; Ichord, R.N.; Margulies, S.S.; Yodh, A.G. Diffuse Optical Monitoring of Hemodynamic Changes in Piglet Brain with Closed Head Injury. *J. Biomed. Opt.* **2009**, *14*, 034015, doi:10.1117/1.3146814.

187. Ruesch, A.; Yang, J.; Schmitt, S.; Acharya, D.; Smith, M.A.; Kainerstorfer, J.M. Estimating Intracranial Pressure Using Pulsatile Cerebral Blood Flow Measured with Diffuse

Correlation Spectroscopy. *Biomed Opt Express* **2020**, *11*, 1462–1476, doi:10.1364/BOE.386612.

188. Han, S.; Proctor, A.R.; Vella, J.B.; Benoit, D.S.W.; Choe, R. Non-Invasive Diffuse Correlation Tomography Reveals Spatial and Temporal Blood Flow Differences in Murine Bone Grafting Approaches. *Biomed Opt Express* **2016**, *7*, 3262–3279, doi:10.1364/BOE.7.003262.

189. Roche-Labarbe, N.; Carp, S.A.; Surova, A.; Patel, M.; Boas, D.A.; Grant, P.E.; Franceschini, M.A. Noninvasive Optical Measures of CBV, StO2, CBF Index, and rCMRO2 in Human Premature Neonates' Brains in the First Six Weeks of Life. *Hum. Brain Mapp.* **2010**, *31*, 341–352, doi:10.1002/hbm.20868.

190. Rajaram, A.; Milej, D.; Suwalski, M.; Kebaya, L.; Kewin, M.; Yip, L.; de Ribaupierre, S.; Han, V.; Diop, M.; Bhattacharya, S.; et al. Assessing Cerebral Blood Flow, Oxygenation and Cytochrome c Oxidase Stability in Preterm Infants during the First 3 Days after Birth. *Sci Rep* **2022**, *12*, 181, doi:10.1038/s41598-021-03830-7.

191. Durduran, T.; Zhou, C.; Buckley, E.M.; Kim, M.N.; Yu, G.; Choe, R.; Gaynor, J.W.; Spray, T.L.; Durning, S.M.; Mason, S.E.; et al. Optical Measurement of Cerebral Hemodynamics and Oxygen Metabolism in Neonates with Congenital Heart Defects. *J. Biomed. Opt.* **2010**, *15*, 037004, doi:10.1117/1.3425884.

192. Sutin, J.; Vyas, R.; Feldman, H.A.; Ferradal, S.; Hsiao, C.-H.; Zampolli, L.; Pierce, L.J.; Nelson, C.A.; Morton, S.U.; Hay, S.; et al. Association of Cerebral Metabolic Rate Following Therapeutic Hypothermia with 18-Month Neurodevelopmental Outcomes after Neonatal Hypoxic Ischemic Encephalopathy. *eBioMedicine* **2023**, *94*, 104673, doi:10.1016/j.ebiom.2023.104673.

193. Inocencio, I.M.; Kaur, N.; Tran, N.T.; Wong, F.Y. Cerebral Haemodynamic Response to Somatosensory Stimulation in Preterm Lambs Is Enhanced Following Sildenafil and Inhaled Nitric Oxide Administration. *Front. Physiol.* **2023**, *14*, 1101647, doi:10.3389/fphys.2023.1101647.

194. Roche-Labarbe, N.; Fenoglio, A.; Aggarwal, A.; Dehaes, M.; Carp, S.A.; Franceschini, M.A.; Grant, P.E. Near-Infrared Spectroscopy Assessment of Cerebral Oxygen Metabolism in the Developing Premature Brain. *J Cereb Blood Flow Metab* **2012**, *32*, 481–488, doi:10.1038/jcbfm.2011.145.

195. Côté-Corriveau, G.; Simard, M.-N.; Beaulieu, O.; Chowdhury, R.A.; Gagnon, M.-M.; Gagnon, M.; Ledjiar, O.; Bernard, C.; Nuyt, A.M.; Dehaes, M.; et al. Associations between Neurological Examination at Term-Equivalent Age and Cerebral Hemodynamics and Oxygen

Metabolism in Infants Born Preterm. *Front Neurosci* **2023**, *17*, 1105638, doi:10.3389/fnins.2023.1105638.

196. Lin, P.-Y.; Roche-Labarbe, N.; Dehaes, M.; Fenoglio, A.; Grant, P.E.; Franceschini, M.A. Regional and Hemispheric Asymmetries of Cerebral Hemodynamic and Oxygen Metabolism in Newborns. *Cereb Cortex* **2013**, *23*, 339–348, doi:10.1093/cercor/bhs023.

197. Dumont, V.; Giovannella, M.; Zuba, D.; Clouard, R.; Durduran, T.; Guillois, B.; Roche-Labarbe, N. Somatosensory Prediction in the Premature Neonate Brain. *Dev Cogn Neurosci* **2022**, *57*, 101148, doi:10.1016/j.dcn.2022.101148.

198. Busch, D.R.; Lynch, J.M.; Winters, M.E.; McCarthy, A.L.; Newland, J.J.; Ko, T.; Cornaglia, M.A.; Radcliffe, J.; McDonough, J.M.; Samuel, J.; et al. Cerebral Blood Flow Response to Hypercapnia in Children with Obstructive Sleep Apnea Syndrome. *Sleep* **2016**, *39*, 209–216, doi:10.5665/sleep.5350.

199. Nourhashemi, M.; Mahmoudzadeh, M.; Heberle, C.; Wallois, F. Preictal Neuronal and Vascular Activity Precedes the Onset of Childhood Absence Seizure: Direct Current Potential Shifts and Their Correlation with Hemodynamic Activity. *Neurophotonics* **2023**, *10*, 025005, doi:10.1117/1.NPh.10.2.025005.

200. Cowdrick, K.R.; Akbar, M.; Boodooram, T.; Harris, L.H.; Bai, S.; Brothers, R.O.; Arrington, M.; Lee, S.Y.; Khemani, K.; Gee, B.; et al. Impaired Cerebrovascular Reactivity in Pediatric Sickle Cell Disease Using Diffuse Correlation Spectroscopy. *Biomed. Opt. Express* **2023**, *14*, 5696, doi:10.1364/BOE.499274.

201. Rajaram, A.; Yip, L.C.M.; Milej, D.; Suwalski, M.; Kewin, M.; Lo, M.; Carson, J.J.L.; Han, V.; Bhattacharya, S.; Diop, M.; et al. Perfusion and Metabolic Neuromonitoring during Ventricular Taps in Infants with Post-Hemorrhagic Ventricular Dilatation. *Brain Sciences* **2020**, *10*, 452, doi:10.3390/brainsci10070452.

202. Devonshire, I.M.; Papadakis, N.G.; Port, M.; Berwick, J.; Kennerley, A.J.; Mayhew, J.E.W.; Overton, P.G. Neurovascular Coupling Is Brain Region-Dependent. *NeuroImage* **2012**, *59*, 1997–2006, doi:10.1016/j.neuroimage.2011.09.050.

203. Jaillon, F.; Li, J.; Dietsche, G.; Elbert, T.; Gisler, T. Activity of the Human Visual Cortex Measured Non-Invasively by Diffusing-Wave Spectroscopy. *Opt. Express, OE* **2007**, *15*, 6643–6650, doi:10.1364/OE.15.006643.

204. Mesquita, R.C.; Faseyitan, O.K.; Turkeltaub, P.E.; Buckley, E.M.; Thomas, A.; Kim, M.N.; Durduran, T.; Greenberg, J.H.; Detre, J.A.; Yodh, A.G.; et al. Blood Flow and Oxygenation Changes Due to Low-Frequency Repetitive Transcranial Magnetic Stimulation of the Cerebral Cortex. *JBO* **2013**, *18*, 067006, doi:10.1117/1.JBO.18.6.067006.

205. Udina, C.; Avtzi, S.; Mota-Foix, M.; Rosso, A.L.; Ars, J.; Kobayashi Frisk, L.; Gregori-Pla, C.; Durduran, T.; Inzitari, M. Dual-Task Related Frontal Cerebral Blood Flow Changes in Older Adults with Mild Cognitive Impairment: A Functional Diffuse Correlation Spectroscopy Study. *Front Aging Neurosci* **2022**, *14*, 958656, doi:10.3389/fnagi.2022.958656.

206. Edlow, B.L.; Kim, M.N.; Durduran, T.; Zhou, C.; Putt, M.E.; Yodh, A.G.; Greenberg, J.H.; Detre, J.A. The Effects of Healthy Aging on Cerebral Hemodynamic Responses to Posture Change. *Physiol. Meas.* **2010**, *31*, 477, doi:10.1088/0967-3334/31/4/002.

207. Shoemaker, L.N.; Milej, D.; Mistry, J.; St. Lawrence, K. Using Depth-Enhanced Diffuse Correlation Spectroscopy and near-Infrared Spectroscopy to Isolate Cerebral Hemodynamics during Transient Hypotension. *Neurophoton.* **2023**, *10*, doi:10.1117/1.NPh.10.2.025013.

208. Johnson, T.W.; Dar, I.A.; Donohue, K.L.; Xu, Y.Y.; Santiago, E.; Selioutski, O.; Marinescu, M.A.; Maddox, R.K.; Wu, T.T.; Schifitto, G.; et al. Cerebral Blood Flow Hemispheric Asymmetry in Comatose Adults Receiving Extracorporeal Membrane Oxygenation. *Front Neurosci* **2022**, *16*, 858404, doi:10.3389/fnins.2022.858404.

209. Shang, Y.; Cheng, R.; Dong, L.; Ryan, S.J.; Saha, S.P.; Yu, G. Cerebral Monitoring during Carotid Endarterectomy Using Near-Infrared Diffuse Optical Spectroscopies and Electroencephalogram. *Phys. Med. Biol.* **2011**, *56*, 3015, doi:10.1088/0031-9155/56/10/008.

210. Kaya, K.; Zavriyev, A.I.; Orihuela-Espina, F.; Simon, M.V.; LaMuraglia, G.M.; Pierce, E.T.; Franceschini, M.A.; Sunwoo, J. Intraoperative Cerebral Hemodynamic Monitoring during Carotid Endarterectomy via Diffuse Correlation Spectroscopy and Near-Infrared Spectroscopy. *Brain Sci* **2022**, *12*, 1025, doi:10.3390/brainsci12081025.

211. Mesquita, R.C.; Putt, M.; Chandra, M.; Yu, G.; Xing, X.; Han, S.W.; Lech, G.; Shang, Y.; Durduran, T.; Zhou, C.; et al. Diffuse Optical Characterization of an Exercising Patient Group with Peripheral Artery Disease. *J Biomed Opt* **2013**, *18*, 057007, doi:10.1117/1.JBO.18.5.057007.

212. Favilla, C.G.; Mesquita, R.C.; Mullen, M.; Durduran, T.; Lu, X.; Kim, M.N.; Minkoff, D.L.; Kasner, S.E.; Greenberg, J.H.; Yodh, A.G.; et al. Optical Bedside Monitoring of Cerebral Blood Flow in Acute Ischemic Stroke Patients During Head-of-Bed Manipulation. *Stroke* **2014**, *45*, 1269–1274, doi:10.1161/STROKEAHA.113.004116.

213. Wu, K.C.; Sunwoo, J.; Sheriff, F.; Farzam, P.; Farzam, P.Y.; Orihuela-Espina, F.; LaRose, S.L.; Monk, A.D.; Aziz-Sultan, M.A.; Patel, N.; et al. Validation of Diffuse Correlation Spectroscopy Measures of Critical Closing Pressure against Transcranial Doppler Ultrasound in Stroke Patients. *JBO* **2021**, *26*, 036008, doi:10.1117/1.JBO.26.3.036008.

214. Kim, M.N.; Edlow, B.L.; Durduran, T.; Frangos, S.; Mesquita, R.C.; Levine, J.M.; Greenberg, J.H.; Yodh, A.G.; Detre, J.A. Continuous Optical Monitoring of Cerebral Hemodynamics during Head-of-Bed Manipulation in Brain-Injured Adults. *Neurocrit Care* **2014**, *20*, 443–453, doi:10.1007/s12028-013-9849-7.

215. Shang, Y.; Gurley, K.; Symons, B.; Long, D.; Srikuea, R.; Crofford, L.J.; Peterson, C.A.; Yu, G. Noninvasive Optical Characterization of Muscle Blood Flow, Oxygenation, and Metabolism in Women with Fibromyalgia. *Arthritis Res Ther* **2012**, *14*, R236, doi:10.1186/ar4079.

216. Matsuda, Y.; Nakabayashi, M.; Suzuki, T.; Zhang, S.; Ichinose, M.; Ono, Y. Evaluation of Local Skeletal Muscle Blood Flow in Manipulative Therapy by Diffuse Correlation Spectroscopy. *Front. Bioeng. Biotechnol.* **2022**, *9*, doi:10.3389/fbioe.2021.800051.

217. Bangalore-Yogananda, C.-G.; Rosenberry, R.; Soni, S.; Liu, H.; Nelson, M.D.; Tian, F. Concurrent Measurement of Skeletal Muscle Blood Flow during Exercise with Diffuse Correlation Spectroscopy and Doppler Ultrasound. *Biomed Opt Express* **2017**, *9*, 131–141, doi:10.1364/BOE.9.000131.

218. Gurley, K.; Shang, Y.; Yu, G. Noninvasive Optical Quantification of Absolute Blood Flow, Blood Oxygenation, and Oxygen Consumption Rate in Exercising Skeletal Muscle. *J. Biomed. Opt* **2012**, *17*, 0750101, doi:10.1117/1.JBO.17.7.075010.

219. Henry, B.; Zhao, M.; Shang, Y.; Uhl, T.; Thomas, D.T.; Xenos, E.S.; Saha, S.P.; Yu, G. Hybrid Diffuse Optical Techniques for Continuous Hemodynamic Measurement in Gastrocnemius during Plantar Flexion Exercise. *J. Biomed. Opt* **2015**, *20*, 125006, doi:10.1117/1.JBO.20.12.125006.

220. Sunar, U.; Rohrbach, D.; Rigual, N.; Tracy, E.; Keymel, K.; Cooper, M.T.; Baumann, H.; Henderson, B.H. Monitoring Photobleaching and Hemodynamic Responses to HPPH-Mediated Photodynamic Therapy of Head and Neck Cancer: A Case Report. *Opt. Express* **2010**, *18*, 14969, doi:10.1364/OE.18.014969.

221. Yu, G. Near-Infrared Diffuse Correlation Spectroscopy in Cancer Diagnosis and Therapy Monitoring. *J. Biomed. Opt.* **2012**, *17*, 010901, doi:10.1117/1.JBO.17.1.010901.

222. Li, T.; Lin, Y.; Shang, Y.; He, L.; Huang, C.; Szabunio, M.; Yu, G. Simultaneous Measurement of Deep Tissue Blood Flow and Oxygenation Using Noncontact Diffuse Correlation Spectroscopy Flow-Oximeter. *Sci Rep* **2013**, *3*, 1358, doi:10.1038/srep01358.

223. Dong, L.; Kudrimoti, M.; Irwin, D.; Chen, L.; Kumar, S.; Shang, Y.; Huang, C.; Johnson, E.L.; Stevens, S.D.; Shelton, B.J.; et al. Diffuse Optical Measurements of Head and Neck

Tumor Hemodynamics for Early Prediction of Chemoradiation Therapy Outcomes. *J. Biomed. Opt* **2016**, *21*, 085004, doi:10.1117/1.JBO.21.8.085004.

224. Poon, C.-S.; Langri, D.S.; Rinehart, B.; Rambo, T.M.; Miller, A.J.; Foreman, B.; Sunar, U. First-in-Clinical Application of a Time-Gated Diffuse Correlation Spectroscopy System at 1064 Nm Using Superconducting Nanowire Single Photon Detectors in a Neuro Intensive Care Unit. *Biomed Opt Express* **2022**, *13*, 1344–1356, doi:10.1364/BOE.448135.

225. Tagliabue, S.; Lindner, C.; da Prat, I.C.; Sanchez-Guerrero, A.; Serra, I.; Kacprzak, M.; Maruccia, F.; Silva, O.M.; Weigel, U.M.; de Nadal, M.; et al. Comparison of Cerebral Metabolic Rate of Oxygen, Blood Flow, and Bispectral Index under General Anesthesia. *Neurophotonics* **2023**, *10*, 015006, doi:10.1117/1.NPh.10.1.015006.

226. Mourant, J.R.; Fuselier, T.; Boyer, J.; Johnson, T.M.; Bigio, I.J. Predictions and Measurements of Scattering and Absorption over Broad Wavelength Ranges in Tissue Phantoms. *Appl Opt* **1997**, *36*, 949–957, doi:10.1364/ao.36.000949.

227. Ntziachristos, V. Going Deeper than Microscopy: The Optical Imaging Frontier in Biology. *Nat Methods* **2010**, *7*, 603–614, doi:10.1038/nmeth.1483.

228. Assorted Spectra Available online: https://omlc.org/spectra/ (accessed on 14 May 2024).

229. Goodman, J.W. Some Fundamental Properties of Speckle*. *J. Opt. Soc. Am.* **1976**, *66*, 1145, doi:10.1364/JOSA.66.001145.

230. Hua, T.; Xie, H.; Wang, S.; Hu, Z.; Chen, P.; Zhang, Q. Evaluation of the Quality of a Speckle Pattern in the Digital Image Correlation Method by Mean Subset Fluctuation. *Optics & Laser Technology* **2011**, *43*, 9–13, doi:10.1016/j.optlastec.2010.04.010.

231. Lecompte, D.; Smits, A.; Bossuyt, S.; Sol, H.; Vantomme, J.; Van Hemelrijck, D.; Habraken, A.M. Quality Assessment of Speckle Patterns for Digital Image Correlation. *Optics and Lasers in Engineering* **2006**, *44*, 1132–1145, doi:10.1016/j.optlaseng.2005.10.004.

232. Moreira, A.; Prats-Iraola, P.; Younis, M.; Krieger, G.; Hajnsek, I.; Papathanassiou, K.P. A Tutorial on Synthetic Aperture Radar. *IEEE Geosci. Remote Sens. Mag.* **2013**, *1*, 6–43, doi:10.1109/MGRS.2013.2248301.

233. Sandhu, R.; Singh, N.; Dhankhar, J.; Gandhi, K.; Sharma, R. Dynamic Light Scattering (DLS) Technique, Principle, Theoretical Considerations and Applications.

234. Stetefeld, J.; McKenna, S.A.; Patel, T.R. Dynamic Light Scattering: A Practical Guide and Applications in Biomedical Sciences. *Biophys Rev* **2016**, *8*, 409–427, doi:10.1007/s12551-016-0218-6.

235. Cao, A. Light Scattering. Recent Applications. *Analytical Letters* **2003**, *36*, 3185–3225, doi:10.1081/AL-120026567.

236. *Optical Methods and Instrumentation in Brain Imaging and Therapy*; Madsen, S.J., Ed.; Springer New York: New York, NY, 2013; ISBN 978-1-4614-4977-5.
237. Ninck, M.; Untenberger, M.; Gisler, T. Diffusing-Wave Spectroscopy with Dynamic Contrast Variation: Disentangling the Effects of Blood Flow and Extravascular Tissue Shearing on Signals from Deep Tissue. *Biomed. Opt. Express* **2010**, *1*, 1502, doi:10.1364/BOE.1.001502.
238. Boas, D.A. DIFFUSE PHOTON PROBES OF STRUCTURAL AND DYNAMICAL PROPERTIES OF TURBID MEDIA: THEORY AND BIOMEDICAL APPLICATIONS.
239. Kienle, A.; Patterson, M.S. Determination of the Optical Properties of Semi-Infinite Turbid Media from Frequency-Domain Reflectance Close to the Source. *Phys. Med. Biol.* **1997**, *42*, 1801–1819, doi:10.1088/0031-9155/42/9/011.
240. Durduran, T. Noninvasive Measurements of Tissue Hemodynamics with Hybrid Diffuse Optical Methods. *Med. Phys.* **2004**, *31*, 2178–2178, doi:10.1118/1.1763412.
241. Forti, R.M.; Hobson, L.J.; Benson, E.J.; Ko, T.S.; Ranieri, N.R.; Laurent, G.; Weeks, M.K.; Widmann, N.J.; Morton, S.; Davis, A.M.; et al. Non-Invasive Diffuse Optical Monitoring of Cerebral Physiology in an Adult Swine-Model of Impact Traumatic Brain Injury. *Biomed. Opt. Express* **2023**, *14*, 2432, doi:10.1364/BOE.486363.
242. Koban, L.; Ninck, M.; Li, J.; Gisler, T.; Kissler, J. Processing of Emotional Words Measured Simultaneously with Steady-State Visually Evoked Potentials and near-Infrared Diffusing-Wave Spectroscopy. *BMC Neurosci* **2010**, *11*, 85, doi:10.1186/1471-2202-11-85.
243. Zirak, P.; Delgado-Mederos, R.; Martí-Fàbregas, J.; Durduran, T. Effects of Acetazolamide on the Micro- and Macro-Vascular Cerebral Hemodynamics: A Diffuse Optical and Transcranial Doppler Ultrasound Study. *Biomed. Opt. Express* **2010**, *1*, 1443, doi:10.1364/BOE.1.001443.
244. Shang, Y.; Zhao, Y.; Cheng, R.; Dong, L.; Irwin, D.; Yu, G. Portable Optical Tissue Flow Oximeter Based on Diffuse Correlation Spectroscopy. *Opt. Lett.* **2009**, *34*, 3556, doi:10.1364/OL.34.003556.
245. Ackerson, B.J.; Dougherty, R.L.; Reguigui, N.M.; Nobbmann, U. Correlation Transfer - Application of Radiative Transfer Solution Methods to Photon Correlation Problems. *Journal of Thermophysics and Heat Transfer* **1992**, *6*, 577–588, doi:10.2514/3.11537.
246. Dougherty, R.L.; Ackerson, B.J.; Reguigui, N.M.; Dorri-Nowkoorani, F.; Nobbmann, U. Correlation Transfer: Development and Application. *Journal of Quantitative Spectroscopy and Radiative Transfer* **1994**, *52*, 713–727, doi:10.1016/0022-4073(94)90037-X.

247. Kienle, A.; Patterson, M.S.; Dögnitz, N.; Bays, R.; Wagnières, G.; Van Den Bergh, H. Noninvasive Determination of the Optical Properties of Two-Layered Turbid Media. *Appl. Opt.* **1998**, *37*, 779, doi:10.1364/AO.37.000779.

248. Gagnon, L.; Gauthier, C.; Hoge, R.D.; Lesage, F.; Selb, J.; Boas, D.A. Double-Layer Estimation of Intra- and Extracerebral Hemoglobin Concentration with a Time-Resolved System. *J. Biomed. Opt.* **2008**, *13*, 054019, doi:10.1117/1.2982524.

249. Lesage, F.; Gagnon, L.; Dehaes, M. Diffuse Optical-MRI Fusion and Applications.; Azar, F.S., Intes, X., Eds.; San Jose, CA, February 7 2008; p. 68500C.

250. Kienle, A.; Glanzmann, T. *In Vivo* Determination of the Optical Properties of Muscle with Time-Resolved Reflectance Using a Layered Model. *Phys. Med. Biol.* **1999**, *44*, 2689–2702, doi:10.1088/0031-9155/44/11/301.

251. Mesquita, R.C.; Durduran, T.; Yu, G.; Buckley, E.M.; Kim, M.N.; Zhou, C.; Choe, R.; Sunar, U.; Yodh, A.G. Direct Measurement of Tissue Blood Flow and Metabolism with Diffuse Optics. *Phil. Trans. R. Soc. A.* **2011**, *369*, 4390–4406, doi:10.1098/rsta.2011.0232.

252. Farrell, T.J.; Patterson, M.S.; Wilson, B. A Diffusion Theory Model of Spatially Resolved, Steady-State Diffuse Reflectance for the Noninvasive Determination of Tissue Optical Properties *in Vivo*. *Med. Phys.* **1992**, *19*, 879–888, doi:10.1118/1.596777.

253. Kienle, A.; Patterson, M.S. Improved Solutions of the Steady-State and the Time-Resolved Diffusion Equations for Reflectance from a Semi-Infinite Turbid Medium. *J. Opt. Soc. Am. A* **1997**, *14*, 246, doi:10.1364/JOSAA.14.000246.

254. Li, J.; Qiu, L.; Poon, C.-S.; Sunar, U. Analytical Models for Time-Domain Diffuse Correlation Spectroscopy for Multi-Layer and Heterogeneous Turbid Media. *Biomed. Opt. Express* **2017**, *8*, 5518, doi:10.1364/BOE.8.005518.

255. Schätzel, K. Noise in Photon Correlation and Photon Structure Functions. *Optica Acta: International Journal of Optics* **1983**, *30*, 155–166, doi:10.1080/713821145.

256. Koppel, D.E. Statistical Accuracy in Fluorescence Correlation Spectroscopy. *Phys. Rev. A* **1974**, *10*, 1938–1945, doi:10.1103/PhysRevA.10.1938.

257. Helton, M.; Rajasekhar, S.; Zerafa, S.; Vishwanath, K.; Mycek, M.-A. Numerical Approach to Quantify Depth-Dependent Blood Flow Changes in Real-Time Using the Diffusion Equation with Continuous-Wave and Time-Domain Diffuse Correlation Spectroscopy. *Biomed. Opt. Express* **2023**, *14*, 367, doi:10.1364/BOE.469419.

258. Dong, L.; He, L.; Lin, Y.; Shang, Y.; Yu, G. Simultaneously Extracting Multiple Parameters via Fitting One Single Autocorrelation Function Curve in Diffuse Correlation

Spectroscopy. *IEEE Trans. Biomed. Eng.* **2013**, *60*, 361–368, doi:10.1109/TBME.2012.2226885.

259. Bishop, C.M. Neural Networks for Pattern Recognition.

260. Jordan, M.I.; Mitchell, T.M. Machine Learning: Trends, Perspectives, and Prospects. *ARTIFICIAL INTELLIGENCE*.

261. Ripley, B.D. Pattern Recognition via Neural Networks.

262. Karhunen, J.; Raiko, T.; Cho, K. Chapter 7 - Unsupervised Deep Learning: A Short Review. In *Advances in Independent Component Analysis and Learning Machines*; Bingham, E., Kaski, S., Laaksonen, J., Lampinen, J., Eds.; Academic Press, 2015; pp. 125–142 ISBN 978-0-12-802806-3.

263. Jing, L.; Tian, Y. Self-Supervised Visual Feature Learning With Deep Neural Networks: A Survey. *IEEE Trans. Pattern Anal. Mach. Intell.* **2021**, *43*, 4037–4058, doi:10.1109/TPAMI.2020.2992393.

264. Zhu, X.; Goldberg, A.B. *Introduction to Semi-Supervised Learning*; Synthesis Lectures on Artificial Intelligence and Machine Learning; Springer International Publishing: Cham, 2009; ISBN 978-3-031-00420-9.

265. Girija, S.S. TensorFlow: Large-Scale Machine Learning on Heterogeneous Distributed Systems.

266. Paszke, A.; Gross, S.; Massa, F.; Lerer, A.; Bradbury, J.; Chanan, G.; Killeen, T.; Lin, Z.; Gimelshein, N.; Antiga, L.; et al. PyTorch: An Imperative Style, High-Performance Deep Learning Library.

267. Hochreiter, S.; Schmidhuber, J. Long Short-Term Memory. *Neural Comput* **1997**, *9*, 1735–1780, doi:10.1162/neco.1997.9.8.1735.

268. Pradhan, P.; Guo, S.; Ryabchykov, O.; Popp, J.; Bocklitz, T.W. Deep Learning a Boon for Biophotonics? *Journal of Biophotonics* **2020**, *13*, e201960186, doi:10.1002/jbio.201960186.

269. Zhu, X.; Sobhani, P.; Guo, H. Long Short-Term Memory Over Recursive Structures.

270. Le Cun, Y.; Jackel, L.D.; Boser, B.; Denker, J.S.; Graf, H.P.; Guyon, I.; Henderson, D.; Howard, R.E.; Hubbard, W. Handwritten Digit Recognition: Applications of Neural Network Chips and Automatic Learning. *IEEE Commun. Mag.* **1989**, *27*, 41–46, doi:10.1109/35.41400.

271. Agarap, A.F. Deep Learning Using Rectified Linear Units (ReLU) 2019.

272. Karlik, B.; Olgac, A.V. Performance Analysis of Various Activation Functions in Generalized MLP Architectures of Neural Networks.

273. Xu, G.; Ren, T.; Chen, Y.; Che, W. A One-Dimensional CNN-LSTM Model for Epileptic Seizure Recognition Using EEG Signal Analysis. *Front. Neurosci.* **2020**, *14*, 578126, doi:10.3389/fnins.2020.578126.

274. Xiao, D.; Chen, Y.; Li, D.D.-U. One-Dimensional Deep Learning Architecture for Fast Fluorescence Lifetime Imaging. *IEEE J. Select. Topics Quantum Electron.* **2021**, *27*, 1–10, doi:10.1109/JSTQE.2021.3049349.

275. Ioffe, S.; Szegedy, C. Batch Normalization: Accelerating Deep Network Training by Reducing Internal Covariate Shift 2015.

276. Selb, J.; Stott, J.J.; Franceschini, M.A.; Sorensen, A.G.; Boas, D.A. Improved Sensitivity to Cerebral Hemodynamics during Brain Activation with a Time-Gated Optical System: Analytical Model and Experimental Validation. *J. Biomed. Opt.* **2005**, *10*, 011013, doi:10.1117/1.1852553.

277. Selb, J.; Boas, D.A.; Chan, S.-T.; Evans, K.C.; Buckley, E.M.; Carp, S.A. Sensitivity of Near-Infrared Spectroscopy and Diffuse Correlation Spectroscopy to Brain Hemodynamics: Simulations and Experimental Findings during Hypercapnia. *Neurophoton* **2014**, *1*, 015005, doi:10.1117/1.NPh.1.1.015005.

278. Fang, Q.; Boas, D.A. Monte Carlo Simulation of Photon Migration in 3D Turbid Media Accelerated by Graphics Processing Units. *Opt. Express* **2009**, *17*, 20178, doi:10.1364/OE.17.020178.

279. Wang, Q.; Li, Y.; Xiao, D.; Zang, Z.; Jiao, Z.; Chen, Y.; Li, D.D.U. Simple and Robust Deep Learning Approach for Fast Fluorescence Lifetime Imaging. *Sensors* **2022**, *22*, 7293, doi:10.3390/s22197293.

280. Henderson, R.K.; Johnston, N.; Mattioli Della Rocca, F.; Chen, H.; Day-Uei Li, D.; Hungerford, G.; Hirsch, R.; Mcloskey, D.; Yip, P.; Birch, D.J.S. A 192×128 Time Correlated SPAD Image Sensor in 40-Nm CMOS Technology. *IEEE J. Solid-State Circuits* **2019**, *54*, 1907–1916, doi:10.1109/JSSC.2019.2905163.

281. Pellegrini, S.; Rae, B.; Pingault, A.; Golanski, D.; Jouan, S.; Lapeyre, C.; Mamdy, B. Industrialised SPAD in 40 Nm Technology. In Proceedings of the 2017 IEEE International Electron Devices Meeting (IEDM); IEEE: San Francisco, CA, USA, December 2017; p. 16.5.1-16.5.4.

282. Freund, I. Joseph W. Goodman: Speckle Phenomena in Optics: Theory and Applications: Roberts & Company (Englewood, Colorado), 2007. *J Stat Phys* **2007**, *130*, 413–414, doi:10.1007/s10955-007-9440-8.

283. Marti, D.; Aasbjerg, R.N.; Andersen, P.E.; Hansen, A.K. MCmatlab: An Open-Source, User-Friendly, MATLAB-Integrated Three-Dimensional Monte Carlo Light Transport Solver with Heat Diffusion and Tissue Damage. *J. Biomed. Opt.* **2018**, *23*, 1, doi:10.1117/1.JBO.23.12.121622.

284. S. Jacques, T. Li, and S. Prahl, "MCXYZ," OMLC, 2019, Https://Omlc.Org/Software/Mc/Mcxyz/Index.Html.

285. A. J. F. Siegert *On the Fluctuations In Signals Returned by Many Independently Moving Scatterers*; Massachusetts Institute of Technology, 1943;

286. Fercher, A.F.; Briers, J.D. Flow Visualization by Means of Single-Exposure Speckle Photography. *Optics Communications* **1981**, *37*, 326–330, doi:10.1016/0030-4018(81)90428-4.